

UNIVERSITAT POLITÈCNICA DE VALÈNCIA

Departamento de Comunicaciones



Photonic Millimeter Wave Signal Generation and Transmission Over Hybrid Links in 5G Communication Networks

Ph. D. Thesis

by

Luis Vallejo Castro

Supervisor: Dr. Beatriz Ortega Tamarit

Valencia, September 2022

Universitat Politècnica de València

Institute of Telecommunications and Multimedia Applications

Photonics Research Labs

8G Building

Cno. de Vera, s/n

46022, Valencia

Spain

Tel: +34 963879580

Web: www.iteam.upv.es - www.prl.upv.es

E-mail: info@iteam.upv.es

Veni, Vidi, Vici.
- Julio Cesar

*To my father,
who never saw this adventure.
To my loved ones,
for their support and encouragement.*

About the author

Luis Vallejo Castro was born in Malaga, Andalucia, Spain, in 1991. He received the B. Sc. and the M. Sc. Degree in Telecommunication Engineering from Universidad de Malaga, Malaga, Spain, in 2016 and 2017, respectively. During his postgraduated Erasums program in 2017, he submitted and defended the Master Thesis, based on low noise amplifiers, at Universitat Kassel, Kassel, Germany.

From November 2017 to February 2018, he worked as a Test & Verification Engineer, in particular with GS-8800 and GS-9000 Test Systems and 2G/3G/A-GPS samples management led by Emilio Mira Escarti, at Keysight Technologies, Malaga, Spain.

In March 2018, he started his Ph. D. and joined to the Instituto de Telecomunicaciones y Aplicaciones Multimedia (iTEAM), Photonic Research Labs (PRL), Universitat Politecnica de Valencia, Valencia, Spain. His Ph. D., under the supervision of Dr. Beatriz Ortega Tamarit, is focused on microwave photonics, millimeter wave (mmW) signal generation, radio over fiber/free-space optics (RoF/FSO) for 5G and beyond, and optical access networks. During his Ph. D., he spent one month in 2019 and two months in 2021 stay in Czech Technical University (CTU) in Prague, Prague, Czech Republic, under the supervision of Prof. Stanislav Zvánovec. At CTU, he collaborated and carried out experiments based on mmW signal generation and transmission over hybrid fiber/FSO links and wireless transmission at mmW frequencies. He has been author or co-author of over 20 papers and conference contributions covering a wide range of fields related microwave photonics and optical networks.

Since January 2022, he joined, as a postdoctoral researcher, the Bangor University's Digital Signal Processing (DSP) Centre of Excellence, Bangor University, Bangor, United Kingdom, led by Prof. Jianming Tang. His current research focuses on mmW signal generation using free-running lasers, data transmission at mmW frequencies over hybrid optical fiber/FSO, wireless links at mmW frequencies and optical access networks.

He can be contacted at luivalc2@iteam.upv.es, l.vallejocastro@bangor.ac.uk and luis.valca91@gmail.com.

OrCID: [0000-0001-8028-6608](https://orcid.org/0000-0001-8028-6608)

ResearcherID: [F-6508-2019](https://orcid.org/F-6508-2019)

Web: www.prl.upv.es - www.dsp-centre.bangor.ac.uk

Bangor, United Kingdom, July 2022

Acknowledgements

My journey started when I finished the M. Sc. in Telecommunications Engineering at Universidad de Malaga in 2017. I was working at Keysight Technologies, when I applied the Ph. D. position at Universitat Politecnica de Valencia. In the early 2018, two months after the first phone call from my future supervisor, I moved to Valencia and my Ph. D. began. My Ph. D. life was like undertaking a four-year challenging and exciting journey with loads of memorable experience. Over the years, it has been a period of intense learning for me both personally and professionally. The success and final outcome of this Thesis required consistent guidance, constant support and motivation. Writing this Thesis has had a significant impact on me. To be honest, it has not finished yet.

First and foremost, I would like to sincerely thank and give my Eternal Gratitude to my advisor Dr. Beatriz Ortega Tamarit, Bea, for giving me the opportunity to start this adventure and participate in the research group, and for asking interesting questions which helped to shape the directions this Thesis. I extend my gratitude for her excellent guidance, (vast) patience and (gigantic) dedication, for providing me with an excellent atmosphere to carry out research and for helping me regardless of the time of day. Working with her has made me to grow professionally. She is not only an advisor for my academic and research work, but also a mentor for my future career, and life. I hope I did not disappoint her.

I want to express my gratitude to Dr. José Mora Almerich and Dr. Vicenç Almenar Terré. Although we did not make lot of works together, both helped and advised me anytime and anywhere.

I would like to acknowledgment my colleagues in the Photonics Research Labs for maintaining a friendly atmosphere at work. In particular, I want to thank you Ana, Erika and Aitor for all the “fruitful” discussions, including gossips, which actually helped me academically and personally. I miss our breakfasts, coffee and lunches. I also want to thank Juan A. for our short period together under Bea’s supervision in Valencia. I am sure that our walk of life will cross again.

I was very honoured to have had the chance of collaborating with the Wireless and Fiber Optics team at Czech Technical University in Prague led by Prof. Stanislav Zvánovec. I visited Prague twice during my Ph. D. and you (all) made me feel like my home. If I get a chance visit you third time, I would stay there. Děkuji vám: Stan, Jan, Matěj, Shivani and Ailing.

Another person, who I am also deeply indebted to, is my friend Dong, Dr. Dong-Nhat Nguyen, and his lovely wife, Ái. Since we met, working with him and life out work was always easy in Prague, Valencia or anywhere. In addition, his fantastic experimental and simulations skills, his endless energy, enthusiasm, patience, and idea creation to research always motivated and inspired me. Much experimental work would not have been done without his help in the in-depth suggestions and experimental preparation.

I am also very grateful to Prof. Jianming Tang of Bangor University’s Digital Signal Processing Centre of Excellence for giving me the opportunity to be part of his group, and his patience. I also would like to show my gratitude to my colleagues at Bangor University: Shan, Omaro, JP and Tushar.

This Section would not be finished without a special thanks to my family, especially my mother, and my sister and brother-in-law, and my brothers for their unconditional support. They were always there for me.

Of course, I cannot forget my friends who were always available every time. For Málaga: thank Pepe, Jeni, Alex and Vanessa; you make my life happier every time I come back home. For Valencia: thank Nùria, Hugo, Cristina, María, Carlos, Lucía; you make me Valencia more beautiful.

Furthermore, I would like to acknowledge the financial support given by Research Excellence Award Programme GVA PROMETEO 2017/103 *Future Microwave Photonics* and

European Network for High Performance Integrated Microwave Photonics (EUIMWP)
CA16220.

Last but not least, my thanks to the people who dropped out this journey.

Bangor, United Kingdom, July 2022

Contents

CONTENTS	XI
LIST OF FIGURES	XIII
LIST OF TABLES	XIX
LIST OF ACRONYMS	XXI
ABSTRACT	XXV
RESUMEN	XXVII
RESUM	XXIX
CHAPTER 1. INTRODUCTION	1
1.1. CONTEXT.....	1
1.1.1. Evolution of mobile wireless systems	1
1.1.2. On the way to 5G.....	2
1.1.3. Motivation for this Thesis	5
1.2. OBJECTIVES	6
1.3. THESIS STRUCTURE	7
CHAPTER 2. ENABLING ARCHITECTURES AND TECHNOLOGIES FOR 5G NETWORKS	9
2.1. CLOUD-RADIO ACCESS NETWORK.....	9
2.1.1. Evolution of radio access networks	9
2.1.2. C-RAN architecture.....	10
2.2. MILLIMETER WAVES.....	13
2.3. MICROWAVE PHOTONICS TECHNOLOGIES IN 5G	15
2.3.1. Photonic signal generation	15
2.3.2. Radio over fiber signal transmission.....	25
2.4. FREE-SPACE OPTICS	29
2.4.1. FSO scheme	29
2.4.2. FSO limitations	30
2.4.3. FSO applications	32
2.5. CONCLUSIONS	33
CHAPTER 3. PHOTONIC MMW SIGNAL GENERATION BASED ON CARRIER- SUPPRESSED EXTERNAL MODULATION	35
3.1. ANALYTICAL FORMULATION.....	35
3.2. EXPERIMENTAL SETUP AND CHARACTERIZATION	37
3.3. MULTIPLE SIGNAL GENERATION.....	40
3.4. RECONFIGURABLE MMW SIGNAL GENERATION	43
3.5. FOUR-WAVE MIXING AIDED SIGNAL GENERATION	45
3.6. IMPACT OF TURBULENT FSO ON PHOTONICALLY MMW GENERATED SIGNALS	47
3.7. CONCLUSIONS	51
CHAPTER 4. DML-BASED DATA TRANSMISSION OVER PHOTONICALLY GENERATED MMW SIGNALS	53
4.1. DIRECTLY MODULATED LASERS.....	53
4.2. ANALYTICAL FORMULATION AND LINK FREQUENCY RESPONSE FOR DML-BASED LINKS	55
4.3. TRANSMISSION MEASUREMENTS OVER LOCALLY AND REMOTELY GENERATED MMW SIGNALS.	59
4.3.1. Evaluation of links performance	59
4.3.2. Evaluation of non-linear distortions	65
4.4. USABILITY OF AN OPTICAL FRONTHAUL OPERATING AT 40 GHZ	75
4.4.1. Simulations	75

4.4.2. Experimental system capability	79
4.4.3. Multiband measurements	82
4.5. CONCLUSIONS	83
CHAPTER 5. EXTERNAL MODULATION-BASED DATA TRANSMISSION OVER PHOTONICALLY GENERATED MMW.....	85
5.1. EXTERNAL DATA MODULATION.....	85
5.2. OPTICAL CS-DSB SIGNAL TRANSMISSION.....	86
5.3. COMPARISON OF DSB AND CS-DSB SCHEMES	89
5.4. IMPACT OF FSO TURBULENCES ON DATA TRANSMISSION	92
5.4.1. Impact of turbulence strength	92
5.4.2. Impact of non-uniform turbulent distributions	93
5.5. CONCLUSIONS	99
CHAPTER 6. BIDIRECTIONAL FRONTHAUL LINKS	101
6.1. FULL-DUPLEX TRANSMISSION OF 5G NR SIGNALS IN 39 GHZ BAND.....	101
6.1.1. Downlink characterization	102
6.1.2. Uplink characterization	105
6.2. HETEROGENOUS 60/25 GHZ SIGNAL TRANSMISSION.....	106
6.2.1. Experimental setup and system optimization	106
6.2.2. Bidirectional signal transmission measurements.....	109
6.3. CONCLUSIONS	111
CHAPTER 7. CONCLUSIONS AND FUTURE WORK	113
7.1. CONCLUSIONS	113
7.2. FUTURE WORK	114
APPENDIX A.....	117
A.1. COMPLEX DATA SIGNAL ON IM-DD SYSTEMS	117
A.2. ERROR VECTOR MAGNITUDE.....	118
A.3. BIT ERROR RATE	119
A.4. SIGNAL GENERATORS AND ANALYZERS.....	120
LIST OF PUBLICATIONS.....	123
JOURNALS	123
CONFERENCE PROCEEDINGS	124
REFERENCES	127

List of figures

Figure 1.1. Evolution of mobile wireless systems.	1
Figure 1.2. Global mobile devices trend.....	2
Figure 1.3. Usage scenarios of IMT for 2020 [4].....	3
Figure 1.4. Key capabilities (a) and their importance in different usage scenarios (b) for 5G networks [4].	4
Figure 1.5. Enabling technologies to shape the 5G requirements.....	5
Figure 2.1. RAN architecture evolution: (a) traditional base station, (b) base station splitted into RRH and BBU and (c) C-RAN with RRHs.	10
Figure 2.2. C-RAN architecture.	11
Figure 2.3. Example of a city network based on optical fiber and FSO fronthaul links.	12
Figure 2.4. C-RAN structures: (a) fully and (b) partially centralized.	13
Figure 2.5. (a) Atmospheric gas spectral attenuation and (b) free space loss.	15
Figure 2.6. Basic scheme of a microwave photonic link.	15
Figure 2.7. Basic scheme of photonic mmW signal generation: photomixing.	16
Figure 2.8. Classification of photonic mmW signal generation techniques.....	17
Figure 2.9. Optical injection locking of two slave lasers.	17
Figure 2.10. Scheme of an optical phase lock loop.	18
Figure 2.11. Scheme of an optical injection locking and phase locking system.....	19
Figure 2.12. (a) Dual-wavelength scheme based on a fiber ring laser and (b) spectra of the two cascaded FBGs [48].	19
Figure 2.13. (a) Optical spectrum of mode locked laser, (b) zoom of the frequency comb with 10 GHz FSR, (c) electrical spectrum at 70 GHz and (d) electrical spectrum at 120 GHz [54].	20
Figure 2.14. (a) Optical spectrum of SC light source (bottom shows magnified scale) and (b) SSB phase noise of 50 GHz generated signals [60].....	21
Figure 2.15. (a) Photonic integrated waveguide electro-optic phase modulator in perspective view, (b) schematic diagram of mmW generation using PM and (c) optical spectrum at the output of the PM.	22
Figure 2.16. Mach-Zehnder structures: (a) single drive and (b) dual-drive.	23
Figure 2.17. Diagram of FWM-aided photonic mmW signal generation.....	24
Figure 2.18. Schematic diagram for mmW signal generation based on SBS. Insets shows the principle of selective sideband amplification.	25
Figure 2.19. Typical RoF link schematic using: (a) directly and (b) external modulation.	26
Figure 2.20. RoF links based on (a) D-RoF and (b) A-RoF.	27
Figure 2.21. RoF schemes based on different electrical carrier frequency signals.....	27
Figure 2.22. (a) FSO system layout, (b) Thorlabs 50-1550A-APC Single Mode Pigtailed GRIN Fiber Collimator and (c) Thorlabs F810APC-1550 Air-Spaced Doublet Collimator.....	29
Figure 2.23. (a) Wavelength attenuation under clear weather conditions due to absorption [11], (b) attenuation vs visibility during heavy fog [94].	30
Figure 2.24. General schematic of a FSO link.	31
Figure 2.25. Example of thermal turbulences in a typical scenario [100].	31
Figure 3.1. (a) Diagram of typical optical sidebands generated by a MZM and (b) normalized power and field curves vs bias voltage of MZM.	37
Figure 3.2. Experimental setup of 40 - 90 GHz mmW signal generation [107].	38
Figure 3.3. (a) Measured optical spectra at the PD input for OB2B, 10 km SSMF link, and 10 km SSMF and 70 cm FSO link; and (b) RF power spectrum for OB2B.....	39
Figure 3.4. (a) Side-mode suppression ratio (RBW = 0.02 nm) and (b) RF electrical power (RBW = 3 kHz) vs frequency signal.	39
Figure 3.5. Schematic layout of multiple mmW signal generation and distribution system. Insets show: (i) output spectral response of 8 channel AWG with 100 GHz channel spacing	

and (ii) measured output/input power-voltage characteristic of MZM-1/2 as function of the bias voltage [108].	40
Figure 3.6. Measured optical spectra at PD input (RBW = 0.02 nm): (a) port #1: $\lambda_1 = 1549.90$ nm, $f_{RF1} = 7$ GHz and (b) port #3: $\lambda_2 = 1551.52$ nm, $f_{RF2} = 12$ GHz.	41
Figure 3.7. (a) Electrical spectrum at $f_{mmW1} = 14$ GHz (port #1, $\lambda_1 = 1549.90$ nm), (b) electrical spectrum $f_{mmW3} = 24$ GHz (port #3, $\lambda_2 = 1551.52$ nm) and (c) RF power level measured at different scenarios.	42
Figure 3.8. Phase noise level measured at different scenarios (RBW = 10 kHz). Inset show the phase noise measurement at scenario F for channel 1 (port #1, $f_{mmW1} = 14$ GHz, $\lambda_1 = 1549.90$ nm) and 3 (port #3, at $f_{mmW3} = 24$ GHz, $\lambda_2 = 1551.52$ nm).	43
Figure 3.9. Experimental setup of photonic multiple mmW signal generation and dynamically reconfigurable signal distribution. Inset shows the optical spectrum of five multiplexed optical channels when CH#1 and #2 are modulated by 20 and 15 GHz, respectively.	43
Figure 3.10. Measurements at different BSs after hybrid SSMF/FSO transmission when optical signal is launched into AWG port #2: (a) optical and (b) electrical spectra.	44
Figure 3.11. (a) AWG algorithm routing: BS# where the signal is radiated versus optical carrier wavelength when is launched into different AWG inputs and (b) RF spectrum at 40 GHz (carried by 1547.47 nm) generated at different BS according to the AWG input port (span = 1 MHz).	45
Figure 3.12. Experimental setup of SOA-aided photonic signal generation [109].	45
Figure 3.13. Optical spectra of 11 GHz modulated signal (RBW = 0.02 nm): after MZM-1, (b) after SOA (dashed line show the filter transmission) and (c) after DOBPF.	46
Figure 3.14. Electrical spectra for 42, 66 and 90 GHz mmW signals (RBW = 1 kHz, span = 100 kHz): (a)-(c) OB2B and (d)-(f) hybrid link.	47
Figure 3.15. (a) Experimental setup of signal transmission and (b) temperature structure distributions and (c) photograph of the experimental FSO channel at Photonic Research Labs in Universitat Politecnica de Valencia [100].	48
Figure 3.16. Optical spectra of CS-DSB (RBW = 0.02 nm): (a) 26 GHz and (b) 40 GHz.	49
Figure 3.17. Impact of induced turbulence: (a) electrical spectra and (b) dependence of electrical power and mmW frequency.	49
Figure 3.18. Phase noise measurements at 26 GHz (RBW = 220 kHz).	50
Figure 4.1. (a) Direct modulation scheme and (b) power-current laser curve.	54
Figure 4.2. Schematic for (a) local and (b) remote configurations [126].	55
Figure 4.3. Comparison of theoretical (dashed lines) and experimental (solid lines) electrical output power at baseband (left side) and mmW (right side) band: (a)-(b) OB2B, (c)-(d) local and (e)-(f) remote configurations, respectively. Both local and remote configurations are obtained over 25 km SSMF link.	59
Figure 4.4. Experimental setups for: (a) local and (b) remote MWP signal generation [126].	60
Figure 4.5. Optical spectrum of optically carrier suppressed modulated signal over 25 km SSMF at P1 in setup (a) –blue- and P2 in setup (b) –red- in Figure 4.4.	61
Figure 4.6. Measured electrical spectra after photodetection with different configurations: (a) OB2B, (b) and (c) local signal generation with 10 and 25 km fiber link, respectively, and, (d) and (e) remote signal generation with 10 and 25 km fiber link, respectively. Insets show the detail of the data band at baseband and at mmW band.	62
Figure 4.7. EVM comparison at baseband and mmW bands between local and remote setups for QPSK signal (IF = 500 MHz) over 40 GHz for 10 and 25 SSMF links: (a) EVM vs RoP (local setup), (b) EVM vs ReP (local setup) and, (c) EVM vs RoP (remote setup) and (d) EVM vs ReP (remote setup).	63
Figure 4.8. Constellations at 3 dBm RoP for: (a) OB2B and, (b) local and (c) remote setups over over 25 km SSMF link.	64
Figure 4.9. EVM and ReP for different setups vs frequency over 25 km fiber link: (a)-(b) OB2B, (c)-(d) local setup and (e)-(f) remote setup, at baseband and millimeter wave band, respectively.	64
Figure 4.10. Multiple data generator scheme.	65

Figure 4.11. Experimental second-order HD ($2W_{RF} - 2W_1$) for OB2B, local and remote configuration (left axis). EB2B signal measurement is included as a reference (right axis)...	66
Figure 4.12. Experimental second-order IMD ($2W_{RF} - (W_2 - W_1)$) for OB2B, local and remote configuration (left axis). EB2B signal measurement is included as a reference (right axis)...	67
Figure 4.13. Experimental second-order IMD ($2W_{RF} - (W_2 + W_1)$) for OB2B, local and remote configuration. EB2B signal measurement is included as a reference.	68
Figure 4.14. Electrical spectra of transmitted signals with different bandwidths for local configuration: (a) 50 MHz, (b) 150 MHz; and remote configuration: (c) 50 MHz and (d) 150 MHz. Insets show the detail of the spectrum at baseband (left) and mmW band (right).....	69
Figure 4.15. Electrical spectra of dual band transmitted signals, centered at $f_1 = 1$ GHz and $f_2 = 2$ GHz: (a) local configuration and (b) remote configuration.....	69
Figure 4.16. Electrical spectra measurements after photodetection of three-band signal transmission under: (a) local scheme and (b) remote scheme. Measurements shown in (c) and (d) correspond to electrical spectra measurement when only one band is transmitted under local and remote schemes, respectively.	70
Figure 4.17. Electrical spectra of three-band transmitted signal under: (a) OB2B, (b) local and (c) remote schemes for similar electrical power level.	70
Figure 4.18. EVM measurements of different QPSK signal bandwidth centered at 39.9 GHz ($f_1 = 100$ MHz) vs RoP (top) and ReP (bottom): (a) and (d) 50 MHz; (b) and (e) 100 MHz; (c) and (f) 150 MHz bandwidth.	71
Figure 4.19. In-band recovered QPSK signal constellations of $f_1 = 100$ MHz with RoP = 3 dBm at 39.9 GHz under local (top) and remote (bottom): (a) and (c) 50 MHz; (b) and (d) 150 MHz.....	71
Figure 4.20. OB2B, local and remote scheme measurements of EVM for evaluating out of band intermodulation at the frequency $2f_{RF} - f_2$ vs RoP (top) and ReP (bottom). (a) and (c) corresponds to a dual-band transmission ($f_1 = 1$ GHz and $f_2 = 2$ GHz); (b) and (d) are measured when f_2 is only transmitted.	72
Figure 4.21. QPSK signal constellations for the second band located at $f_2 = 2$ GHz over remote scheme when (a) both bands and (b) only one are transmitted (-2.48 dBm RoP).....	73
Figure 4.22. OB2B, local and remote scheme measurements of EVM vs RoP (top) and ReP (bottom) carried by $2f_{RF} - f_{1,2}$: (a), (c) dual-band transmission ($f_1 = 1$ GHz and $f_2 = 2$ GHz); (b), (d) only $f_1 = 1$ GHz is transmitted.	73
Figure 4.23. QPSK signal constellations of $f_1 = 1$ GHz over remote scheme when (a) f_1 and f_2 (b) only f_1 is transmitted (-2.48 dBm RoP).	74
Figure 4.24. EVM for OB2B, local and remote configurations of data carried by $2f_{RF} - f_3$ vs ReP when three bands are transmitted (top) and only f_3 is transmitted (bottom). Frequency bands are $f_1 = 200$ MHz, $f_2 = 325$ MHz and different f_3 as: (a), (d) $f_3 = 400$ MHz; (b), (e) $f_3 = 525$ MHz and (c), (f) $f_3 = 650$ MHz.	74
Figure 4.25. Signal constellations of f_3 signal under local (a, b) and remote (c, d) schemes: (a), (c) three bands transmission and (b), (d) single band is transmitted.	75
Figure 4.26. Diagram layout of the M-QAM DML and CS-MZM for mmW up-conversion [133]. Insets: (i) and (iv) electrical spectra of the modulation data and after opto-electronic conversion (RBW = 10 MHz) and, (ii) and (iii) optical spectra at the DML and MZM output (RBW = 0.001 nm).....	75
Figure 4.27. Simulated OB2B EVM performance for different signal bandwidth: (a) 4-QAM, (b) 16-QAM, and (c) 64-QAM. Insets show the obtained constellations at RoP of -4 dBm for 1, 1.5 and 3 GHz, respectively.	77
Figure 4.28. Simulated EVM performance after OB2B, 10 and 20 km SSMF link with 1 GHz signal bandwidth for different modulations: (a) 4-QAM, (b) 16-QAM and (c) 64-QAM. Insets show constellation with 4 dBm RoP for 10 and 20 km fiber transmission.	78
Figure 4.29. Simulated EVM performance when DML is employed with null, low, moderate and high chirp and 1 GHz signal bandwidth is transmitted over 10 km SSMF: (a) 4-QAM, (b) 16-QAM and (c) 64-QAM. Insets show constellations for low, moderate and high chirp value, at RoP of -3 dBm.	79

Figure 4.30. Measured EVM of 4-QAM for different signal bandwidths: (a) OB2B, (b) SSMF and (c) Hybrid links. Insets (a.1), (b.1) and (c.1) show the comparison between simulation and experimental results for 1 GHz and 3 dBm RoP. Constellations for 3 dBm RoP: (a.2), (b.2) and (c.2) with 100 MHz bandwidth, and (a.3), (b.3) and (c.3) with 500 MHz bandwidth.	80
Figure 4.31. Measured EVM of 16-QAM for different signal bandwidths: (a) OB2B, (b) SSMF and (c) hybrid links. Insets show the constellations when 6 dBm RoP.	81
Figure 4.32. Measured EVM of 64-QAM for different signal bandwidths: (a) OB2B, (b) SSMF and (c) hybrid links. Insets show the constellations when 6 dBm RoP.	82
Figure 4.33. Data throughput obtained from bandwidth results in Figure 4.30, Figure 4.31 and Figure 4.32 vs minimum RoP for 10 km SSMF link at EVM limit.	82
Figure 4.34. EVM of 16-QAM multiband data signal over 10 km fiber link with: (a) 100 MHz and (b) 200 MHz bandwidth. Insets: (i) electrical spectra of multiband signal (RBW = 100 kHz), (ii) constellations of band 2 with 3 dBm RoP.	83
Figure 5.1. (a) Diagram layout of external modulation and (b) MZM optical power – voltage characteristic curve.	86
Figure 5.2. Experimental setup for optical mmW generation at 26 GHz with the seamless transmission. Insets illustrate spectra at given points [140].	87
Figure 5.3. Measured optical spectra (RBW = 0.02 nm).	87
Figure 5.4. Electrical spectra w/o and w/ EBPf employed for 200 MHz bandwidth.	88
Figure 5.5. Measured EVM of 64-QAM and 200 MHz bandwidth at 26 GHz.	89
Figure 5.6. (a) Schematic of Setups A and B, and (b) optical channel.	90
Figure 5.7. Optical spectra of (a) Setup A at P1, and (b) Setup B at P2.	91
Figure 5.8. Measurements of EVM vs SSMF length for Setup A and B, using QPSK and 64-QAM signals with various bandwidth at 27 GHz.	91
Figure 5.9. Frequency response for various SSMF lengths in (a) Setup A and (b) Setup B.	92
Figure 5.10. EVM vs SNR under weak and strong AT for Setup A (blue) and B (red) at 27 GHz after 10 km SSMF and 4 m FSO link with 400 MHz bandwidth for (a) QPSK and (b) 64-QAM.	93
Figure 5.11. Electrical spectra for Setup A with 400 MHz 64-QAM for T0 and T1 ($f_c = 25$ GHz).	93
Figure 5.12. System layout of simulated M-QAM signal transmission at 25 GHz under thermal turbulence [110].	94
Figure 5.13. C_n^2 spatial distribution of proposed scenarios: (a) U1, U2 and U3, (b) N1, (c) N2 and (d) N3. Dashed line represents the mean value in each non-uniform scenario.	94
Figure 5.14. EVM vs RoP for (a) 4-QAM, (b) 16-QAM, (c) 64-QAM. Insets (i)-(iii) show constellation diagrams for U1 and U3 scenarios under RoP of 4 dBm for 4-, 16- and 64-QAM, respectively.	96
Figure 5.15. Experimental turbulence chamber at Czech Technical University labs in Prague and (b) temperature (dashed line) and C_n^2 (solid line) for different turbulence profiles.	98
Figure 5.16. Experimental EVM vs received optical (a) and electrical (b) power for 4-QAM and 64-QAM modulation formats.	98
Figure 5.17. Experimental BER vs received (a) optical and (b) electrical power for 4-QAM and 64-QAM modulation formats.	99
Figure 5.18. Constellations at 0 dBm RoP: (a)-(c) 64-QAM and (d)-(f) 4-QAM for D1, D2 and D3 turbulence distributions. Corresponding EVM values are displayed in the constellations.	99
Figure 6.1. (a) Experimental setup of the proposed full-duplex based 5G mmW frequencies, (b) DML frequency response, (c) optical spectra measured in DL and (d) optical spectra measured in UL [144].	102
Figure 6.2. Measured EVM at different (a) IF and (b) generated mmW frequencies in OB2B DL configuration.	103
Figure 6.3. (a) Measured EVM versus RoP for a single user – 4 Gbit/s 16-QAM and (b) constellation diagrams for OB2B, 10 km SSMF and hybrid configurations.	103

Figure 6.4. Measured EVM versus RoP for each band after (a) OB2B and (b) hybrid transmissions. (c) – (d) are the corresponding received RF spectra and constellation diagrams (as insets) of OB2B and hybrid transmissions, respectively.....	104
Figure 6.5. Calculated BER versus received RF power for each band after hybrid transmission.....	105
Figure 6.6. Performance of the 37 GHz 5G NR 64-QAM at 2.4 Gbit/s as a function of input RF power.	105
Figure 6.7. 2.4 Gbit/s 64-QAM over 37 GHz UL transmission experiments: (a) Measured EVM versus the RoP and (b) calculated BER versus received RF power after OB2B, 10 km SSMF and hybrid transmissions. (c) – (d) are the received RF spectra and constellation diagrams for OB2B and hybrid links, respectively.	106
Figure 6.8. Experimental setup: (a) downlink at 60 GHz and uplink at 25 GHz and (b) photograph of the coupling from fiber to FSO. Insets show the signal spectra: (i) DML output, (ii) MZM output.	107
Figure 6.9. (a) DL Signal parameters optimization: measurement of EVM vs. P_{data} for OB2B and SSMF: RoP = -3 dBm; SSMF + radio and full-link: RoP = 8 dBm and (b) UL signal parameters optimization: measurement of EVM vs P_{LO} for different configurations (RoP = 8 dBm) including the EB2B measurement.	109
Figure 6.10. EVM vs RoP for 64-QAM with different configuration in both links: (a) 61 GHz DL (b) 25 GHz UL. Corresponding insets show constellations for DL: (i) OB2B (RoP = -3 dBm), (ii) full-link (RoP = 8 dBm); and for UL: (iii) radio and OB2B (RoP = 3 dBm), (iv) full-link (RoP = 9 dBm).	110
Figure 6.11. EVM vs ReP for 64-QAM signal for: (a) 61 GHz DL, (b) 25 GHz UL.	110
Figure 6.12. EVM vs SNR measured for DL with different modulation formats: (a) 16-QAM, (b) 64-QAM. Insets: Constellations of transmitted signals over the full-link with an SNR of 28 dB.....	111
Figure A.1. (a) I/Q electrical modulator and (b) demodulator scheme.....	117
Figure A.2. Block diagram of an IM-DD system using OFDM signals. (a) Transmitter and (b) receiver.	118
Figure A.3. Transmitter (a) and receiver (b) block diagram of OFDM signals in IM-DD system using up conversion.....	118
Figure A.4. EVM diagram.	118
Figure A.5. BER vs EVM performance curves for M-QAM modulation format [143].	120
Figure A.6. Signal generators employed in this Thesis: (a) Tektronix AWG7122C and (b) Rohde & Schwarz SMW200A -front and rear view.	121
Figure A.7. Signal analyzers employed in this Thesis: (a) Tektronix DPO72004CC and (b) Rohde & Schwarz FSW43.....	121

List of tables

Table 2.1. NR operating bands in FR2.....	14
Table 3.1. Analytical terms of optical field at the MZM output (normalized to E_o).	36
Table 3.2. Analytical optical sidebands and Bessel functions from 1 to 3 order of optical field at the MZM output (E_o normalized) when $V_{bias} = V_{\pi}$ (null bias point).....	37
Table 3.3. Definition of experimental scenarios.	41
Table 3.4. Definition of optical channels.	44
Table 3.5. Refractive index and temperature structure parameters of different temperature distributions ($L_p = 1.2$ m).....	49
Table 3.6. Phase noise measurements in dBc/Hz of 26 GHz generated signals at different offsets (RBW = 220 Hz).....	50
Table 4.1. Analytical terms of the photocurrent $i_{PD}(t)$ at baseband and mmW band in OB2B, local and remote configurations.	57
Table 4.2. Theoretical and experimental parameters.	58
Table 4.3. Simulation parameters.	76
Table 5.1. Simulation parameters.	95
Table 5.2. Definition of scenarios.	95
Table 6.1. Experimental parameters.	108
Table A.1. LTE EVM thresholds [147].	119
Table A.2. 5G EVM threshold for FR2 [28].	119

List of acronyms

1G	First generation
2G	Second generation
3D	Three-dimensional
3G	Third generation
3GPP	3rd Generation Partnership Project
4G	Fourth generation
5G	Fifth generation
6G	Sixth generation
ADC	Analog-to-digital converter
ANT	Antenna
A-RoF	Analog-radio over fiber
ASE	Amplified spontaneous emission
AT	Atmospheric turbulence
AVR	Augmented-virtual reality
AWG	Arrayed waveguide gratings
AWGN	Additive white Gaussian noise
B5G	Beyond 5G
BB	Baseband
BBoF	Baseband-over fiber
BBU	Baseband unit
BER	Bit error rate
BPSK	Binary phase shift keying
BS	Base station
BW	Bandwidth
CAPEX	Capital expenditure
CH	Channel
CIR	Carrier-to-interference ratio
CIRC	Circulator
CO	Central office
COVID-19	Coronavirus disease-2019
CPRI	Common public radio interface
C-RAN	Cloud-radio access network
CS	Carrier-suppressed
CW	Continuous wave
DAC	Digital-to-analog converter
DAS	Distributed antenna systems
DC	Direct current
DFB	Distributed feedback laser
DG	Data generator
DL	Downlink
DML	Directly modulated laser

DOBPF	Dual optical band pass filter
DPO	Digital phosphor oscilloscope
DR	Dynamic range
D-RoF	Digital-radio over fiber
DSB	Double sideband
DSP	Digital signal processing
EA	Electrical amplifier
EB2B	Electrical back-to-back
EBPF	Electrical band pass filter
EC	Electrical combiner
eCPRI	Enhance-common public radio interface
EDFA	Erbium-doped fiber amplifier
eMBB	Enhanced-mobile broadband
EMI	Electromagnetic interference
ETSI	European Telecommunications Standards Institute
EVM	Error vector magnitude
FBG	Fiber Bragg grating
FEC	Forward error correction
FH	Fan heater
FPL	Fabry-Perot laser
FR	Frequency range
FSL	Free space loss
FSO	Free-space optics
FSR	Free spectrum range
FWM	Four-wave mixing
GaAs	Gallium arsenide
GRIN	Gradient-index
GSM	Global System for Mobile
HD	Harmonic distortion
IF	Intermediate frequency
IFFT	Inverse fast Fourier transform
IFoF	Intermediate frequency-over fiber
IMD	Intermodulation distortion
IM-DD	Intensity modulation – direct detection
IMT	International Mobile Telecommunications
InP	Indium phosphide
IoT	Internet of things
I/Q	In-phase and quadrature
IR	Infrared
ISI	Inter-symbol interference
ISO	Isolator
ITU	International Telecommunication Union
L1 – 3	Layer 1 – 3
LD	Laser diode

LiNbO ₃	Lithium niobate
LNA	Low-noise amplifier
LO	Local oscillator
LOS	Line-of-sight
LTE	Long-term evolution
LTE-A	LTE-Advance
M2M	Machine-to-machine
MCF	Multi-core fiber
MIMO	Multiple-input multiple-output
ML	Master laser
MLL	Mode-locked laser
mMTC	Massive machine-type communications
mmW	Millimeter wave
MWP	Microwave photonics
MZM	Mach-Zehnder modulator
NAS	Network-attached storage
NGC	Net coding gain
NR	New radio
NRZ	Non-return-to-zero
O&M	Operation and management
OB2B	Optical back-to-back
OBPF	Optical band pass filter
OBSAI	Open base station architecture initiative
OC	Optical coupler
ODN	Optical distribution network
OFDM	Orthogonal frequency-division multiplexing
OFM	Optical frequency multiplication
OIL	Optical injection locking
OIPL	Optical injection phase locking
ONU	Optical network unit
OOK	On-off keying
OPEX	Operation expenditure
OPLL	Optical phase lock loop
ORI	Open radio interface
OS	Optical switch
OSA	Optical spectrum analyzer
OWC	Optical wireless communication
PAM	Pulse-amplitude modulation
PC	Polarization controller
PCF	Photonic crystal fiber
PD	Photodetector
PIC	Photonics integrated circuit
PM	Phase modulator
PRBS	Pseudo-random binary sequence

QAM	Quadrature amplitude modulation
QoE	Quality of experience
QoS	Quality of service
QPSK	Quadrature phase shift keying
RAN	Radio access network
RBW	Resolution bandwidth
ReP	Received electrical power
RF	Radio frequency
RFoF	Radio frequency-over fiber
RFSA	RF spectrum analyzer
RIN	Relative intensity noise
RN	Remote node
RoF	Radio over fiber
RoFSO	Radio over FSO
RoP	Received optical power
RRH	Radio remote head
Rx	Receiver
SA	Signal analyzer
SBS	Stimulated Brillouin scattering
SC	Supercontinuum
SCM	Sub-carrier multiplexing
SFDR	Spurious free dynamic range
SG	Signal generator
SL	Slave laser
SMF	Single mode fiber
SMS	Short message service
SMSR	Side-mode suppression ratio
SNR	Signal-to-noise ratio
SOA	Semiconductor optical amplifier
SSB	Single-sideband
SSMF	Standard single mode fiber
TM	Test model
Tx	Transmitter
UE	User equipment
UHD	Ultra-high-definition
UL	Uplink
URLLC	Ultra-reliable and low latency communications
USA	United States of America
VLC	Visible light communication
VOA	Variable optical attenuator
VR	Virtual reality
WDM	Wavelength-division multiplexing
WiFi	Wireless fidelity
WiMax	Worldwide interoperability for microwave access

Abstract

The fifth generation (5G) standard is the potential key to meet the exponentially increasing demand of the emerging applications, services and mobile end users. 5G technology will offer an extremely low latency of 1 ms, peak data rate of 10 Gbit/s, high contention density up to 10^6 devices/km² and enable high mobility up to 500 km/h. This Thesis proposes several solutions based on enabling technologies for deploying 5G networks. Cloud-radio access network (C-RAN) architecture is employed in conjunction with microwave photonics techniques as a promising solution to generate and transmit millimeter wave (mmW) signals in the next generation of mobile communications. Radio over fiber (RoF) has been demonstrated as a good option to face the challenge of mmW wireless distribution, due to long transmission distance, large bandwidth and immunity to electromagnetic interference, as some of the main advantages. Moreover, this technology can be extended with free-space optical (FSO) communications in Radio over FSO systems (RoFSO) as wireless networks.

In this Thesis, mmW signals are photonically generated by carrier suppressed double sideband (CS-DSB) external modulation and distributed over hybrid RoF/FSO fronthaul links. Signals up to 90 GHz frequency with phase noise levels below -87 dBc/Hz have been experimentally generated. Moreover, multiple generated signals allow reconfigurable distribution in wavelength-division multiplexed (WDM) channels from a central office to the base stations, and the impact of turbulent FSO channels on photonically generated mmW signals has been evaluated in terms of power signal fluctuations and phase noise.

A directly modulated laser (DML) is proposed as a major solution for signal transmission over hybrid optical links employing optical frequency multiplication scheme, i.e. CS-DSB, for mmW signal generation. Moreover, local and remote photonic mmW signal generation schemes are theoretically and experimentally evaluated and compared for practical deployment in C-RAN fronthaul network. The remote configuration leads to a higher electrical output power, i.e. 15 dB higher in 25 km fiber links, than the local generation setup in the mmW band due to the combined effect of chirp and fiber dispersion. Furthermore, the impact of harmonic and intermodulation distortion on data transmission is experimentally studied, which measured results shows that wideband signals with in-band distortion and multiband signals with out-of-band distortion are examples that need to be transmitted over local generation mmW approach instead of remote approach. Furthermore, for the sake of obtaining the DML usability in terms of bandwidth, theoretical and experimental evaluation of the effect of fiber dispersion and chirp over different M-quadrature amplitude modulation (QAM) signals bandwidth is also presented. Both experimental and simulation results show that larger signal bandwidths lead to higher optical power penalties due to the combined effect of fiber dispersion and laser chirp.

Another data transmission approach based on the cascade of two external modulators is also employed in the Thesis. In this case, the experimental demonstration of optical signal generation employing CS-DSB and signal transmission over hybrid fiber and FSO fronthaul network is completed with a seamless antenna link leading to successful transmission of 64/256-QAM 5G signals with 200 MHz bandwidth. The CS-DSB and DSB schemes are also investigated for the sake of comparison and results demonstrate that the CS-DSB scheme is robust against chromatic dispersion-induced fading for the frequency up to 40 GHz and single mode fiber length of 30 km, whereas the DSB format seems more appropriate for an antenna seamless transmission. Furthermore, experimental evaluation of the impact of turbulent FSO links on photonically generated mmW signals with different thermal distributions has been performed and data signal degradation has been quantified according to the turbulence conditions.

As final demonstrators, the Thesis includes a full-duplex transmission system employing 39 GHz downlink (DL) and 37 GHz uplink (UL) 5G signals over hybrid links with maximum bit rate of 1 Gbit/s single-user and 3 Gbit/s three-users for DL, and 2.4 Gbit/s for UL, respectively;

and 60 GHz (DL) and 25 GHz (UL) OFDM LTE signal transmission over an heterogeneous optical fronthaul infrastructure consisting of 10 km optical fiber, 100 m FSO channel and 2 m wireless radio link.

Resumen

El estándar de quinta generación (5G) es la clave potencial para satisfacer el aumento exponencial en la demanda de nuevas aplicaciones, servicios y usuarios. La tecnología 5G ofrecerá una latencia extremadamente baja de 1 ms, una velocidad máxima de datos de 10 Gbit/s, una alta densidad de conexión de hasta 10^6 dispositivos/km² y permitirá una alta movilidad de los dispositivos de hasta 500 km/h. En esta Tesis se proponen varias soluciones basadas en tecnologías habilitadoras para el despliegue de redes 5G. La arquitectura de la red de acceso de radio en la nube (*cloud-radio access network*, C-RAN) se emplea junto con las técnicas de Fotónica de Microondas como una solución prometedora para generar y transmitir señales de ondas milimétricas (*millimeter wave*, mmW) en la próxima generación de comunicaciones móviles. La tecnología radio sobre fibra (*radio over fiber*, RoF) ha demostrado ser una buena opción para enfrentarse al desafío de la distribución inalámbrica mmW debido a la gran distancia de transmisión, el gran ancho de banda y la inmunidad a las interferencias electromagnéticas, entre algunas de las principales ventajas. Además, esta tecnología se puede ampliar con comunicaciones ópticas de espacio libre (*free-space optics*, FSO) en sistemas de radio sobre FSO (*radio over FSO*, RoFSO) en las redes inalámbricas.

En esta Tesis, las señales mmW se generan fotónicamente mediante modulación externa de doble banda lateral con supresión de portadora (*carrier suppression-double sideband*, CS-DSB) y se distribuyen a través de enlaces fronthaul híbridos RoF/FSO. Se han generado experimentalmente señales de hasta 90 GHz de frecuencia, con niveles de ruido de fase por debajo de -87 dBc/Hz. Además, la generación múltiple de señales permite la distribución reconfigurable en canales multiplexados por división de longitud de onda (*wavelength-division multiplexed*, WDM) desde una oficina central hasta las estaciones base, y se ha evaluado el impacto de las turbulencias producidas en los canales FSO sobre las señales mmW generadas fotónicamente en términos de fluctuaciones de potencia y ruido de fase de la señal.

Se propone la técnica de modulación directa de un láser (*directly modulated laser*, DML) como solución principal para la transmisión de datos a través de enlaces ópticos híbridos que emplean un esquema de multiplicación de frecuencias ópticas, es decir, CS-DSB, para la generación de señales de mmW. En concreto, se evalúan teórica y experimentalmente los esquemas de generación fotónica local y remoto de señales mmW y se comparan para su implementación práctica en la red frontal de la C-RAN. La configuración remota conduce a una mayor potencia eléctrica de salida que la configuración de generación local en la banda de mmW, de forma específica, 15 dB más en enlaces de fibra de 25 km debido al efecto combinado del *chirp* y la dispersión de la fibra. Además, se estudia experimentalmente el impacto de la distorsión armónica y de la intermodulación en la transmisión de datos, cuyos resultados muestran que las señales de banda ancha con distorsión dentro de la banda y las señales multibanda con distorsión fuera de banda son ejemplos de señales que deben transmitirse a través del esquema de generación local en lugar de la generación remota. Igualmente, con el fin de obtener la capacidad que ofrece el DML en términos de ancho de banda, también se presenta una evaluación teórica y experimental del efecto de la dispersión de la fibra y el *chirp* sobre diferentes anchos de banda de señales de M-modulación de amplitud en cuadratura (*quadrature amplitude modulation*, QAM). Tanto los resultados experimentales como los de simulación muestran que los anchos de banda más grandes de señal conducen a penalizaciones de potencia óptica más altas debido al efecto combinado de ambos.

No obstante, la Tesis también incluye otro enfoque para la transmisión de datos basado en el uso de otro modulador externo. En este caso, la demostración experimental de la generación de señales ópticas empleando CS-DSB y la transmisión de señales a través de fibra híbrida y red frontal FSO se completa con un enlace de antena que permite transmitir señales 5G 64/256-QAM con un ancho de banda de 200 MHz. La investigación realizada con los sistemas CS-DSB y DSB también permiten compararlos y los resultados demuestran que

el esquema CS-DSB es robusto frente al desvanecimiento inducido por la dispersión cromática para frecuencias de hasta 40 GHz y una longitud de fibra monomodo de 30 km, mientras que el formato DSB parece más apropiado para la transmisión a través de un enlace radio entre antenas. Además, se ha realizado una evaluación experimental impacto las turbulencias producidas en los canales FSO sobre las señales mmW generadas fotónicamente con diferentes distribuciones térmicas y se ha cuantificado la degradación de la señal de datos de acuerdo con las condiciones de la turbulencia.

Como demostradores finales, esta Tesis incluye un sistema de transmisión full-dúplex que emplea señales 5G en enlace descendente (*downlink*, DL) a 39 GHz y en enlace ascendente (*uplink*, UL) a 37 GHz sobre enlaces híbridos con una tasa de bits máxima de 1 Gbit/s para un solo usuario y 3 Gbit/s para tres usuarios en DL, y 2,4 Gbit/s para un usuario en UL, respectivamente; y la transmisión de señales OFDM LTE de 60 GHz (DL) y 25 GHz (UL) sobre una infraestructura heterogénea de frontal óptico que consiste en fibra óptica de 10 km, un canal FSO de 100 m y un enlace de radio inalámbrico de 2 m.

Resum

L'estàndard de quinta generació (5G) és la clau potencial per a satisfer l'augment exponencial en la demanda de noves aplicacions, serveis i usuaris. La tecnologia 5G oferirà una latència extremadament baixa d'1 ms, una velocitat màxima de dades de 10 Gbit/s, una alta densitat de connexió de fins a 10^6 dispositius/km² i permetrà una alta mobilitat dels dispositius de fins a 500 km/h. En aquesta tesi es proposen diverses solucions basades en tecnologies habilitadores per al desplegament de xarxes 5G. L'arquitectura de la xarxa d'accés de ràdio en el núvol (*cloud-radio access network*, CRAN) s'empra junt amb les tècniques de Fotònica de Microones com una solució prometedora per a generar i transmetre senyals d'ones mil·limètriques (*millimeter wave*, mmW) en la pròxima generació de comunicacions mòbils. La tecnologia ràdio sobre fibra (*radio over fiber*, RoF) ha demostrat ser una bona opció per a enfrontar-se al desafiament de la distribució sense fil mmW a causa de la gran distància de transmissió, el gran ample de banda i la immunitat a les interferències electromagnètiques, entre alguns dels principals avantatges. A més, aquesta tecnologia es pot ampliar amb comunicacions òptiques d'espai lliure (*free-space optics*, FSO) en sistemes de ràdio sobre FSO (*radio over FSO*, RoFSO) en les xarxes sense fil.

En aquesta Tesi, els senyals mmW es generen fotònicament per mitjà de modulació externa de doble banda lateral amb supressió de portadora (*carrier suppression-double sideband*, CS-DSB) i es distribueixen a través d'enllaços frontals híbrids RoF/FSO. S'han generat experimentalment senyals de fins a 90 GHz de freqüència, amb nivells de soroll de fase per davall de -87 dBc/Hz. A més, la generació múltiple de senyals permet la distribució reconfigurable en canals multiplexats per divisió de longitud d'ona (*wavelength-division multiplexed*, WDM) des d'una oficina central fins a les estacions base, i s'ha avaluat l'impacte de les turbulències produïdes en els canals FSO sobre els senyals mmW generades fotònicament en termes de fluctuacions de potència i soroll de fase del senyal.

Aquest treball proposa la tècnica de modulació directa d'un làser (*directly modulated laser*, DML) com solució principal per a la transmissió de dades a través d'enllaços òptics híbrids que fan servir un esquema de multiplicació de freqüències òptiques, és a dir, CS-DSB, per a la generació de senyals de mmW. En concret, s'avalua teòric i experimentalment els esquemes de generació fotònica local i remot de senyals mmW i es comparen per a la seua implementació pràctica a la xarxa frontal de la C-RAN. La configuració remota condueix a una major potència elèctrica d'eixida que la configuració de generació local en la banda de mmW, de forma específica 15 dB més en enllaços de fibra de 25 km a causa de l'efecte combinat del chirp i la dispersió de la fibra. A més, s'estudia experimentalment l'impacte de la distorsió harmònica i de la intermodulació en la transmissió de dades; els resultats mostren que els senyals de banda ampla amb distorsió dins de la banda i els senyals multibanda amb distorsió fora de banda són exemples de senyals que han de transmetre's a través de l'esquema de generació local en lloc de la generació remota. Igualment, amb el fi d'obtenir la capacitat que ofereix el DML en termes d'amplada de banda, també es presenta una avaluació teòrica i experimental de l'efecte de la dispersió de la fibra i el chirp sobre diferents amplitudes de banda de senyals de M-modulació d'amplitud en quadratura (*quadrature amplitude modulation*, QAM). Els resultats experimentals com els de simulació mostren que l'amplada de banda més gran de senyal condueix a penalitzacions de potència òptica més alta a causa de l'efecte combinat de tots dos.

No obstant això, la Tesis també inclou altre enfocament per a la transmissió de dades basat amb l'ús d'altre modulador extern. En aquest cas, la demostració experimental de la generació de senyals òptics emprant CS-DSB i la transmissió de senyals a través de fibra híbrida i xarxa frontal FSO es completa com un enllaç d'antena que permet transmetre senyals 5G 64/256-QAM amb un ample de banda de 200 MHz. La investigació realitzada amb els sistemes CS-DSB i DSB també permeten comparar-los i els resultats demostren que l'esquema CS-DSB és robust davant l'esvaïment induït per la dispersió cromàtica per a

freqüències de fins a 40 GHz i una longitud de fibra monomode de 30 km, mentre que el format DSB pareix més apropiat per a la transmissió a través d'un enllaç ràdio entre antenes. A més, s'ha avaluat experimentalment l'impacte de les turbulències produïdes en els canals FSO sobre els senyals mmW generades fotònicament amb diferents distribucions tèrmiques i s'ha quantificat la degradació del senyal de dades d'acord amb les condicions de la turbulència.

Com a demostradors finals, aquesta Tesi inclou un sistema de transmissió full-dúplex que emprava senyals 5G en enllaç descendent (DL) a 39 GHz i en enllaç ascendent (UL) a 37 GHz sobre enllaços híbrids amb una taxa de bits màxima d'1 Gbit/s per a un sol usuari i 3 Gbit/s per a tres usuaris en DL, i 2,4 Gbit/s per a un usuari en UL, respectivament; i la transmissió de senyals OFDM LTE de 60 GHz (DL) i 25 GHz (UL) sobre una infraestructura heterogènia de frontal òptic que consisteix en fibra òptica de 10 km, un canal FSO de 100 m i un enllaç de ràdio sense fil de 2 m.

Chapter 1. Introduction

Houston... we've had a problem.

– Jack Swigert, NASA

The aim of this Chapter is to introduce the reader into the context, motivation and objectives of this Thesis. An overview of the evolution of the different generations of mobile communications networks is presented showing the main motivations for this work. Based on the current and future challenges arising from the increasing demand and new emerging services, the objectives of this Thesis are defined. Finally, this Chapter also describes the structure of this Thesis, providing hints and summarizing the contents of the different Sections.

1.1. Context

1.1.1. Evolution of mobile wireless systems

Mobile communications play a crucial role in modern life since they have been closely integrated in the daily life of the whole society. The race of mobile communications, shown in Figure 1.1, began in the 1980s when first generation (1G) emerged [1]. The evolution of mobile network from 1G to fifth generation (5G), and the sixth generation (6G) forecast is not a one-step process, but consists of several generations (approximately every ten years) which introduce new features, capabilities and technologies. However, the world mobile communications have undergone remarkable changes and enormous growth in the last few decades.

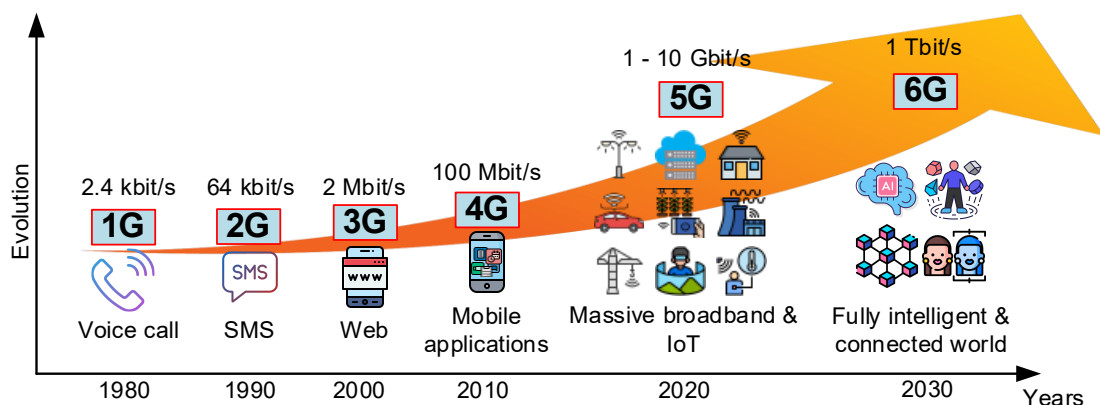


Figure 1.1. Evolution of mobile wireless systems.

In the early 1990s, the second generation (2G) was introduced, based on the Global System Mobile (GSM) standard. It supported a data rate up to 64 kbit/s for voice and short message services (SMS), providing advantages such as security, efficiency and data services.

Third generation (3G) was launched in 2000 and the target was basically to increase the speed of data transmission up to 2 Mbit/s for multimedia services. In order to achieve global roaming, the 3rd Generation Partnership Project (3GPP) defined the technical specification and continued the work of new standards.

In 2009, the fourth generation (4G) commonly known as Long-Term Evolution (LTE) was deployed. It provides data rate up to 100 Mbit/s which enables benefits such as service at any time as per user requirements anywhere, mobile broadband internet access or multi-service capacity by integrating previously existing technologies.

The 5G deployment started in 2019 as the planned successor of 4G. It has been designed with an extended capacity to allow next-generation user experiences and deliver new services. The aim of 5G is to make revolutionary advances in data rate, latency, network reliability, energy efficiency and massive connectivity.

Finally, the future mobile communications beyond 5G is the 6G which may roll out sometime around 2030. The technical requirements are significantly more stringent than those in 5G which will require more advanced enabling technologies than 5G.

1.1.2. On the way to 5G

The capabilities of mobile generation usually determine the available services, e.g. SMS, multimedia services or access to multiple sites on the web via internet. However, the introduction of mobile smartphones, tablets or wearables devices enable the emerging multimedia services such as cloud access, high-definition video streaming or social networking, among many other applications, leading to the exponential growth of data traffic. As expected in [2], over 70% of the global population will have a mobile device and over 10% of global mobile devices will be 5G by 2023 (Figure 1.2). Besides these foresights, an unprecedented number of people had to change their workplace from office to home during the COVID-19 pandemic in 2020 [3], which means a significant growth of mobile data traffic between 10% and 20% during the lockdown periods.

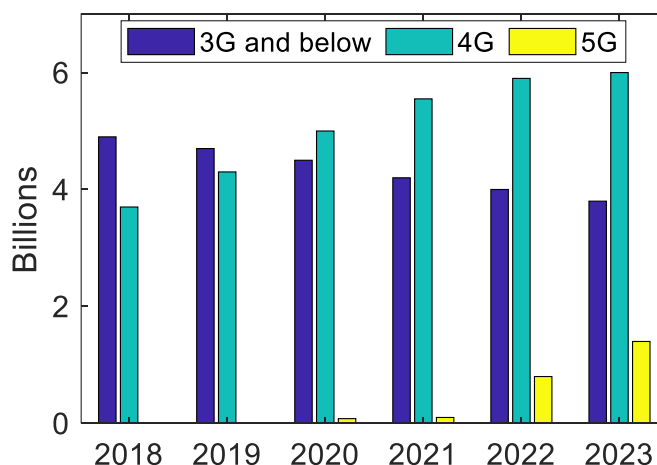


Figure 1.2. Global mobile devices trend.

Mobile devices play evolving roles in everyday life. Future systems should be able to support new services and applications requiring very high data rate, ultra-low latency and high reliability applications, and large number of connected devices [4]. The system designed should guaranteed the demand of high data rate, leading by the multimedia services such as ultra-high definition (UHD) videos, immersive video conferencing, virtual reality (VR) or augmented-virtual reality (AVR). The ultra low latency and high reliability should support the user experience of instantaneous connectivity without waiting times, which is a key factor of cloud services, VR and AVR, as well as the future deployment of new applications in health, office, entertainment, and other sectors. Moreover, machine-to-machine (M2M) communications with real time constraints has been increased in the last years, such as driverless cars, enhanced mobile cloud services, real-time traffic control optimization, emergency and disaster response, smart grid, electronic-health or efficient industrial communications. According the forecast, there will be a massive number of concurrent users and devices in the near future. Examples are shopping malls, stadiums, open air events or other public events that attract a lot of people which means a large number of machines/devices per unite area. Indeed, every object will be connected to internet. Theses connected “things”, called Internet of things (IoT), can be sensors, cameras, vehicles, wearables, etc., Therefore, users should expect a satisfactory end-user experience in presence of large number of connected devices.

The International Telecommunication Union (ITU) defines the usage scenarios and applications of the future development for International Mobile Telecommunications (IMT)-2020 [4], illustrated in Figure 1.3. Enhanced-mobile broadband (eMBB) is focused in human use cases for access to multimedia content, services and data, such as three-dimensional (3D) video, UHD screens, augmented reality or work and play in the cloud. The ultra-reliable and low latency communications (URLLC) address the requirements for capabilities such as throughput, latency and availability. Some examples include wireless control of industrial manufacturing or production processes, remote medical surgery, distribution automation in a smart grid, transportation safety and self-driving car, among others. Finally, massive machine-type communications (mMTC) are characterized by a very large number of connected devices, e.g. IoT or smart home/building or cities, typically transmitting a relatively low volume of non-delay sensitive data.

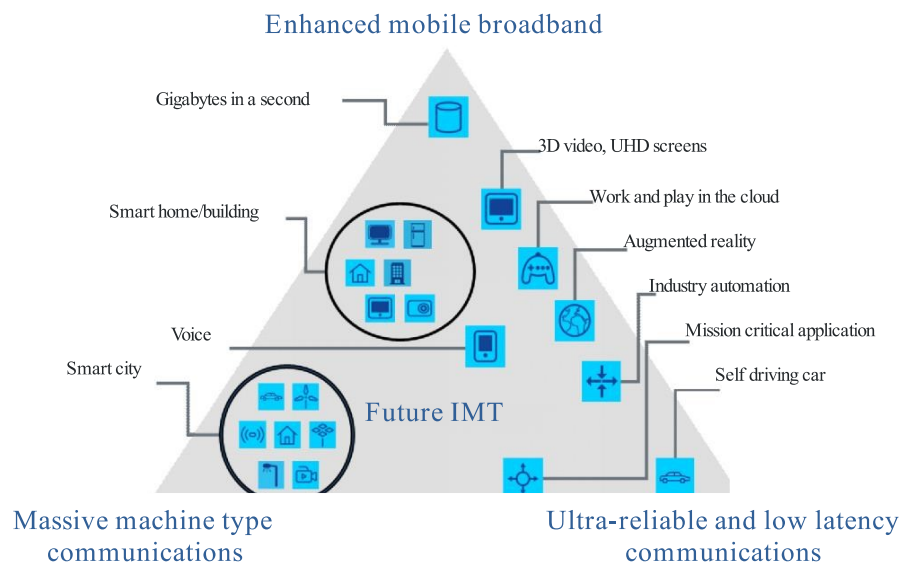


Figure 1.3. Usage scenarios of IMT for 2020 [4].

The 5G will support improved performance such as high data rates, low latency and increased reliability. It will accommodate the increasing traffic and demand stemming from M2M and IoT communications. However, there are many different inherent issues related to the development of the infrastructure, e.g. economic or health issues. Other issues are concerned with bandwidth (BW) access and sharing since the current bandwidth is not enough for the expected massive use of the mobile infrastructure.

The challenges towards 5G are shown in Figure 1.4(a), as defined by IMT-2020 standard as main targets for research and investigation for 5G networks, devices and services [4]. Among them, the peak data rate is expected to reach 10 Gbit/s, although under certain conditions and scenarios would support up to 20 Gbit/s while the user experience data rates would support a variety of scenarios. For wide area coverage cases, e.g. in urban and sub-urban areas, a user experience data rate of 100 Mbit/s is expected to be enabled. The spectrum efficiency will vary between scenarios and could be up to three times higher compared to IMT-Advanced (marketed as 4G) in some scenarios. It is expected to support 10 Mbit/s/m² area traffic capacity, for example in hot spots, and a connection density of 10⁶ devices/km². However, the energy consumption for the radio access network (RAN) should not be greater than previous deployed networks. The network energy efficiency should be improved by a factor at least as great as the predicted traffic capacity increase of IMT-2020 relative to IMT-Advanced. IMT-2020 would be able to provide as lower latency as 1 ms over-the-air latency, adequate for supporting services with very low latency requirements. It is also expected to enable high mobility up to 500 km/h with acceptable quality of service (QoS), for instance in high-speed trains.

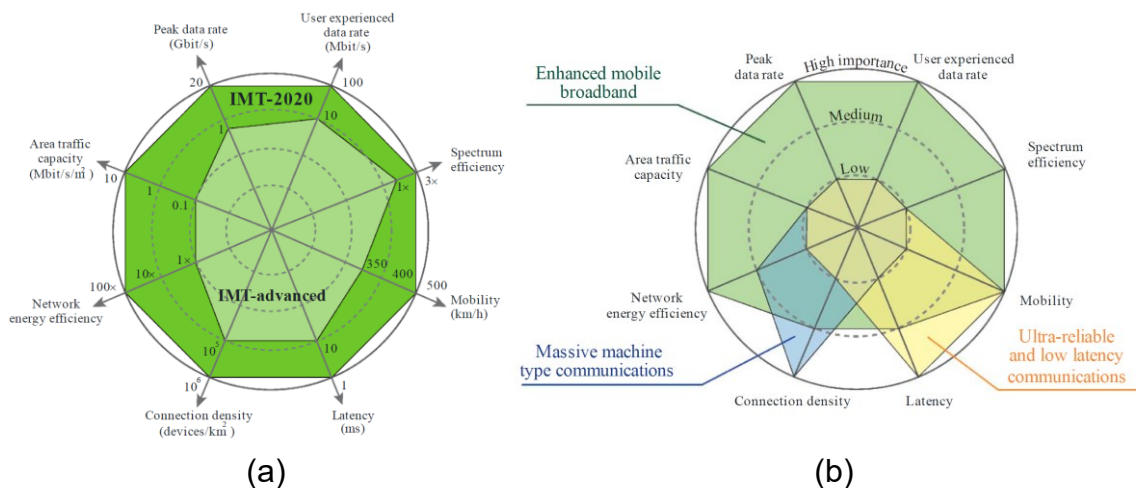


Figure 1.4. Key capabilities (a) and their importance in different usage scenarios (b) for 5G networks [4].

The ITU also defines the usage scenario for IMT-2020, displayed in Figure 1.4(b), in terms of the key capabilities. The majority of required performances is covered in eMBB scenario, i.e. data rate, area traffic capacity, peak data rate, mobility, energy efficiency and spectrum efficiency although their strongly depends on the concrete application. For example, in a hotspot, it requires high data rate, but the mobility is limited. The low latency is the most relevant parameter in URLLC scenarios in order to enable reliable critical applications, e.g. health care industry. Indeed, high mobility requirements are required as well, e.g. intelligent transportation systems. In contrast, mMTC scenarios need to support enormous number of devices in the network, i.e. high connection density is required, e.g. many small sensors which may occasionally transmit at low bit rate and zero/very low mobility.

The required key capabilities, and the disruptive use cases and applications guide the innovation on transmission, networking, and computing technologies. The potential enabling technologies, illustrated in Figure 1.5, show the extraordinary advances required to shape the 5G requirements [5]. A detailed discussion of the relevant enabling technologies is outside the scope of this Thesis, and only the main principles are described.

Some of these technologies are mainly architectural, i.e. towards device-centric schemes while other hardware-based enabling technologies include the use of millimeter wave (mmW) spectrum for the wireless channel and realizing massive multiple-input multiple-output (MIMO) at the base station as part of the new air interface optimized for high frequencies and massive connectivity. Moreover, an all-optical network employing the optical transmission and switching wherever possible is desired. Also, small cells play an important role to provide high data rates, frequency reuse and potential energy and cost reductions. In this respect, microwave photonics is essential to provide signal generation, transport and processing, i.e. distributed antenna systems (DAS). Controller/user-plane split can address coverage and capacity separately while the number of network layers and pool resources can be reduced by using network functions virtualization/software-defined networking/cloud networks. The goal of energy efficiency across all network entities is rolled out by energy-efficient hardware and energy-management techniques. Finally, service-oriented networking, traffic management and big-data-driven networking intelligence are based on the use of an intelligent agent to manage the quality of experience (QoE), routing, mobility and resource allocation; redesign network-attached storage (NAS) protocols, services and service complexity.

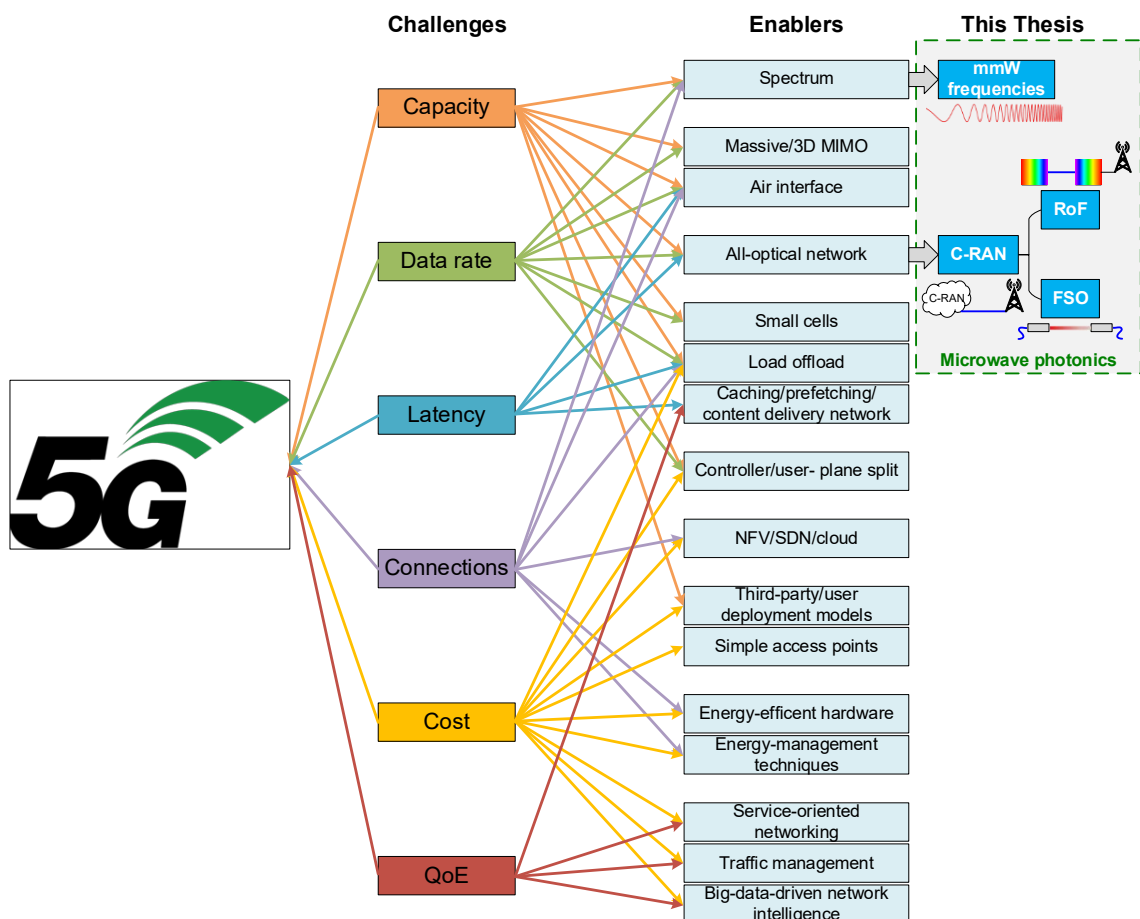


Figure 1.5. Enabling technologies to shape the 5G requirements.

1.1.3. Motivation for this Thesis

Legacy mobile generations, i.e. 4G and below, employ traditional RAN that consist in locating the radio and baseband processing functionalities in the same place. These networks are no longer able to provide the 5G requirements, e.g. 4G (LTE) performance include 1 Gbit/s peak data rate, latency of 10 ms and connection density of 10^5 devices/km² [6, 7]. Therefore, cloud-RAN (C-RAN), based on a centralized concept, has been proposed as a promising architecture for 5G networks [8]. Most of the processing functionalities are located in a central location

where multiples cells are connected. Therefore, multiples benefits such as cost savings, enhance capacity and coverage, or network flexibility are achieved.

The gigabit per second throughput cannot be allocated by using traditional frequency bands, i.e. below 6 GHz. Many research groups, organization and companies proposed the mmW spectrum which exhibits great amount of available bandwidth [5]. mmWs can support the requirements for high data rate as well as low latency, and flexible connectivity for a wide range of users. However, mmW generation in electrical domain is limited by the electronic devices. Therefore, mmW generation in optical domain is an excellent solution [9, 10].

Moreover, electrical signal transmission experiences high attenuation, i.e. wireless transmission exhibits exponential dependence with free space loss (FSL), especially at high frequencies. Consequently, mmW transmission along large distance, i.e. wired or wireless, may not be feasible. Nevertheless, radio over fiber (RoF) is a technology which can overcome the attenuation issues, among other benefits [9, 5]. RoF uses optical fiber, whose attenuation is below 1 dB/km, as wired transmission medium to transport electrical signals. Therefore, it can transport high bit rate along long distances. Free-space optics (FSO) has increased recently the interested of the researchers due to its similar performances to optical fibers [11]. It employs the air as no guide transmission medium by using infrared (IR) beams. Although its transmission distance is not as longer as optical fiber, it can be used where optical fiber cannot be deployed.

Future mobile communications, i.e. 6G networks, will support novel scenarios such as holographic-type communications, extended reality, ubiquitous intelligence, tactile internet, multi-sense experience and digital twin amongst others. Accordingly, the technical requirements for 6G are significantly more stringent than those in 5G networks, and include minimal latency of 0.1 ms, user experience of 1 Gbit/s and peaks rate of 1 Tbit/s. Therefore, advanced enabling technologies will be required to provide new spectrum, virtual infrastructures, air interfaces, architectures and paradigms in 6G networks [12]. The mmW technology, already introduced by the 5G new radio, is still essential in 6G networks due to the huge bandwidth, small antenna size and larger arrays with narrow beams. Analog-RoF (A-RoF) solutions provide cost-efficient, low latency and large bandwidth links in C-RAN where the availability and costs of the optical infrastructure become critical, especially due to small-cell environment [5, 13, 8, 14].

1.2. Objectives

In this context, the global objective of this Ph. D. Thesis is to propose and demonstrate photonics-based transmission solutions for the fronthaul link of C-RAN employing mmW frequencies to be deployed in 5G and beyond 5G (B5G) networks. More concretely, the following specific objectives can be formulated for this work:

- To demonstrate high quality frequency signal generation using microwave photonics techniques in the mmW range. This objective includes full characterization of the generated signals to validate the approaches for future deployment in real networks. The generation of multiple and reconfigurable signals is also required according to the evolution of wireless communication networks.
- To propose and demonstrate data transmission over photonically generated mmW signals using a directly modulated laser (DML) in C-RAN. Different configurations for signal generation will be theoretically and experimentally evaluated, and compared in terms of performance, i.e. system response and non-linearities, for the sake of providing useful guidelines for network deployment.
- To evaluate the bandwidth usability of DML-based fronthaul link using photonically generated mmW signals.
- To demonstrate data transmission employing alternative approaches based on external modulation and evaluate their performance.

- To evaluate the impact of turbulences in FSO links on the data transmitted over photonically generated mmW signals.
- To demonstrate bidirectional signal transmission over a hybrid fronthaul link including fiber, FSO and wireless links at mmW frequencies.

1.3. Thesis structure

The structure of this manuscript is based in seven Chapters organized as follows.

Chapter 2 presents the enabling architectures and technologies for 5G studied and developed in this Thesis. It describes the main concepts of C-RAN architecture, microwave photonics-based technologies for mmW signal generation and RoF techniques for signal transmission as well as free-space optics technology to extend wireless coverage.

Chapter 3 is dedicated to the photonically mmW signal generation based on carrier suppressed external modulation. It includes the analytical formulation and the experimental characterization of mmW generated signals, also showing flexible and reconfigurable structures for multiple mmW signal generation. The Chapter also covers the mmW signal generation aided by non-linear effects for the sake of extending the frequency operation range. Finally, the impact of turbulence in the FSO channel is studied with regards to the photonically generated and transmitted signals.

Chapter 4 is devoted to data signal transmission based on laser direct modulation over photonically generated mmW signals. The link frequency response is theoretically studied under different configurations, i.e. local and remote generation approaches. Subsequently, transmission measurements allow the evaluation of link performances and non-linear distortion effects. Finally, simulations and experimental measurements lead to obtain the system bandwidth constraints.

Chapter 5 presents the data signal transmission based on external modulation as an alternative approach to transmit data over photonically generated mmW signals. It starts with traditional double sideband signal transmission scheme and continues with a comparison between the former and carrier suppression scheme showing the main limitations of both schemes. Finally, this Chapter also presents the theoretical and experimental evaluation of the impact of turbulences in the FSO channel when data signal is transmitted.

Chapter 6 presents two experimental full-duplex setups for 5G networks based on photonically generated mmW signals. The first experiment is based on 5G New Radio (NR) signals at 39 GHz band where downlink, uplink and wireless range characterization are shown. The second one employs 60 GHz for downlink and 25 GHz for uplink over a hybrid link based on 10 km standard single mode fiber (SSMF), 100 m FSO channel and 2 m seamless radio link.

Chapter 7 is dedicated to summarise the main conclusions of this Thesis and describe future research lines.

Finally, Appendix A is included to describe complex data signal modulation and demodulation employing intensity modulation – direct detection (IM-DD) systems, the signal analysis by using the error vector magnitude (EVM) and bit error rate (BER) signal quality parameters and the employed signal generators and analyzers.

Chapter 2. Enabling architectures and technologies for 5G networks

Nana korobi, ya oki.

Fall down seven times, stand up eight times.

– Japanese proverb

This Chapter is focused on the new architectures and emerging technologies for next RAN, i.e. 5G and B5G. The evolution of RAN is discussed and an overview of legacy networks is presented, followed by the description of the architecture and structures of C-RAN as the preferred network scheme, and its potential approaches. The use of mmW signals is considered a potential technology that will assist 5G network in achieving the required performance parameters. The role of microwave photonics (MWP) is explained along the Chapter with special focus on photonic mmW signal generation techniques and RoF techniques, and, finally, FSO transmission, as enabling technologies for future deployment of C-RANs.

2.1. Cloud-radio access network

The RAN is the network infrastructure which connects the user terminal to the core network and therefore, requires high capacity, although is often constrained. Indeed, it is the major part of the mobile telecommunication system evolving from 1G to 5G and beyond. RAN development, which includes mobile network technologies and architectures, has been an interesting topic for researchers over last decade since power consumption, total bandwidth and efficient use of resources are included as critical parameters for network deployment.

2.1.1. Evolution of radio access networks

From 1G up to today's 5G communication networks, the RAN has extended its functionality according to the different standard requirements. In the early years, it was based on distributed sites where the radio components and signal processing units were placed close to each other. In order to be 24/7 availability as well as provide the increasing demands for high throughput, it requires every site to be in continuous mode operation and has peak throughput which demands high computational capability. However, this architecture causes many troubles such as high-power consumption, and therefore operation expenditure (OPEX), limited network capacity and low average hardware efficiency related to capital expenditure (CAPEX). Based

on the placement and implementation of the radio sites, the evolution of RAN has evolved through three main stages described as follows [15].

Base stations (BS), antennas, radio remote heads (RRH) and baseband units (BBU) are common components in legacy RANs [16, 17]. In traditional cellular network (1G and 2G), as shown in Figure 2.1(a), the BSs perform the baseband processing and radio frequency (RF) functionalities, i.e. all functions are located in the remote BSs. RRH and BBU can be separated up to tens of meters depending on the topology of the cell site, leading to power losses. Since there is no fronthaul network, the site is connected to the core network by a coaxial cable, and therefore, the latency and the bit rate are limited. This topology leads to high power consumption and an inefficient use of the resources.

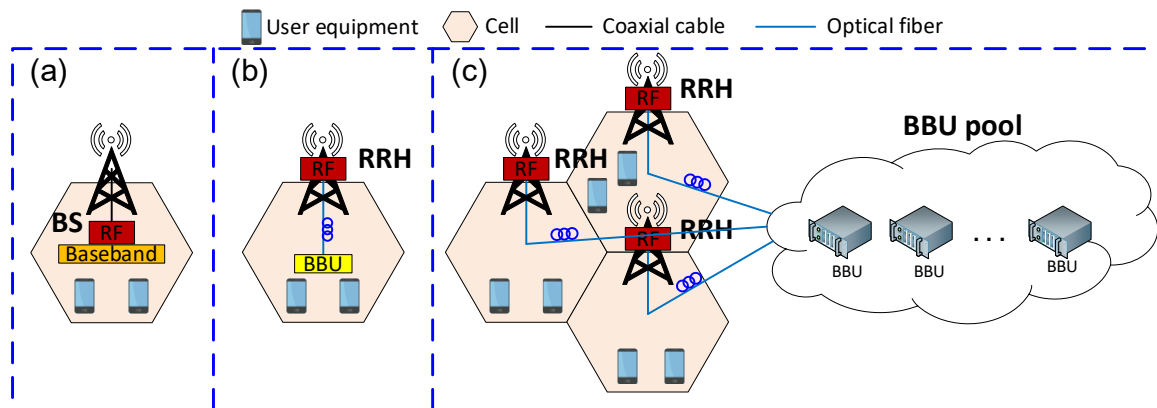


Figure 2.1. RAN architecture evolution: (a) traditional base station, (b) base station splitted into RRH and BBU and (c) C-RAN with RRHs.

The second stage is shown in Figure 2.1(b). For 3G and 4G networks, the BS is divided into RRHs and BBUs. The RF part is moved into the RRHs at the remote site meanwhile the BBU can be far from the site (tens of kilometres). The fronthaul link, which is usually made by optical fiber, connects each RRH to a dedicated BBU, allowing to reduce the latency. This RAN can use the digital-RoF (D-RoF) protocol as well as common public radio interface (CPRI) or open base station architecture initiative (OBSAI) [15, 18, 19]. It allows much lower power consumption and higher data rates. However, resource allocation cannot respond to data traffic demand conditions.

Finally, in C-RAN architecture the baseband resources are pooled as shown in Figure 2.1(c) [8]. The BBUs are centralized into a pool which can be also virtualized and allows to be shared between RRHs. This architecture, as well as the previous benefits, allows for dynamically resource allocation depending on the data traffic demand conditions, i.e. high hardware efficiency. It allows to decrease the CAPEX and OPEX, reduce the energy consumption, increase the network scalability, simplify network management and maintenance, improve the spectral efficiency and the network throughput, and facilitate load balancing [15].

2.1.2. C-RAN architecture

The RAN should be able to satisfy current low latency and high reliability requirements as well as optimize cost and energy power consumption. C-RAN introduces the approach of centralized, collaborative and cloud system. It centralizes BBUs from many remote sites in a pool and move the RF part into the RRHs [20, 8]. In C-RAN, the entire network is split into hexagonal cells. It typically consists of three main components: RRHs, BBU pool and fronthaul network, as depicted in Figure 2.2. The backhaul network connects different central offices (CO) and the gateway provides connectivity to the core network through the transport network, whose links typically employ optical fibers [13].

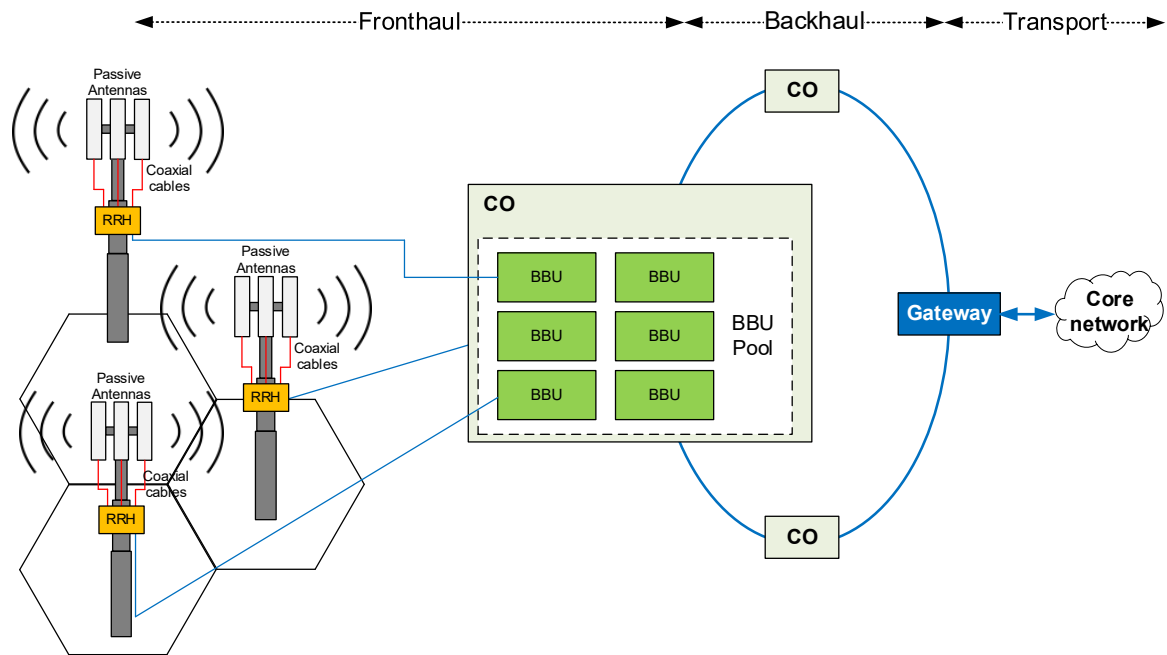


Figure 2.2. C-RAN architecture.

The RRH consists of transmitting and receiving RF components such as power amplifiers, low-noise amplifiers (LNA), analog-to-digital/digital-to-analog converters (ADC/DAC) and antenna system. It is installed on the tower near the passive antennas which allows low electrical losses. It basically transmits the RF signals to user equipments (UE) in downlink and forwards the signals from UEs to BBU pool in the uplink. The complexity and energy consumption are reduced due to signal processing is done at BBU pool. The centralized BBU enables easy and reduced RRH deployment cost in each cell site, which allows to cover large scale scenarios.

The BBU pool is located at a centralized site, such as cloud or data center, and consists of a multiple BBU nodes. It relies on hardware and software with high computational and storage capabilities. As baseband signal processing is conducted in BBU, resources are dynamically allocated and reconfigured based on data traffic demand of UEs and the time-varying radio channels, allowing efficient utilization of BBUs and less power consumption. BBU pool can be shared between RRHs at different remote sites, providing high bandwidth-efficiency.

The link connecting RRHs and BBUs is commonly referred as fronthaul link and is the responsible for traffic data exchange between them. Therefore, it has to carry a large amount of baseband data in real time, provide low latency and handle the requirements of multiples RRHs [21, 22].

2.1.2.1. Fronthaul link in C-RAN

There are different transport solutions, such as optical fiber, FSO, wireless fidelity (WiFi) or radio communications, which can be employed as fronthaul link between the RRHs and BBUs [21, 22]. Among them, high frequency radio communications, i.e. mmW solution, exhibits unexploited vast spectrum capacity. In spite of FSL, which increases with frequency, additional loss factors come into play, such as atmospheric gases attenuation and weather induced fading. Some of the wireless telecommunication and chipset suppliers such as Huawei, Qualcomm or Ericsson have been considering employing the unlicensed spectrum around 5 GHz frequency band, although the majority of such low-frequency bands have been employed by the existing networks. Conventionally, the fronthaul links are mainly optical fibers which can be realized with single mode fiber (SMF) or multi-core fiber (MCF) [13, 23]. In any case, optical fiber is the preferred solution due to its characteristics such as large capacity, low losses and

immunity to the RF signals. Furthermore, FSO is an excellent alternative in areas where optical fiber cannot be deployed due to the characteristics of the optical channel.

This link connects the RRHs to BBUs through a high speed digital fronthaul protocol which allows to transmit the digitized in-phase and quadrature (I/Q) waveforms by using typical protocols such as CPRI and OBSAI [24, 22]. Both of them contains vendor specific elements, then the full interoperability is not guaranteed. The new open radio interface (ORI), initiated by European Telecommunications Standards Institute (ETSI), can support multi-vendor interoperability between BS elements [22]. However, the CPRI is widely used in fronthaul links due to its efficient mapping methods.

Figure 2.3 illustrates an example of using optical signal transport and distribution in a typical city. In this example, multiple communication technologies are employed. COs are connected to the network core through a backhaul link using optical fibers whereas fronthaul links connect RRHs to the COs and might be based on hybrid photonic technologies, i.e. optical fiber, and FSO mostly where optical fiber is unfeasible. Finally, wireless RF communication, e.g. in high frequency mmW bands, is used to connect mobile users and RRHs.

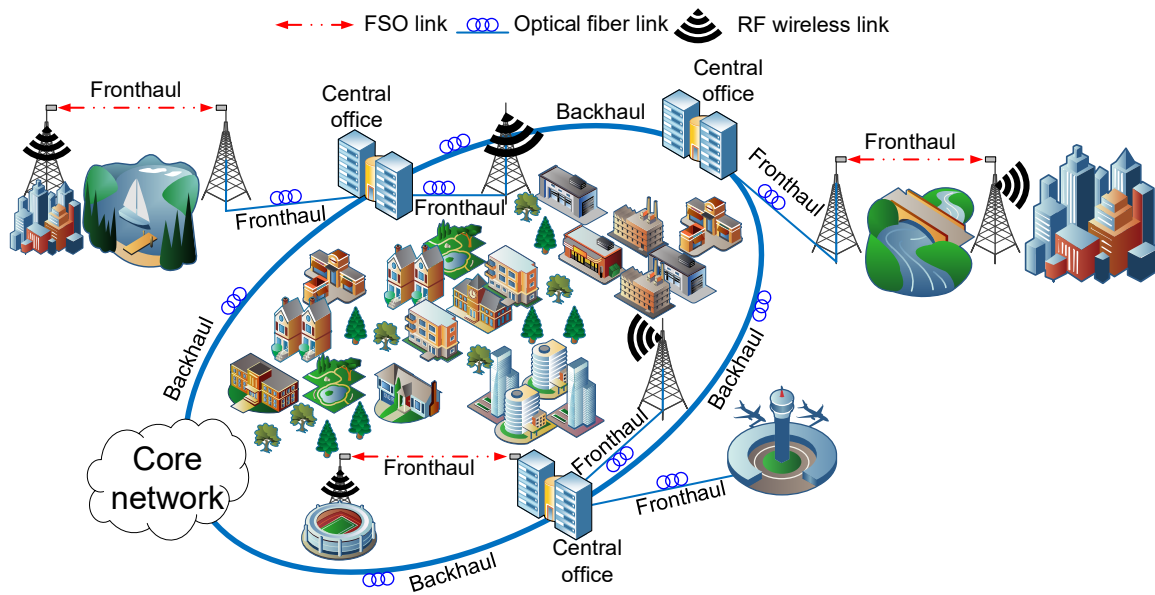


Figure 2.3. Example of a city network based on optical fiber and FSO fronthaul links.

2.1.2.2. C-RAN types

According to the splitting of RRH and BBU functionalities and the fronthaul link, C-RAN can be categorized into two types [20, 15]: fully and partially centralized C-RAN.

In fully centralized C-RAN, Figure 2.4(a), all functions of Layer 1 (L1) (i.e. sampling, modulation, resource block, etc.), Layer 2 (L2) (i.e. transport-media access control) and Layer 3 (L3) (i.e. radio resource control) are located at the BBU as well as the operation and management (O&M) layer. The main advantages of fully C-RAN are easy expansion of network coverage, easy upgrading of network capacity, support to multi-standard operation, enhancement of network resource sharing, and support to multi-cell collaborative signal processing. However, the high bandwidth requirements and the transmission of baseband I/Q signal between RRH and BBU must be addressed.

In partially centralized C-RAN (Figure 2.4(b)), RRH performs L1 functionalities, i.e. radio and baseband functions, whereas functions of L2 and L3 are held at the BBU. It requires low transmission bandwidth between RRH and BBU due to the baseband processing is moved to the RRH. Nevertheless, some drawbacks, such as low flexibility in network upgrades and less convenience for multi-cell collaborative signal are presented.

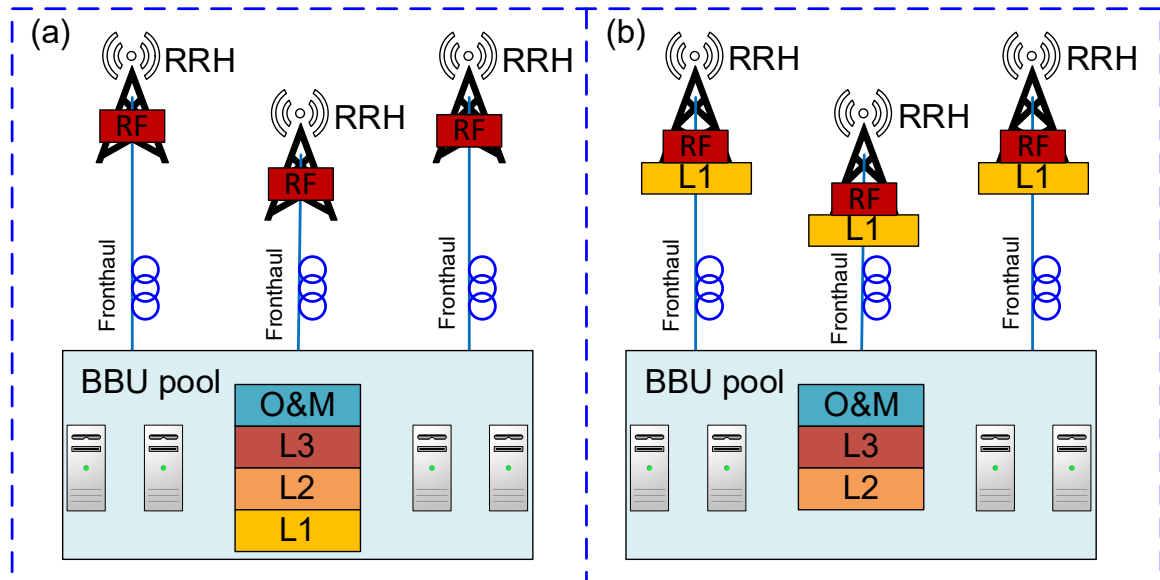


Figure 2.4. C-RAN structures: (a) fully and (b) partially centralized.

The appropriate choice of C-RAN structure depends on the network characteristics and requirements. In all cases, if the service provider needs to increase the network coverage or to split the cells in order to improve the capacity, new RRHs have to be deployed and, then, connected to the BBU pool. On the other hand, if it notices an increasing network load, it will just need to upgrade the hardware in the BBU pool in order to increase the processing capacity.

2.2. Millimeter waves

Since G. Marconi demonstrated the capability of using electromagnetic waves to transmit signals wirelessly in 1890s, frequency spectrum has been evolved rapidly due to the developments in communication systems. There are two key points in terms of the frequency spectrum designed for different generations of mobile communications. Firstly, frequency bands have been gradually released for a larger channel bandwidth that can allocate the demands for higher data rates. Secondly, all the released frequency bands are currently below 4 GHz due to lower frequencies are less susceptible to blockage and weather changes, and the components are more cost-friendly and power-efficient.

With the incredible growth of the number of consumer wireless devices in use, the 5G incorporates the mmW frequencies bands (30 to 300 GHz), as a main enabling technology, that will assist in achieving the high data rate and increased available bandwidth of cellular systems [25, 26]. The lower-frequency spectrum adjacent to 4G bands would provide an easier transition to 5G due to component maturity and the nature of the signal propagation characteristics. However, it is not a viable option mainly due two reasons. First, the sub-6 GHz spectrum has already been very crowded, filled with distributed bands dedicated to cellular communications, satellite and aerial communications, and wireless local area networks (WLANs). Secondly, mmW frequencies exhibits an enormous available frequency spectrum.

The latest mobile standard, 5G NR, supports sub-6 GHz frequency range 1 (FR) [27] and mmW frequencies bands between 24.25 and 52.6 GHz (FR2) [28]. According to [28], the Table 2.1 specifies FR2 frequency bands and the channel bandwidths of the 5G NR standard. Many countries have released a number of mmW bands for 5G NR communications in the K-band (European countries or China), Ka-band (European countries, USA or Japan) and V-band (European countries, USA or China).

Table 2.1. NR operating bands in FR2.

Band	Frequencies (GHz)	Common name	Bandwidth (MHz)
n257	26.50 – 29.50	Ka-band	50 – 400
n258	24.25 – 27.50	K-band	
n259	39.50 - 43.50	V-band	
n260	37.00 – 40.00	Ka-band	
n261	27.50 – 28.35	Ka-band	
n262	47.20 – 48.20	V-band	

Besides its huge available bandwidth, i.e. 270 GHz, mmW bands have several benefits compared with the existing wireless technologies [25, 26, 29]. Owing to short wavelengths, the component size can be reduced which enables large antenna arrays with small physical dimension. With the same antenna size, more antenna elements can be packed at mmW frequencies than at microwave bands and, then, the formed beam can be narrower which may be employed in other applications like radar detection. Furthermore, mmW signals enable to work with small-cell networks and frequency re-use is allowed due to low interferences, i.e. short wavelength and highly directional beams; and propagation characteristics, i.e. short range. Finally, there is still unlicensed mmW spectrum (Release 17, 5G NR-U) [30], i.e. 57 to 71 GHz, for various communication applications, e.g. Industry 4.0 and internal information technology infrastructure [31].

However, mmW signals present several challenges in terms of electronic circuit design and propagation [29]. On the one hand, mmW signals are susceptible to non-linear distortion produced by electrical amplifiers due to hardware manufacturing imperfections. Besides, phase noise is another huge challenge in the design of electronic components, which degrades severely the signal and poses great dare to mmW communications due to high oscillation frequency. On the other hand, the physical obstacles in real applications will weaken the mmW signals reducing the transmission range since its poor diffraction. Moreover, in terms of attenuation, mmW signals are affected by atmospheric gases, free space losses and weather fading.

Atmospheric attenuation is important for mmW propagation, especially in some specific bands, primarily due to oxygen and water vapor [32]. Figure 2.5(a) shows the RF signal attenuation due to atmospheric gasses calculated for pressure of 1,013.25 hPa, temperature of 15°C, and for the cases of a water vapour density of 7.5 g/m³ (Standard), and a dry atmosphere (Dry), i.e. water vapour density of 0 g/m³. For example, oxygen absorption at sea-level pressures forms a broad absorption band around 60 GHz, where mmW signals can suffer up to 14.8 dB attenuation over 1 km transmission. Furthermore, FSL is calculated by using the Friis transmission equation and becomes extremely significant at high frequencies [33]. Figure 2.5(b) plots the FSL at different frequencies over 1 km transmission range. For example, the FSL over 1 km transmission is 92.5 dB at 1 GHz and up to 128 dB at 60 GHz.

Finally, mmW signals can suffer more severe degradation due to weather conditions such as rain, snow, sleet, hail and fog, than lower frequencies [34]. For instance, dense fog can increase the loss up to 0.96 dB/km when transmitting 60 GHz mmW signal whereas heavy rainfall leads to 4.77 dB/km.

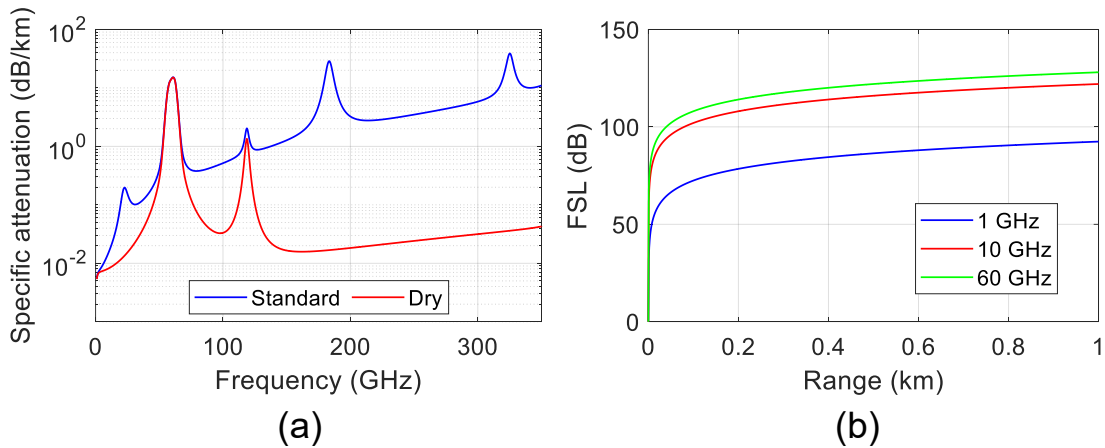


Figure 2.5. (a) Atmospheric gas spectral attenuation and (b) free space loss.

2.3. Microwave photonics technologies in 5G

MWP can be defined as an interdisciplinary approach which connects microwave and optical areas, employing opto-electronic devices for transmission, generation and processing of optical and electrical signals [10, 9]. It can be used for applications such as broadband wireless access networks, sensor networks, radar, satellite communications, instrumentation, warfare systems, ultrafast non-invasive measurements, terahertz spectroscopy and imaging, and radio astronomy amongst others [10, 9]. Figure 2.6 shows a fundamental scheme of a simple microwave photonic link. Microwave signals are converted into the optical domain, before transmission through photonic link, at the transmitter side by electrical-to-optical converter. At the receiver side, the optical signal is converted back into the electrical domain by optical-to-electrical converter.

Among the numerous topics theoretically and experimentally investigated in the previous literature, photonic generation of mmW signals, optically controlled phased array antennas, RoF techniques and photonic DAC/ADC can be identified as enabling technologies for future networks deployment.

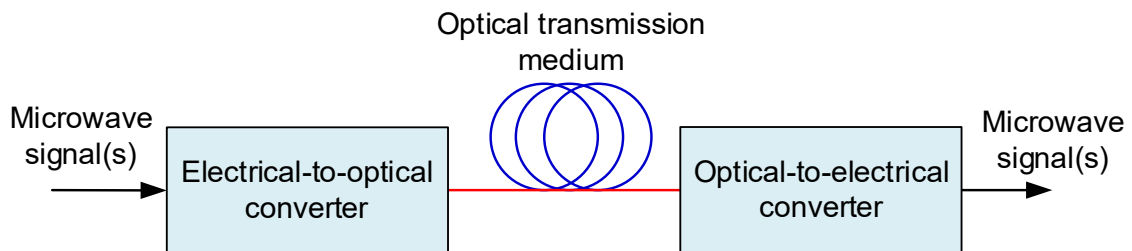


Figure 2.6. Basic scheme of a microwave photonic link.

2.3.1. Photonic signal generation

One of the most challenging approaches in microwave is the high frequency signal generation, e.g. mmW signals which frequency range is 30-300 GHz. The high frequency electrical signal generation using conventional electronics schemes shows some limitations because of the frequency restrictions of electronic devices and equipment. Microwave signals are traditionally generated by oscillators based on two or three terminal devices, e.g. diodes, crystal resonators or transistors. In addition, multiple electrical stages are required for high frequency generation with increased cost and complexity. These approaches are good for many applications, but such microwave electrical generation techniques do not satisfy the emerging applications which require higher frequency signals. Moreover, the distribution of mmW in electrical domain is not practical because of the high losses associated to the electrical transmission lines (e.g.

coaxial cable or waveguides) or wireless communications. Photonic mmW signal generation approaches are highly compatible with photonic signal distribution techniques, e.g. RoF or FSO schemes.

2.3.1.1. Photomixing

Photonic mmW signal generation is extremely attractive due to the ability to generate high frequency signals up to THz band just limited by the photodetector (PD) bandwidth with low phase noise, high tunability and immunity to electromagnetic interference compared to the traditional techniques in electrical domain [9, 10].

Optical heterodyning is the simplest mmW signal generation scheme [9, 35]. As shown in Figure 2.7, it is based on the beating of two optical fields at different wavelengths in the PD with wavelength spacing equal to the desired mmW frequency:

$$\begin{aligned} E_1(t) &= E_{01}e^{j(w_1t+\phi_1(t))} \\ E_2(t) &= E_{02}e^{j(w_2t+\phi_2(t))}, \end{aligned} \quad (2.1)$$

where E_{01} and E_{02} are the amplitude, w_1 and w_2 are the angular frequency, and ϕ_1 and ϕ_2 are the phase of the electrical fields.

The PD provides the opto-electronic conversion where the electrical current detected by the photodiode can be calculated as [36]:

$$i_{PD}(t) = \Re \cdot P(t) = \Re \cdot |E(t) \cdot E^*(t)|^2, \quad (2.2)$$

where \Re (A/W) is the photodiode responsivity, $P(t)$ is the detected optical power and $E(t)$ is the amplitude of the electromagnetic field at the input of the photodiode. After the opto-electronic conversion, the photocurrent at the PD output is obtained and expressed as follows [35, 9]:

$$i_{PD}(t) = \Re \cdot \{E_{01}^2 + E_{02}^2 + 2E_{01}E_{02} \cos[(w_1 - w_2)t + \phi_1(t) - \phi_2(t)]\}. \quad (2.3)$$

The two first terms represent the direct current (DC) component, and the third one is the RF signal generated at the frequency given by their difference, i.e. $w_1 - w_2$. This technique is capable of generating signals with a frequency up to THz range, just limited by the PD bandwidth.

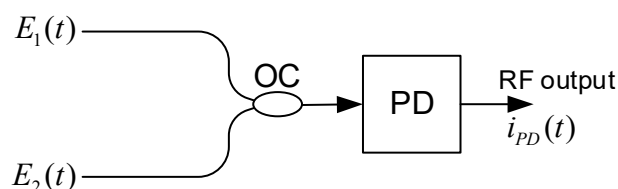


Figure 2.7. Basic scheme of photonic mmW signal generation: photomixing.

However, the generated RF signal exhibits high phase noise due to the optical sources are not correlated in phase. Previous works in the literature demonstrate that the phase noise derived from optical domain can severely degrade multi-carrier modulation mobile formats [37].

In order to mitigate this system limitation, numerous photonic approaches have already proposed in the literature to generate low phase noise RF signals with the two optical waves being locked in phase [9, 38]. As it is shown in Figure 2.8, these techniques can be categorized into four groups according to the lock phase method: optical phase control (injection locking, phase lock loop and injection phase locking), multimode light sources (dual-wavelength, mode locked and supercontinuum), external modulation (phase and intensity), and non-linear effects (stimulated Brillouin scattering and four-wave mixing), as explained in the following sub-Sections.

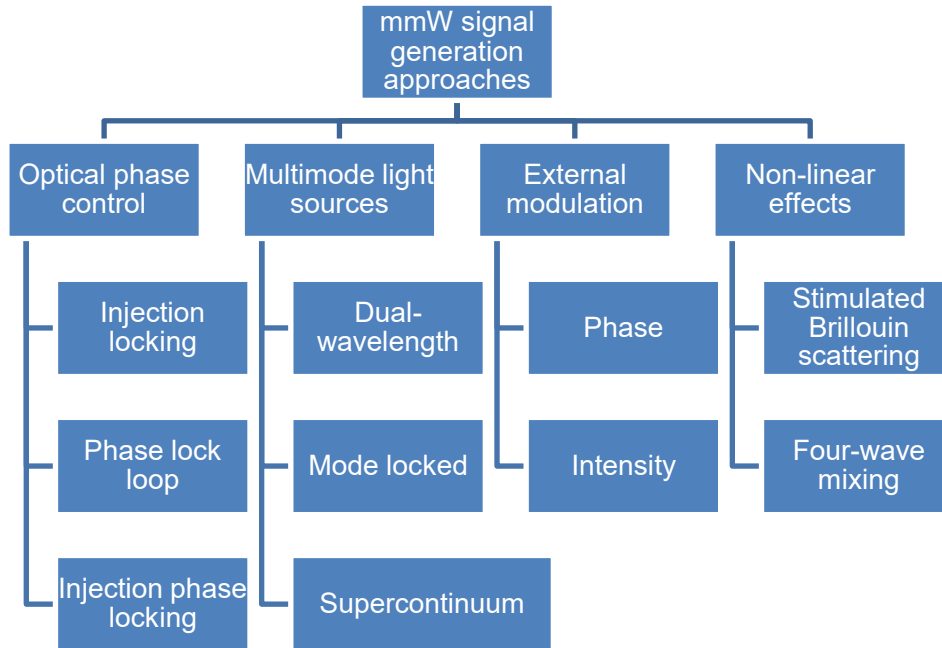


Figure 2.8. Classification of photonically mmW signal generation techniques.

2.3.1.2. Optical injection locking

The optical injection locking (OIL) technique is based on two or more lasers, usually named master-slave laser scheme, where a free-running slave laser is injected with coherent light from a master laser (ML). Therefore, the slave laser (SL) follows the master's phase. Figure 2.9 shows an OIL scheme that is composed of a master laser and two slave lasers. As it is well known, different orders of optical sidebands are generated by frequency modulation at ω_{RF} angular frequency spacing. The optical output signal of the master laser is then launched into the slave lasers. The slave lasers work as free-running mode, where their wavelengths are close to the master laser second sidebands, i.e. $\pm 2^{\text{nd}}$. Therefore, the wavelength of slave lasers is locked to the $\pm 2^{\text{nd}}$ order sidebands, i.e. OIL is achieved. Then, in this scheme, the wavelengths at the output of slave lasers is phase correlated, and the mmW signal generated at the PD output shows reduced phase noise.

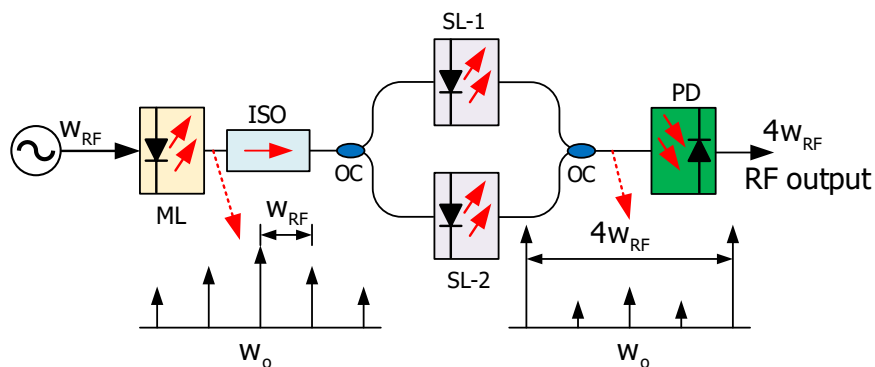


Figure 2.9. Optical injection locking of two slave lasers.

Several experiments have been demonstrated in the literature, e.g. a 64 GHz mmW signal has been generated with low phase noise and optical spectra with lower than 1 Hz linewidth has been successfully obtained [8] and slave lasers have been replaced by a Fabry-Perot laser (FPL) in [39]. Moreover, recent works demonstrate photonically generated mmW signals for 5G communications in full-duplex schemes [40, 41]. However, the main drawback is the need

of, at least, two lasers and other optical components (i.e. isolators, circulators, optical couplers...) which increase the complexity and cost.

2.3.1.3. Optical phase lock loop

In this technique, named optical phase lock loop (OPLL), a feedback loop enables the electronic control of the phase of the certain optical source. As shown in Figure 2.10, the phase of the electrical signal generated after beating the optical wavelength at PD is compared with the RF reference at a mixer followed by a low-pass loop filter. The phase difference between the signal and the RF reference produces an error voltage that controls the phase of one of the laser source by changing the injection current. Then, the phase of one laser is actively locked to a second laser.

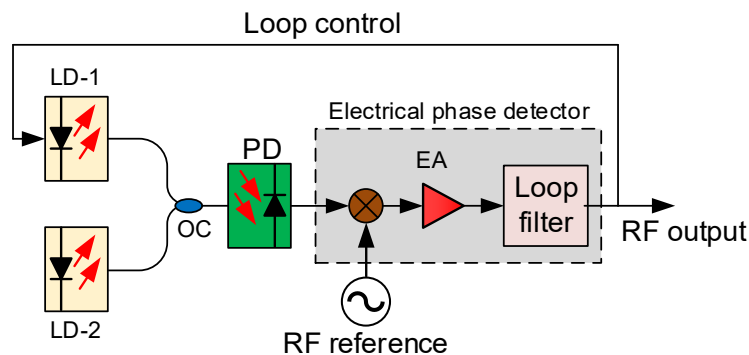


Figure 2.10. Scheme of an optical phase lock loop.

The OPLL technique presents a limitation due to the linewidth of the lasers, which limits the loop delay time and bandwidth of the OPLL [42, 43]. Narrow linewidth lasers are required for short feedback loops [9]. However, in order to reduce the feedback frequency, an OPLL incorporating a frequency down conversion module is proposed and demonstrated in [44]. Such module allows to employ lower-frequency components in the phase control loop and then, the feedback loop can control the phase of both laser sources.

Multiple works have demonstrated in the literature such as 6 to 34 GHz signal with a linewidth less than 1 mHz is generated in [45]. In [46], it is reported a phase comparison of the 20.5 GHz generated mmW between carrier-suppressed (CS) Mach-Zehnder modulator (MZM) and OPLL schemes.

2.3.1.4. Optical injection phase locking

The techniques above described, OIL and OPLL, can be combined in a single locking system called optical injection phase locking (OIPL) as shown in Figure 2.11. The output light of the master laser is split by a coupler into two fiber arms. In one of them, the light is launched into the modulator before being injected into the slave laser, and this is locked to one sideband of the modulated signal by OIL. The other arm is combined with the output of the slave laser in a second coupler and beaten at the PD. The generated signal at PD output is compared with the RF reference by the phase detector which controls the slave phase laser to achieve phase-locking.

As demonstrated in the literature, OIPL shows lower phase noise compared with single OIL or OPLL, i.e. wide frequency tuning (4 to 60 GHz), wide locking range (30 GHz) and low phase noise (93 dBc/Hz at 10 kHz offset from 36 GHz generated carrier) [47]. However, OIPL inherits the OIL and OPLL drawbacks, i.e. complexity, cost, laser linewidth limitation and the use of high frequencies component in the feedback loop.

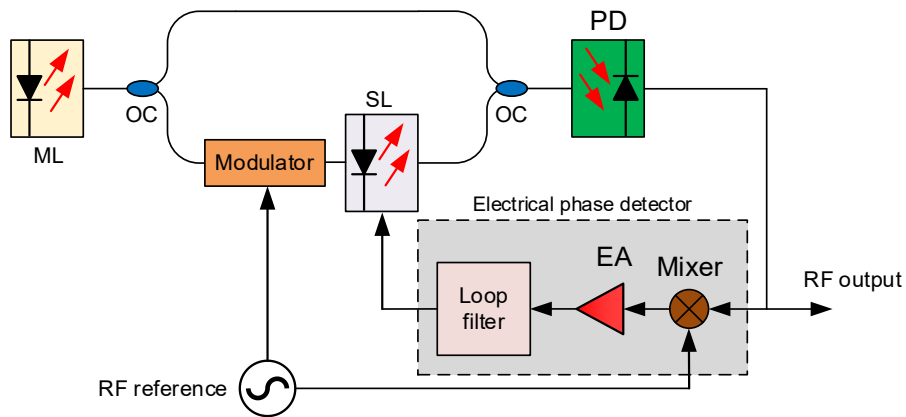


Figure 2.11. Scheme of an optical injection locking and phase locking system.

2.3.1.5. Dual-wavelength

Among the multimode light source approaches, microwave signals can also be generated by using a dual-wavelength laser, where two wavelengths of laser sources are not locked in phase. However, since the two wavelengths are generated from the same cavity, the phase correlation between the wavelengths is higher than employing two independent free-running laser sources.

In the fiber laser cavity depicted in Figure 2.12(a) [48], the insertion of Fiber Bragg grating-1 (FBG) with two ultra-narrow transmission bands, which are selected by the two reflection bands of FBG2 (see Figure 2.12(b)), leads to the spectral response of the two cascaded FBGs shown in Figure 2.12(c). The signal is launched into the PD and, since both wavelengths have been generated at the same cavity, they share the same gain cavity and the phase fluctuations between the two wavelength signals are low.

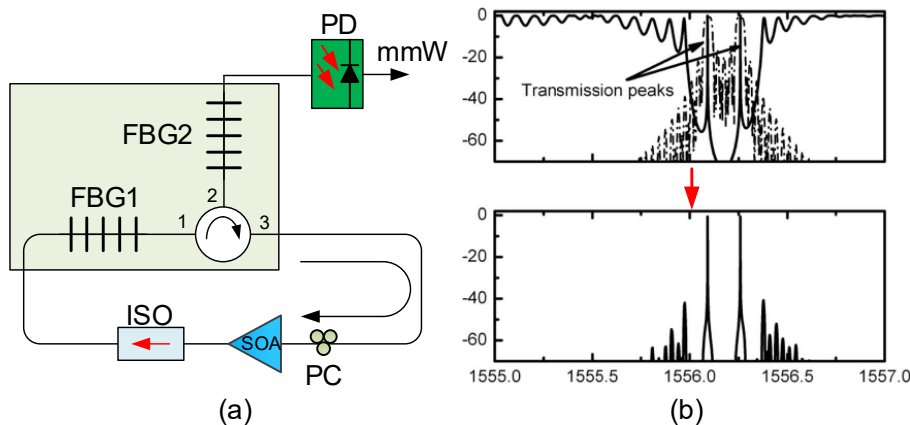


Figure 2.12. (a) Dual-wavelength scheme based on a fiber ring laser and (b) spectra of the two cascaded FBGs [48].

Moreover, dual-wavelength lasers can be monolithically integrated chips where the two wavelengths share the same cavity [49, 50]. This allows to reduce the packaging size and optical delays inside the chip, as well as cost effective production, even tighter packaging, and fewer alignment issues. In [49], a mmW signal is generated in the 5-110 GHz frequency range by using integrated indium phosphide (InP) dual-wavelength lasers while in [50], a 146 GHz carrier wave frequency is generated and 1 Gbit/s on-off keying (OOK) data signal is transmitted successfully in a free-running state.

2.3.1.6. Mode locked laser

Mode-locked lasers (MLL) sources are very attractive solution for microwave signal generation. The term “mode-locking” means to the phase coupling of the numerous modes of the source. The phases of the spectral components are locked when they differ only by a constant phase shift, and therefore, narrow beat-note signal linewidth can be generated [51].

Passive MLL is limited by the fundamental repetition rate frequency which is inversely proportional to the cavity length. However, active mode-locking generates high repetition rate pulses by modulating the cavity loss or phase periodically through an intra-cavity electro-optic modulator at a harmonic cavity frequency. Hybrid mode-locking exists where active and passive techniques are combined and the phase noise of the resulting beat note can be improved considerably [52, 53].

Several mmW generation experiments using MLLs have been demonstrated in the literature. For example, Figure 2.13(a) shows the optical spectrum of a mode-locked FPL [54]. A zoom of the frequency comb is displayed in Figure 2.13(b) while Figure 2.13(c) and (d) depict the generated mmW at 70 and 120 GHz. In other works, mmW signals can be generated with frequencies up to 320 GHz [53, 55, 56, 57].

Furthermore, MLLs can be fabricated in photonics integrated circuit (PIC) with small footprint, lower power consumption, improved alignment and immunity to vibration [58].

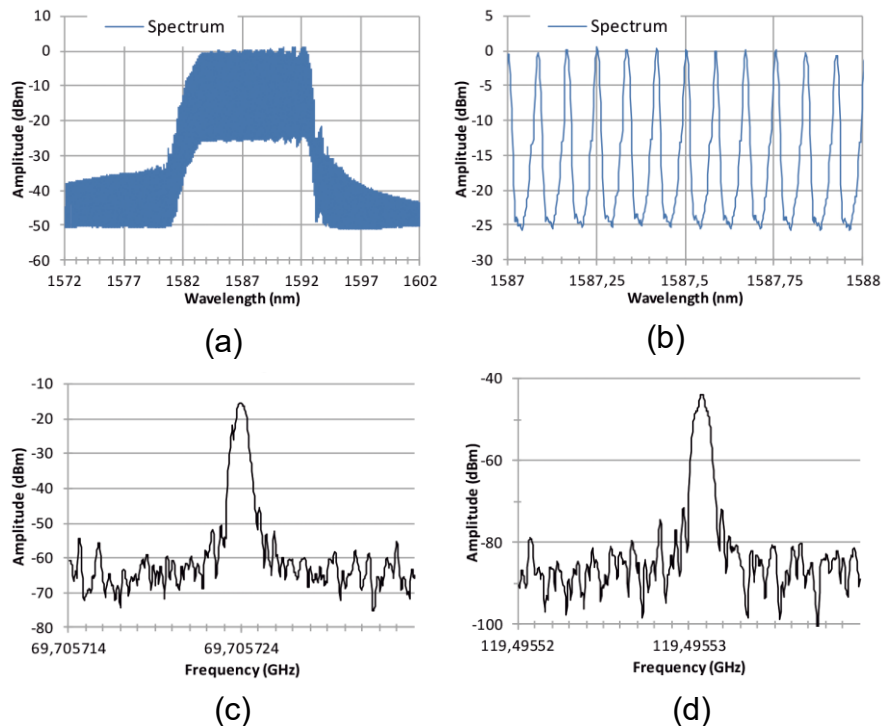


Figure 2.13. (a) Optical spectrum of mode locked laser, (b) zoom of the frequency comb with 10 GHz FSR, (c) electrical spectrum at 70 GHz and (d) electrical spectrum at 120 GHz [54].

2.3.1.7. Supercontinuum lasers

The supercontinuum (SC) sources emit broadband near-infrared laser light. The term “supercontinuum” is usually defined as broadband light generated from the non-linear frequency conversion of a laser. This yields an optical source that preserves the spatial coherence properties.

SC lasers have been investigated in the literature, such as demonstrations of the SC light generation based on the non-linear dispersion-flattened photonic crystal fiber (PCF) [59], or the generation and transmission of four 40 GHz RoF channels using a SC multi-wavelength lightwave source based on PCF.

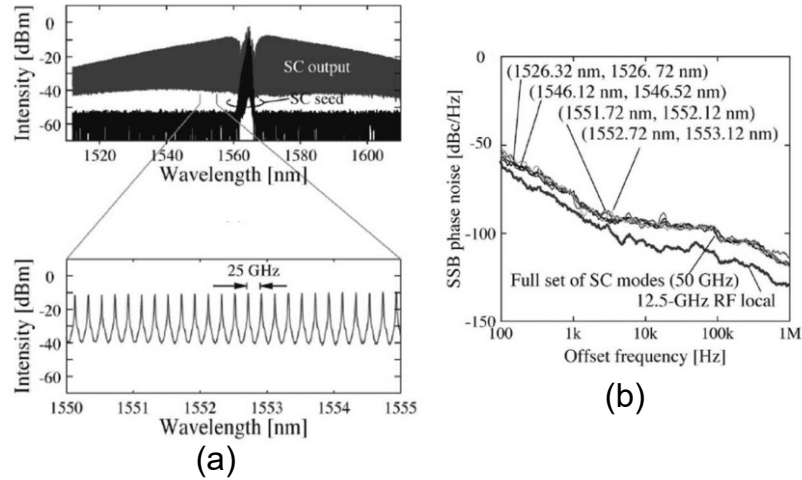


Figure 2.14. (a) Optical spectrum of SC light source (bottom shows magnified scale) and (b) SSB phase noise of 50 GHz generated signals [60].

In [60], a single SC light source working as a multiwavelength light source leads to a frequency spacing of the comb laser of 25 GHz (Figure 2.14(a)). Therefore, the employed photonic-up conversion technique is the optical heterodyning, where the beat signal is generated with square-law photodetection of two SC modes (25 GHz spacing). Figure 2.14(b) shows the measured phase noise of 50 GHz generated mmW signal using different SC modes. The phase noise at 10 kHz frequency offset is -96.1 dBc/Hz, which is almost the same phase noise characteristics for all 50 GHz generated signals by beating.

2.3.1.8. Phase modulator

Methods with one laser plus an external optical modulator show great potential for producing high purity mmW signal. The external modulator is an optical waveguide where the electro-optic effect changes the optical properties of certain material when an electric field is applied. Most electro-optic devices, e.g. a phase modulator (PM), are based on Pockels effect, i.e. the proportional modification of the refractive index of the material by applying an electric field. This effect is found in crystals such as lithium niobate (LiNbO_3), III-V semiconductors such as gallium arsenide (GaAs) or InP as well as poled polymers [36]

Phase modulation approach is shown in Figure 2.15(a) where a PM is employed. A PM is an external modulator which can control the optical phase of an optical wave. The PM generates all optical sidebands including the optical carrier. No DC bias is required and mmW signal with large frequency and high spectral purity can be generated locally and remotely [9].

As shown in Figure 2.15(b), the PM is fed by a continuous wave (CW) lightwave given by:

$$E_{in}(t) = E_0 e^{j[w_0 t + \phi_o(t)]}, \quad (2.4)$$

where E_0 is the amplitude, w_0 is the angular frequency, and $\phi_o(t)$ are phase of the optical signal; and it is driven by a RF electrical signal given by:

$$v(t) = V_{RF} \cos(w_{RF} t + \phi_{RF}(t)), \quad (2.5)$$

where V_{RF} is the voltage amplitude, w_{RF} is the RF angular frequency and $\phi_{RF}(t)$ is the phase.

The output of the PM is given by [61, 62]:

$$E_{out}(t) = E_0 \sum_{n=-\infty}^{\infty} J_n(\eta) \cos \left[\left[(w_0 + n w_{RF}) t + n \phi_{RF}(t) + \phi_o(t) + n \frac{\pi}{2} \right] \right], \quad (2.6)$$

where η is the modulation index, $\eta = \frac{V_{RF}\pi}{V_\pi}$ and V_π denotes the half-wave voltage of the phase modulator, and $J_n(\cdot)$ is the n^{th} Bessel function of first kind, which gives the amplitude of the n^{th} optical sideband, as it can be observed in Figure 2.15(c). By tuning the power level of the RF driving signal, the modulation index can be set that the optical power in the desired optical sideband is maximized. Note that the arrow direction shows the relationship between the phase of the sidebands and the phase of the optical carrier.

As PM produces all optical sidebands, an optical filter may be employed for carrier suppressing (notch filter) or selecting the optical sidebands with the desired wavelength spacing (band pass filter). Then, after photodetection, a mmW signal is generated by the desired frequency.

A major advantage of PM modulator approach is a tunable mmW signal generation by using an optical filter, which simplifies the scheme [61]. Furthermore, since the PM does not require bias, there is no bias-drifting related problems.

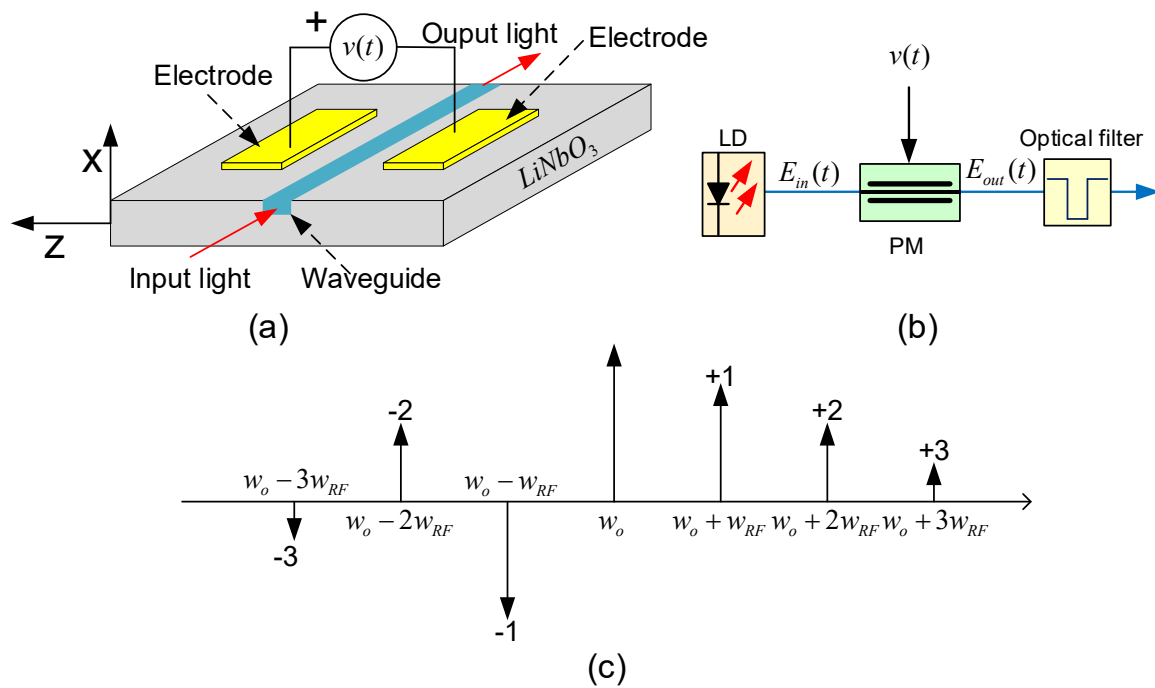


Figure 2.15. (a) Photonic integrated waveguide electro-optic phase modulator in perspective view, (b) schematic diagram of mmW generation using PM and (c) optical spectrum at the output of the PM.

By using an electrical driving signal from 18.8 to 25 GHz [61], two bands of mmW signals from 37.6 to 50 GHz and from 75.2 to 100 GHz with high signal quality are generated. In [62] mmW signal is generated with low phase noise and the frequencies cover from 75 to 140 GHz. An 88 and 90 GHz mmW signal with up to 1 Gbaud 16-quadrature amplitude modulation (QAM) data signal have been successfully generated and transmitted in [63]. In [64], 133 GHz D-band multi-frequency vector mm-wave signal over 80 km SSMF transmission and 10 m wireless has been demonstrated.

2.3.1.9. Intensity modulator

Another approach also based on external modulation employs an interferometric structure, i.e. Mach-Zehnder interferometer, which is used in combination with PM, as depicted in Figure 2.16, where the phase modulation is converted into intensity modulation.

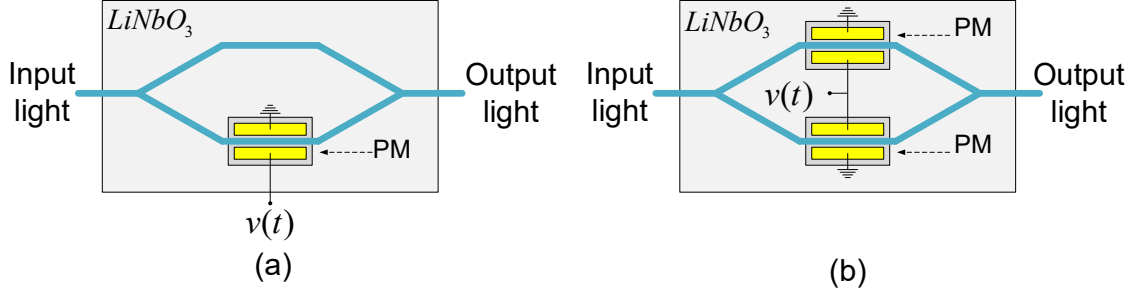


Figure 2.16. Mach-Zehnder structures: (a) single drive and (b) dual-drive.

This MZM is based on a Mach-Zehnder interferometer under two main configurations, which are single (Figure 2.16(a)) and dual drive (Figure 2.16(b)). In the single drive structure shown in Figure 2.16(a), the lower arm includes signal phase modulation before combination of signals travelling through both arms. In this modulator there is always a residual phase modulation, called chirp, which produces an instantaneous frequency change.

Furthermore, dual drive structure shown Figure 2.16(b) include one PM in each arm. The PMs are driven by two RF signals, $v_1(t)$ and $v_2(t)$. When identical signals are applied to each arm with a relative phase of 180° , i.e. $v_1(t) = -v_2(t) = \frac{v(t)}{2}$, the dual drive MZM works in push-pull configuration. Figure 2.16(b) shows the configuration of the driving signal pads. The output field of dual drive MZM is given by:

$$E_{out}(t) = \frac{E_{in}(t)}{2} \left\{ e^{j\frac{v(t)}{2V_\pi}\pi} + e^{-j\frac{v(t)}{2V_\pi}\pi} \right\} = E_{in}(t) \cos\left(\frac{v(t)}{2V_\pi}\pi\right), \quad (2.7)$$

where the relative phase of the output light is expressed as

$$\angle E_{out}(t) = \angle E_{in}(t) + \angle e^{j\frac{v(t)}{2V_\pi}\pi} + \angle e^{-j\frac{v(t)}{2V_\pi}\pi} = \angle E_{in}(t). \quad (2.8)$$

From equation (2.8), dual drive MZM in push-pull configuration can ideally remove the chirp since opposite relative phases are induced in both interferometer arms.

Although this technique suffers from high driving voltage, severe DC bias drift and imbalanced optical paths [65, 66], the MZM based on LiNbO_3 can offer high extinction ratio, high bandwidth, high optical input power handling, compactness and reliability. Intensity modulation operating point defines the optical modulation, such as double sideband (DSB) whose optical sidebands can be filtered out, or CS-DSB whose optical carrier is suppressed (explained in Chapter 3). Then, the modulation type can be selected depending on the targeted application. The use of external modulation techniques for mmW signal generation exhibits an excellent compromise and it will be the preferred approach during this Thesis.

2.3.1.10. Non-linear effects

Non-linear effects can assist the photonic mmW signal generation where two phase-correlated optical carriers are employed. The phase-correlated optical carriers may be generated by different method such as OIL, OPLL, OIPL or external modulation as described above, and non-linear effects such as four-wave mixing (FWM) or stimulated Brillouin scattering (SBS) contribute to the mmW signal generation.

FWM is a non-linear effect which occurs in the semiconductor optical amplifier (SOA). It is based on Kerr effect related to the third-order electric susceptibility. Consider that an optical signal composed of three different angular frequencies, w_{p1} , w_{p2} as the pump signals and w_{probe} as the probe signal, is launched into a non-linear medium. The angular frequency w_{idler} of the newly emerging signal is given by [67]:

$$w_{idler} = w_{p1} + w_{p2} - w_{probe}. \quad (2.9)$$

When an optical signal with only two different optical frequencies (w_p and w_{probe}) experiences FWM, a special case arises which is called partially degenerate FWM and leads to the following:

$$w_{idler} = 2w_p - w_{probe}. \quad (2.10)$$

Figure 2.17 shows a FWM scheme also employing external modulation. When an optical signal which includes just two different optical frequencies, $(w_o + nw_{RF})$ and $(w_o - nw_{RF})$, entering into the SOA, the emergence of two new idlers can be expressed as:

$$\begin{aligned} w_{idler1} = w_{+nth} &= 2(w_o + nw_{RF}) - (w_o - nw_{RF}) = (w_o + 3nw_{RF}) \\ w_{idler2} = w_{-nth} &= 2(w_o - nw_{RF}) - (w_o + nw_{RF}) = (w_o - 3nw_{RF}). \end{aligned} \quad (2.11)$$

The new optical sidebands (w_{idler1} and w_{idler2}) are generated with frequency spacing of $3n$ times that of RF driving signal. Finally, the new optical sidebands are filtered out and a mmW signal at $6nf_{RF}$ is generated after opto-electronic conversion at PD.

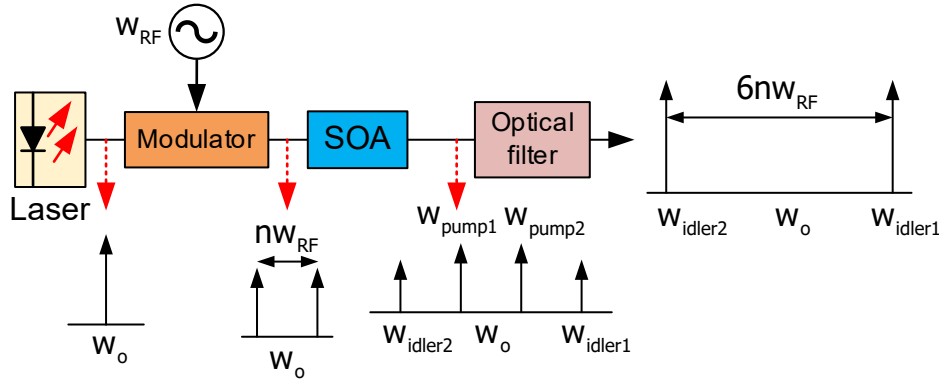


Figure 2.17. Diagram of FWM-aided photonic mmW signal generation.

FWM is a good approach for optical frequency multiplication up to large frequencies, as will be implemented in this Thesis, in spite of cost related issues. Examples in the literature report a 42 GHz mmW signal, i.e. 12-tupling the microwave source frequency, generated with noise level lower than -83 dBc/Hz at 10 kHz offset in [68]. In [33], the feasibility of optical mmW signal generation up to 210 GHz using frequency 12 times that of the RF driving signal has been demonstrated.

However, SBS is another well-known non-linear effect which occurs at low pump power in an optical fiber and degrades the link performance in optical fiber networks due to the signal energy is transferred to the backscattered signal [69]. Nevertheless, SBS has frequency selective amplification characteristic that can be employed for mmW signal generation [70]. The concept of Brillouin selective sideband amplification is shown in Figure 2.18 [70]. Inset (i) shows the optical sidebands generated by modulating the optical carrier. The pump laser is coupled into the SSMF and the counter-propagating Brillouin Stokes gain is generated at the frequency of w_{BS} (inset (ii)). Therefore, the optical sideband is amplified provided it falls within the Brillouin gain spectrum in a copropagation manner, as shown in inset (iii). Finally, the optical signal is launched into the PD and a mmW signal with low phase noise is generated from the beating of both sidebands.

The mmW signal generation employing SBS has several properties [70] for signal amplification. Consequently, it usually keeps below the SBS threshold and the implementation is much less expensive than an erbium-doped fiber amplifier (EDFA) or SOA. It has very narrow gain bandwidth that is advantageous for the efficient selective sideband amplification, although it may not be useful for wideband signals. Finally, the gain is generally high, but this is accompanied by higher amplifier noise caused by the spontaneous emission.

There are several works in which the SBS is utilized for mmW signal generation. For example, a 10.87 GHz mmW signal is generated due to optical heterodyning of the CW laser signal and Brillouin Stokes frequency in [69]. In [71] [72], the MZM generates sidebands up to 6th order, but just 5th sideband is amplified by SBS. Thus, the beating of the 5th sideband and the carrier generate a 40 GHz mmW signal with a phase noise of less than -90 dBc/Hz.

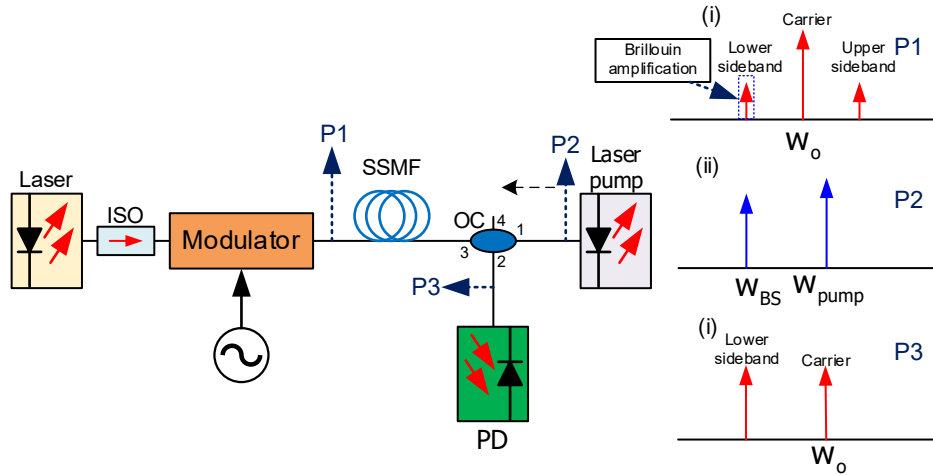


Figure 2.18. Schematic diagram for mmW signal generation based on SBS. Insets shows the principle of selective sideband amplification.

2.3.2. Radio over fiber signal transmission

RoF has been considered as an enabling technology for next generation communication networks. It consists of transporting an electrical signal through an optical fiber. In the transmitter, an optical carrier is modulated by an electrical signal. After optical signal transmission over the optical link, the electrical signal is recovered after photodetection at the receiver.

The basic scheme to realize this link is shown in Figure 2.19(a). The RF electrical signal is converted into optical domain through a laser which is directly modulated. Then, the optical signal is propagated along an optical fiber. Finally, the PD, which holds the opto-electronic conversion, recovers the transmitted electrical signal. This link is called in the literature intensity modulation – direct detection (IM-DD). Figure 2.19(b) shows a RoF approach which employs an external modulator based on MZM operating at linear point. The external modulator, which is driven by the electrical signal, modulates the optical signal coming from the laser. The resulting optical signal is transmitted over the fiber and launched into the PD. The PD performs the opto-electronic conversion and the electrical signal can be recovered. In both approaches, since multiple optical sidebands are injected into the PD, high order harmonics are generated after optical beating. Harmonics in the generated electrical signal can be controlled by optical signal filtering or MZM operating point, as it will explained in Chapter 3.

RoF technology offers technical performance benefits over traditional data transmission through coaxial cables [13, 8]. Optical carrier frequencies are in the range of 193.4 THz at 1550 nm in contrast to microwave signals with about tens of GHz. Therefore, the huge bandwidth available in optical fiber systems makes them as an elegant and simple approach to deliver wideband data signals. Indeed, optical fiber presents immunity to electromagnetic interference (EMI) due to the dielectric material. These characteristics also provide privacy and security against eavesdropping.

The optical fiber attenuation, which is below 1 dB/km at the main transmission windows, is very low compared to the coaxial cables. For example, fiber attenuation is typically 0.2 dB/km at 1550 nm and does not vary with the modulating RF, meanwhile a commercial typical attenuation of a coaxial cable at 70 GHz is up to 6 dB/m [73]. Therefore, the distribution

distance of optical signals is several times higher compared with electrical signals. Indeed, the transmission power may be greatly reduced.

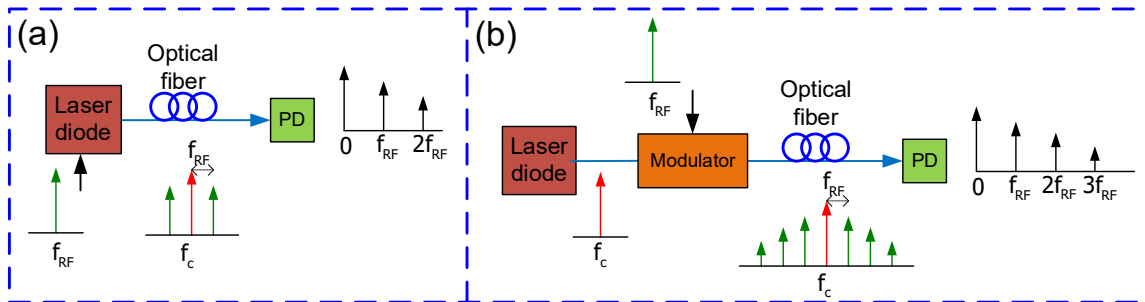


Figure 2.19. Typical RoF link schematic using: (a) directly and (b) external modulation.

Moreover, RoF is able to transport and multiplex multiple RF signals using sub-carrier multiplexing (SCM) or wavelength-division multiplexing (WDM). In SCM, multiple RF signals are aggregated at single wavelength meanwhile, in WDM, each wavelength is modulated at a given RF signal. Moreover, mode multiplexing and multicore fibers can be also employed in RoF links to extend the operational flexibility. Thus, RoF can be used to distribute multi-operator and multi-service traffic.

2.3.2.1. RoF transmission schemes

The RoF signal transmission can be digital or A-RoF, depending on the data format of the electrical data signal.

Figure 2.20(a) shows D-RoF scheme which involves the digitalization of analog RF signal before signal transmission over optical fiber. In this scheme, the analog RF signal is first converted to a binary electronic pulse in an ADC and after is launched into transmitter for electro-optical conversion. The resultant optical signal is transmitted over fiber. After signal photodetection at the optical receiver, a DAC must be used prior to the RF wireless transmission. The CPRI, enhanced-CPRI (eCPRI) and OBSAI protocols are commonly used as interfacing approaches [8, 18]. However, D-RoF approach consists of digitizing the analog radio signal with fine quantization resolution to guarantee high fiber link fidelity at the cost of vast optical bandwidth consumption. Indeed, this translates into continuously equipment upgrades, including the installation of supplementary optical fiber links and/or high-speed transceivers [18].

In A-RoF systems, the analog radio signals are directly modulated onto an optical carrier at the transmitter, as depicted in Figure 2.20(b). The RF signal simply modulates an optical carrier at electro-optical converter and transmitted over fiber. At the receiver, the RF signal is recovered using an opto-electronic converter and may be directly transmitted over RF wireless link. There is not signal quantization which is translated into higher bandwidth efficiency compared to a D-RoF option [18, 74]. However, A-RoF signal transmission suffers severe impairments such as chromatic dispersion, noise and distortion [8]. Finally, the non-linear characteristics of the opto-electronic devices, especially at the transmitter, are the key contributors to signal distortion, i.e. as intermodulation distortion (IMD).

In terms of electrical carrier frequency, three schemes can be distinguished: baseband-over fiber (BBoF), intermediate frequency-over fiber (IFoF) and radio frequency-over fiber (RFoF), as depicted in Figure 2.21.

In RFoF scheme, electrical signals at high frequency, i.e. mmW frequencies, can be transmitted directly over the optical fiber. Therefore, frequency up conversion is not needed at the remote antenna sites which simplifies the architecture. Nevertheless, high speed and bandwidth PDs are required at the receiver side, increasing the implementation cost. Moreover, the fiber chromatic dispersion drawback degrades the optical signal, which is even worse at higher frequency signals.

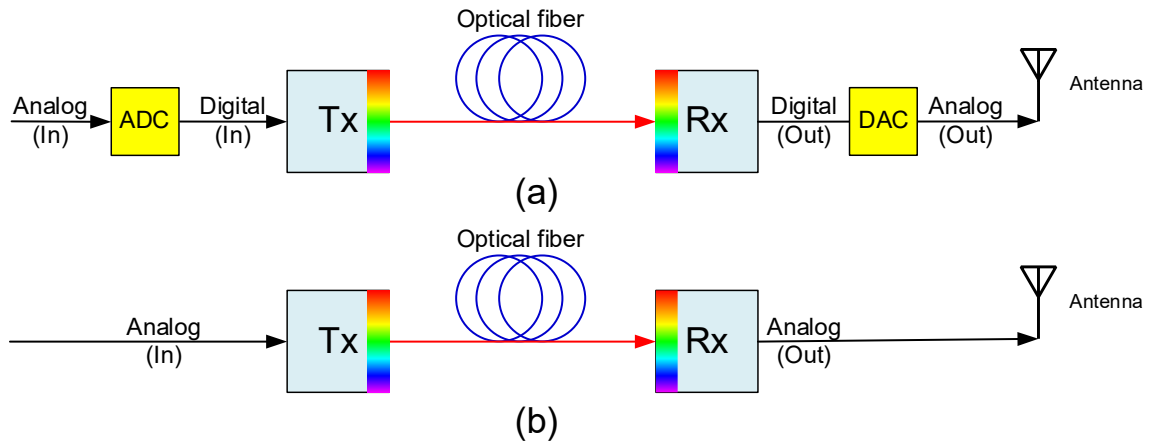


Figure 2.20. RoF links based on (a) D-RoF and (b) A-RoF.

IFoF scheme transport the signals at lower intermediate frequency (IF) whereas BBoF scheme transmits the signals at baseband frequency. Both schemes, IFoF and BBoF, require up-conversion to mmW frequency at the antenna BS. The system needs lower-speed opto-electronic devices and the impact of fiber chromatic dispersion is lower than RFoF. However, high complex and costly devices, like mmW local oscillator (LO) and high-speed mixers, are needed for frequency up-conversion. These drawbacks also limit the upgradability and scalability, in particular when additional carrier frequencies are required.

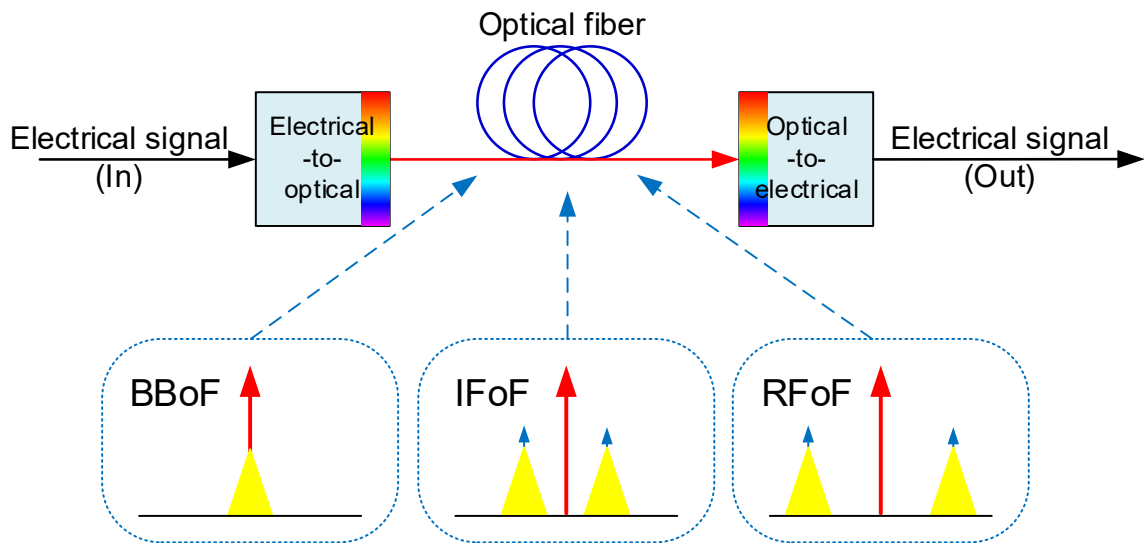


Figure 2.21. RoF schemes based on different electrical carrier frequency signals.

2.3.2.2. RoF applications

RoF is widely used in different application scenarios, as explained in this Section. In wireless networks, e.g. 4/5G, WiFi, worldwide interoperability for microwave access (WiMax), etc., radio signals are carried over fiber optics to a center location. RoF is also a key enabling technology for 5G NR standard in C-RAN as fronthaul link between the BBU pool and the RRH.

Moreover, the massive deployment of mobile devices at home generates a rapid traffic growth in radio mobile networks. The new WiFi standard 802.11.ad operates at 60 GHz frequency band and is suitable to handle the new data traffic demand at home area networks. However, this system experiences higher propagation losses compared with the low frequency WiFi standards (2.4 and 5 GHz), limiting the coverage. RoF is a promising solution to solve this problem due to simplicity and high bandwidth [75].

Finally, radio astronomy systems require extremely radio sensitive and electromagnetic compatible signals. Indeed, immunity to EMI, very low power level of the receiver signals and low noise are required in these systems. For that purpose, RoF is proposed to be used between the front-ends receptors and the post-processing unit [76].

2.3.2.3. RoF impairments and limitations

Naturally, the employed components in RoF systems impose impairments and limitations on the optical signals, which distort the received RF signals. These impairments tend to limit the frequency/bandwidth and transmission distance of the RF signal.

The output signal emitted by the light source is commonly modulated by the RF signal by an external modulator, which can provide reduced chirp as well as high bandwidth. However, spurious out-of-band spectral components can be generated due to the modulator non-linear response [77]. These spectral components lead to IMD, which reduce the carrier-to-interference ratio (CIR) and severely degrade the RF signal at the receiver. Additionally, DC bias voltage drift [78] and the imperfect splitting ratio of external modulator branches [79] can produce degradation at the recovered RF signal.

DMLs, where the electrical signal is applied to the laser, are often used in RoF systems in order to reduce the cost and complexity. The frequency chirp of the DML combined with fiber dispersion, results in power fading [80, 81] besides non-linear frequency system response, which leads to harmonic distortion (HD) and IMD. Moreover, clipping distortion can be arisen when the injected modulating signal current occasionally drops below the laser threshold current, i.e. turning the laser off, or enters saturation.

The system performance is deteriorated by chromatic dispersion in RoF links, specially for long distances. In optical DSB modulated signals, the sidebands undergo different amount of phase shift relative to the optical carrier when are transmitted over fiber links. After the square law photodetection, this phase difference can induce destructive interference of the beat signal which arises a power fading of generated RF signal. The power fading varies periodically depending on the chromatic dispersion, transmission distance and frequency parameter as can be obtained from the RF power expression [82]:

$$P_{RF} \propto \cos^2 \left[\frac{\pi LD}{c} \lambda_o^2 f_{RF}^2 \right], \quad (2.12)$$

where $L(m)$ is the fiber length, $D(\text{ps}/\text{nm} \cdot \text{km})$ is the fiber chromatic dispersion parameter, $c(\text{m}/\text{s})$ is the vacuum lightwave speed, $\lambda_o(m)$ is the wavelength of the lightwave and $f_{RF}(\text{Hz})$ is the electrical signal frequency. Multiple techniques have been demonstrated to overcome the impact of the chromatic dispersion [83]. Optical single sideband or optical carrier suppression schemes are immune to chromatic dispersion induced fading. Other proposals include a modulation diversity receiver, which can compensate the power fading whereas cascaded MZMs should be employed for wideband signals [83, 84].

Besides, the transmitted pulses over different frequencies experience different group velocities, they misplace their temporal overlap after some propagation distance. This effect, named bit walk-off, causes inter-symbol interference (ISI) [85].

The PD usually works at linear region. However, at high received optical power, non-linearities begin to dominate which induces a RF signal distortion. Furthermore, multiple optical sidebands may be launched into the PD, which can produce undesired harmonics at the PD output after photomixing.

Noise sources in RoF links [86] are mainly due to relative intensity noise (RIN) at laser diode and thermal noise and shot noise at PD. These noise sources may impose a limitation on the signal-to-noise ratio (SNR) of the received RF signal.

Additionally, the use of optical amplifiers, like EDFAs, provide the amplified spontaneous emission (ASE) noise. The effect of ASE noise also produces a reduction of SNR although it can be partially mitigated by proper optical filtering.

2.4. Free-space optics

FSO is presented as a potential enabling technology for 5G and beyond. It is an optical communications technology which transmits optical signals wireless through unguided transmission medium. It is based on the ancient civilizations that used fire beacons or smoke signals for communications. The first optical communication through free spaces, based on sunlight, was done by Alexander Graham Bell in 1880 [87]. In current FSO systems, extremely narrow laser beams at IR wavelength are transmitted employing the air as transmission medium instead of optical fiber or any optical system guiding the light.

The competitors of FSO are the optical fiber, wireless RF communications and the copper cable-based. However, FSO exhibits several advantages since it provides better security, cheap network installation and easy maintenance and upgrades. Moreover, it employs IR wavelength so it has similar transmission bandwidth capabilities, achieving high data rates, compared with optical fiber. FSO losses are much lower than RF losses due to high directivity. For example, the atmospheric attenuation for the transmission window 1520-1600 nm is lower than 0.2 dB/km with clear visibility [11] whereas the RF losses strongly depend on the electrical frequency, e.g. 60 dB at 25 GHz for 1 m wireless distance (Section 2.1). FSO system is an excellent alternative in areas where the optical fiber cannot be installed. Thus, it is an excellent solution for high-capacity wireless links, e.g. fronthaul link. Finally, the optical carrier at THz frequencies is still unlicensed so does not require license fees.

Optical wireless transmission using FSO has been extensively studied in the literature. For example, a 40 Gbit/s has been experimentally transmitted over 20 m FSO in [88]. In [89], 50 m outdoor experiments between two buildings with 8×25 Gbit/s pulse-amplitude modulation-4 (PAM) has been demonstrated. Recently, a 20 Gbit/s data signal of 5G mmW and sub-THz signals through a 20 km fiber, 500 m optical wireless and up to 2 m RF wireless link has been transmitted [90].

2.4.1. FSO scheme

An FSO system basically consists of three subsystems: transmitter, channel and receiver, as illustrated in Figure 2.22(a). The transmitter, which usually includes an optical source and modulator, emits a modulated electrical signal over an optical carrier. A collimating lens and a mechanical alignment stage are usually employed in order to transmit extremely narrow beamwidths. The channel is the atmosphere which is affected by atmospheric turbulence, dynamic misalignment and atmospheric path loss. Finally, the receiver is the responsible for collecting the transmitted optical beam and recovering the data electrical signal. A typical receiver consists of a focusing lens, a mechanical alignment stage to collect the optical signal and a PD that converts the optical power into an output current.

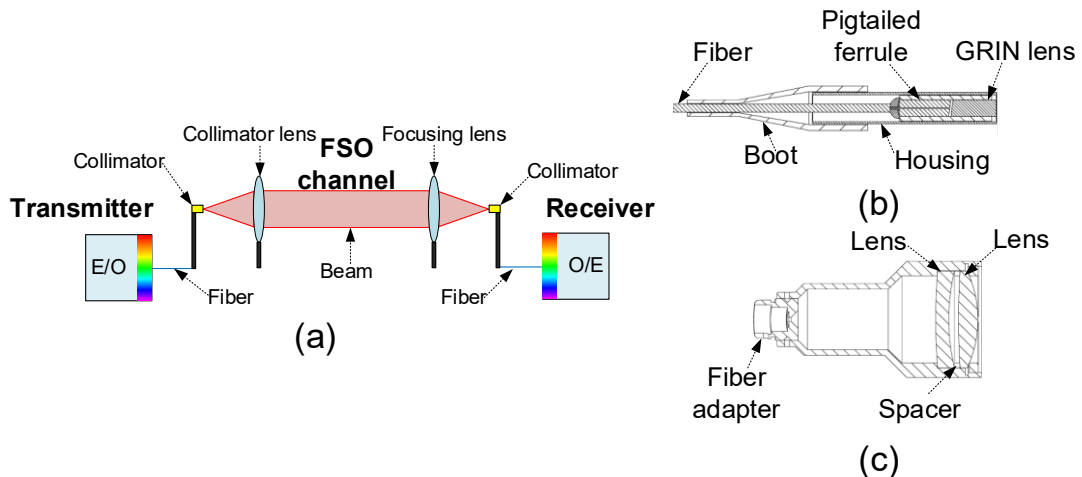


Figure 2.22. (a) FSO system layout, (b) Thorlabs 50-1550A-APC Single Mode Pigtailed GRIN Fiber Collimator and (c) Thorlabs F810APC-1550 Air-Spaced Doublet Collimator.

Figure 2.22(b) shows a commercial pigtailed fiber collimator (Thorlabs 50-1550A-APC). It uses gradient-index (GRIN) lenses which are coupled to standard single mode fiber. It is designed to be used in pairs, with a free-space beam between the lenses, and may also need collimator/focusing lenses. Figure 2.22(c) displays an air-spaced doublet collimator (Thorlabs F810APC-1550), which leads to be pre-aligned to collimate a laser beam. It does not have any movable parts; they are compact and not susceptible to misalignment. Both collimators are employed in this Thesis.

2.4.2. FSO limitations

FSO presents some limitations because of the transmission medium and physical characteristics of its installation location. The main impairments which affect to the performances are line-of-sight (LOS) obstructions, atmospheric attenuation, solar interference, misalignments, beam divergence and atmospheric turbulence (AT) [11, 91, 92, 93].

2.4.2.1. FSO signal attenuation

Optical signal through the FSO channel undergoes atmospheric attenuation due to absorption and scattering process [94]. Total atmospheric attenuation is given by atmospheric attenuation coefficient, α_{atm} , which is expressed as combination of absorption and scattering of light.

The atmospheric absorption strongly depends on the wavelength, as shown in Figure 2.23(a) [11]. The absorption occurs principally in response to water particles (i.e. moisture), carbon-dioxide and ozone. However, there are some transmission windows with very low attenuation, for instance 780–850 and 1520–1600 nm. The attenuation of near-IR wavelengths is < 0.2 dB/km under clear atmosphere. Furthermore, the majority of available optical components are designed at 1550 nm.

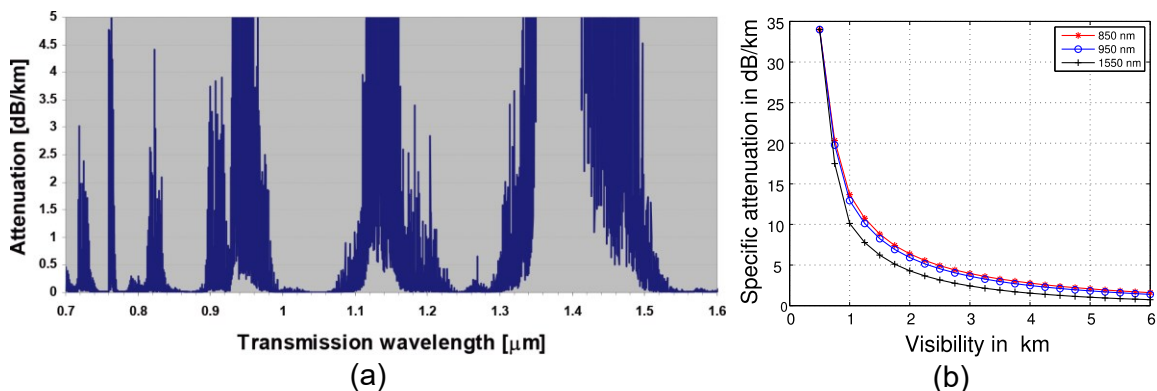


Figure 2.23. (a) Wavelength attenuation under clear weather conditions due to absorption [11], (b) attenuation vs visibility during heavy fog [94].

Weather conditions such as clouds, fog, rain or snow, also play a key role due to scattering of optical signals, strongly dependent on the wavelength. If the size of the atmospheric particles is comparable with the optical wavelength, Mie scattering is produced [94], which is the dominant near IR wavelength range. For example, Figure 2.23(b) displays the specific attenuation versus visibility range during heavy fog, showing that the attenuation coefficient is higher than 30 dB/km with a visibility range < 1 km.

2.4.2.2. Beam divergence

Geometric losses caused by beam divergence between transmitter and receiver have to be considered, mainly for long-range outdoor FSO links [95, 96]. Figure 2.24(a) illustrates the transmitter and receiver subsystems, and the free space channel. The transmitted beam is spread out over the channel due to diffraction. When the receiver aperture is not able to collect the whole transmitted beam, it results into power losses.

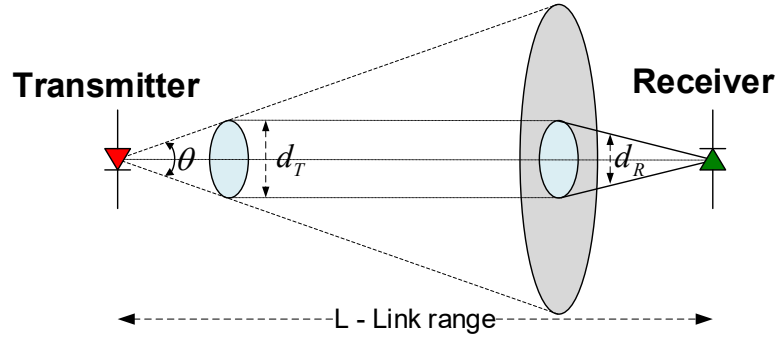


Figure 2.24. General schematic of a FSO link.

The attenuation due to FSO beam divergence losses, α_{FSO} , can be determined according to [11, 97, 98].

$$\alpha_{FSO} = \frac{P_{Rx}}{P_{Tx}} = \frac{d_R^2}{(d_T + \theta L)^2} 10^{-\alpha_{atm} \frac{L}{10}}, \quad (2.13)$$

where d_R (m) and d_T (m) are diameters of the receiver and transmitter aperture, θ (mrad) is the beam divergence, L (km) is the FSO range and α_{atm} (dB/km) is the atmospheric attenuation, as mentioned above.

2.4.2.3. Atmospheric turbulence

Furthermore, FSO is affected by AT created by thermal distributions, as shown in Figure 2.25, along the FSO link where multiple thermal sources, such as air-conditioned systems, rivers, factories, etc. can be involved. In this case, scintillation is produced almost entirely by small temperature variations, resulting in index-of-refraction fluctuations which contribute to the signal degradation. It can be described by many statistical models, e.g. lognormal model, exponential model, and recently Gamma-Gamma model, which is suitable for both weak and strong turbulence [99].

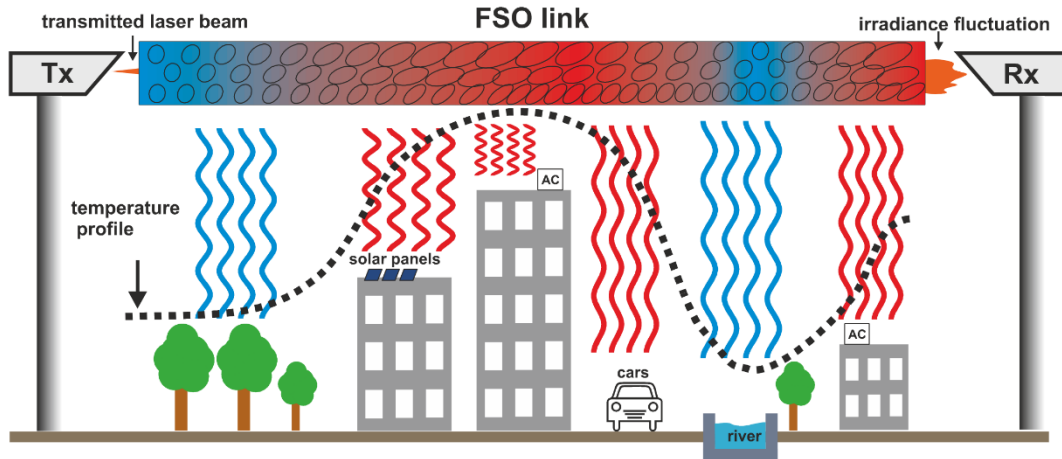


Figure 2.25. Example of thermal turbulences in a typical scenario [100].

The scintillation is characterized following the Gamma-Gamma atmospheric turbulence model [99] by log-amplitude variance, named as Rytov variance σ_R^2 . It can be calculated for a uniform refractive index structure parameter (C_n^2) as:

$$\sigma_R^2 = 1.23k^{7/6} C_n^2 L^{11/6}, \quad (2.14)$$

where k is the wave number and L is the horizontal distance travelled by the optical field/radiation. The C_n^2 parameter, which determines the strength of the turbulence, is specified by:

$$C_n^2 = \left(79 \cdot 10^{-6} \cdot \frac{P_a}{T^2}\right)^2 C_T^2, \quad (2.15)$$

where P_a is the atmospheric pressure in millibars, T is the absolute temperature in Kelvin and C_T^2 is the temperature structure parameter, which is defined as:

$$C_T^2 = \frac{(T_1 - T_2)^2}{L_p^{2/3}}, \quad (2.16)$$

where T_1 and T_2 are the temperatures at two separated points by a distance L_p .

Hence, the probability of a given optical power after transmission over a FSO link, $\text{Prob}(P_{FSO})$, is given by the following distribution:

$$\text{Prob}(P_{FSO}) = \frac{2(\alpha\beta)^{(\alpha+\beta)/2-1}}{\Gamma(\alpha)\Gamma(\beta)} K_{\alpha-\beta}(2\sqrt{\alpha\beta}P_{FSO}), \quad (2.17)$$

where $\Gamma(\cdot)$ is the Gamma function, $K_{\alpha-\beta}(\cdot)$ is the second kind modified Bessel function and $1/\alpha$ and $1/\beta$ are the variances of small- and large-scale eddies, which are calculated from the Rytov variance as follows:

$$\alpha = \exp\left[\frac{0.49\sigma_R^2}{\left(1 + 1.11\sigma_R^{12/5}\right)^{5/6}}\right] - 1$$

$$\beta = \exp\left[\frac{0.51\sigma_R^2}{\left(1 + 0.69\sigma_R^{12/5}\right)^{5/6}}\right] - 1. \quad (2.18)$$

Finally, the intensity fluctuations are characterized by the probability distribution, which is classified as weak turbulence ($\sigma_R^2 < 1$), moderate turbulence ($\sigma_R^2 \approx 1$) or strong turbulence ($\sigma_R^2 > 1$).

2.4.3. FSO applications

FSO advantages allow a high number of FSO uses, such as mentioned below [101, 102, 103]. FSO can be used up to 1 km for connecting users such as outdoor wireless access, last-mile, enterprise connectivity and point-to-point links. It is also an excellent solution where optical fiber cannot deploy or is very costly, for example for railway, highway or river crossings. It is an excellent supplement to traditional radio and fiber link due to high-speed link which can carry high data rates. FSO can be used as fronthaul and backhaul links (shown in Figure 2.3).

FSO can be deployed in areas with a rapid data traffic growth due to a temporary massive end user, for example near a football match or a concert. It also can be employed as rapid replacement of broken cable-links.

The main advantages of FSO links compared to microwave links are frequency independence of FSO losses, high data rates at low signal power or non-interference EMI with RF signals. This makes possible applications for satellite and deep space links, links between satellite and ground stations, and links between aircraft and high-altitude platforms, amongst others.

2.5. Conclusions

This Chapter presents a review of the enabling architectures and technologies for 5G networks, specially focusing in those which have been employed along the Thesis. The purpose of the Chapter is to provide a general overview of C-RAN, mmW signals, MWP approaches for signal generation and RoF techniques, and FSO, as driving technologies for future networks deployment.

The evolution of the traditional RAN architectures and the concepts of C-RAN have been revised. C-RAN has the potential to reduce the network deployment and operation cost as well as improve system, mobility and coverage performances for 5G networks. However, since the amount of data exchange between RRHs and COs is significantly increased, the implementation of fronthaul link is one of the main challenges for C-RAN deployments.

Since new standard requires high data rates and spectral efficiency, mmW signals are proposed as a key enabling technology for 5G NR, which can meet the drastic increase of wireless traffic capacity. Although mmW signal exhibits several benefits, its propagation characteristics and high frequency signals generation set out several challenges which MWP can address.

MWP enables photonic signal generation and transport approaches which can satisfy the 5G requirements. Photonically mmW signal generation techniques allow to reduce the bandwidth constraint of electrical devices. Among all the techniques which have been reviewed in the Chapter, intensity modulation based on MZM is particularly very attractive in terms of complexity, performance and cost, and therefore, has been chosen for the experimental work developed in this Thesis. Furthermore, RoF enables the transparent mmW signal transmission over fiber when the mmW signal is photonically generated. Therefore, its main benefits such as large bandwidth, low losses, immunity to RF interference and low power consumption, can be fully exploited.

Finally, special attention has been paid in the literature during the recent years to FSO as part of fronthaul link. It is presented as an alternative technology of optical fiber deployment since it exhibits similar benefits showing complementary features, i.e. high bandwidth and bit rate, unlicensed THz bands, lower losses than electrical wireless transmission and extending range where optical fiber cannot be deployed. However, optical signals experience attenuation due to absorption and scattering process, and misalignment. Furthermore, FSO channel can be affected by atmospheric turbulences, as has been described above, due to multiple thermal sources along the channel. Huge number of applications, such as temporary installation, inaccessible location deploy or fast communication recover of broken cables, can be deployed using FSO technology.

Chapter 3. Photonic mmW signal generation based on carrier-suppressed external modulation

We live in a society exquisitely dependent on science and technology, in which hardly anyone knows anything about science and technology.

– Carl Sagan

In this Chapter, photonic mmW signal generation based on carrier-suppressed external modulation is described as the main approach employed in the Thesis. CS-DSB modulation is employed to generate high frequency signals and full optical and electrical signal characterization is provided. Based on the same scheme, the Chapter also presents multiple signal generation for 5G deployment networks which is further exploited to provide reconfigurable mmW signal generation. Moreover, non-linear FWM in a SOA has been employed to assist photonically mmW signal generation in order to further reduce the component bandwidth requirements. Finally, the effect of induced thermal turbulence on mmW signals is experimentally and analytically evaluated along FSO links which are deployed as part of the fronthaul link in C-RAN, as explained in Chapter 2.

3.1. Analytical formulation

Schemes for mmW signal generation based on MZM linear bias point lead to spectra with all optical sidebands including the optical carrier (see Figure 2.19) and a filter is required to select bands with proper spacing. In our approach, the MZM is biased at non-linear region, more specifically CS-DSB is employed as an excellent solution for the mmW signal generation at double the RF frequency, i.e. $f_{mmW} = 2f_{RF}$. In this case, only ± 1 -order sidebands are the desired optical signals.

Assume that an incoming CW lightwave in the modulator can be formulated as:

$$E_{in}(t) = E_0 e^{j[w_o t + \phi_o(t)]}, \quad (3.1)$$

where E_0 is the constant amplitude, w_o is the angular frequency and $\phi_o(t)$ is phase of the optical signal. The MZM, shown in Figure 2.16(b) is driven by a $v(t)$ signal consisting of an electrical sinusoidal signal given as:

$$v(t) = V_{bias} + V_{RF} \cos(w_{RF} t + \phi_{RF}(t)), \quad (3.2)$$

where V_{bias} is the DC bias voltage, V_{RF} , w_{RF} and $\phi_{RF}(t)$ are the amplitude, angular frequency and phase of the RF driving signal, respectively.

Therefore, combining equations (2.7) and (3.2), the output electrical field after modulation can be expressed as [104]:

$$E_{out}(t) = E_{in}(t) \left\{ \cos(b) \cos(m \cos(w_{RF}t + \phi_{RF}(t))) - \sin(b) \sin(m \cos(w_{RF}t + \phi_{RF}(t))) \right\}, \quad (3.3)$$

where $b = \frac{V_{bias}}{2V_{\pi}}\pi$ is the constant phase shift induced by the DC bias voltage and $m = \frac{V_{RF}}{2V_{\pi}}\pi$ is the phase modulation index.

Combining equations (3.1) and, (3.3) with Jacobi-Anger expansion and Bessel functions, the output of the MZM is given by:

$$\begin{aligned} E_{out}(t) = & E_o \cos(b) J_0(m) \cos(w_o t + \phi_o(t)) \\ & + E_o \sum_{n=1}^{\infty} [(-1)^n \cos(b) J_{2n}(m) \{ \cos([w_o + 2nw_{RF}]t + 2n\phi_{RF}(t) \\ & + \phi_o(t) - n\pi) + \cos([w_o - 2nw_{RF}]t - 2n\phi_{RF}(t) + \phi_o(t) + n\pi) \}] \\ & + E_o \sum_{n=1}^{\infty} [(-1)^n \sin(b) J_{2n-1}(m) \{ \cos([w_o + (2n-1)w_{RF}]t \\ & + [2n-1]\phi_{RF}(t) + \phi_o(t) - n\pi) \\ & + \cos([w_o - (2n-1)w_{RF}]t - [2n-1]\phi_{RF}(t) + \phi_o(t) + n\pi) \}], \end{aligned} \quad (3.4)$$

where $J_n(\cdot)$ is the Bessel function of the first kind of order n^{th} . Table 3.1 shows the corresponding optical sideband and the associated term from equation (3.4) controlled by b parameter.

Table 3.1. Analytical terms of optical field at the MZM output (normalized to E_o).

Sidebands	$E_{out}(t)$ term
Carrier (cos(b))	$J_0(m) \cos(w_o t + \phi_o(t))$
Even (cos(b))	$(-1)^n \cdot J_{2n}(m) \cos([w_o + 2nw_{RF}]t + 2n\phi_{RF}(t) + \phi_o(t) - n\pi)$ $(-1)^n \cdot J_{2n}(m) \cos([w_o - 2nw_{RF}]t - 2n\phi_{RF}(t) + \phi_o(t) + n\pi)$
Odd (sin(b))	$(-1)^n \cdot J_{2n-1}(m) \cos([w_o + (2n-1)w_{RF}]t + [2n-1]\phi_{RF}(t) + \phi_o(t) - n\pi)$ $(-1)^n \cdot J_{2n-1}(m) \cos([w_o - (2n-1)w_{RF}]t - [2n-1]\phi_{RF}(t) + \phi_o(t) + n\pi)$

Figure 3.1(a) illustrates typical optical sidebands of a MZM. As it can be seen, the amplitude of the optical sidebands corresponds to associated Bessel functions. Note that the $\pm 1^{\text{st}}$ and $\pm 2^{\text{nd}}$ optical sidebands exhibit 180° phase shift respect to the carrier, according to equation (3.4) (see Table 3.1).

Figure 3.1(b) shows the optical power ($P_{opt} = |E|^2$) and optical field curves vs bias voltage. The operating point of MZM is controlled by changing the applied voltage on the electrodes. There are four regions of operation depending on the bias point (V_{bias}). Positive and negative quadrature (Quad+ and Quad-, respectively), held when $V_{bias} = \pm V_{\pi}/2$, correspond to linear regions usually employed for electro-optic modulation while peak and null are non-linear regions that can be used for pulse generation.

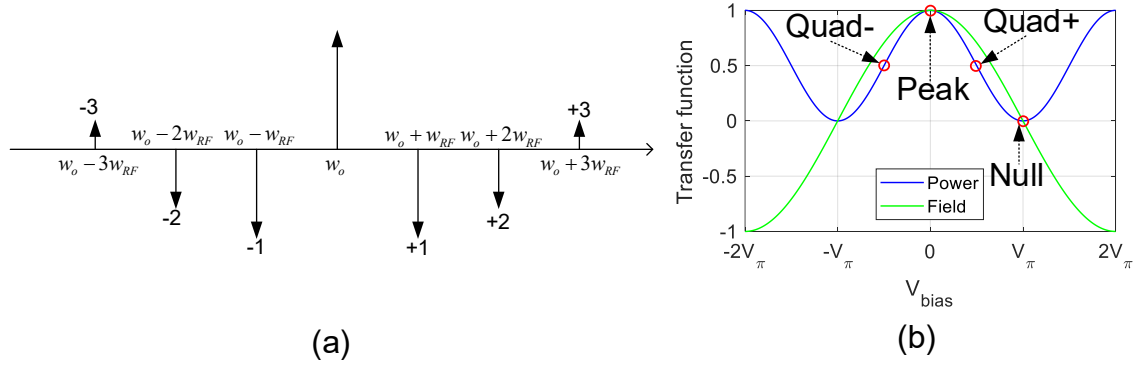


Figure 3.1. (a) Diagram of typical optical sidebands generated by a MZM and (b) normalized power and field curves vs bias voltage of MZM.

Assuming driving and optical signal with null phase, $\phi_{RF}(t) = 0$ and $\phi_o(t) = 0$, CS-DSB modulation can be set at $V_{bias} = V_{\pi}$, i.e. $\cos(b) = 0$ and $\sin(b) = 1$, and leads to the following expression for the output optical field (odd sidebands):

$$E_{out}(t) = E_o \sum_{n=1}^{\infty} \{(-1)^n J_{2n-1}(m) [\cos([w_o + (2n-1)w_{RF}]t - n\pi) + \cos([w_o - (2n-1)w_{RF}]t + n\pi)]\}. \quad (3.5)$$

The amplitudes of the generated sidebands are proportional to the corresponding associated odd Bessel functions, $J_{2n-1}(m)$, with the phase modulation index m . When phase modulation index is high enough, high optical sidebands orders can be ignored. If $V_{RF} = V_{\pi}$, the maximum phase modulation index is $\frac{\pi}{2}$, and the argument of Bessel functions is $0 < m < \frac{\pi}{2}$. As it is shown in Table 3.2, higher order bands can be ignored according to Bessel functions, and the output of the MZM can be simplified as [79]:

$$E_{out}(t) = -J_1(m)E_o [\cos([w_o + w_{RF}]t) + \cos([w_o - w_{RF}]t)]. \quad (3.6)$$

Table 3.2. Analytical optical sidebands and Bessel functions from 1 to 3 order of optical field at the MZM output (E_o normalized) when $V_{bias} = V_{\pi}$ (null bias point).

n	$J_{2n-1}(m)$	Sidebands
1	0.5668	$-J_1(m) [\cos([w_o + w_{RF}]t) + \cos([w_o - w_{RF}]t)]$
2	0.0690	$J_3(m) [\cos([w_o + 3w_{RF}]t) + \cos([w_o - 3w_{RF}]t)]$
3	0.022	$-J_5(m) [\cos([w_o + 5w_{RF}]t) + \cos([w_o - 5w_{RF}]t)]$

This approach shows the advantage of robustness of the system to fiber dispersion-induced RF power penalties [105] as well as the reduced electronic bandwidth requirements at the transmitter. However, due to non-linear bias point, high RF driving power is required to obtain a desirable modulation depth [106]. Throughout this Thesis, external CS-DSB modulation is employed for mmW signal generation in different scenarios and applications, as explained below.

3.2. Experimental setup and characterization

In this Section, mmW signal generation and distribution over hybrid fiber/FSO network system is demonstrated and experimentally characterized [107]. As depicted in Figure 3.2, an optical wavelength is modulated by a RF signal, f_{RF} , by using a MZM biased at zero transmission point ($V_{bias} = V_{\pi}$). The optical signal is amplified by an EDFA and then transported through

SSMF and FSO links. Finally, opto-electrical conversion is held at the PD, where the first sidebands are beaten and a mmW signal is generated at double frequency, $f_{mmW} = 2f_{RF}$, to be radiated by an antenna at a given BS. Therefore, the electric bandwidth of the RF source is reduced by half and, since the carrier is suppressed at the modulation itself, an optical filter is not required.

In the experimental setup shown Figure 3.2, a CW optical signal is emitted at a wavelength of 1550.12 nm by a distributed feedback (DFB) laser (EXFO IQS) with 10 dBm output power. The signal state of polarization is adjusted by a polarization controller (PC) and launched into the dual-drive MZM (Sumitomo Osaka Cement T.DEH1.5-40X-ADC-Y-Z) with 30 GHz bandwidth and null bias point at 6.5 V. The electrical driving signal is generated by a signal generator (SG) (Agilent PNA-X N4373C) with 18 dBm output power in the frequency range 20 - 45 GHz. The carrier suppressed modulated optical signal is amplified by an EDFA (Amonics EDFA-23-B-FA) with 13 dBm output power to be transmitted over 10 km SSMF link and launched into the 70 cm FSO system by using GRIN lenses (Thorlabs 50-1550A-APC) with an aperture of 1.8 mm and plano-convex lenses with a diameter of 25.4 mm. Note that optical losses at the FSO link are measured as 4.6 dB. Finally, the signal is monitored using after 90/10 optical coupler (OC) by optical spectrum analyzer (OSA) (Yokogawa AQ6370C), whereas the mmW signal is generated after beating the modulated sidebands at the 50 GHz PD (Finisar XPDV2320R) and is monitored by the RF spectrum analyzer (RFSA) (Anritsu MS2760A).

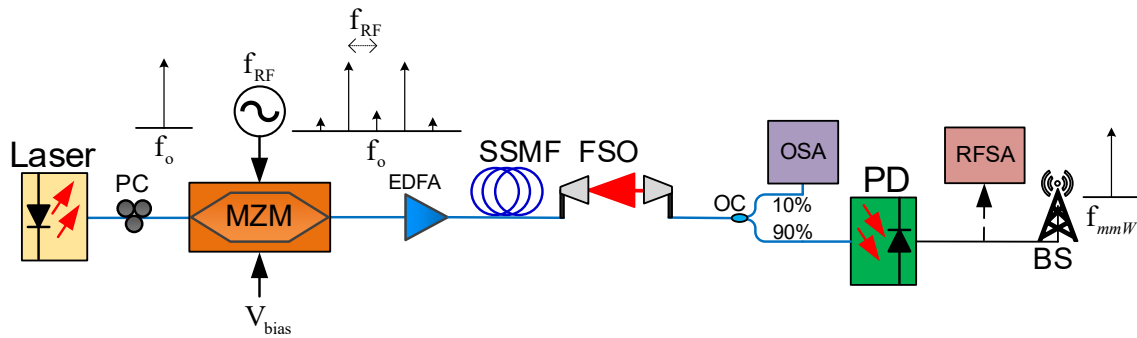


Figure 3.2. Experimental setup of 40 - 90 GHz mmW signal generation [107].

The measured optical spectra at the PD input for optical back-to-back (OB2B) configuration is shown in Figure 3.3(a). The side-mode suppression ratio¹ (SMSR) is larger than 30 dB for frequencies below 60 GHz and is reduced up to 19.1 dB at 90 GHz, due to the MZM bandwidth limitation. Higher order sidebands are measured to be below 40 dB (40 GHz) and 27 dB (90 GHz) respect to the main sidelobes. Optical spectra after fiber (red trace) and hybrid (green trace) transmission show similar behaviour than OB2B. As expected, optical signals after hybrid link shows higher attenuation than fiber and OB2B transmission.

After photodetection, a mmW signal is generated at different frequencies. The RF spectrum at optical OB2B configuration is depicted in Figure 3.3(b) where similar RF power values are obtained for all frequencies. The maximum RF power for OB2B system is -34 dBm at 40 GHz measured by an RFSA with a resolution bandwidth (RBW) of 3 kHz.

¹ The side-mode suppression ratio (SMSR) is defined as suppression level between optical carrier and sidebands.

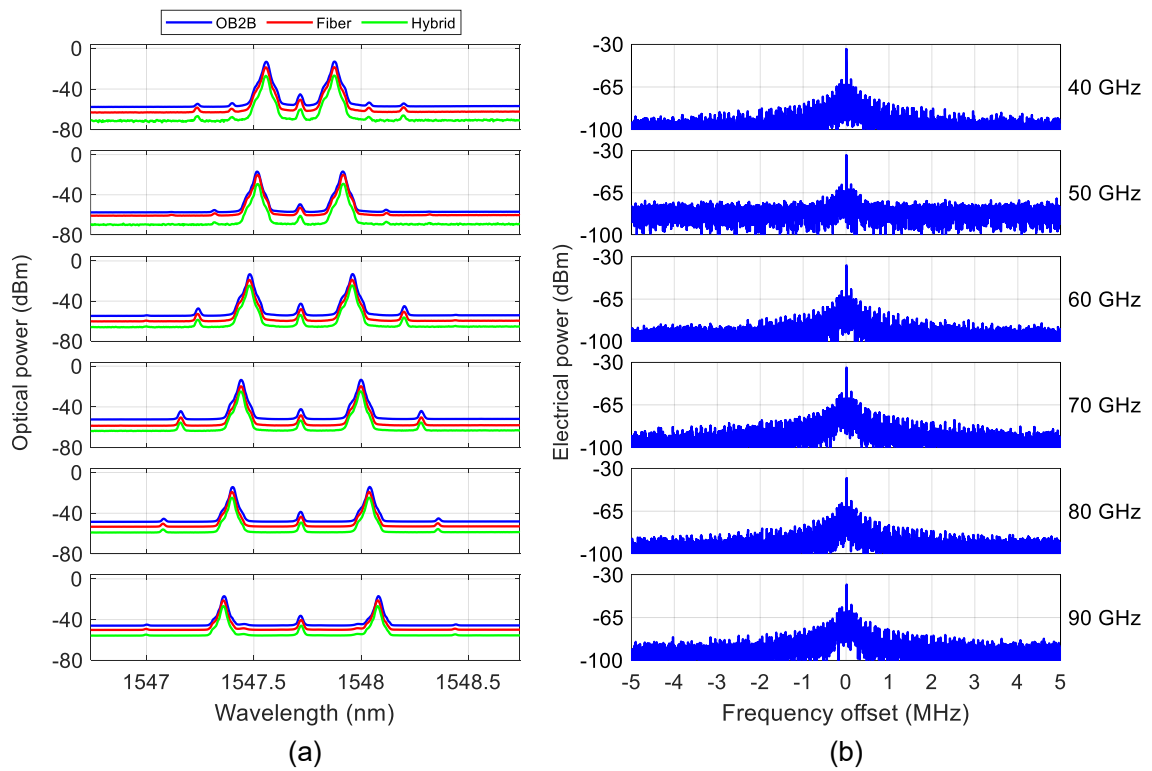


Figure 3.3. (a) Measured optical spectra at the PD input for OB2B, 10 km SSMF link, and 10 km SSMF and 70 cm FSO link; and (b) RF power spectrum for OB2B.

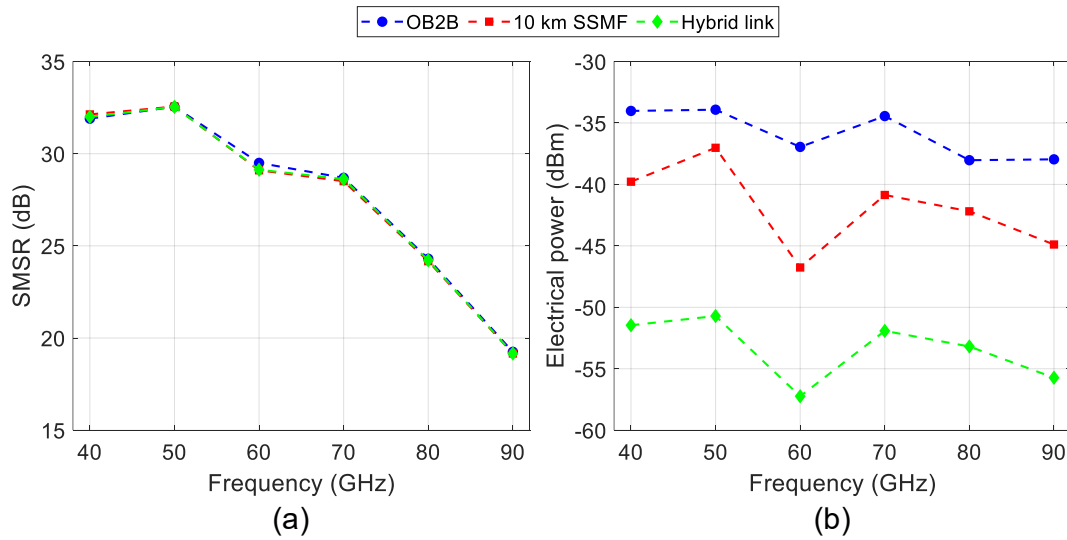


Figure 3.4. (a) Side-mode suppression ratio (RBW = 0.02 nm) and (b) RF electrical power (RBW = 3 kHz) vs frequency signal.

Figure 3.4 displays the measured SMSR and RF power for a particular frequency in order to compare the performance of links with different frequencies. Figure 3.4 (a) exhibits similar values for OB2B, fiber and hybrid links. The measurements show less than 0.5 dB difference between links. The SMSR shows -3 dB at 60 GHz compared with lower frequencies. Then, the SMSR sharply drops down to 19.2 dB, which is due to the frequency response of the devices, as mentioned above.

Figure 3.4(b) shows the RF measured power for a particular generated frequency. As expected, the OB2B configuration shows the maximum RF power level, for example -34 dBm at 40 GHz. However, the RF power level decreases when the frequency increases due to the overall system frequency response.

3.3. Multiple signal generation

In this Section, we extend the schematic presented above to generate multiple signals with increased performance and flexibility. The scheme of the experimental setup for multiple mmW signal generation based on the CS-DSB external modulation is shown in Figure 3.5 [108]. In this experiment, each wavelength is modulated at CO by a RF signal (f_{RF}) using a MZM biased at V_{π} (null point), as described in previous Section. Therefore, the carrier is suppressed without the need of any optical filter, and two first order optical sidebands are generated. In the setup, multiple optical signals are multiplexed at the CO and distributed along the optical network which includes optical fiber and FSO links. At the remote node (RN), the optical signals are distributed by a demultiplexer, and each optical channel is routed towards the corresponding BS. After beating both optical sidebands at the PD in the BS, the generated mmW signal can be further amplified and radiated by an antenna.

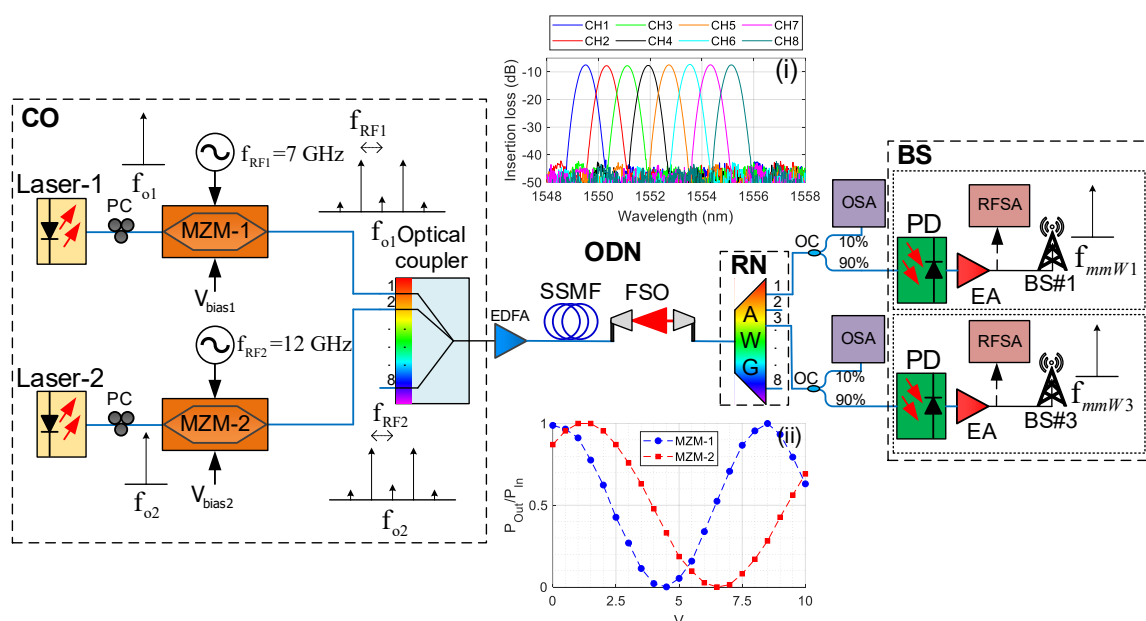


Figure 3.5. Schematic layout of multiple mmW signal generation and distribution system. Insets show: (i) output spectral response of 8 channel AWG with 100 GHz channel spacing and (ii) measured output/input power-voltage characteristic of MZM-1/2 as function of the bias voltage [108].

In the experimental setup, two lasers (EXFO IQS) (CW Laser-1 and Laser-2) emit optical carrier signals with 10 dBm output power at 1549.90 and 1551.52 nm wavelength, respectively. After optimizing the polarization state of the input signals by PCs, the optical signals are modulated by MZM-1 (Avanex PowerBit F-10) and MZM-2 (Sumitomo Osaka Cement T DEH1.5-40). Inset (ii) of Figure 3.5 displays the experimental optical power-voltage curve of both MZMs where CS-DSB bias point is 4.5 and 6.5 V for MZM-1 and MZM-2, respectively. MZM-1 and MZM-2 are driven by RF driving signals which are generated by SGs (Agilent PNA-X N4373C and PSG E8267C) at frequencies of 7 GHz and 12 GHz with 18 and 23 dBm output power, respectively. The optical modulated signals are multiplexed by an optical coupler and the losses are compensated by an EDFA (Amonics EDFA-23-B-FA) with 13 dBm output power.

The resulting optical signal is transmitted by the optical distribution network (ODN) composed of 10 km SSMF and 70 cm FSO system. The FSO link is identical as described in single frequency experiments in previous Section, i.e. 4.6 dB insertion losses.

At RN, the optical signal is launched into the 1x8 arrayed waveguide grating (AWG) (NEL AWG0808SPM) with a free spectrum range (FSR) of 100 GHz (0.8 nm), as it is shown in inset (i) of Figure 3.5 where optical channels come out from output ports #1 and #3, respectively. The AWG output ports are connected to 90/10 OC allowing the monitoring of optical signal by OSA (Yokogawa AQ6370C), whereas the mmW signal is generated at the PD (Finisar XPDV2320R) at BS#1 and BS#3, and monitored by the RFSA (Agilent MXA N9020A).

For the sake of providing optical and electrical signal characterization, five scenarios have been tested based on different fiber and FSO link lengths, as detailed in Table 3.3, and compared with OB2B link (scenario A). The scenarios B and C consist of fiber links, i.e. 10 and 25 km SSMF whereas the scenario D is purely FSO link. The hybrid link (scenario E) is formed by 10 km SSMF and 70 cm FSO, i.e. scenarios B and D, and, when a RF amplification is applied after photodetection, it is denominated scenario F.

Table 3.3. Definition of experimental scenarios.

Scenarios	Optical distribution network	Insertion loss (dB)
A	OB2B	0
B	10 km SSMF link	3.2
C	25 km SSMF link	5.6
D	70 cm FSO link	4.6
E	10 km SSMF + 70 cm FSO	7.8
F	10 km SSMF + 70 cm FSO (with post-detection RF amplification)	-

Figure 3.6(a) and (b) show the measured optical spectra at AWG output ports #1 and #3. The measured SMSR is 20 dB and larger than 30 dB at 7 GHz for port #1 and at 12 GHz for port #3, respectively. The high order optical sidebands show power levels below 35 dB with respect to the fundamental sidebands. Besides, the crosstalk between adjacent channel is -33 and -42 dB for port #1 and port #3, respectively. Note that the AWG nominal crosstalk is 30 dB.

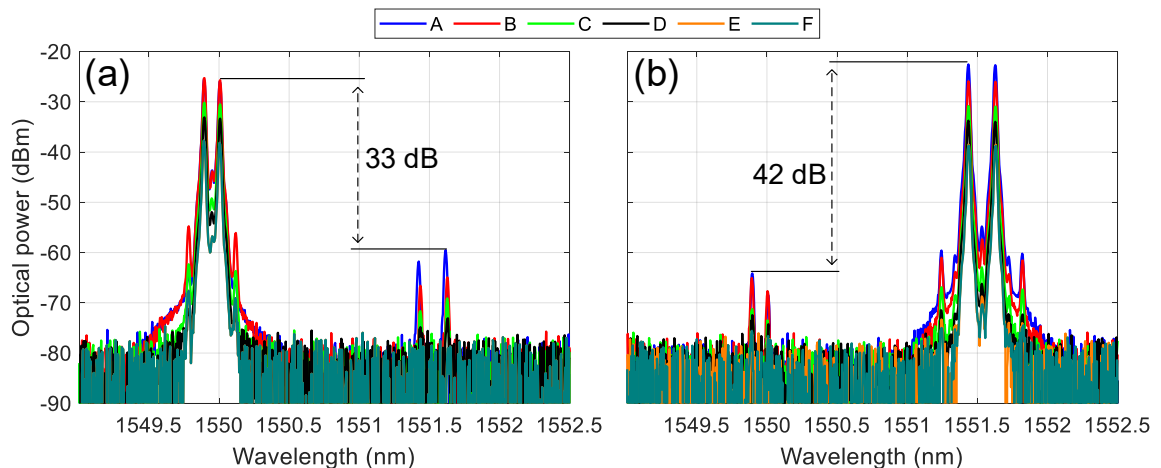


Figure 3.6. Measured optical spectra at PD input (RBW = 0.02 nm): (a) port #1: $\lambda_1 = 1549.90$ nm, $f_{RF1} = 7$ GHz and (b) port #3: $\lambda_2 = 1551.52$ nm, $f_{RF2} = 12$ GHz.

The 14 and 24 GHz mmW signal (port #1 and #3) are generated after direct photodetection at the receiver. The RF spectra of both frequencies are depicted in Figure 3.7(a) and (b). The measured linewidth is 60 kHz in all scenarios using a RBW of 51 kHz. Figure 3.7(c) shows the RF received power for a particular scenario A-D for both frequencies in order to compare the

performance for different radio frequencies. Similar received RF power values at 14 and 24 GHz are obtained for scenarios A-E. The measured electrical power is around -41 dBm for scenarios A and B, meanwhile it is reduced by 9.9, 16 and 25.2 dB for scenarios C-E, respectively, compared with OB2B for 14 and 24 GHz. A 6 dB difference between 14 and 24 GHz is observed in scenario F due to the frequency response of the amplifier (SHF Communication Technologies AG SHF 810) and adapters.

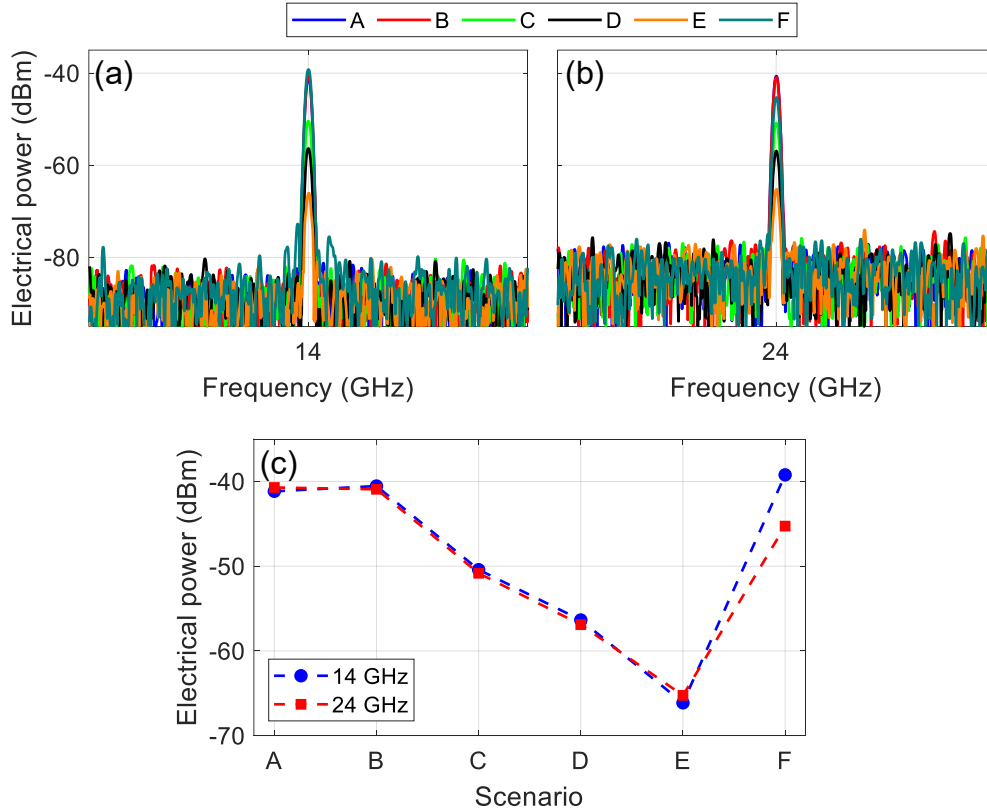


Figure 3.7. (a) Electrical spectrum at $f_{mmW1} = 14$ GHz (port #1, $\lambda_1 = 1549.90$ nm), (b) electrical spectrum $f_{mmW3} = 24$ GHz (port #3, $\lambda_2 = 1551.52$ nm) and (c) RF power level measured at different scenarios.

Phase noise is critical in communications systems since it characterizes the spectral purity of the signal, which is caused by time domain instabilities called as phase jitter. Figure 3.8 shows the phase noise level measurements at 14 and 24 GHz at different scenarios. The best phase noise at 100 kHz is -87.4 and -93.3 dBc/Hz for OB2B at 14 and 24 GHz, respectively. The phase noise of the generated mmW signal is affected by the electrical driving signal, the linewidth of the optical carrier and the chromatic-dispersion effect in the fiber [104]. In this system, the measured phase noise of scenarios A-D, i.e. under -75 dBc/Hz, is a reasonable level compared with, e.g. the nominal phase noise of signal generator Agilent PSG E8267C (-108 dBc/Hz from 10 GHz to 20 GHz at 20 kHz frequency offset). As expected, scenario E shows higher phase noise, i.e. -69 dBc/Hz at 24 GHz due to very low received RF power. It decreases down to -87 dBc/Hz at 100 kHz frequency offset when post-detection amplification is applied (scenario F) for both frequencies, as shown in the inset of Figure 3.8. Note that a 10 dB difference at 1 MHz offset is measured between 14 and 24 GHz signals due to the frequency response of the amplifier.

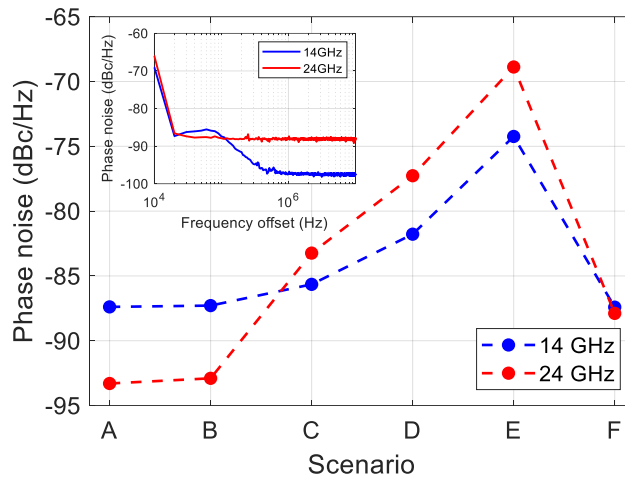


Figure 3.8. Phase noise level measured at different scenarios (RBW = 10 kHz). Inset show the phase noise measurement at scenario F for channel 1 (port #1, $f_{mmW1} = 14$ GHz, $\lambda_1 = 1549.90$ nm) and 3 (port #3, at $f_{mmW3} = 24$ GHz, $\lambda_2 = 1551.52$ nm).

3.4. Reconfigurable mmW signal generation

In this Section, multiple mmW signal generation is proposed for dynamic allocation of particular frequencies to different BSs is depicted in Figure 3.9 [108].

The scheme, based on Figure 3.5, employs an optical switch (OS) (Sercarlo SW8x3-9N-FC/PC) in the remote node for dynamic allocation of optical channels, and a cyclic 18x18 ports AWG (NEL A0818GPMFS-B203A) is employed for demultiplexing optical channels. In this case, five optical channels are used to generate and deliver signals at different frequencies in mmW bands. Optical waves emitting by DFBs at $\lambda_1 - \lambda_5$ are modulated by five MZMs similar to those employed in Figure 3.5 at 7.5 - 20 GHz frequency range in order to generate mmW signals at 15 - 40 GHz, respectively. Table 3.4 shows the detailed proposed wavelength and frequencies. Inset of Figure 3.9 illustrates the measured optical spectrum of the multiplexed optical signal when channels CH#1 and #2 (1547.47 and 1548.25 nm) are modulated by the corresponding RF signals.

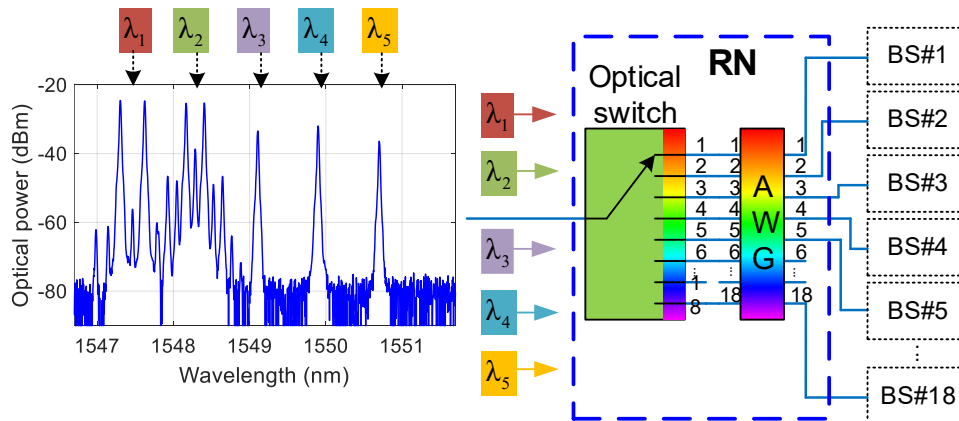


Figure 3.9. Experimental setup of photonic multiple mmW signal generation and dynamically reconfigurable signal distribution. Inset shows the optical spectrum of five multiplexed optical channels when CH#1 and #2 are modulated by 20 and 15 GHz, respectively.

Table 3.4. Definition of optical channels.

Channel	Wavelength (nm)	RF (GHz)	mmW (GHz)
CH#1	1547.47	20	40
CH#2	1548.25	15	30
CH#3	1549.10	12.5	25
CH#4	1549.85	10	20
CH#5	1550.70	7.5	15

Figure 3.10 shows the optical and electrical measurements when the optical signal is launched through port #2 in the AWG after 10 km SSMF and 70 cm FSO. Figure 3.10(a) shows the carrier suppressed and modulated sidebands at different channels after AWG signal routing. The crosstalk level between channels is better than -28 dB meanwhile a minimum SMSR of 17.8 dB is observed due to the differences in their frequency response and polarization sensitivity. The electrical spectra shown in Figure 3.10(b) is measured by the RFSA and minimal electrical power of -40 dBm is measured and, phase noise levels below 85 dBc/Hz and linewidths under 60 kHz are obtained at all BS#s.

Figure 3.11(a) shows every wavelength carrying the particular mmW signal and its corresponding BS# for different AWG input ports, for example the dashed box in Figure 3.11(a) correspond to the ones depicted in Figure 3.11(b). The electrical spectra displayed in Figure 3.11(b) correspond to different BSs when the OS is configured to launch the optical signal into a given input. For instance, the 40 GHz mmW signal, carried by optical channel CH#1 (1547.47 nm) is distributed to BS#17 or BS#16 when the signal is launched into AWG port #4 or #5, respectively. Similarly, optical signals can be switched to different AWG input port and, after direct detection, routed to a particular BS. The utilization of remote software assisted control of OS may provide future dynamic mobile fronthaul mobile networks with the highest performance, expandability and reachability.

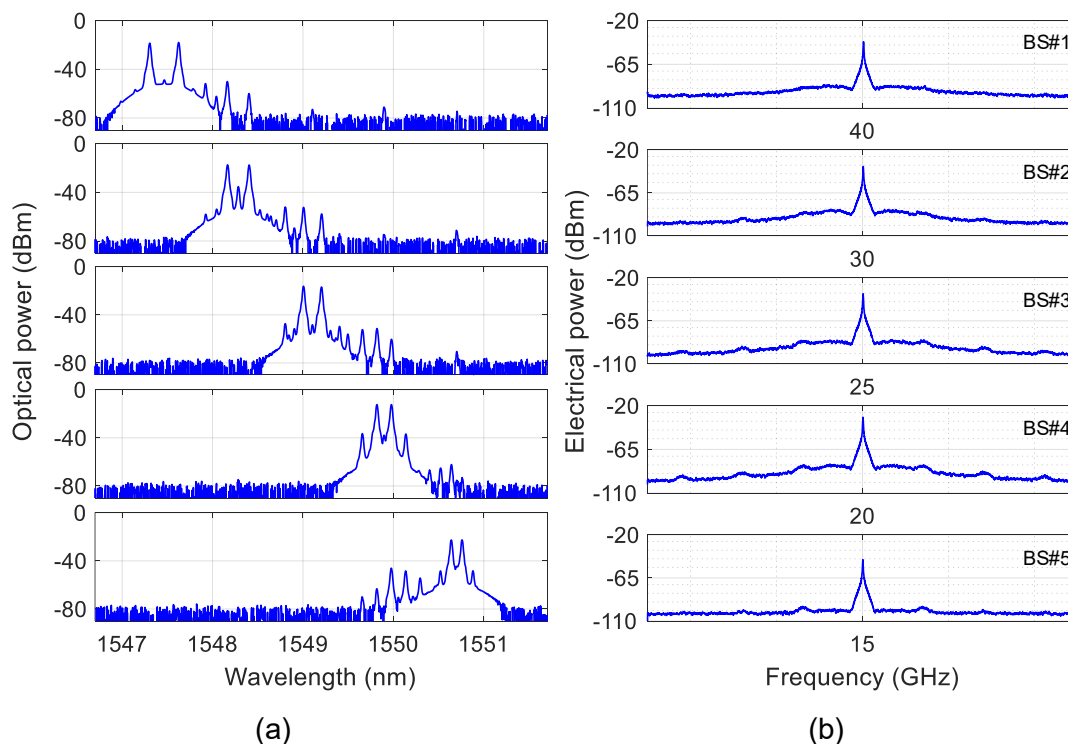


Figure 3.10. Measurements at different BSs after hybrid SSMF/FSO transmission when optical signal is launched into AWG port #2: (a) optical and (b) electrical spectra.

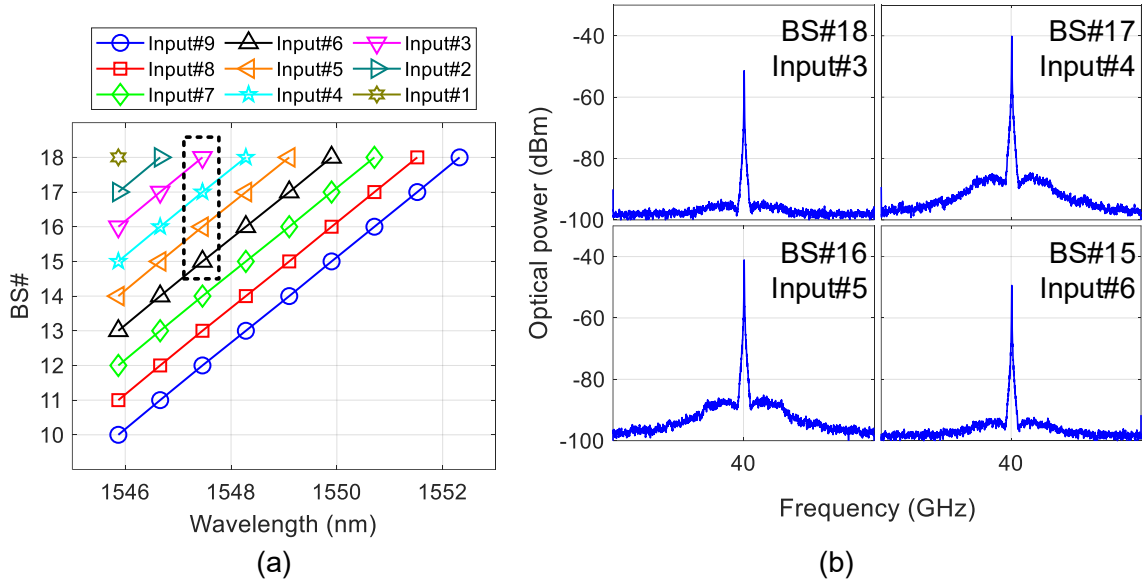


Figure 3.11. (a) AWG algorithm routing: BS# where the signal is radiated versus optical carrier wavelength when is launched into different AWG inputs and (b) RF spectrum at 40 GHz (carried by 1547.47 nm) generated at different BS according to the AWG input port (span = 1 MHz).

3.5. Four-wave mixing aided signal generation

This Section proposes to complement the mmW signal generation system based on CS-DSB to generate two phase-correlated wavelengths in order to extend the achievable mmW frequency. These wavelengths are employed as pump signals to produce two idlers by nonlinear FWM mechanism which is held in an SOA [109] (see Chapter 2). The SOA-based FWM shows advantages such as simple configuration, small package and easy to integrate.

The experimental setup of the FWM aided mmW signal generation is shown in Figure 3.12. An optical carrier emitted by the laser is launched into a MZM biased at null transmission point. The optical signal is modulated by an electrical signal clock from a signal generator. Then, optical carrier and even-order sidebands are suppressed, and higher odd-order sidebands can be ignored. The two wavelengths are then launched into the SOA as two pumps. Then, two idlers are generated due to FWM. According to the FWM, the spacing of two idler wavelengths satisfies equation (2.11), $(\omega_c - 3\omega_{RF})$ and $(\omega_c + 3\omega_{RF})$. Finally, after the PD, a mmW signal which frequency is six times the RF frequency of the driving signal is generated ($\omega_{mmW} = 6\omega_{RF}$). Moreover, the generated mmW signal exhibits very narrow linewidth.

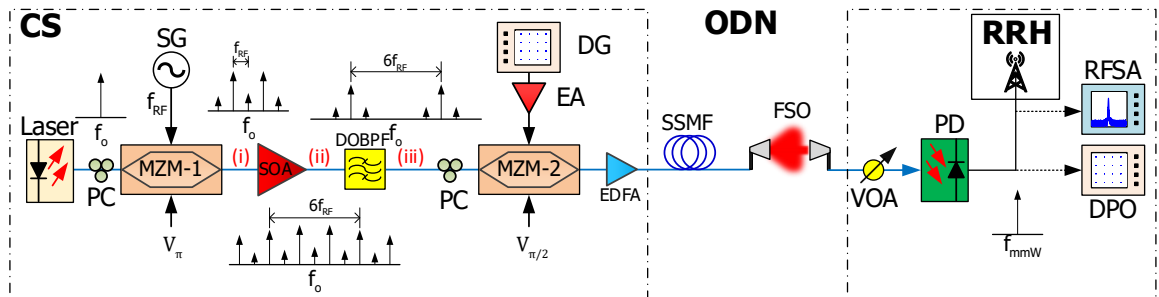


Figure 3.12. Experimental setup of SOA-aided photonic signal generation [109].

In the experiments, a 42 - 90 GHz mmW is generated using a RF frequency of 7 - 15 GHz. At CO, a laser (EXFO IQS-2403BLD) emits an optical carrier at 1550.12 and 10 dBm output power. The MZM-1 (Sumitomo T DEH1.5-40X-ADC-Y-Z) is driven by a SG (Agilent E8267C) with RF frequency of 7-15 GHz and 20 dBm output power. The MZM-1 output optical signal, which mainly contains the first order sidebands, $\pm f_{RF}$, is launched into SOA (Optospeed COST

267 Bulk), where FWM produces new bands, as explained above. As will be described in Chapter 5, when data transmission is required, the optical signal is launched into a second MZM (MZM-2) (Avanex PowerBit F10), which is biased at linear point. A dual optical bandpass filter (DOBPF) (Finisar Waveshaper 4000s) filters out both bands separated by $6f_{RF}$, where the electronic bandwidth is reduced by six times in the CS. Before signal transmission over the ODN, the signal is amplified by an EDFA (Accelink EDFA-MW-BA-40). As in previous Sections, the ODN is composed of 10 km SSMF and 70 cm FSO. Finally, the opto-electronic conversion is held in a PD with 50 GHz bandwidth (u2t Photonics, BPDV2020R) for mmW generation and data recovery in the corresponding RRHs. The RF spectrum is measured by the RFSA Anritsu MS2760A (9 kHz - 110 GHz).

Figure 3.13 depicts the measured optical spectra of the modulated signal when 11 GHz frequency is employed. Two optical sidebands with 11 GHz spacing and 19 dB carrier suppressed ratio are observed in Figure 3.13(a), whereas Figure 3.13(b) shows the sidebands generated by FWM and the DOBPF spectral response configured for proper filtering. Figure 3.13(c) shows the resulting spectrum after filtering out in the DOBPF, where the spacing is six times the RF signal frequency, i.e. 66 GHz.

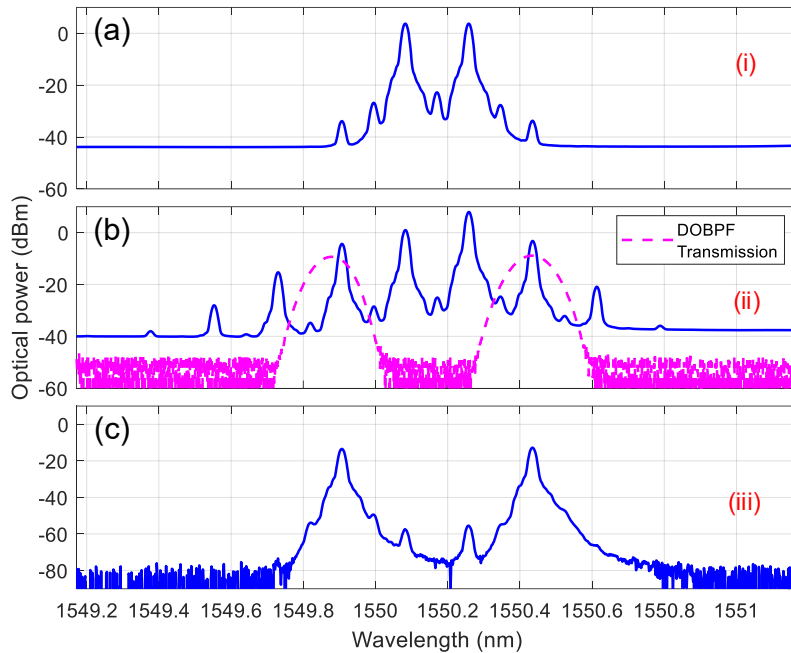


Figure 3.13. Optical spectra of 11 GHz modulated signal (RBW = 0.02 nm): (a) after MZM-1, (b) after SOA (dashed line show the filter transmission) and (c) after DOBPF.

Figure 3.14 shows the electrical spectra of generated mmW signals at 42, 66 and 90 GHz after OB2B (Figure 14(a)-(c)) and hybrid link (Figure 14(d)-(f)) signal propagation. The signals show -14 , -19 and -24 dBm peak electrical power for generated frequencies of 42, 66 and 90 GHz, respectively. The measured linewidth is below 100 Hz (RBW = 1 kHz) and phase noise level at 100 kHz has been experimentally measured as -80 dBc/Hz. After transmission through ODN, the electrical spectra are shown in Figure 14(d)-(f), where generated mmW signal suffers power reduction, e.g. -18 dB at 42 GHz, due to the ODN losses.

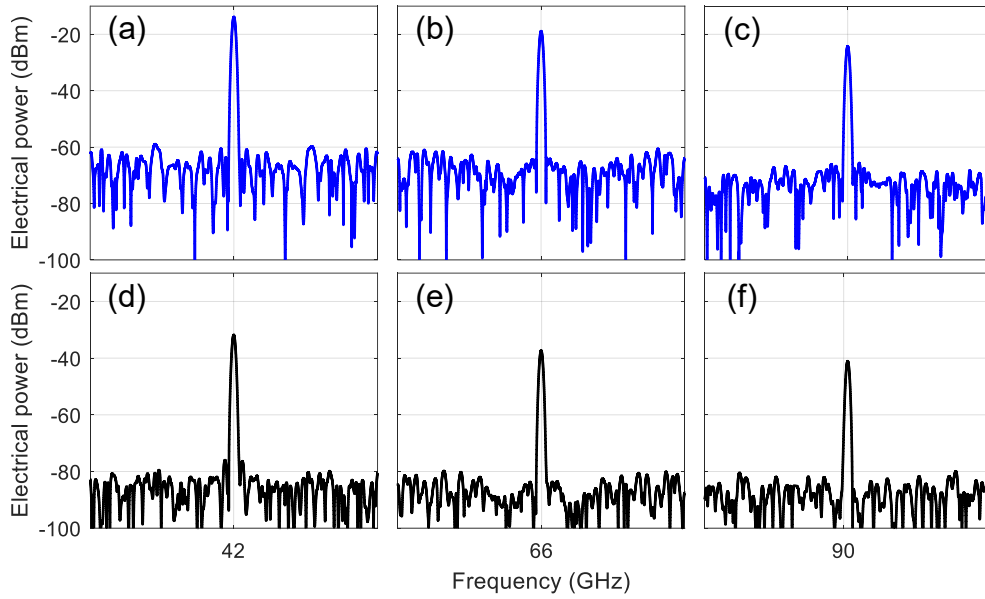


Figure 3.14. Electrical spectra for 42, 66 and 90 GHz mmW signals (RBW = 1 kHz, span = 100 kHz): (a)-(c) OB2B and (d)-(f) hybrid link.

3.6. Impact of turbulent FSO on photonically mmW generated signals

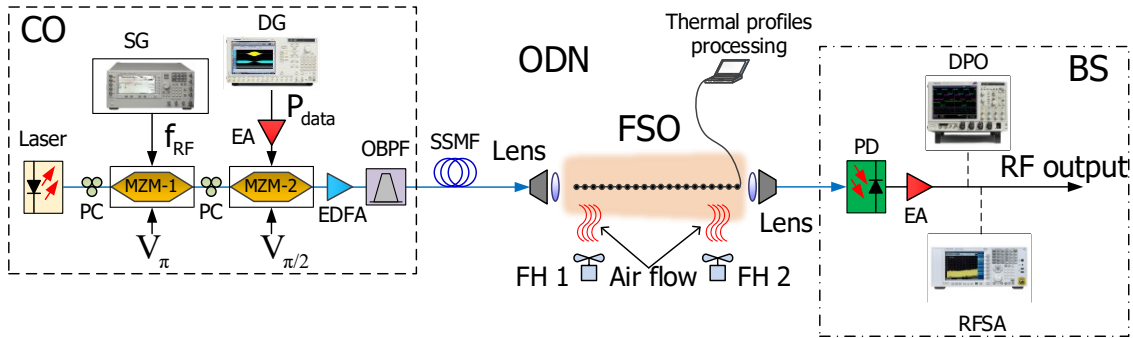
As described in Chapter 2, the atmospheric turbulence in FSO has a significant impact on the signal propagation, and therefore, it degrades the photonically generated mmW signal. In this Section, we experimentally study the impact of non-uniform AT distribution along the FSO link on the transmission of mmW signals, which are photonically generated by using optical external intensity modulator biased at the null transmission point [110].

The experimental setup of signal transmission and distribution over hybrid SSMF/FSO links is illustrated in Figure 3.15(a). In this experiment, a DFB laser (EXFO IQS) at 1550.12 nm wavelength with 10 dBm output optical power is modulated by MZM-1 (Photline MX-LN-40). MZM-1 is driven by an RF signal, f_{RF} , with 22 dBm RF output power, which is generated by SG (Agilent PSG E8267C), and is biased at null transmission point ($V_{\pi} = 6.4$ V) to obtain CS-DSB modulated signal. The purpose of the MZM-2 (Avanex PowerBit F-10) biased at linear point is data signal modulation, as will be described in Chapter 4. The modulated optical signal is first amplified by EDFA (Amonics EDFA-23-B-FA) with 13 dBm output constant power and then, filtered out optical bandpass filter (OBPF) (Finisar Waveshaper 4000S) with 1.5 nm bandwidth to reduce the ASE noise. The optical signal is launched into 1.4 km SSMF followed by 1.2 m FSO channel using a pair of air-spaced doublet collimators (Thorlabs F810APC-1550).

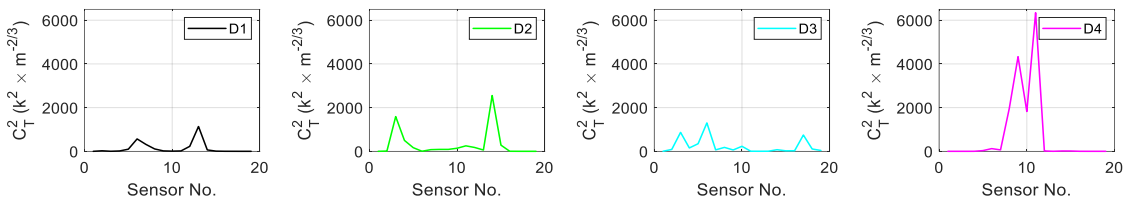
The induced artificial turbulence shown in Figure 3.15(b) is produced in the FSO channel, shown in Figure 3.15(c), according to four different spatial temperature distributions (D1–D4). Turbulence is generated by two fan heaters which introduce temperature gradients into the FSO channel, and measured by 20 temperature sensors equidistantly situated along the FSO link with 6 cm spacing. The distributions are expressed in terms of temperature structure parameter, C_T^2 , along the link. According to Figure 3.15(b), D1 introduces almost uniform turbulence meanwhile D2 and D3 increase the thermal gradient near to the receiver and transmitter, respectively. Finally, D4 represents a high peak turbulence in the middle of the link. In a real scenario, D2 and D3 can be induced by thermal flow close to the building/masts of transmitting/receiving FSO heads meanwhile D4 can be caused by increased airflow over the street canyons, roads or air-condition outlets, as indicated in Chapter 2.

Finally, as in previous schemes, the mmW signal $f_{mmW} = 2f_{RF}$ is generated by the beating of modulated sidebands at PD (Finisar BPD2020R), and amplified by an RF electrical amplifier

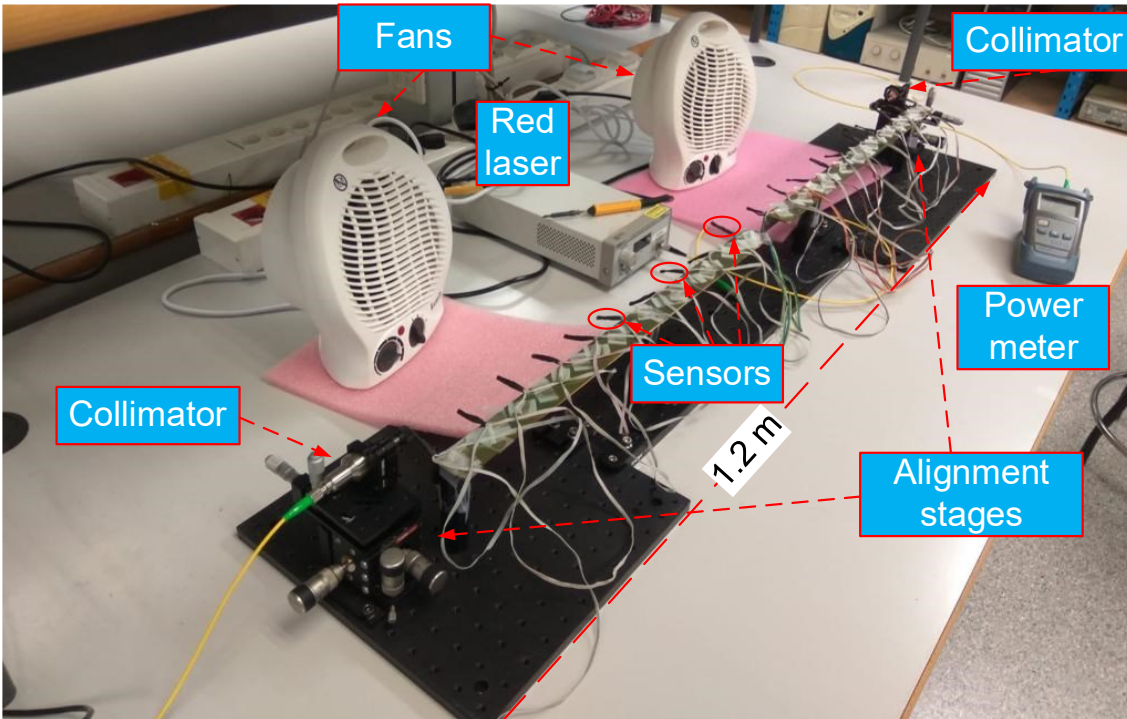
(EA) (SHF Communication Technologies AG SHF-810). The RF spectrum is measured by the RFSA.



(a)



(b)



(c)

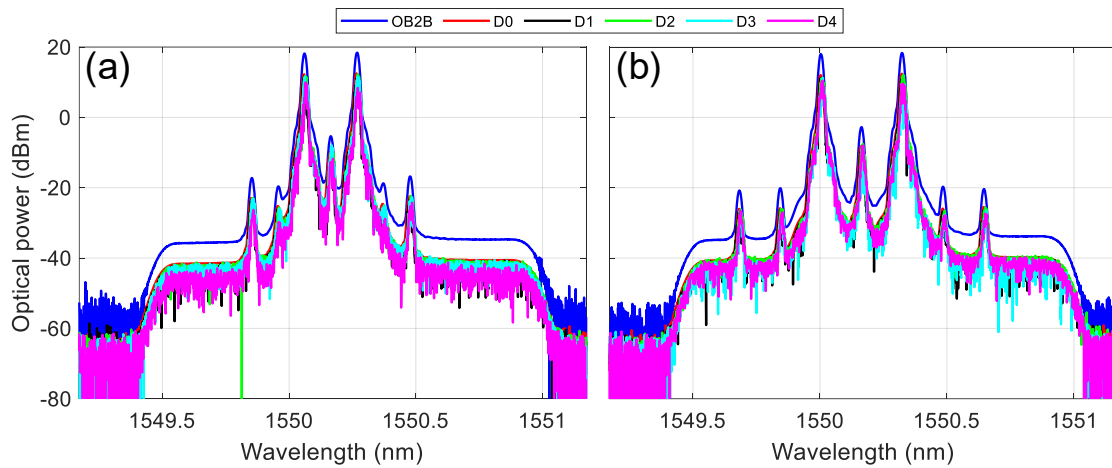
Figure 3.15. (a) Experimental setup of signal transmission and (b) temperature structure distributions and (c) photograph of the experimental FSO channel at Photonic Research Labs in Universitat Politècnica de València [100].

The averaged C_T^2 and C_n^2 corresponding to D1-D4 temperature distributions in our experiment are shown in Table 3.5. Note that the spacing between adjacent sensors is $L_p = 0.06$ m, the atmospheric pressure $P_a = 1024$ mbar and wavelength $\lambda = 1550.12$ nm. Therefore, calculated Rytov variance, i.e. $\sigma_R^2 < 0.05$ in all cases, leads to a weak turbulence regime in this experimental setup.

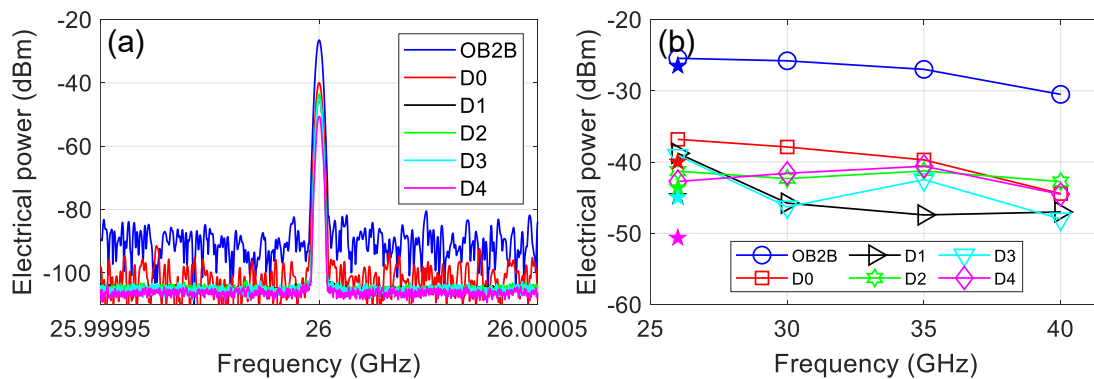
Table 3.5. Refractive index and temperature structure parameters of different temperature distributions ($L_p = 1.2$ m).

Turbulent scenario	$C_T^2 (\text{K}^2 \text{m}^{-2/3})$	$C_n^2 (\text{m}^{-2/3})$
D1	138.01	$1 \cdot 10^{-10}$
D2	315.59	$2.3 \cdot 10^{-10}$
D3	227.83	$1.5 \cdot 10^{-10}$
D4	775.43	$5.7 \cdot 10^{-10}$

Figure 3.16(a) and (b) show the consequence of turbulence on the optical signal transmitted over FSO channel under different thermal distributions (D1-D4) comparing with OB2B for 26 and 40 GHz, respectively. The induced turbulence produces optical signal fluctuation which consequence is an optical power reduction by values up to 3 and 4 dB for the highest impact turbulence distribution with respect to D0 at 26 and 40 GHz, respectively.


Figure 3.16. Optical spectra of CS-DSB (RBW = 0.02 nm): (a) 26 GHz and (b) 40 GHz.

The effect of turbulence along the FSO channel in terms of RF power and noise floor is shown in Figure 3.17(a) and (b). Note that the RF spectrum shown in Figure 3.17(a) employs trace average mode due to the signal fluctuations. The measured RF power for OB2B is -26.5 dBm, whereas -40 dBm is measured after transmission over hybrid link without induced turbulence (D0) and the power is reduced by 12 dB when turbulence is applied in the FSO channel. Nevertheless, no effects on the signal linewidth can be observed.


Figure 3.17. Impact of induced turbulence: (a) electrical spectra and (b) dependence of electrical power and mmW frequency.

The measured RF electrical power in the frequency range of 26 - 40 GHz is depicted in Figure 3.17(b). As expected, the RF electrical power decrease due to the overall frequency response when the frequency increase, as OB2B and D0 show with total drop of 7.7 dB. By the high-resolution RFSA, star markers at 26 GHz are measured, where each color represents different temperature distribution according to D1–D4 profiles. However, due to the optical power fluctuation, the total drop is not constant under thermally induced turbulence. The electrical power drop is about 2 dB for D2 and D4 meanwhile values over 8 dB are measured for D1 and D3.

Finally, the phase noise measurements at 26 GHz by RFSA for different temperature distributions are shown in Figure 3.18 where Table 3.6 summarizes phase noise results at different offsets. The OB2B phase noise at 100 kHz is measured as -103.4 dBc/Hz, whereas it is increased up to -95.9 dBc/Hz for D0. From Figure 3.18, the impact of D1-D4 turbulence results is a higher phase noise level due to power decrease and noise floor increase. Among phase noise at 100 kHz in D1-D4 turbulence profiles, D2 with a turbulence level close to the receiver shows the lowest phase noise, whereas D1 and D3 with turbulence level uniformly distributed and increased close to the transmitter shows the highest phase noise, respectively.

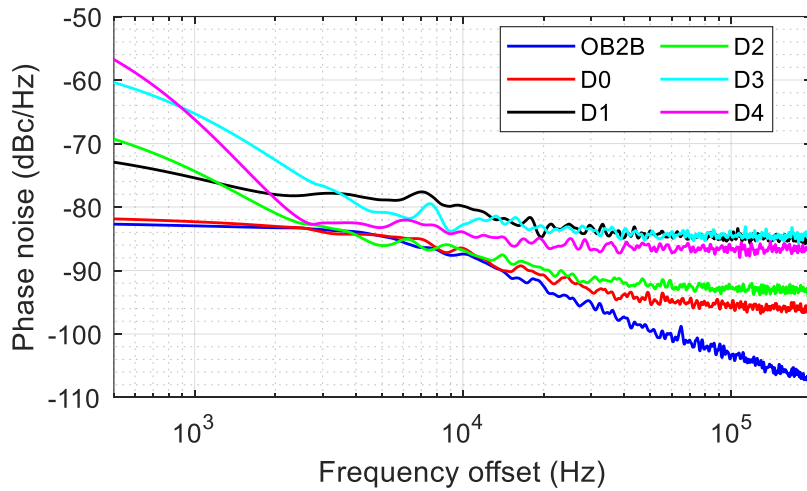


Figure 3.18. Phase noise measurements at 26 GHz (RBW = 220 kHz).

Table 3.6. Phase noise measurements in dBc/Hz of 26 GHz generated signals at different offsets (RBW = 220 Hz).

	Frequency offset		
	1 kHz	10 kHz	100 kHz
OB2B	-83.00	-87.40	-103.40
D0	-82.30	-86.50	-95.90
D1	-75.40	-79.90	-84.90
D2	-74.40	-86.80	-92.80
D3	-65.30	-82.80	-84.30
D4	-66.20	-83.90	-86.80

Measured results confirm that a turbulence distribution with an increased turbulence level in the middle of the link leads higher electrical power reduction down to 10.7 dB compared with non-turbulent scenario. The phase noise results confirm higher phase noise level due to both power decrease and increased noise floor under different turbulent scenarios. Main results include -39.97 dBm electrical power and -103.36 dBc/Hz phase noise for uniform turbulence

distribution, and -50.64 dBm and -86.75 dBc/Hz electrical power and phase noise, respectively, for increased turbulence level in the middle of FSO link.

3.7. Conclusions

This Chapter presents the analytical formulation of CS-DSB scheme based on MZM which is employed in this Thesis. Therefore, mmW signals are generated by using a MZM at CS-DSB bias point, as a very simple approach which does not need optical filters. After description and formulation of the approach, the Chapter presents the main results obtained in the experimental work. Different frequency signals in the 40 - 90 GHz range have been generated with RF power level higher than -40 dBm and full signals characterization has been provided. Main results include carrier suppression levels between 20 and 30 dB and phase noise level as low as 87 dBc/Hz at 14 and 24 GHz.

Furthermore, multiple signal generation in the 15-40 GHz range and distribution over the hybrid optical network including optical fiber and FSO link has been demonstrated. High-quality RF signals with low phase noise are generated at the BSs, while an AWG and an optical switch provide signal reconfiguration at the RN showing the high potential of the proposed system for future deployment of dynamic 5G networks.

Moreover, the non-linear FWM effect in a SOA has been employed to generate higher mmW signal frequencies. This scheme offers the possibility of generating higher mmW frequencies while requirements in terms of electronic component bandwidth are reduced, i.e. mmW signals in the range 42 - 90 GHz have been generated and transmitted over hybrid fiber/FSO links by using 7 - 15 GHz RF driving signals.

Finally, the impact of thermally induced turbulence distributions in FSO has been experimentally evaluated on mmW signal transmission. Non-uniform weak induced turbulence has been generated in the frequency range of 24 - 40 GHz and its impact on optical spectrum, electrical power and phase noise has been measured and studied over 1.2 m FSO channel. Induced turbulence produces optical power fluctuations which causes RF power reduction, and therefore, the phase noise increases. The measurement results show slightly worse optical and electrical signal degradation when FSO channel is under peak turbulence in the middle of the link.

Chapter 4. DML-based data transmission over photonically generated mmW signals

When one door closes, another opens; but we often look so long and so regretfully upon the closed door that we do not see the one which has opened for us.

– Alexander Graham Bell

This Chapter presents the work done on data transmission over photonically generated mmW signals using the technique described in previous Chapter. More concretely, the direct modulation of a laser is employed as the data transmission approach in optical C-RAN. A brief description of the approach is explained followed by the theoretical analysis of signal transmission under local and remote mmW signal generation setups for the sake of comparison and provide main guidelines for future deployment. The Chapter includes comprehensive theoretical and experimental results of the system frequency response, transmission performance, non-linearities and bandwidth usability. Experimental results are conducted towards the evaluation of the impact of DML chirp combined with the fiber dispersion in good agreement with the theoretical study.

4.1. Directly modulated lasers

In microwave photonics systems, the optical source provides the optical carrier and the information signal must be encoded onto the optical carrier. Intensity, frequency and phase modulation can be employed for encoding the electrical signal before optical transmission encoded into [111, 112]. However, intensity modulation is a common approach.

The fundamental of direct modulation is depicted in Figure 4.1(a). In this scheme, the laser acts as the optical source and the modulation device. The laser injection current includes a constant bias current (I_{bias}) and a data signal ($i(t)$). The data signal is superimposed on the bias current. Hence, the optical signal is intensity modulated, where optical power varies in accordance with the data signal and can be delivered by optical links. After signal transmission over optical channel, the data signal is recovered using square law detection at the PD. This approach is called IM-DD and the main benefits are its practical simplicity and low cost [113].

The optical field at the output of the DML is given by:

$$E(t, z = 0) = \sqrt{P(t)} e^{j\varphi(t)} e^{j\omega_0 t}, \quad (4.1)$$

where $P(t)$ and $\varphi(t)$ are the output optical intensity and phase, respectively and ω_o is the angular frequency of the electrical field. Once the optical signal is propagated through the optical fiber with length L , the optical intensity is detected by means of a square-law photodetector (see equation (2.2)) which leads to the photocurrent, $i_{PD}(t)$, given by:

$$i_{PD}(t) = \mathfrak{R} \cdot |E(t, z = L)|^2, \quad (4.2)$$

where \mathfrak{R} is the photodiode responsivity. From equation (4.2), the optical power varies only with variations in the amplitude of the electric field, i.e. information is recovered at the receiver side by detecting the intensity of received light.

The typical power-current curve showing the relationship between driving current and output optical power (power-current, P-I) is shown in Figure 4.1(b). The laser threshold current, I_{th} , is the lowest excitation level at which the laser's output is dominated by stimulated emission rather than by spontaneous emission. Therefore, a proper bias current is required to avoid signal clipping and to ensure linearity. Note that it has been considered a strictly linear relationship between the current and the optical power, but the relation is non-linear in practice.

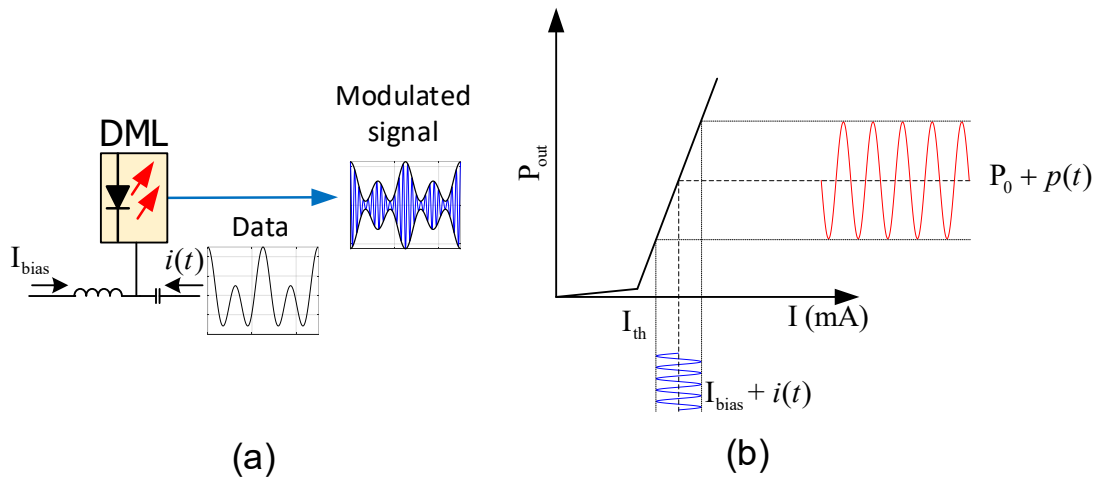


Figure 4.1. (a) Direct modulation scheme and (b) power-current laser curve.

Modulation using DML is robust, simple, low cost and widely used. It has significant benefits over the use of external modulation in terms of power consumption, fabrication complexity and compactness, especially for short optical transmission distance [114]. It is a simple technique compared with external modulation and provides lower bandwidths than external modulation, i.e. with typical values of tens of Gbit/s due to the delay and relaxation oscillation frequency which limit the data modulation bandwidth [115]. However, laser clipping and non-linearity giving rise to intermodulation and HD at the receiver may need to be considered. Modulated optical signal is susceptible to laser chirp (spectral broadening), which also experiences degradation induced by the chromatic dispersion [116]. Therefore, DMLs are generally more suitable for applications in low bit rate systems and interconnects [114]. Moreover, RIN in the laser diode also causes signal degradation, which impact is added to the thermal and shot noise at the PD side.

Chirp is an effect on instantaneous wavelength of the modulated light when the current laser varies as result of modulation, $\Delta\nu(t)$. The interaction between phase and intensity modulation in a laser is described with the help of the laser rate equations as [117, 116] and leads to:

$$\Delta\nu(t) = \frac{\alpha}{4\pi} \left\{ \frac{1}{P(t)} \frac{d}{dt} P(t) + \kappa P(t) \right\}, \quad (4.3)$$

where $P(t)$ is the instantaneous optical power, α is the linewidth enhancement factor and κ is a laser-specific parameter known as the adiabatic chirp constant. In equation (4.3), first term

is the transient chirp and is related with the variation of the emitting optical power meanwhile second term is the adiabatic chirp (κ) is associated with the instantaneous emitting optical power. Typical values of the rate of frequency shift are 50 to 500 MHz/mA with a total shift of 1.5 to 15 GHz and 1550 nm lasers show higher shifts than 1310 nm lasers [118]. Unfortunately, chirp parameters are not often specified by vendors, but typical α values range from 2 to 6 while κ takes values between $1 \cdot 10^{12}$ and $30 \cdot 10^{12}$ Hz/W [119, 116].

When the optical signal is transmitted over optical fiber, the chirp interplays with chromatic dispersion of the optical fiber and several significant effects on the performance at the received signal. Moreover, non-linear behaviour of DML leads to HD, i.e. the output at the n^{th} harmonic of the modulation frequency, and IMD, namely IMD2 and IMD3, which describe the spectral power at the sum and difference terms of two and three modulation frequencies, respectively [118, 116, 120].

However, DMLs are potentially more suitable than externally modulated transmitters for 5G networks. Previous works have successfully demonstrated the use of DMLs [116, 121, 122, 123, 124, 125] for signal transmission, e.g. a 112 Gbit/s dual-polarization 16-QAM signal using a 35 GHz DML [121] or 28-Gbaud PAM-4 and 56-Gbit/s non-return-to-zero (NRZ) signals employing a 30 GHz DML at 1310 nm [122].

4.2. Analytical formulation and link frequency response for DML-based links

In C-RAN architectures, the CO usually directly transmits mmW signals through fronthaul link using over optical fiber. This is called remote configuration, and fiber chromatic dispersion has a significant impact on the link performance for high frequencies, as explained in Chapter 2. In local configuration, the CO can directly transmit multiple aggregated IF modulated bands e.g. in low speed DMLs, and the up-conversion is held at the RRH. The main advantages are the use of low-speed opto-electronic devices and reduced impact of fiber chromatic dispersion since IF signal would be transmitted over fiber and the photonic up-conversion would be held before photodetection. However, the complexity and costs of RRHs are increased due to the high-speed RF components, such as local oscillator or mixers, are required.

Local and remote architectures for photonic mmW signal generation are shown in Figure 4.2. A DML located at the BBU emits an optical carrier centered at the angular optical frequency ω_0 , which is directly modulated by data in both configurations. On the one hand, in the local configuration shown in Figure 4.2(a), the optical signal after DML is launched into the SSMF and then, it is up-converted by the single tone signal with an angular modulation frequency given by w_{RF} at the MZM which is biased at null point for carrier suppressed modulation (see Chapter 3). On the other hand, in the remote configuration shown in Figure 4.2(b), the optical signal after DML is launched into the CS-MZM to be modulated by an electrical single tone signal at w_{RF} , and then, the resulting optical signal is transmitted over the SSMF link.

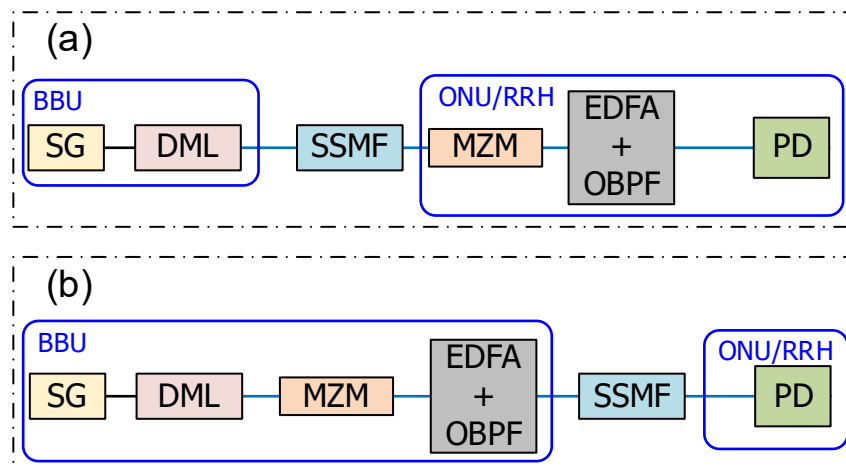


Figure 4.2. Schematic for (a) local and (b) remote configurations [126].

An analytical study of the frequency response of local and remote configuration as well as OB2B is presented in [126]. The output electric field of a laser emitting at ω_0 , which is directly modulated by a single tone at an angular modulation frequency of $\omega = 2\pi f$, can be described by [117]:

$$E_{DML}(t) = \sqrt{P_o(1 + m_{AM} \cdot \cos \omega t)} e^{jm_{PM} \cos(\omega t + \Delta\varphi)} e^{j\omega_0 t}, \quad (4.4)$$

where P_o is the laser output power and m_{AM} and m_{PM} are the amplitude and phase modulation indexes, respectively. The phase difference between amplitude and phase modulation introduced by the laser is $\Delta\varphi$. It is possible to obtain the laser small-signal transfer function characterizing the chirp effect, which relates the amplitude and phase modulation terms to the linewidth enhancement factor, α , and the adiabatic laser chirp, κ (see also equation (4.3)) as [117]:

$$\frac{m_{PM}}{m_{AM}} \cdot e^{j\Delta\varphi} = \alpha \left(1 - j \frac{\kappa P_o}{\omega} \right). \quad (4.5)$$

In this small-signal regime, the intensity of electric field at the output of the light source can be defined as:

$$E_{DML}(t) = \sqrt{P_o} [1 + m_+ \cdot e^{j\omega t} + m_- \cdot e^{-j\omega t}] e^{j\omega_0 t}, \quad (4.6)$$

where the index modulations, m_+ and m_- , are expressed in terms of amplitude, m_{AM} , and phase m_{PM} modulation index, as follows:

$$\begin{aligned} m_+ &= \frac{1}{2} (m_{AM} + jm_{PM} e^{j\Delta\varphi}) \\ m_- &= \frac{1}{2} (m_{AM} + jm_{PM} e^{-j\Delta\varphi}). \end{aligned} \quad (4.7)$$

Furthermore, let us consider the response of a MZM driven by a single tone at RF, $\omega_{RF} = 2\pi f_{RF}$, given by:

$$h_{MZM}(t) = \cos(\varphi_{DC} + 2m_{RF} \cos \omega_{RF} t), \quad (4.8)$$

where φ_{DC} is the phase signal change caused by DC bias ($\varphi_{DC} = \pi/2$ in carrier suppression) and m_{RF} is the modulation RF index. Considering small-signal regime, we can obtain the following:

$$h_{MZM}(t) = \cos \varphi_{DC} + m_{RF} \sin \varphi_{DC} \cdot (e^{j\omega_{RF} t} + e^{-j\omega_{RF} t}). \quad (4.9)$$

Under small-signal assumption, the following expression can be calculated for OB2B configuration from equations (4.6) and (4.9):

$$E_{B2B}(t) = E_{DML}(t) \cdot h_{MZM}(t). \quad (4.10)$$

Moreover, the impulse response of the signal propagation in SSMF fiber, $h_{SSMF}(t)$, can be expressed as [127]:

$$h_{SSMF}(t) = \frac{1}{\sqrt{j2\pi\beta_2 L}} e^{j\frac{\pi}{2\beta_2 L} t^2}, \quad (4.11)$$

where L is the fiber length, and the dispersion parameter β_2 is the second derivative of the propagation constant with respect to the angular optical frequency ω_0 .

According to the schematic depicted in Figure 4.2(a) for the local configuration scheme, where the modulation process is held after the transmission of the DML output field over the dispersive element, the electric field at the input of the photodiode in this case, $E_{LC}(t)$, can be obtained from the following expression:

$$E_{LC}(t) = [E_{DML}(t) \otimes h_{SSMF}(t)] \cdot h_{MZM}(t). \quad (4.12)$$

Using equations (4.6), (4.9), (4.11) and (4.12), the electric field $E_{LC}(t)$ is obtained as:

$$\begin{aligned}
 E_{LC}(t) = \sqrt{P_o} e^{j\omega_o t} \left\{ \cos \varphi_{DC} + \cos \varphi_{DC} e^{j\frac{1}{2}\beta L \omega^2} (m_+ \cdot e^{j\omega t} + m_- \cdot e^{-j\omega t}) \right. \\
 + m_{RF} \sin \varphi_{DC} (e^{j\omega_{RF} t} + e^{-j\omega_{RF} t}) \\
 + m_{RF} \sin \varphi_{DC} e^{j\frac{1}{2}\beta L \omega^2} (m_+ \cdot e^{j(\omega_{RF} + \omega)t} + m_- \cdot e^{-j(\omega_{RF} + \omega)t}) \\
 \left. + m_{RF} \sin \varphi_{DC} e^{j\frac{1}{2}\beta L \omega^2} (m_- \cdot e^{j(\omega_{RF} - \omega)t} + m_+ \cdot e^{-j(\omega_{RF} - \omega)t}) \right\}. \quad (4.13)
 \end{aligned}$$

However, the remote configuration shown in Figure 4.2(b) leads to a general expression for $E_{RC}(t)$ given by the convolution between the dispersive element and the electric field after the modulation process:

$$E_{RC}(t) = [E_{DML}(t) \cdot h_{MZM}(t)] \otimes h_{SSMF}(t). \quad (4.14)$$

Concretely, the electric field for remote configuration $E_{RC}(t)$ can be obtained from equations (4.6), (4.9), (4.11) by means of equation (4.14) as:

$$\begin{aligned}
 E_{RC}(t) = \sqrt{P_o} e^{j\omega_o t} \left\{ \cos \varphi_{DC} + \cos \varphi_{DC} e^{j\frac{1}{2}\beta L \omega^2} (m_+ \cdot e^{j\omega t} + m_- \cdot e^{-j\omega t}) \right. \\
 + m_{RF} \sin \varphi_{DC} e^{j\frac{1}{2}\beta L \omega_{RF}^2} (e^{j\omega_{RF} t} + e^{-j\omega_{RF} t}) \\
 + m_{RF} \sin \varphi_{DC} e^{j\frac{1}{2}\beta L (\omega_{RF} + \omega)^2} (m_+ \cdot e^{j(\omega_{RF} + \omega)t} + m_- \cdot e^{-j(\omega_{RF} + \omega)t}) \\
 \left. + m_{RF} \sin \varphi_{DC} e^{j\frac{1}{2}\beta L (\omega_{RF} - \omega)^2} (m_- \cdot e^{j(\omega_{RF} - \omega)t} + m_+ \cdot e^{-j(\omega_{RF} - \omega)t}) \right\}. \quad (4.15)
 \end{aligned}$$

Table 4.1. Analytical terms of the photocurrent $i_{PD}(t)$ at baseband and mmW band in OB2B, local and remote configurations.

Config.	$i_{PD}(t)$	
OB2B	$\Re P_o m_{AM} \cdot [\cos^2 \varphi_{DC} + 2m_{RF}^2 \sin^2 \varphi_{DC}]$	(4.16)
w	$\Re P_o m_{AM} [\cos^2 \varphi_{DC} + 2m_{RF}^2 \sin^2 \varphi_{DC}]$ $\cdot \left[\sqrt{1 + a^2} \cos \left(\frac{1}{2} \beta_2 L w^2 + a \tan a \right) \right.$ $\left. + ja \frac{\kappa P_o}{\Omega} \sin \left(\frac{1}{2} \beta_2 L w^2 \right) \right]$	(4.17)
	$\Re P_o \left[\sqrt{1 + a^2} \cos \left(\frac{1}{2} \beta_2 L w^2 + a \tan a \right) + ja \frac{\kappa P_o}{w} \sin \left(\frac{1}{2} \beta_2 L w^2 \right) \right]$ $\cdot [m_{AM} \cos^2 \varphi_{DC}$ $+ 2m_{AM} m_{RF}^2 \sin^2 \varphi_{DC} \cos(\beta_2 L w_{RF} \Omega)]$	(4.18)
OB2B	$\Re P_o m_{AM} m_{RF}^2 \sin^2 \varphi_{DC}$	(4.19)
$2w_{RF} \pm w$	$\Re P_o m_{AM} m_{RF}^2 \sin^2 \varphi_{DC}$ $\cdot \left[\sqrt{1 + a^2} \cos \left(\frac{1}{2} \beta_2 L w^2 + a \tan a \right) \right.$ $\left. + ja \frac{\kappa P_o}{w} \sin \left(\frac{1}{2} \beta_2 L w^2 \right) \right]$	(4.20)
	$\Re P_o m_{AM} m_{RF}^2 \sin^2 \varphi_{DC}$ $\cdot \left[\sqrt{1 + a^2} \cos \left(\frac{1}{2} \beta_2 L (w^2 \pm 2w_{RF} w) + a \tan a \right) \right.$ $\left. + ja \frac{\kappa P_o}{w} \times \sin \left(\frac{1}{2} \beta_2 L (w^2 \pm 2w_{RF} w) \right) \right]$	(4.21)

In all cases, the calculation of the photocurrent $i_{PD}(t)$ in equation (4.2) leads to different terms at baseband and mmW frequencies. For the sake of comparison, Table 4.1 shows the terms obtained for $i_{PD}(t)$, which are proportional to the system transfer function under OB2B, local and remote configurations at ω (baseband) and $2\omega_{RF} \pm \omega$ (mmW band), where the latter corresponds to the signal to be radiated by the base station.

Table 4.2. Theoretical and experimental parameters.

	Parameter	Value
	λ	1553.45 nm
	P_o	4 mW
DML	α	1.5
	κ	14.9 GHz/mW
	m_{RF}	0.1
	φ_{DC}	$\pi/2$
MZM	m_{AM}	0.15
	f_{RF}	20 GHz
SSMF	β_2	-22.1 ps ² /km
	L	25 km

The theoretical system response and the corresponding electrical power measurements at baseband (BB) and mmW frequencies after photodetection are displayed in Figure 4.3 where the parameters have been adjusted to those employed in the experimental setup, as detailed in Table 4.2. A DML (Optical Zonu, OZ516) with a 3 dB bandwidth of 7.75 GHz is employed in the experimental setup and the experimental system response is measured using the SG (Rohde & Schwarz SMW200A) and a signal analyzer (SA) (Rohde & Schwarz FSW43).

Experimental OB2B at BB and mmW frequencies are depicted in Figure 4.3(a) and (b), respectively. Both transfer functions are proportional to the DML frequency response and correspond to the theoretical frequency response detailed in equations (4.16) and (4.19), respectively.

Figure 4.3(c) and (d) show the response for local configuration where both bands, BB and mmW, show similar frequency dependence. Theoretical calculations using equations (4.17) and (4.20) lead to a dispersion induced power fading for a laser directly modulated signal at frequencies given by:

$$w_n \approx \sqrt{\left| \frac{(2n+1)\pi + 2 \operatorname{atan} \alpha}{\beta_2 L} \right|} \quad (n = 0, 1, \dots). \quad (4.22)$$

Using a 25 km fiber link, the first null ($n = 0$) is at the frequency of 15.5 GHz which is out of the laser operating bandwidth. The term related to phase contribution by means of κ is basically not significant in this RF frequency range. Note that experimental measurements at baseband and mmW band are limited by the laser modulation bandwidth and, hence, show strong similarities to OB2B characterization.

In the remote configuration at BB, according to equation (4.18), the first factor leads to the same nulls obtained in equation (4.22), which are out of the measuring frequency range. However, there are also nulls at frequencies causing the cancellation of the second factor in equation (4.18), which are given by:

$$w_n = \frac{(2n+1)\pi}{2} \frac{1}{|\beta_2| L \omega_{RF}} \quad (n = 0, 1, \dots). \quad (4.23)$$

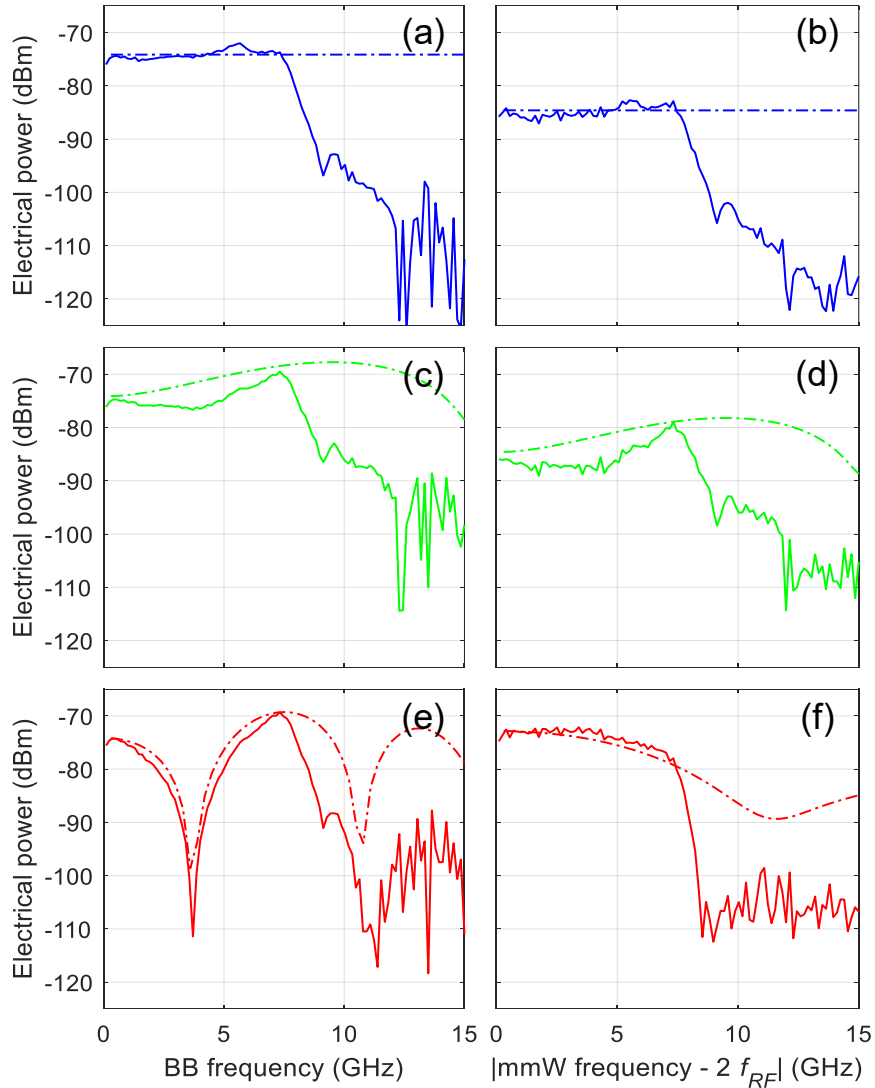


Figure 4.3. Comparison of theoretical (dashed lines) and experimental (solid lines) electrical output power at baseband (left side) and mmW (right side) band: (a)-(b) OB2B, (c)-(d) local and (e)-(f) remote configurations, respectively. Both local and remote configurations are obtained over 25 km SSMF link.

The first null ($n = 0$) is obtained at 3.7 GHz for 25 km SSMF link, as it is shown in Figure 4.3(e) both in the theoretical and experimental curves. On the contrary, the remote configuration at mmW band (equation (4.21)) only includes the term with nulls at frequencies given by (4.22). Therefore, no nulls can be measured due to the laser bandwidth (see Figure 4.3(f)). However, the estimation of equation (4.21) at low frequencies leads to a higher amplitude signal under the remote scheme compared to the local configuration as a result of the combined effect of dispersion and laser chirp, as has been previously observed [128]. Note that a 15 dB signal gain with respect to local or OB2B configuration is measured for values up to 8 GHz transmitted over 40 GHz while this behaviour is not observed in baseband.

4.3. Transmission measurements over locally and remotely generated mmW signals.

4.3.1. Evaluation of links performance

In the following, we evaluate the impact of the local and remote photonic generation of 40 GHz signal over an optical fronthaul based on a DML and CS external modulation for frequency up-

conversion [129]. The experimental setups for local and remote mmW signal generation and transmission approaches are displayed in Figure 4.4. In this experiment, the same DML employed in the previous Section with 5.6 dBm optical power is modulated by a 250 MHz bandwidth quadrature phase shift keying (QPSK) signal centered at 500 MHz, which is generated by the data generator (DG) (Rohde & Schwarz SMW200A) with a power of 5 dBm.

In the local generation scheme shown in Figure 4.4(a), the directly modulated optical signal is transmitted along the SSMF fiber link and, just before the electro-optic conversion, is up-converted by using a CS-MZM. The state of polarization of the optical signal is adjusted by a PC and then the optical signal is launched into the MZM (Sumitomo T.DEH1.5-40X-ADC-Y-Z), which is biased at the null transmission point (V_{π}), i.e. 8.22 V, to obtain the carrier suppressed optical signal. The MZM is driven by a 20 GHz electrical single tone signal with 23 dBm electrical power, generated by a signal generator (Agilent 8267C). A fixed 17.5 dBm output power EDFA (Amonics AEDFA-23-B-FA) is employed to compensate the optical losses, and the ASE noise is afterward filtered out by an OBPF (Alnair BVF-100) with bandwidth $\Delta\lambda = 1.25$ nm. Finally, the opto-electronic conversion is held into the PD (Finisar XPDV3120R) working in linear regime to generate a mmW signal at desired frequency by beating of sidebands.

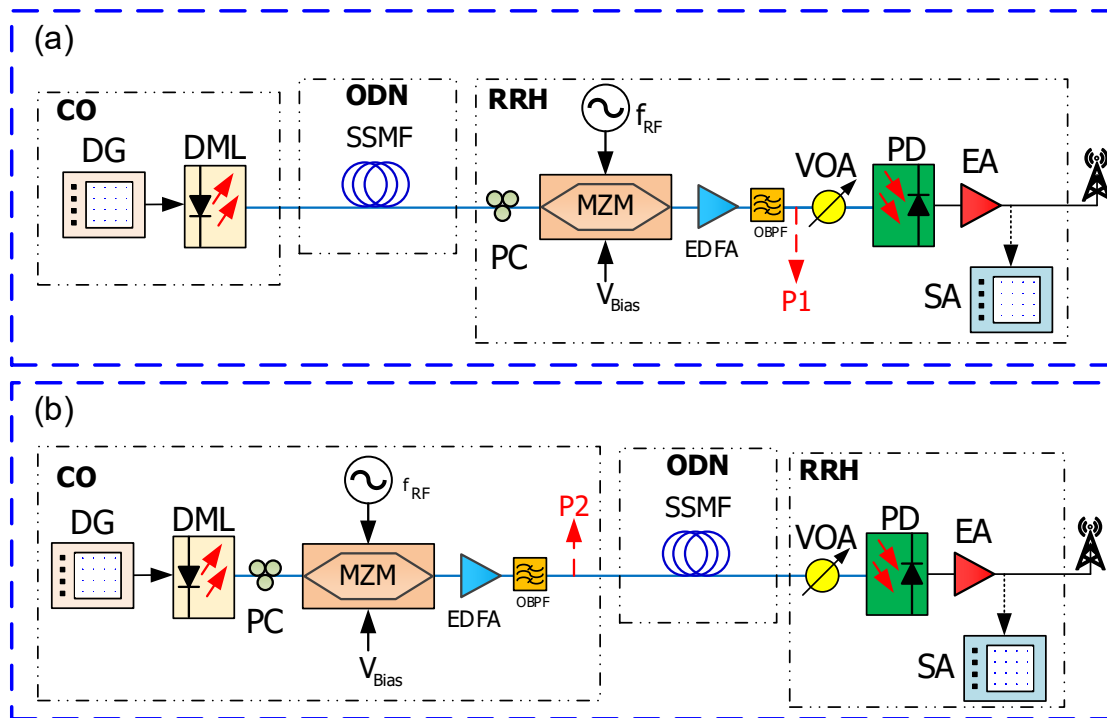


Figure 4.4. Experimental setups for: (a) local and (b) remote MWP signal generation [126].

On the other hand, Figure 4.4(b) shows the remote scheme where the directly modulated optical signal is up-converted in the CS-MZM, driven and biased in the same conditions as in the local scheme, and then transmitted over the SSMF link. Then, the optical signal is amplified and filtered out by the EDFA and OBPF, respectively, and finally, the electrical signal is recovered at the 40 GHz band by the PD.

The optical spectrum at the OBPF output is measured at P1 and P2 points for local and remote schemes, as shown in Figure 4.4(a) and Figure 4.4(b), respectively, by an OSA (Yokogawa AQ6370C), showing a carrier suppression larger than 26 dB (see Figure 4.5). It can be observed that ASE noise level is 10 dB lower in the remote setup due to higher optical power at the input of the EDFA (i.e. lower gain for fixed output power).

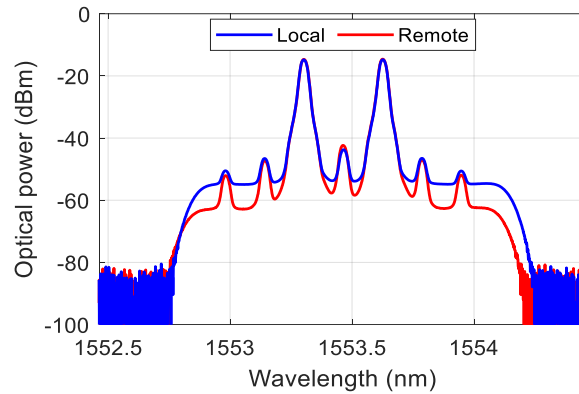


Figure 4.5. Optical spectrum of optically carrier suppressed modulated signal over 25 km SSMF at P1 in setup (a) –blue- and P2 in setup (b) –red- in Figure 4.4.

In the following, the recovered electrical spectra after photodetection for OB2B, local and remote setups are depicted in Figure 4.6. The mmW signal with -27.6 dBm electrical power is generated at 40 GHz, as shown by the electrical spectrum measured under OB2B setup in Figure 4.6(a). The extinction ratio with respect to the original carrier at 20 GHz is higher than 36 dB, the insets show the detail of the data band at baseband (-75 dBm) and also at mmW band (-82 dBm).

Measurements under local configuration for 10 and 25 km SSMF are shown in Figure 4.6(b) and (c), respectively, and lead to similar electrical power levels than OB2B both for baseband and mmW band, according to Figure 4.3(c) and (d) (also in good agreement with equations (4.17) and (4.20)).

On the other hand, Figure 4.6(d) and (e) show the measured electrical spectra for 10 and 25 km SSMF remote setup. No significant differences are found in data baseband with regards to OB2B. However, an electrical power increase of 9 and 16 dB is observed in data bands carried by mmW signal after transmission over 10 and 25 km fiber link, respectively.

These measurements confirm the results presented in the previous Section, where the electrical amplitude at the mmW band under remote configuration is found to be 15 dB larger with respect to OB2B (equation (4.21)) and Figure 4.3(f) due to the system response. However, the remote configuration experiences high IMD products at 40 GHz band in 25 km fiber link (see inset in Figure 4.6(e)). Note that local configuration over the same link, displayed in Figure 4.6(d), does not show IMD signals, which can lead to dramatic penalties under certain signal conditions in remote generation setup, i.e. large bandwidth or multiband signals.

In the following, the EVM standard metric is employed to measure the quality of recovered signals. It contains information about both amplitude and phase errors in the signal and is adopted by various communication standards, i.e. LTE-Advance (LTE-A) or 5G NR (see Appendix A).

The EVM of the recovered signal after photodetection is measured by the SA, where 17.5% threshold level has been considered for QPSK modulation (see Appendix A). Figure 4.7 shows the comparison between local (a)-(b) and remote (c)-(d) setups transmission over 10 and 25 km of SSMF in terms of EVM performance at baseband (0.5 GHz), and also at mmW band (40.5 GHz) versus received optical power (RoP) and received electrical power (ReP), respectively.

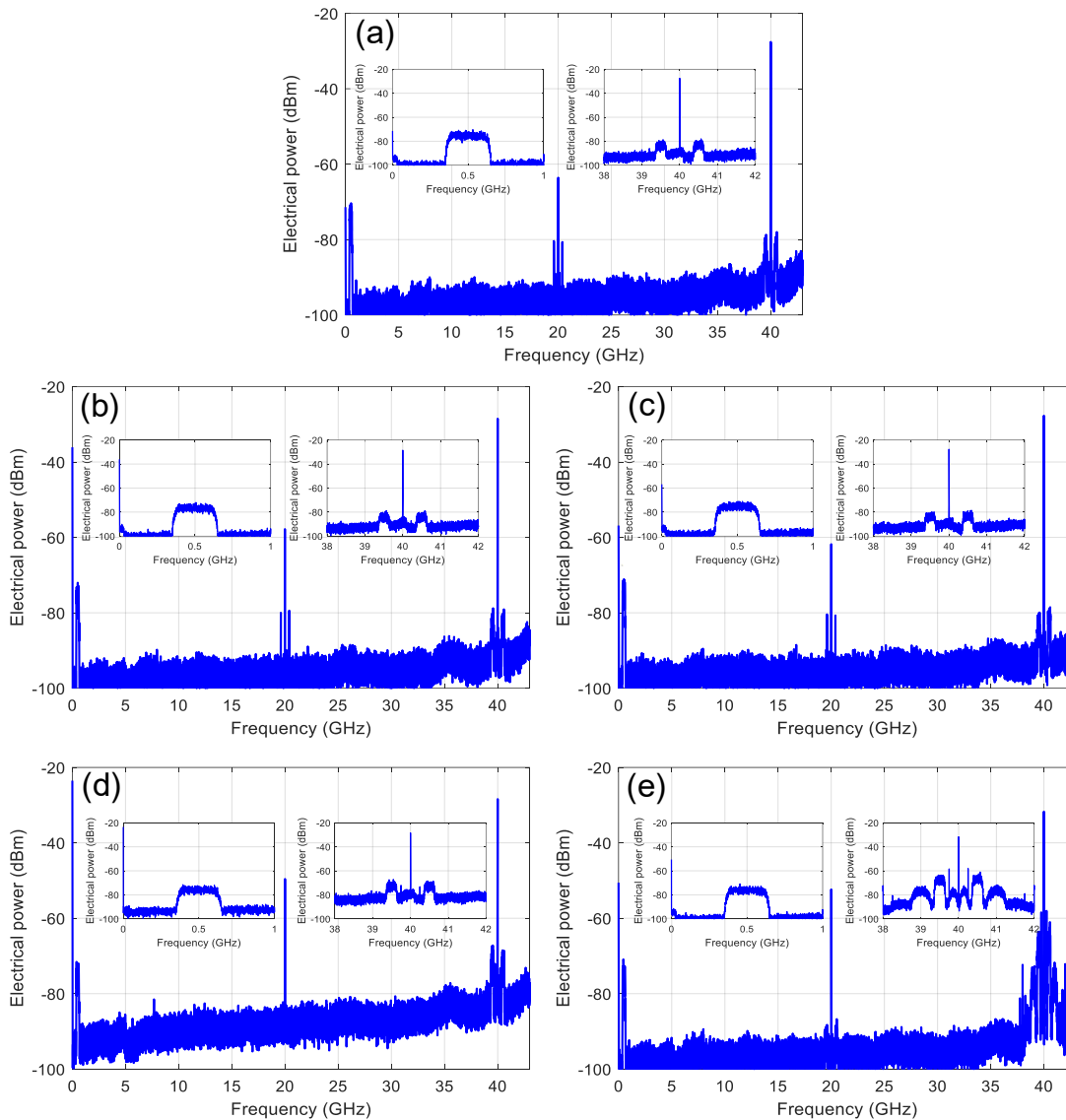


Figure 4.6. Measured electrical spectra after photodetection with different configurations: (a) OB2B, (b) and (c) local signal generation with 10 and 25 km fiber link, respectively, and, (d) and (e) remote signal generation with 10 and 25 km fiber link, respectively. Insets show the detail of the data band at baseband and at mmW band.

In principle, the modulated data would be distorted due to the dispersion after a long-distance transmission. However, the experimental electrical output power at baseband and mmW band shown in Figure 4.3 exhibits that remote configuration in 25 SSMF km link leads to higher power level than OB2B and local setups in good agreement with theoretical predictions. As expected, local setup leads to signal transmission results over 10 and 25 km links with similar performance for a given RoP with respect to the OB2B, shown in Figure 4.7(a), both at baseband and at mmW band, according to the transfer functions in Figure 4.3(c)-(d).

Electrical back-to-back (EB2B) measurements are also shown for the sake of characterizing the quality of the received electrical signal just after generation without any optical impairment. Note that results obtained at 40.5 GHz show higher EVM due to bandwidth limitation of the laboratory equipment, as also shown in EB2B measurements. EVM measurements vs. ReP, shown in Figure 4.7(b), confirm the quality of the signal strictly depends on the measured electrical power for both baseband and mmW band, and no further penalties are present in the system as can be observed from the comparison with the EB2B measurements.

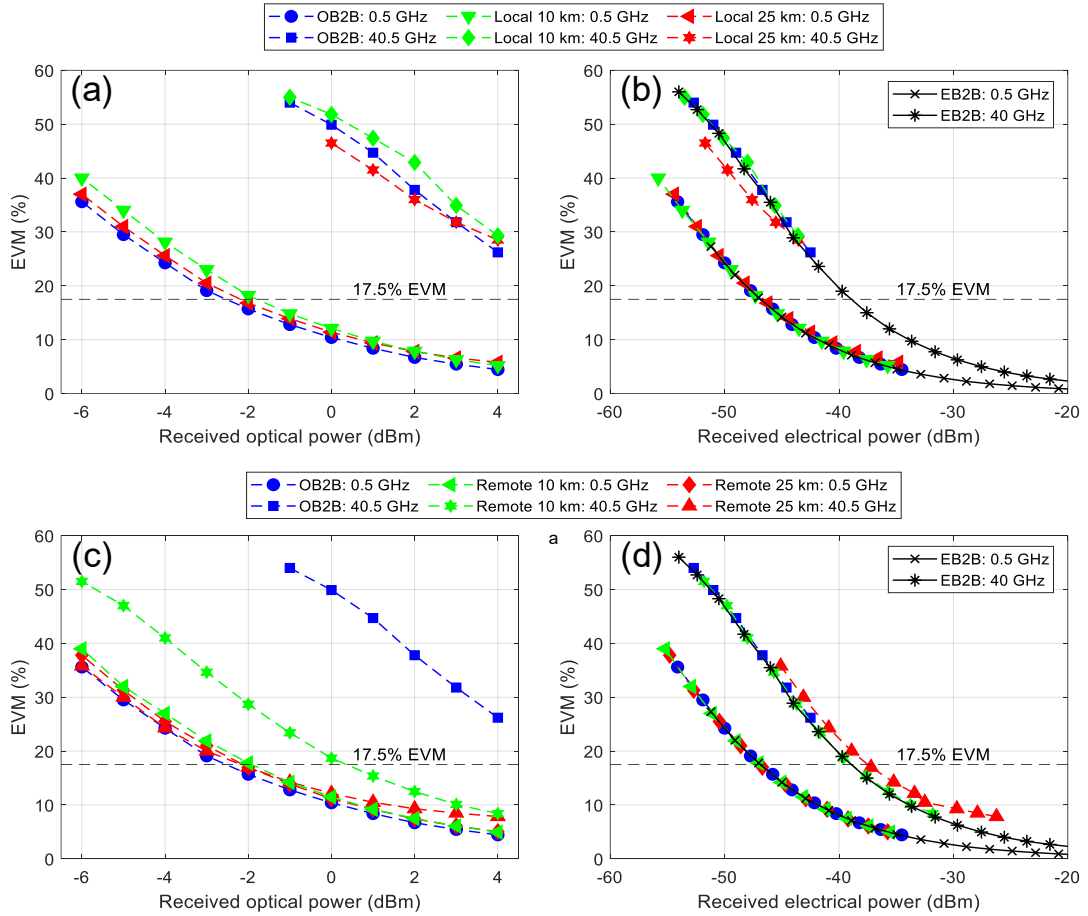


Figure 4.7. EVM comparison at baseband and mmW bands between local and remote setups for QPSK signal (IF = 500 MHz) over 40 GHz for 10 and 25 SSMF links: (a) EVM vs RoP (local setup), (b) EVM vs ReP (local setup) and, (c) EVM vs RoP (remote setup) and (d) EVM vs ReP (remote setup).

Figure 4.7(c) plots that EVM measurements over 10 and 25 km fiber transmission at baseband under remote setup, which are similar to those obtained in OB2B configuration, as expected from Figure 4.3(e) at 0.5 GHz. Note that EVM values in OB2B at 40.5 GHz are significantly larger due to the equipment bandwidth limitations mentioned above. However, in this band, remote setup (Figure 4.7(d)) leads to a significant signal quality improvement, i.e. EVM reduction, according to the frequency response depicted in Figure 4.3(f) which leads to a higher electrical power (i.e. 15 dB gain for 25 km) for fixed RoP. In our experiment, this improvement is estimated as an EVM decrease from 48% to 18.7% and 12.2% over 10 and 25 km, respectively, with 0 dBm RoP since electrical power increases with fiber length for fixed frequency and RoP. Moreover, Figure 4.7(d) shows that EVM depends on the ReP for baseband and mmW band. In the mmW band, EVM measurements in OB2B show 8 dB penalty with respect to baseband due to the bandwidth of the equipment, but no further penalties are present and EVM keeps constant for a given electrical power level despite the fiber length.

Figure 4.8 shows the measured constellations for OB2B and 25 km SSMF for local and remote setups with 3 dBm RoP at 40.5 GHz. Spread symbols with EVM levels above the threshold are shown for OB2B (Figure 4.8(a)) and local (Figure 4.8(b)) configurations. Nevertheless, according to the theoretical predictions explained above, a clearer constellation is recovered for remote configuration (Figure 4.8(c)), which leads to a higher electrical power with fixed RoP, where only a slight distortion is shown for the outer symbols due to the IMD.

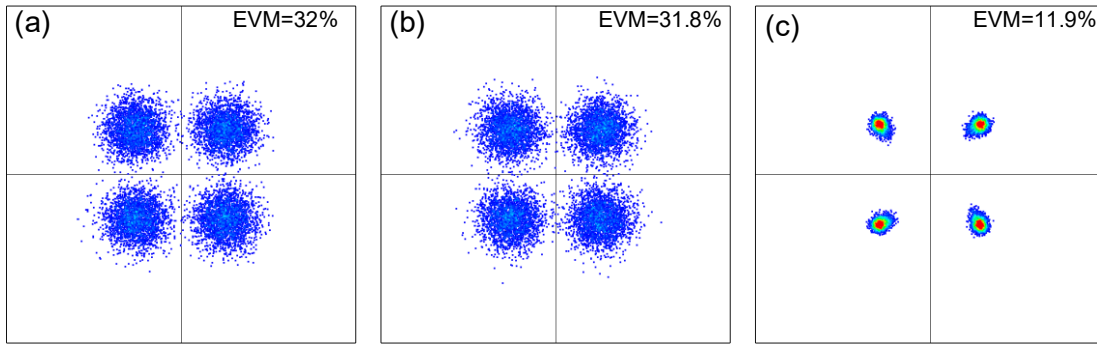


Figure 4.8. Constellations at 3 dBm RoP for: (a) OB2B and, (b) local and (c) remote setups over over 25 km SSMF link.

Finally, the experimental work is completed by evaluating the system performance for different frequencies in order to confirm the theoretical and experimental frequency system response detailed in Table 4.1. Figure 4.9 shows EVM measurements and electrical received power as a function of the central frequency of the 250 MHz bandwidth QPSK signal both at baseband and at mmW band for OB2B, local and remote setups over 25 km fiber link.

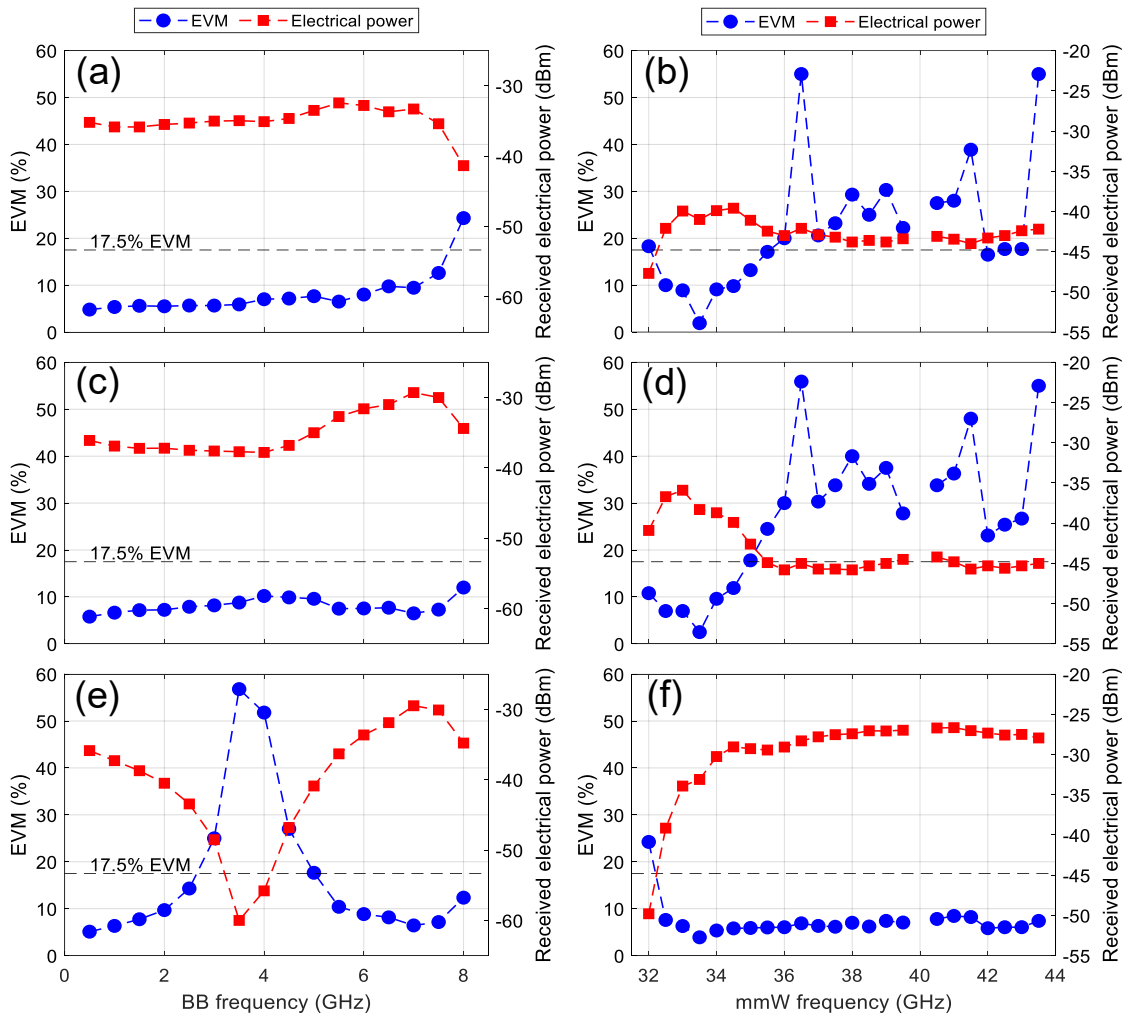


Figure 4.9. EVM and ReP for different setups vs frequency over 25 km fiber link: (a)-(b) OB2B, (c)-(d) local setup and (e)-(f) remote setup, at baseband and millimeter wave band, respectively.

Figure 4.9(a) for OB2B shows a clear correlation between EVM and electrical power, as a result from the DML frequency response (see Figure 4.3(a)). BB measurements are shown up

to 8 GHz due to the 7.75 GHz bandwidth limitation on the DML. Accordingly, measurements in the mmW band are done from 32 GHz (8 GHz below the 40 GHz band) up to 43.5 GHz due to the RFSA bandwidth limitation. Again, the electrical power follows the predicted behavior of the theoretical frequency response (see Figure 4.3(b)) with corresponding EVM values where several EVM fluctuations are observed above the threshold.

Figure 4.9(c) shows the electrical power and EVM values against frequency in baseband for local setup following the measured frequency response in Figure 4.3(c), which is similar to the one measured in OB2B setup. However, Figure 4.9(d) shows some reduction (i.e. 2.5 dB at 35.5 GHz) of the electrical power with respect to the OB2B although a maximum is obtained at 7 GHz offset respect to 40 GHz, due to DML frequency response and also according to Figure 4.3(d). Again, higher EVM values with some fluctuations due to signal processing are obtained above the threshold.

The performance of the remote generation setup is also characterized in frequency. Figure 4.9(e) shows the electrical power decrease (i.e. EVM increase) at 3.7 GHz for remote setup, in good agreement with the notch predicted by equation (4.23) in baseband frequency response. However, Figure 4.9(f) shows a 13 dB increase of electrical power (i.e. reduced EVM) with respect to OB2B along the measurement frequency range up to 35.5 GHz (4.5 GHz below 40 GHz) in accordance to Figure 4.3(f).

4.3.2. Evaluation of non-linear distortions

In the following, we evaluate the impact of HD and IMD in data transmission over local and remote photonicallly generated 40 GHz signal over an optical fronthaul based on a DML and CS external modulation for frequency up-conversion. A comprehensive experimental evaluation of the HD and IMD frequency response of both approaches is provided to identify the optimal setup for concrete application scenarios in 5G/6G networks [130].

The experimental scheme employed in this Section is the same as shown in Figure 4.4, where in this case data signals are generated by the DG scheme displayed in Figure 4.10. Data band is generated, amplified and filtered out by the SG (Tektronix AWG7122C or Rohde & Schwarz SMW200A), EA-1 (SHF Communication Technologies AG SHF-810) and electrical band pass filter (EBPF) (Minicircuits 14780), respectively. Different bands can be generated from other SGs and combined by the electrical combiner (EC) (Minicircuits ZFRSC-42) in multiband scenarios.

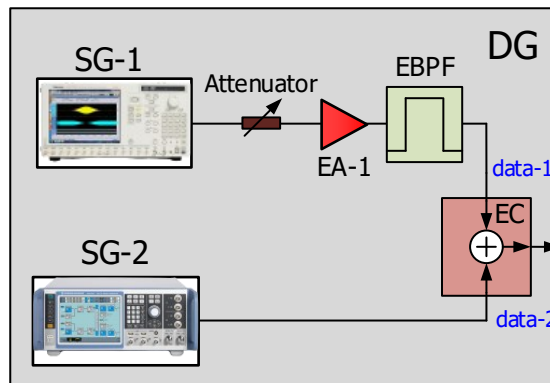


Figure 4.10. Multiple data generator scheme.

We consider multiband signal transmission, i.e. the laser is directly modulated by k -tones with angular modulation frequencies $\omega_k = 2\pi f_k$, which leads to the following time response due to DML non-linear behavior [131, 132]:

$$\begin{aligned}
 h_{DML}(t) = & m_o \\
 & + \sum_k m_+(\omega_k) \cdot e^{j\omega_k t} + m_-(\omega_k) \cdot e^{-j\omega_k t} \\
 & + \sum_k m_+(2\omega_k) \cdot e^{j2\omega_k t} + m_-(2\omega_k) \cdot e^{-j2\omega_k t} \\
 & + \sum_k \sum_{l \neq k} m_+(\omega_k - \omega_l) \cdot e^{j(\omega_k - \omega_l)t} + m_-(\omega_k - \omega_l) \cdot e^{-j(\omega_k - \omega_l)t} \\
 & + \sum_k \sum_{l \neq k} m_+(\omega_k + \omega_l) \cdot e^{j(\omega_k + \omega_l)t} + m_-(\omega_k + \omega_l) \cdot e^{-j(\omega_k + \omega_l)t}
 \end{aligned} \tag{4.24}$$

where $m_{\pm}(2\omega_k)$ accounts for the second-order harmonic distortion and $m_{\pm}(\omega_k \pm \omega_l)$ corresponds to the second-order intermodulation products of the DML.

The electrical current obtained at the PD, $i(t)$, is calculated by equation (2.2). Accordingly, the electrical voltage is given by:

$$V_{RF}(t) = Z_{\Omega} \cdot i(t), \tag{4.25}$$

where Z_{Ω} is the total impedance of the optical receiver.

After photodetection, the most significant distortion terms correspond to the HD at the frequency $2\omega_k$ and the IMD at $\omega_k \pm \omega_l$ in the mmW band of interest (i.e. $2\omega_{RF}$). While the evaluation of $V_{RF}(2\omega_{RF} \pm \omega_k)$ provides the amplitude response of the transmission system operating in the mmW band, the evaluation of V_{RF} at other frequency values such as $V_{RF}(2\omega_{RF} \pm 2\omega_k)$ and $V_{RF}(2\omega_{RF} \pm \omega_k \pm \omega_l)$ allows us to obtain non-linear HD and IMD response, respectively; and therefore, to evaluate the impact on the data transmission [130].

4.3.2.1. Experimental system frequency response

In this case, experimental evaluation of OB2B, local and remote configurations with regards to non-linear response is presented.

Firstly, the EB2B measurement has been done for the sake of characterization of the electrical signal (f_1) applied to the DML where signal generator and analyser are directly connected. The EB2B measurement is included in Figure 4.11, Figure 4.12 and Figure 4.13 where evaluation of $(2\omega_k)$ -, $(\omega_k - \omega_l)$ - and $(\omega_k + \omega_l)$ -type distortion terms are analysed, respectively.

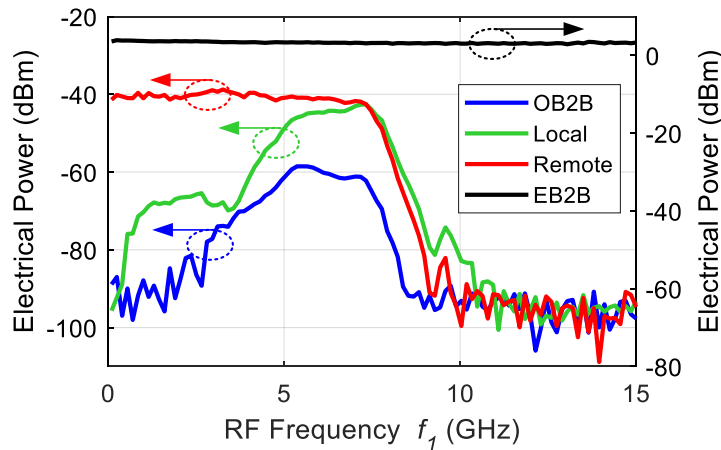


Figure 4.11. Experimental second-order HD ($2\omega_{RF} - 2\omega_l$) for OB2B, local and remote configuration (left axis). EB2B signal measurement is included as a reference (right axis).

With regards to the evaluation of $(2\omega_k)$ -type term, the SG is configured to generate an RF-tone centered at f_1 which is introduced in the DML and the RF power is measured at the frequency $2f_{RF} \pm 2f_1$ for OB2B, local and remote configuration. For the sake of brevity, since lower and upper bands lead to similar results, Figure 4.11 shows the amplitude response for different frequency values f_1 (x-axis) corresponding to the lower band. Firstly, we observe that OB2B amplitude response of Figure 4.11 is directly proportional to the response of the DML. Indeed, we can identify the typical regimes of a DML corresponding to operation frequency close to the relaxation frequency or far from it [117]. According to [129], the amplitude response of the DML leads to a relaxation frequency close to 6.5 GHz where the distortion is higher than in lower frequencies. Frequencies lower than 3.5 GHz lead to signal non-linearities arising mainly from the power-current (P-I) curve and therefore, this low-frequency region is selected due to minimum distortion.

Additionally, Figure 4.11 shows the amplitude response under local configuration for mmW signal generation, which resembles the DML output signal propagated along the same dispersive fiber link. In this sense, maximum response of HD ($2\omega_{RF} - 2\omega_1$) is found in a 2.5 GHz wideband centered at 6.5 GHz in OB2B configuration, similar to local configuration while shows negligible HD at lower frequencies than 3.5 GHz. However, the evaluation of HD under remote configuration leads to a significantly different frequency response. In this case, HD is held all over the frequency band and therefore, significant impact is expected even at low frequencies within the DML modulation band (-40 dBm electrical power). Note that differences between HD in local and remote configurations arise mainly from dispersion effects since the dependence on the laser chirp is identical. Therefore, significant impact on the transmitted signals will be observed under remote configuration, especially when two bands are transmitted satisfying $\omega_2 = 2\omega_1$.

In the following, two RF tones, f_1 and f_2 , are generated with constant frequency spacing of 100 MHz while both subcarriers are tuned simultaneously and the amplitude response is measured at the frequency $2f_{RF} - (f_2 - f_1)$ to obtain the IMD ($2\omega_{RF} - (\omega_2 - \omega_1)$), as shown in Figure 4.12. It can be observed that local configuration leads to similar results than OB2B setup leading to the cancellation of electrical power at this IMD term over the entire frequency range while the remote configuration shows -30 dBm power at low frequencies. This IMD-term distortion will have significant impact when two signals transmitted with ω_1 and ω_2 satisfy $\omega_2 - \omega_1 = \omega_1$, so the first band ω_1 will directly notice the impact of this $(\omega_2 - \omega_1)$ -type IMD term.

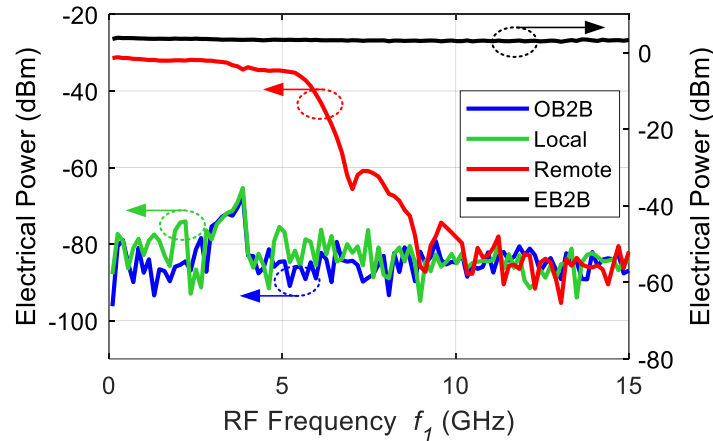


Figure 4.12. Experimental second-order IMD ($2\omega_{RF} - (\omega_2 - \omega_1)$) for OB2B, local and remote configuration (left axis). EB2B signal measurement is included as a reference (right axis).

Finally, the impact of IMD ($2\omega_{RF} - (\omega_1 + \omega_2)$) term has been experimentally obtained by using two RF tones tuned simultaneously at f_1 and f_2 with a constant separation of 100 MHz and measuring the amplitude response at the frequency $2f_{RF} - (f_2 + f_1)$ (see Figure 4.13). Note that in this case, when two signals with ω_1 and ω_2 are transmitted, a third band given by

$\omega_3 = \omega_1 + \omega_2$ will notice the impact of this IMD-term distortion. In this case, the amplitude response of HD ($2\omega_{RF} - 2\omega_1$) and IMD ($2\omega_{RF} - (\omega_2 + \omega_1)$) are very similar for all scenarios.

Although remote setup leads to similar distortion level (-30 dBm in Figure 4.13) than IMD ($2\omega_{RF} - (\omega_2 - \omega_1)$), the evaluation of this IMD term in the mmW band leads to slightly different results in this case compared to previous terms. In this case, OB2B and local configuration show significant values of distortion in the band centered at 6.5 GHz (-55dBm and -38 dBm, respectively) due to the intrinsic characteristic of the DML employed in the experiments.

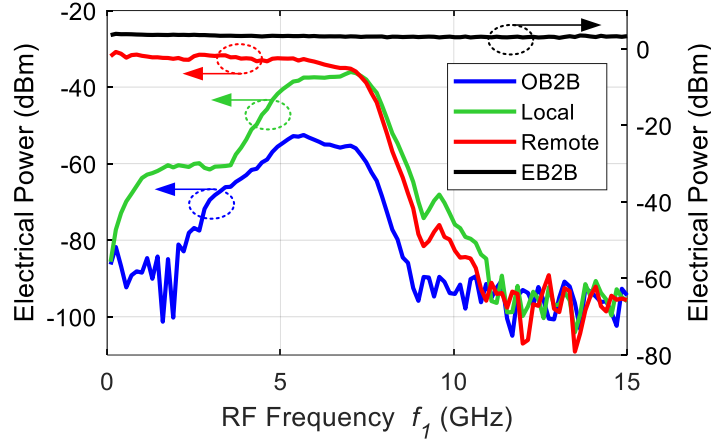


Figure 4.13. Experimental second-order IMD ($2w_{RF} - (w_2 + w_1)$) for OB2B, local and remote configuration. EB2B signal measurement is included as a reference.

4.3.2.2. Electrical spectrum measurements

In this Section, spectral measurements of recovered electrical signals after photodetection are shown in order to identify the non-linear response of the optical fronthaul link under different signal transmission schemes.

The first experiment consists of transmitting a single band QPSK signal centered at 39.9 GHz ($f_{RF} = 20$ GHz, $f_1 = 100$ MHz) with variable bandwidth under OB2B, local and remote configurations. Figure 4.14(a) and (b) shows the whole electrical spectra of 50 and 150 MHz bandwidth signal, respectively, transmitted under local configuration. Insets show the detail at baseband and mmW band where $2w$ -type harmonic distortions cannot be observed in the spectrum. Figure 4.14(c) and (d) displays the spectra obtained when signals are transmitted under remote configuration. In this case, the detail at mmW band (see right inset) shows new frequency terms appeared as a result of system IMD, which is larger for signals with higher bandwidth (i.e. 150 MHz). Note that the electrical power is similar than measured in local setup for both signals at baseband whereas it is significantly different at mmW, where remote scheme leads to higher amplitude signal compared to the local configuration as a result of the combined effect of dispersion and laser chirp as explained in Section 4.2 [129].

In the following, a two-band 50 MHz bandwidth signal at $f_1 = 1$ GHz and $f_2 = 2$ GHz is transmitted. Figure 4.15(a) and (b) show electrical spectra obtained under local and remote configurations, respectively. Corresponding insets show again the details of the spectra at BB and mmW band. As expected, the local scheme leads to similar signal spectra in both bands whereas remote scheme causes several distortion frequency tones in the mmW band.

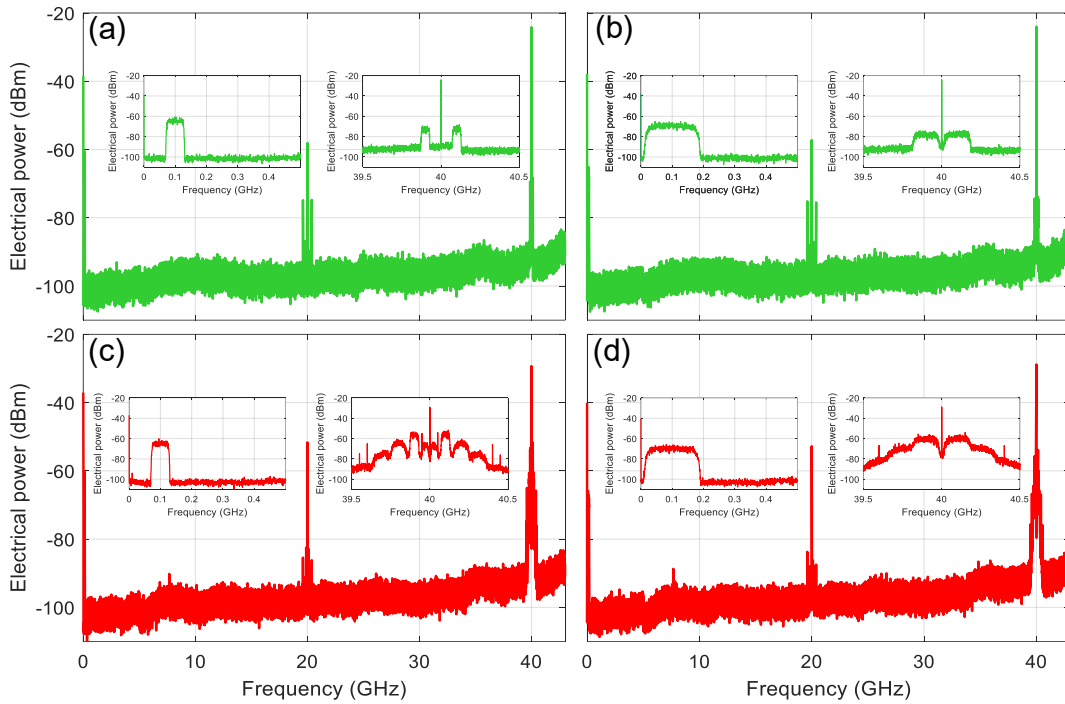


Figure 4.14. Electrical spectra of transmitted signals with different bandwidths for local configuration: (a) 50 MHz, (b) 150 MHz; and remote configuration: (c) 50 MHz and (d) 150 MHz. Insets show the detail of the spectrum at baseband (left) and mmW band (right).

Finally, a signal consisting of three bands centered at 200, 325 and 525 MHz is transmitted over 40 GHz by using the local and remote schemes. As expected, the local configuration shows three bands without any other frequency component due to the absence of system nonlinearities (see Figure 4.16(a)). However, the remote scheme leads at mmW bands to several frequency terms as shown in Figure 4.16(b). Then, measurements are repeated under both transmission schemes by switching off the lower frequency bands (Figure 4.16(c)) and (d) for local and remote setups, respectively) while the 525 MHz band remained unaffected in both schemes. In this case, the non-linear products created from the combination of different frequencies disappear since only one band is transmitted. Additionally, unlike the spectra shown in Figure 4.14(d) where HD is observed due to 150 MHz bandwidth signal centered at $f_1 = 100$ MHz, Figure 4.16(d) shows the spectrum of a 50 MHz bandwidth signal at 525 MHz, and therefore, no HD can be observed due to (2ω) -type terms.

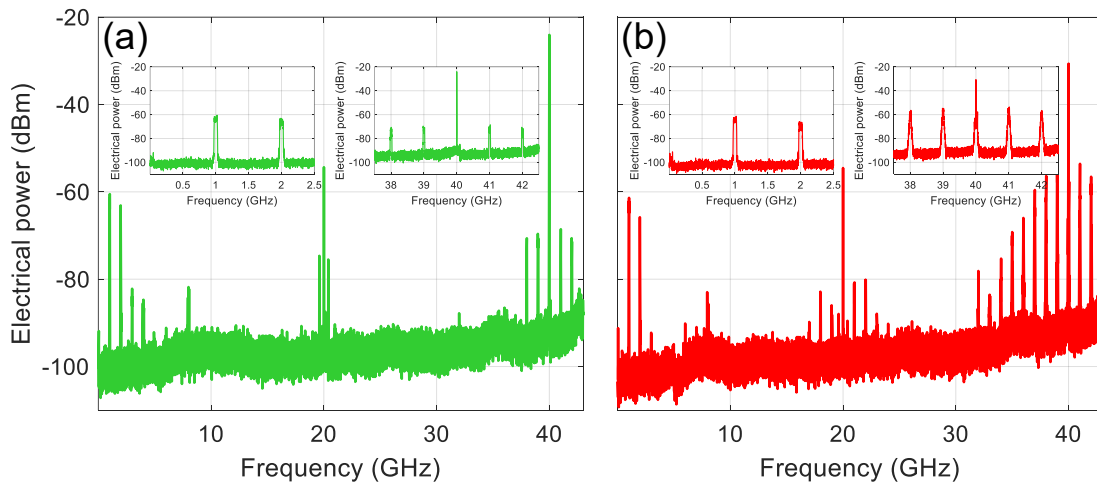


Figure 4.15. Electrical spectra of dual band transmitted signals, centered at $f_1 = 1$ GHz and $f_2 = 2$ GHz: (a) local configuration and (b) remote configuration.

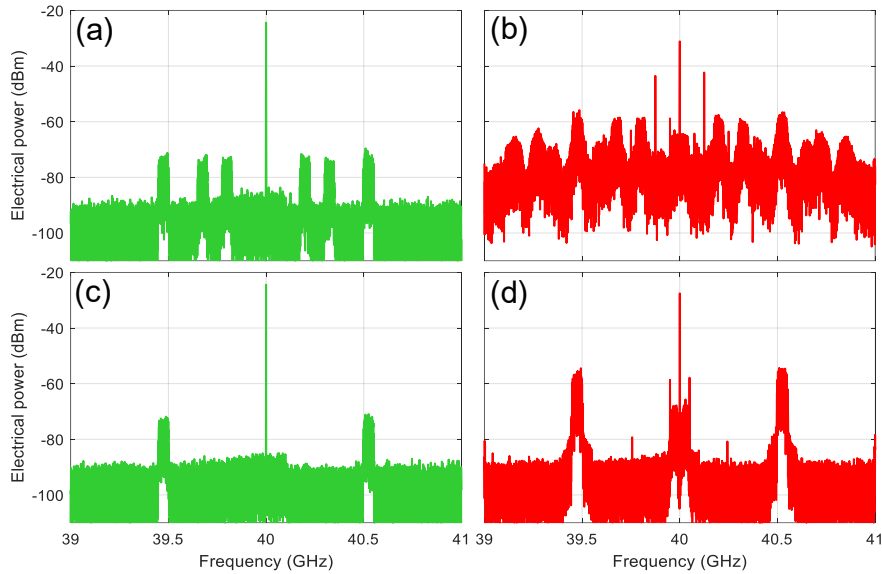


Figure 4.16. Electrical spectra measurements after photodetection of three-band signal transmission under: (a) local scheme and (b) remote scheme. Measurements shown in (c) and (d) correspond to electrical spectra measurement when only one band is transmitted under local and remote schemes, respectively.

However, the power levels are higher under remote configuration in the mmW band (Figure 4.16(a) and (b)) due to the system frequency response, and some non-linearities might be also due to power level. For the sake of verifying the reasons for them, Figure 4.17(a), (b) and (c) show OB2B, local and remote measurements under the same power level conditions. In spite of the equal power level, the non-linearities are clearly shown under remote configuration.

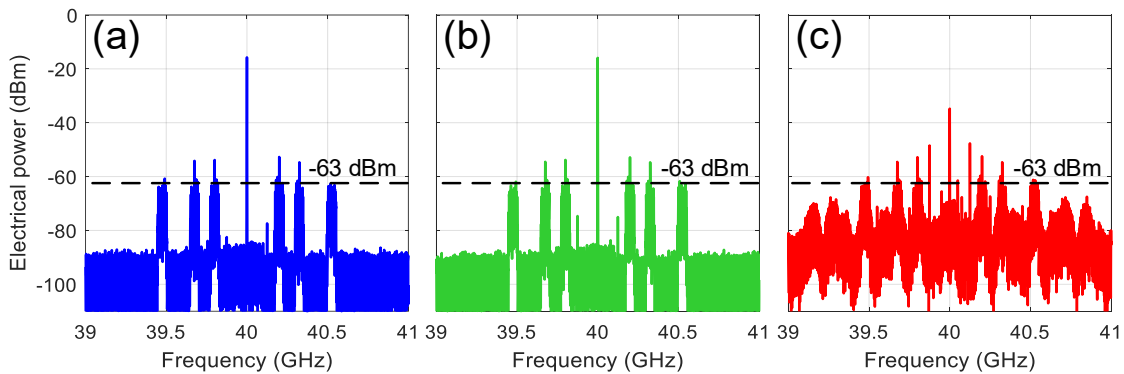


Figure 4.17. Electrical spectra of three-band transmitted signal under: (a) OB2B, (b) local and (c) remote schemes for similar electrical power level.

4.3.2.3. Transmission results

In this Section, the quality of recovered data after signal transmission under local and remote mmW signal generation schemes is evaluated with special focus on the impact of system non-linearities for different signals. The measurements are done in terms of RoP and also ReP as the integrated electrical power of the mmW band over the signal bandwidth which is provided by the vector signal analyser.

A single band QPSK signal ($f_1 = 100$ MHz) of variable bandwidth (50-150 MHz) is transmitted over $2f_{RF} = 40$ GHz. Figure 4.18(a) shows that remote configuration leads lower EVM, than local and OB2B links, as expected from [129] over the whole RoP measurement range for 50 MHz bandwidth signal. However, wider signals with 100 and 150 MHz bandwidth lead better performances just up to a certain value of RoP, i.e. below 0 dBm in our setup (Figure 4.18(b) and (c)). In these cases, remote configuration leads to EVM values which are independent from the RoP due to the impact of non-linear response which prevents to show

the EVM decrease with increasing RoP. Since this effect does not occur in local configuration (i.e. similar response to OB2B), a signal quality outperformance will be achieved under local scheme for RoP values above certain level. Note that EVM measurements in terms of ReP since the signal quality reflects the ReP actual value in all configurations and any deviation from the OB2B curve reports some degradation present in the system. Remote configuration leads to non-linearities which are responsible of the increase of EVM values with respect to OB2B in Figure 4.18(e)-f) for ReP values larger than -62 dBm. Concretely, EVM values have suffered an 18% and 22.5% deterioration with -40 dBm ReP for signals bandwidth signals of 100 and 150 MHz, respectively, with regards to EB2B signal transmission. Note that Figure 4.18(a)-(c) show a 10 dB RoP range which correspond to 20 dB ReP range so the results are equivalent in such range. Moreover, RoP curves lead to observe 15 dB difference between local and remote configurations, which is due to the intrinsic gain obtained in the remote configuration arisen from the combination of fiber dispersion and chirp [85].

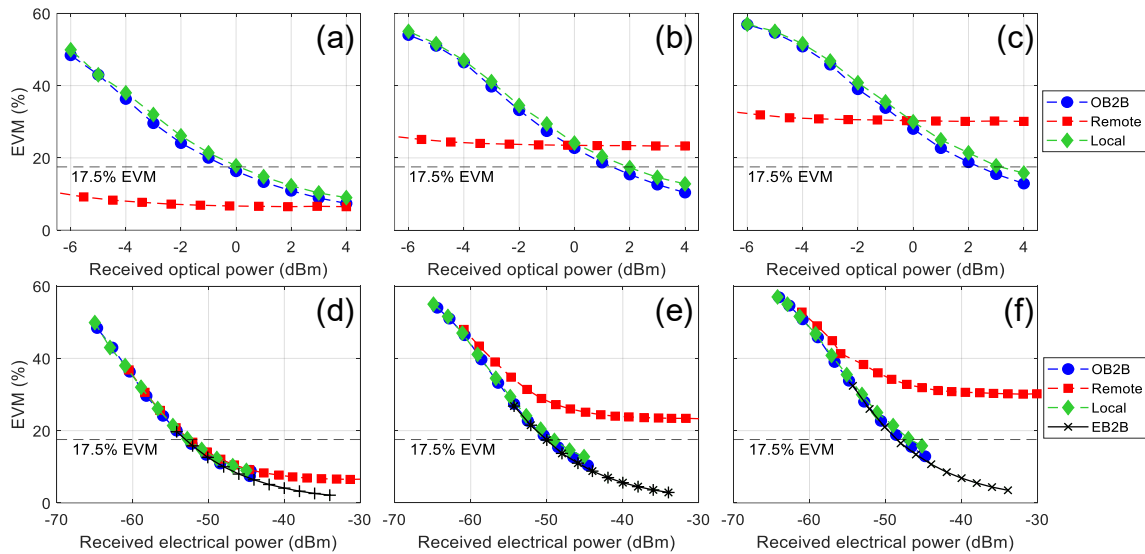


Figure 4.18. EVM measurements of different QPSK signal bandwidth centered at 39.9 GHz ($f_1 = 100$ MHz) vs RoP (top) and ReP (bottom): (a) and (d) 50 MHz; (b) and (e) 100 MHz; (c) and (f) 150 MHz bandwidth.

Figure 4.19 shows the measured constellations with 3 dBm RoP. A signal quality improvement is observed in remote setup compared to local on in 50 MHz bandwidth signal due to the aforementioned higher system response. However, a clear impact of IMD in remote scheme is observed compared to local one in 150 MHz bandwidth QPSK signals accordingly to previous discussion.

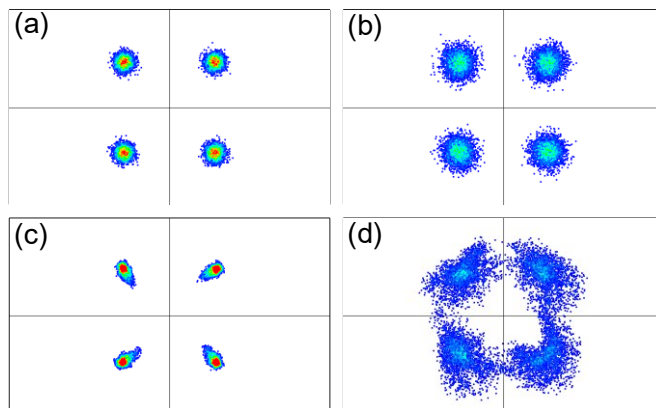


Figure 4.19. In-band recovered QPSK signal constellations of $f_1 = 100$ MHz with RoP = 3 dBm at 39.9 GHz under local (top) and remote (bottom): (a) and (c) 50 MHz; (b) and (d) 150 MHz.

In the following, a 50 MHz bandwidth dual-band ($f_1 = 1$ GHz and $f_2 = 2$ GHz) QPSK data is transmitted to evaluate the EVM performance at $f_2 = 2f_1$ under OB2B, local and remote configurations. In this case, the out of band non-linearity due to the contribution ($2w_1$)-type HD is studied. Figure 4.20 shows the EVM measurement vs RoP (top) and ReP (bottom) for OB2B, local and remote configurations.

As shown in Figure 4.20(a), measurements under remote mmW signal generation scheme lead to a high EVM constant value (38%) over the measured RoP range due to second order HD penalty whereas local measurements of the second band are similar to OB2B.

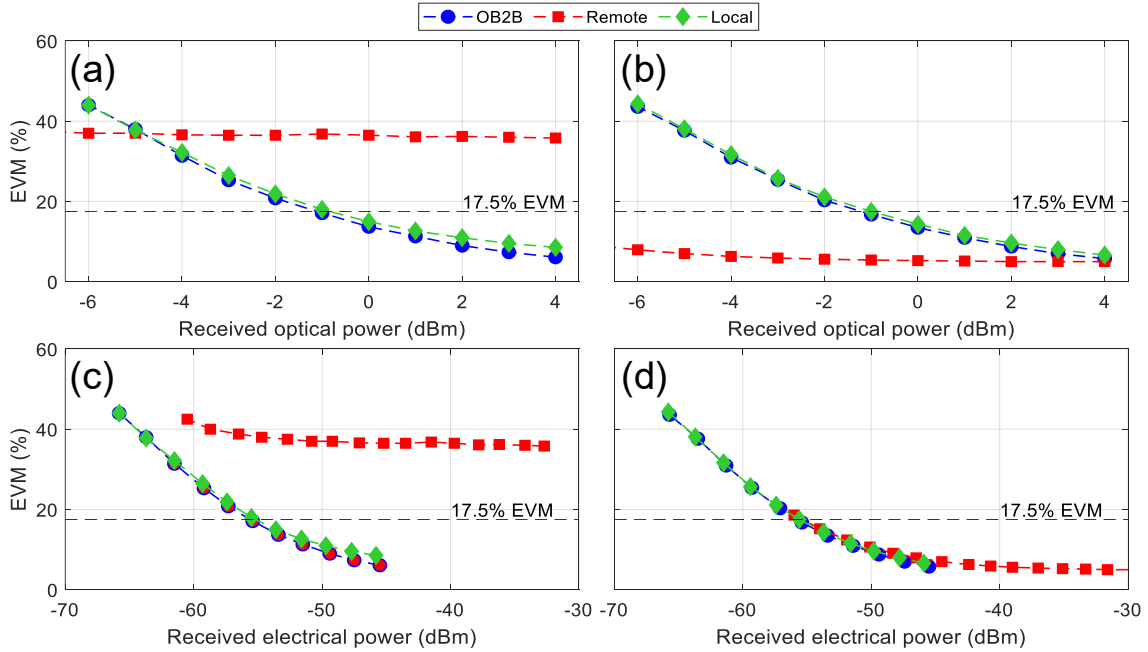


Figure 4.20. OB2B, local and remote scheme measurements of EVM for evaluating out of band intermodulation at the frequency $2f_{RF} - f_2$ vs RoP (top) and ReP (bottom). (a) and (c) corresponds to a dual-band transmission ($f_1 = 1$ GHz and $f_2 = 2$ GHz); (b) and (d) are measured when f_2 is only transmitted.

This is confirmed in Figure 4.20(b) when one band is switched off and those high EVM values are significantly reduced (below 10%) due to the disappearance of ($2w_1$)-type HD contribution. When only one band is transmitted, this band in the remote scheme outperforms the local scheme due to the combined effect of laser chirp and fiber dispersion [129], i.e. high electrical power, as previously mentioned.

EVM measurements vs ReP allow to identify system degradations in addition to the frequency system response, so, as expected, OB2B and local scheme measurements are identical whereas remote scheme shows high EVM values over the threshold (see Appendix A) over the entire ReP measurement range due to IMD penalty, i.e. 38% EVM at -40 dBm ReP. However, when f_1 band is switched off, EVM is again reduced to 6% due to the fact that this penalty mainly disappears, as depicted in Figure 4.20(d).

Figure 4.21(a) and (b) show the recovered signal constellations at f_2 over mmW band in remote scheme when both bands and only f_2 are transmitted for -2.48 dBm RoP, respectively. As can be observed, there is a strong signal distortion of the transmitted data due to second order HD in remote scheme in the former case and therefore, signal transmission cannot be held (Figure 4.21(a)) while the signal quality is good (Figure 4.21(b)) when HD is suppressed.

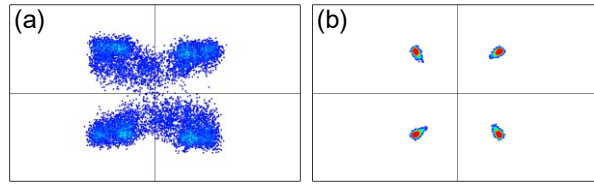


Figure 4.21. QPSK signal constellations for the second band located at $f_2 = 2$ GHz over remote scheme when (a) both bands and (b) only one are transmitted (-2.48 dBm RoP).

In order to evaluate the IMD term corresponding to $(w_2 - w_1)$ term, two RF subcarriers centered at the frequencies $f_1 = 1$ GHz and $f_2 = 2$ GHz with a 50 MHz-bandwidth QPSK data are employed.

Figure 4.22 shows the evaluation of the EVM performance of data carried by both frequencies under OB2B, local and remote setups and also by the f_1 when only this one is transmitted. As shown in Figure 4.22(a), measurements under remote mmW signal generation scheme lead to high EVM constant values over the measured RoP range due to IMD penalty whereas local measurements of the second band are similar to OB2B. Note that data carried over $f_1 = 1$ GHz shows worse quality compared to carrier with $f_2 = 2$ GHz (i.e. higher EVM) as expected from Figure 4.11 and Figure 4.12 since second order HD term affecting f_2 is lower than IMD term affecting f_1 , respectively.

Again, EVM measurements vs ReP are done to identify system degradations, and, as expected, OB2B and local scheme measurements are identical whereas remote scheme shows high EVM values over the threshold over the entire ReP measurement range (52% for f_1 at -40 dBm ReP). Note that measured EVM values are different for both bands due to the reasons explained above. However, when the second band is switched off, $(w_2 - w_1)$ -type IMD does not occur, EVM of f_1 signal drops to 12% at -40 dBm ReP and only slight differences are measured due to the lack of perfect power adjustment in the experimental setup.

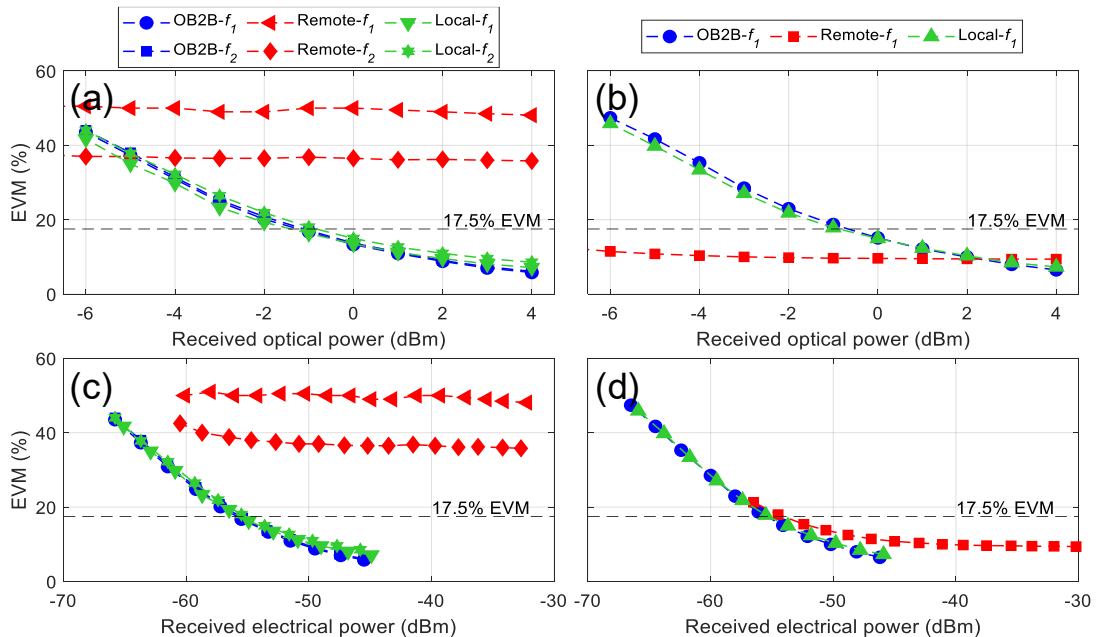


Figure 4.22. OB2B, local and remote scheme measurements of EVM vs RoP (top) and ReP (bottom) carried by $2f_{RF-f_{1,2}}$: (a), (c) dual-band transmission ($f_1 = 1$ GHz and $f_2 = 2$ GHz); (b), (d) only $f_1 = 1$ GHz is transmitted.

Figure 4.23(a) and (b) show the recovered signal constellations at $f_1 = 1$ GHz over remote scheme when both bands and only one are transmitted for -2.48 dBm RoP, respectively. As can be observed, there is a strong signal distortion of the transmitted data due to IMD in remote scheme and therefore signal transmission cannot be held in the former case while the signal quality is good when IMD due to $(w_2 - w_1)$ -term is cancelled.

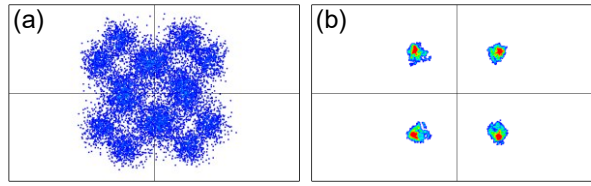


Figure 4.23. QPSK signal constellations of $f_1 = 1$ GHz over remote scheme when (a) f_1 and f_2 (b) only f_1 is transmitted (-2.48 dBm RoP).

Finally, a three-band signal ($f_1 = 200$ MHz, $f_2 = 325$ MHz and $f_3 = 525$ MHz) 50 MHz bandwidth QPSK data is transmitted over 40 GHz to evaluate the impact of (w_2+w_1) -type IMD term. Figure 4.24 plots the EVM performance, which is studied in terms of ReP under OB2B, local and remote configurations of f_3 signal when the three bands are transmitted and when only the third one is transmitted. In this case, Figure 4.24(a) and (c) correspond with the EVM impact of $2w_1$ and $2w_2$, HD, respectively, whereas Figure 4.24(b) corresponds to the (w_2+w_1) -type IMD term.

EVM vs ReP measurements again provide information of signal distortions independently on the frequency system response. Firstly, the EVM values for OB2B and local scenarios are similar for all RF carriers. Moreover, significant distortion under remote configuration is observed when three bands are transmitted showing similar values when $w_3 = 2w_1$ or $w_3 = 2w_2$ but higher in the second scenario with $w_3 = w_1 + w_2$.

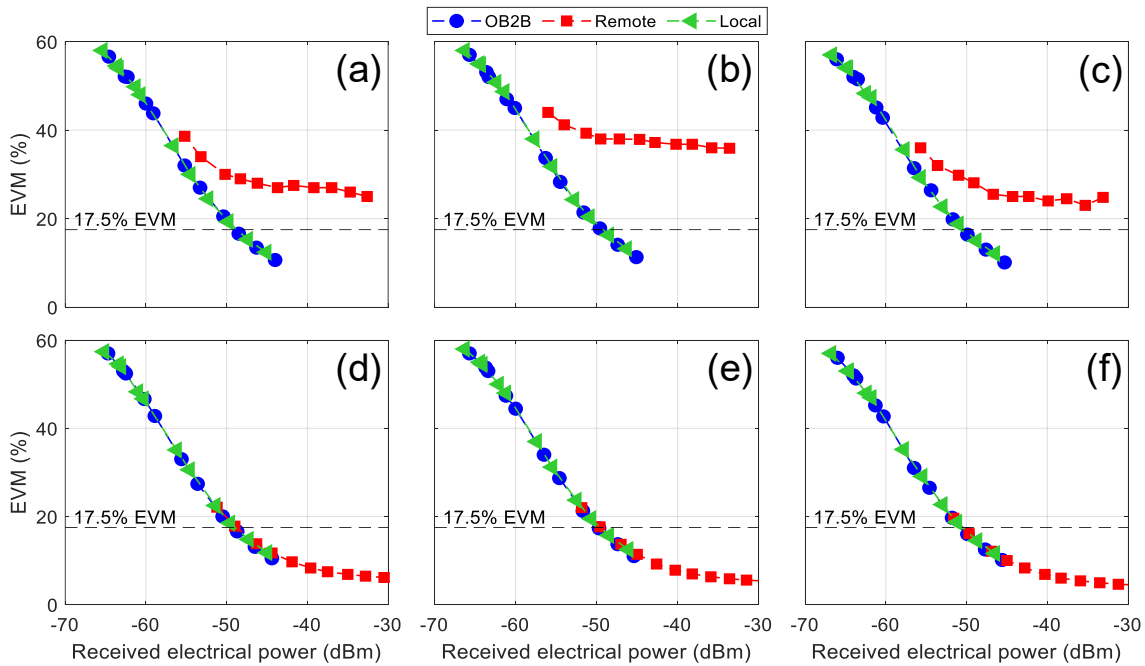


Figure 4.24. EVM for OB2B, local and remote configurations of data carried by $2f_{RF}-f_3$ vs ReP when three bands are transmitted (top) and only f_3 is transmitted (bottom). Frequency bands are $f_1 = 200$ MHz, $f_2 = 325$ MHz and different f_3 as: (a), (d) $f_3 = 400$ MHz; (b), (e) $f_3 = 525$ MHz and (c), (f) $f_3 = 650$ MHz.

According to the results obtained for the frequency response in Figure 4.13, the distortion level for low frequency (< 3.5 GHz) is similar for OB2B and local configuration, and therefore, the EVM performance is very similar while measurements obtained under remote scheme show different behaviour. The EVM is approximately constant for ReP values larger than -50 dBm (38%) (see Figure 4.24(b)) which is higher than the EVM value of 29% obtained in Figure 4.24(a) and (c). The distortion level difference is close to 10 dB for remote configuration comparing the amplitude response. Therefore, it is expected that the impact of second-order IMD is higher than HD contribution.

Constellations under local and remote setup for the scenario with $w_3 = w_1 + w_2$ are shown in Figure 4.25 to show the inability to transmit multiband signals due to IMD under remote

configuration. Clear constellations with reduced EVM values are obtained in case of single band transmission for both setups (see Figure 4.25 (b) and (d)). On the contrary, multiband transmission does not lead to any significant impact under local configuration.

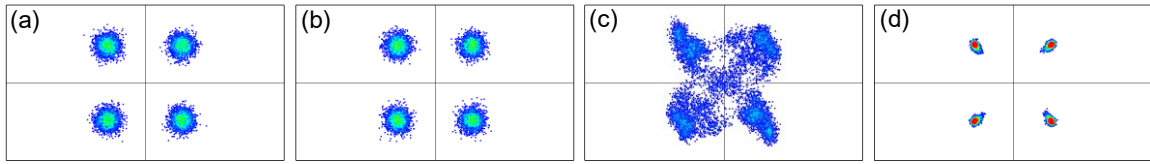


Figure 4.25. Signal constellations of f_3 signal under local (a, b) and remote (c, d) schemes: (a), (c) three bands transmission and (b), (d) single band is transmitted.

4.4. Usability of an optical fronthaul operating at 40 GHz

In this Section, the bandwidth constraints of a cost effective 5G mobile fronthaul using a DML for data modulation and a MZM-based optical double sideband with carrier suppression scheme for remote optical mmW signal generation are numerically and experimentally evaluated [133].

4.4.1. Simulations

The schematic of the fronthaul link employed is similar to the one depicted in Figure 4.4(b), which corresponds to remote architecture for photonic mmW signal generation, but Figure 4.26 shows the diagram layout employed in simulations where the insets show the electrical and optical spectra at different points of the layout. Simulations are carried out by using co-simulation MatLab and Optisystem software.

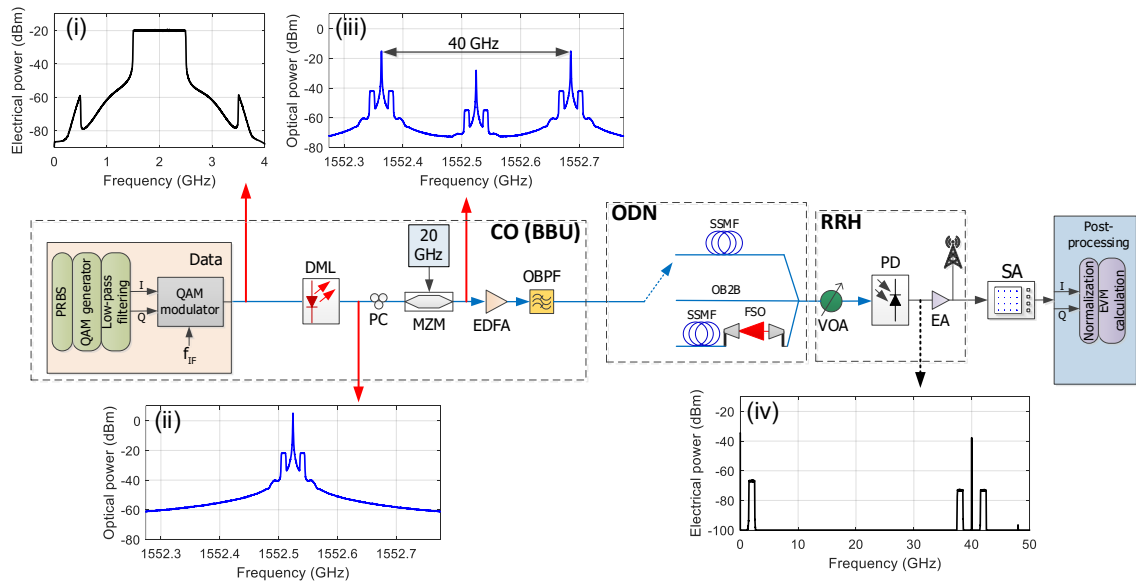


Figure 4.26. Diagram layout of the M-QAM DML and CS-MZM for mmW up-conversion [133]. Insets: (i) and (iv) electrical spectra of the modulation data and after opto-electronic conversion (RBW = 10 MHz) and, (ii) and (iii) optical spectra at the DML and MZM output (RBW = 0.001 nm)

A DFB laser emits an optical carrier which is directly modulated by an electrical M-QAM data signal of Δf bandwidth combined with an IF signal at 2 GHz. The inset (i) of Figure 4.26 shows the electrical spectra of 1 GHz bandwidth modulating signal. The signal is then launched into an MZM, which is biased at the null transmission point and driven by a single-tone RF signal at 20 GHz, which is the half value of the desired mmW frequency at the RRH. Inset (ii) of Figure 4.26 shows the optical spectra of the directly modulated signal and inset (iii) displays the modulated signal at the output of the external modulator exhibiting 13.1 dB of carrier suppression ratio. Therefore, CS modulation helps to reduce the effect of chromatic dispersion.

However, since the modulation scheme is strongly non-linear, and additional distortion terms contribute to signal degradation unless moderate bandwidth and low-level amplitude are employed to guarantee the system feasibility. Optical amplification to compensate losses and filtering to reduce the amplified ASE noise are held before detection. The OB2B characterization is obtained by a direct connection to the PD through a variable optical attenuator (VOA). Inset (iv) of Figure 4.26 shows the spectrum of the recovered signal after photodetection, where mmW signal with central frequency at 40 GHz is generated by beating both optical sidebands at 20 GHz, and the data bands appear at 38 and 42 GHz. Afterwards, an optical fiber link is included before the VOA to implement the penalty induced by 10 km SSMF, which is typical fronthaul link distance. The system parameters employed in the simulations are detailed in Table 4.3.

Table 4.3. Simulation parameters.

	Parameter	Value
Laser	Wavelength	1552.52 nm
	Output power	5.45 dBm
	RIN	-155 dB/Hz
	Bandwidth	$5 \log_2(M) \sqrt{3} \Delta f$
	Linewidth	10 MHz
	Linewidth enhancement factor	1
	Chirp	Null: 0 GHz/mW Low: 4 GHz/mW Moderate: 10 GHz/mW High: 15 GHz/mW
Modulation data	Modulation format	4-, 16-, 64-QAM
	Electrical power	0 dBm
RF signal	Frequency	20 GHz
	Electrical power	18 dBm
MZM	Switching bias voltage	4 V
	Switch RF voltage	4 V
	Insertion loss	3 dB
	Bias voltage	4 V
EDFA	Gain	4 dB
	Noise figure	2 dB
OBPF	Wavelength	1552.52 nm
	Bandwidth	0.64 nm
	Band rejection	60 dB
	Insertion loss	13 dB
Fiber	Length	10, 20 km
	Attenuation	0.2 dB/km
	Chromatic dispersion	16.75 ps/nm·km
PD	Responsivity	0.6 A/W
	Dark current	5 nA
	Thermal noise	$50e-12 \text{ pA/Hz}^{-1/2}$
EA	Gain	35 dB

Note that althroughout this Section, the system performance in terms of EVM is evaluated by decoding the data carried by the baseband instead the mmW band. The reasons for that are the limitations on the equipment, i.e. digital phosphor oscilloscope (DPO) (Tektronix DPO72004C) with 20 GHz bandwidth, we had at the first stages of the research. However, this is a reasonable approach if we observe Figure 4.3(e) and (f), i.e. frequency response of remote setup, which show similar response at BB and mmW frequency, i.e. 2 GHz in both bands. It is worth to remind that remote configuration in the mmW band exhibits 15 dB signal gain with respect to OB2B configuration.

4.4.1.1. Impact of bandwidth

The performance the transmission system is evaluated by measuring EVM and threshold levels (see Appendix A) are set as those corresponding to an Orthogonal Frequency Division Multiplexed (OFDM) signal [27]. Figure 4.27 plots the obtained EVM when OB2B is simulated for 4-, 16- and 64-QAM signals with 1, 1.5 and 3 GHz bandwidths.

The obtained EVM for a 4-QAM signal is depicted in Figure 4.27(a). At 17.5% EVM threshold level (Appendix A), a 0.7 dB increase is requested in the minimum RoP when the bandwidth is extended from 1 to 1.5 GHz, whereas 2.7 dB more power is needed when the signal bandwidth is increased up to 3 GHz. Insets (a.1), (a.2) and (a.4) of Figure 4.27(a) show the constellation of the signal at the RoP of -4 dBm with corresponding EVM values of 4.4%, 5.1% and 9.6% corresponding to 1, 1.5 and 3 GHz bandwidth, respectively. Note that the degradation in the OB2B measurement is significantly larger for 3 GHz bandwidth signal due to the DML non-linear response, which causes IMD [134].

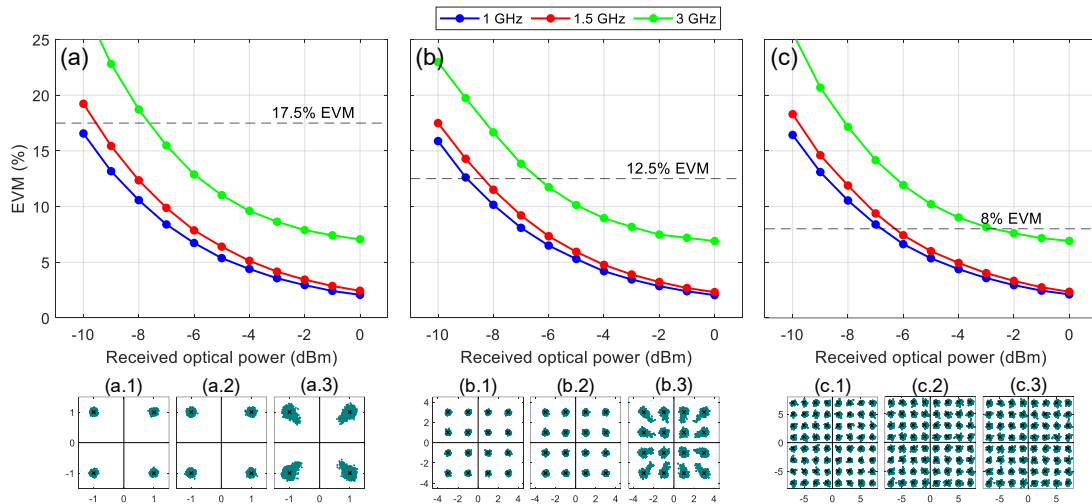


Figure 4.27. Simulated OB2B EVM performance for different signal bandwidth: (a) 4-QAM, (b) 16-QAM, and (c) 64-QAM. Insets show the obtained constellations at RoP of -4 dBm for 1, 1.5 and 3 GHz, respectively.

Figure 4.27(b) displays the simulated results with EVM for 16-QAM. As it can be seen, lower data bandwidth leads the lowest EVM meanwhile higher data bandwidth experiences stronger degradation. Compared to 1 GHz bandwidth, 0.6 and 2.6 dB higher optical power (i.e. power penalty) is required for 1.5 and 3 GHz bandwidths, respectively, in order to obtain similar performance. Constellations, obtained with -4 dBm of optical power, are shown in insets (b.1), (b.2) and (b.3) of Figure 4.27(b), with EVM of 4.2%, 4.8% and 9.0%, respectively.

The 64-QAM EVM simulation results are shown in Figure 4.27(c). Larger bandwidths lead to higher EVM degradation also according to the channel transfer function depicted in Figure 4.3. The optical power difference for 1.5 and 3 GHz respect to the 1 GHz signal bandwidth is 0.5 and 4 dB, respectively. However, the EVM performance keeps below 8% for optical received power higher than -2.7 dBm. The constellations shown in insets (c.1), (c.2) and (c.3) of Figure 4.27(c) correspond to an EVM of 4.4%, 4.9% and 9%, respectively.

4.4.1.2. Impact of fiber dispersion

In the next, the impact of chromatic dispersion using a non-chirp DML in 4-, 16- and 64-QAM signal with 1 GHz bandwidth is simulated and shown in Figure 4.29.

The EVM of 4-QAM signal for OB2B, 10 and 20 km SSMF links is depicted in Figure 4.28(a). The power penalties at EVM threshold (17.5%) are 0.4 and 1.4 dB for 10 and 20 km, respectively. Clear constellation at -4 dBm RoP after 10 km transmission, which are similar to corresponding OB2B, is shown in inset (a.1) of Figure 4.29(a). However, 20 km transmission exhibits spread outer symbols (see inset (a.2) of Figure 4.29(a)).

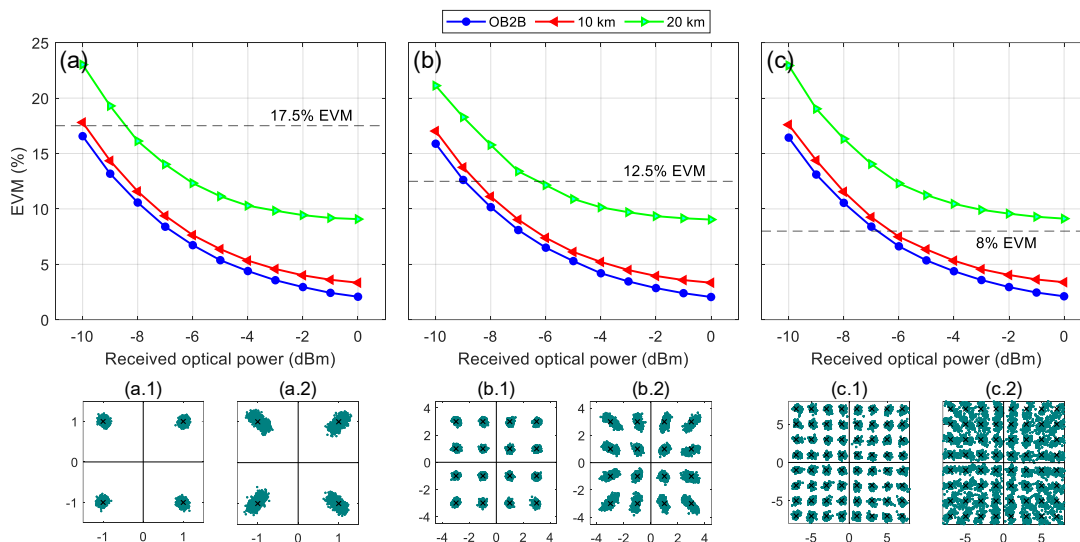


Figure 4.28. Simulated EVM performance after OB2B, 10 and 20 km SSMF link with 1 GHz signal bandwidth for different modulations: (a) 4-QAM, (b) 16-QAM and (c) 64-QAM. Insets show constellation with 4 dBm RoP for 10 and 20 km fiber transmission.

Figure 4.28(b) depicts the simulated the same EVM performance for 16-QAM. In this case, the power penalty at EVM threshold (12.5%) is 1.4 and 3.7 dB for 10 and 20 km, respectively. Insets (b.1) and (b.2) of Figure 4.29(b) shown constellations using 10 and 20 km fiber. Clear constellation can be observed when signal is transmitted over 10 km fiber, whereas large spread symbol is observed when 20 km fiber transmission is employed.

Figure 4.28(c) shows the EVM performance for 64-QAM format, with a power penalty of 0.5 dB for 10 km SSMF at 8% EVM limit. However, 20 km power penalty cannot be measured since the EVM does not meet the 8% EVM limit requirement in the RoP range under study. As expected from previous results, a clear constellation of 10 km fiber transmission is observed ((c.1) of Figure 4.28(c)). However, the degradation of the EVM is significant, as shown in inset (c.2) of Figure 4.28(c) which correspond to 64-QAM signal propagation over 20 km fiber. Non-linear distortion is clearly observed due to the interplay between the DML non-linear response and the fiber chromatic dispersion [134].

4.4.1.3. Impact of laser chirp

In the following, according to the previous simulation results, chirp is also considered with 1 GHz bandwidth signal transmission over 10 km SSMF link to evaluate the overall impact of the interplay of chirp and dispersion on the quality of the received signal. Different chirp values are employed in the simulated schemes based on commercial DMLs [116], as detailed in Figure 4.26, where $\alpha = 1$ is employed for the calculations with non-zero chirp. The simulation results of 4-, 16- and 64-QAM signal are shown in Figure 4.29.

Figure 4.29(a) shows there is no power penalty at 17.5% EVM level when a DML with low chirp characteristic (4 GHz/mW) is modulated by the 4-QAM signal. However, moderate (10 GHz/mW) and high (15 GHz/mW) chirp values lead to penalties of 0.4 and 1 dB, respectively. Insets (a.1), (a.2) and (a.3) of Figure 4.29(a) show the constellations of the recovered signals

with -4 dBm of RoP, where obtained EVMs are 5.5%, 8.1% and 11.1% after 10 km fiber transmission with low, moderate and highly chirped signals, respectively.

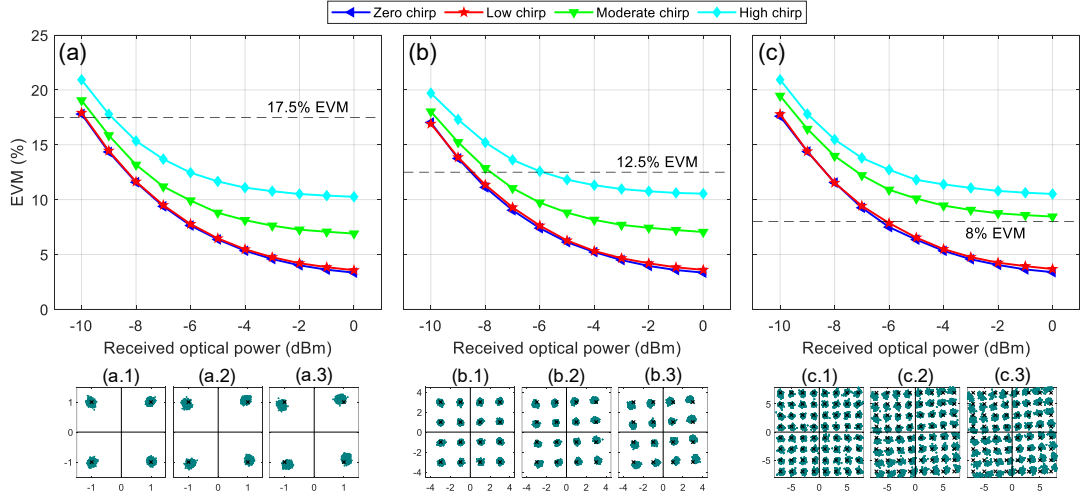


Figure 4.29. Simulated EVM performance when DML is employed with null, low, moderate and high chirp and 1 GHz signal bandwidth is transmitted over 10 km SSMF: (a) 4-QAM, (b) 16-QAM and (c) 64-QAM. Insets show constellations for low, moderate and high chirp value, at RoP of -3 dBm.

The impact of the chirp when the 16-QAM signal with 1 GHz bandwidth is transmitted along 10 km SSMF is shown in Figure 4.29(b). Similarly to the previous case, there is a power penalty below 0.1 dB when low chirp DML is employed signal at threshold EVM level. However, the required RoP is increased by 0.8 and 2.6 dB for moderate and high chirp parameters, respectively. Constellations at -3 dBm RoP are shown in insets (b.1), (b.2) and (b.3) of Figure 4.29(b).

Figure 4.29(c) depicts the simulated EVM for 64-QAM signals. As expected from the previous results, there is no difference between non- and low chirped signals at 8% limit. However, in this case, the obtained EVM values are larger than 8% threshold limit when moderate and high chirp lasers are applied. Constellations in insets (c.1), (c.2) and (c.3) of Figure 4.29(c) show the significant degradation of the received signal caused by the interplay of fiber dispersion and chirp, resulting in rotation with respect to the corresponding constellations obtained in Figure 4.28.

4.4.2. Experimental system capability

The experimental system emulates the optical transceiver at the BBU in the CO, as depicted in Figure 4.26, which consists of a low cost DML and an external MZM where the optical carrier modulated by data is up-converted before signal transmission over a 10 km SSMF link, i.e. remote configuration as explained in Section 4.2. An extended transmission setup based on a hybrid link including 1.5 m FSO segment is also considered to test the optical wireless performance for the sake of increasing the network flexibility [135].

In this experiment, the DFB laser emits an optical signal at 1550 nm with 5.7 dBm optical power which is directly modulated by a M-QAM signal at IF of 2 GHz generated by the DG (Tektronix AWG7122C). Note that the typical laser modulation response exhibits a 3 dB bandwidth of 6.2 GHz. After adjusting the polarization state of the optical signal by a PC, the modulated optical signal is launched into the MZM (Photline MX-LN-40), which is driven by a 20 GHz and 18 dBm signal clock generated by a SG (Agilent 8267C) and biased at null transmission point (V_{π}), i.e. 1.3 V, to obtain the optical carrier suppression. An EDFA (Amonics AEDFA-23-B-FA) with 13 dBm constant output power is employed to compensate for the optical losses and the ASE noise is filtered out by an OBPf (Alnair BVF-100) with $\Delta\lambda = 2$ nm, similarly to previously described experimental setups.

In the experiment, the OB2B signal is first measured, then signal is transmitted through an optical fiber link composed of 10 km SSMF fiber and finally through a full hybrid link with 10 km

of SSMF and 1.5 m long FSO channel which emulates the ODN between the BBU and the RRH. The FSO channel consists of GRIN lenses (Thorlabs 50-1550A-APC) already described in previous Sections. Note that the measured FSO losses are 6.5 dB and therefore another EDFA (Amonics AEDFA-27-B-FA) with 13 dBm constant output power and OBPF (Waveshaper 4000S) with $\Delta\lambda = 2$ nm is needed.

At the RRH side, the optical signal is launched into the PD (u2t BPDV2020R), where 40 GHz electrical signal is generated by beating the first-order sidebands at the PD. Finally, electrical signal is amplified by an EA (SHF Communication Technologies AG SHF-810) with 29 dB gain, and analysed by a RFSA.

In the following, the EVM performance of the proposed system for a wide range of RoP from -3 to 6 dBm is investigated. This measurement is essential in order to determine the system dynamic range and an appropriate RoP level considering the mmW link for practical implementation. More concretely, according to Figure 4.30, there is a 5 dB penalty due to 10 km SSMF at the working frequency, which can be demonstrated as reasonable for the base station since the adequate RoP regime prevents from non-linear limited region of the EA. The system performance is evaluated by using 4-,16- and 64-QAM signals with bandwidth from 50 MHz up to 1000 MHz at 40 GHz carrier frequency and 2 GHz IF.

Figure 4.30 shows the measured EVM of the recovered signals when 4-QAM format is employed. Figure 4.30(a) shows the OB2B where, as expected, larger bandwidths lead to higher EVM values in fiber and hybrid links (Figure 4.30(b) and (c), respectively). The insets (a.1), (b.1) and (c.1) show very good agreement with theoretical simulations for 1 GHz bandwidth and 3 dBm RoP. However, the reliable transmission is achieved for the 4-QAM under 17.5% EVM threshold limit (see Appendix A). The power penalty due to 10 km fiber link is below 0.6 dB for bandwidths 100 and 200 MHz, i.e. 0.3 and 0.6 dB, respectively, and it increases up to 0.8 dB for 1000 MHz. The standard EVM threshold level is fulfilled with -0.3 and 1.5 dBm optical power after SSMF transmission for 500 and 1000 MHz bandwidth, respectively. EVM measurements also show no significant penalties introduced by the hybrid link (Figure 4.30(c)). Insets in Figure 4.30 show the constellations of received signals with 3 dBm RoP where degradation due to fiber link is observed to be almost negligible. Indeed, insets (a.3), (b.3) and (c.3), correspond to larger bandwidth and thus show larger degradation, however EVM values are kept below the standard EVM limit for all signals having a RoP at least of 2 dBm.

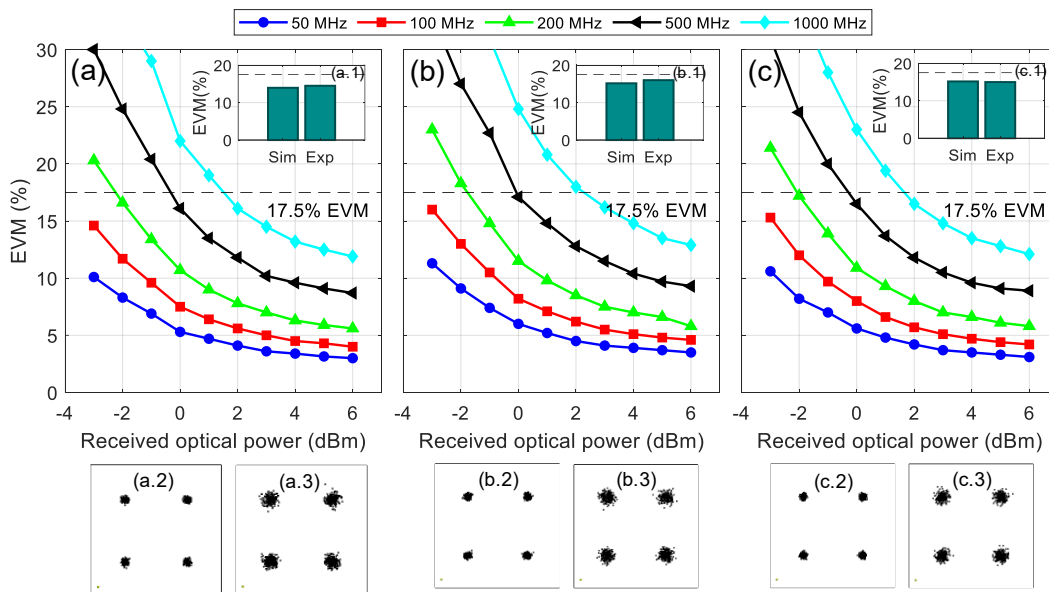


Figure 4.30. Measured EVM of 4-QAM for different signal bandwidths: (a) OB2B, (b) SSMF and (c) Hybrid links. Insets (a.1), (b.1) and (c.1) show the comparison between simulation and experimental results for 1 GHz and 3 dBm RoP. Constellations for 3 dBm RoP: (a.2), (b.2) and (c.2) with 100 MHz bandwidth, and (a.3), (b.3) and (c.3) with 500 MHz bandwidth.

The 16-QAM signals with 50 to 500 MHz bandwidth are also transmitted in our experimental setup and measured EVM values are shown in Figure 4.31. For OB2B, shown in Figure 4.31(a), a RoP of -3 dBm for 50 MHz is required to satisfy the 12.5% EVM meanwhile the optical power is increased up to 3 dBm for 500 MHz bandwidth. The penalty due to the fiber dispersion increases with the bandwidth (Figure 4.31(b)) from 0.5 dB for 50 MHz to 1 dB for 500 MHz. Transmission over the hybrid link do not lead to additional penalties, as shown in Figure 4.31(b). The constellations of 100 MHz bandwidth with 6 dBm RoP (insets (a.1), (b.1) and (c.1)) show low degradation due to fiber transmission meanwhile 500 MHz bandwidth (insets (a.2), (b.2) and (c.2)) experience to higher degradation. However, a successful signal transmission has been demonstrated in all cases.

Figure 4.32 shows the EVM results when 64-QAM signals with different bandwidths are transmitted. OB2B measurements are shown in Figure 4.32(a) and the EVM is kept below 8% when RoP is higher than -1.5, 0.5 and 2.9 dBm for 50, 100 and 200 MHz, respectively. The power penalty due to the SSMF (Figure 4.32(b)) is 0.3, 0.6 and 1.1 dB for 50, 100 and 200 MHz, respectively. As expected from previous results, there is no additional significant penalty due to the FSO link. Again, constellations of 50 MHz (insets (a.1), (b.1) and (c.1)) exhibit lower degradation than the constellation of 200 MHz for all links (insets (a.2), (b.2) and (c.2)), nevertheless the EVM lower than 8% for 64-QAM and 200 MHz bandwidth has been achieved.

According to the experimental measurements, Figure 4.33 illustrates the bit rate in terms of the minimum RoP required to satisfy EVM below the 3GPP limits for 4-, 16- and 64-QAM, respectively, for different data bandwidth. Note that the displayed throughput results correspond to bandwidth from 50 to 1000 MHz for 4-QAM, 50 to 500 MHz for 16-QAM and 50 to 200 MHz for 64-QAM. As expected, 4-QAM signals support larger bandwidth than 16- and 64-QAM signals. The minimum RoP for 4-QAM providing maximal bit rate, i.e. 2 Gbit/s at 1000 MHz bandwidth, is 1.8 dBm meanwhile 4 dBm is needed for 2Gbit/s (500 MHz bandwidth) and 1.2 Gbit/s (200 MHz bandwidth) under 16- and 64-QAM modulation formats, respectively. In other words, to achieve e.g. 2 Gbit/s throughput, it is possible to employ either 4-QAM with 1000 MHz bandwidth or 16-QAM with 500 MHz bandwidth, although 2.2 dB higher RoP is required in the latter case.

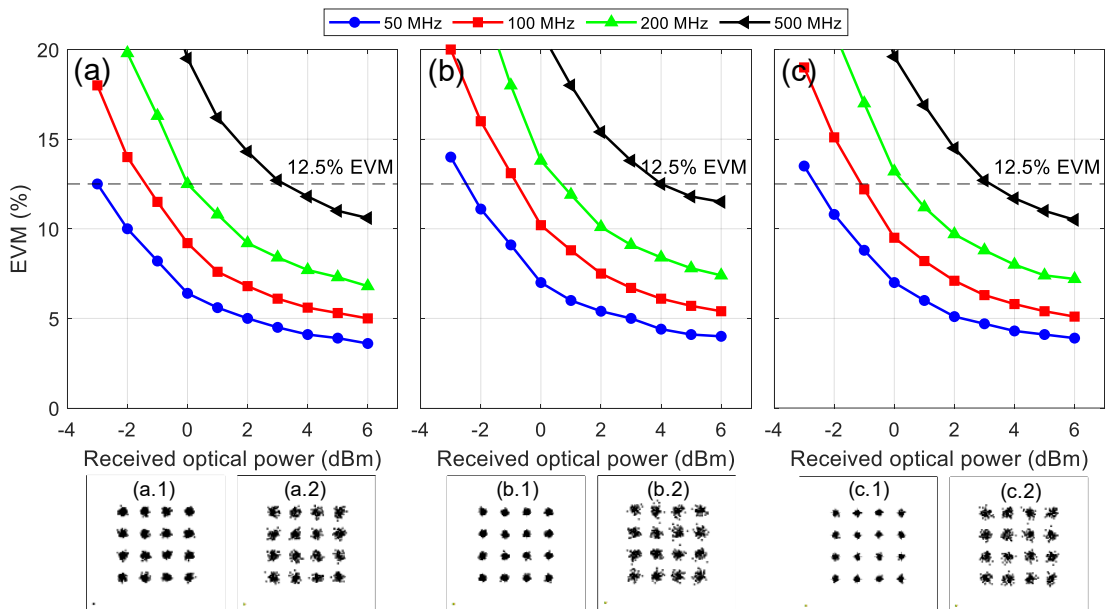


Figure 4.31. Measured EVM of 16-QAM for different signal bandwidths: (a) OB2B, (b) SSMF and (c) hybrid links. Insets show the constellations when 6 dBm RoP.

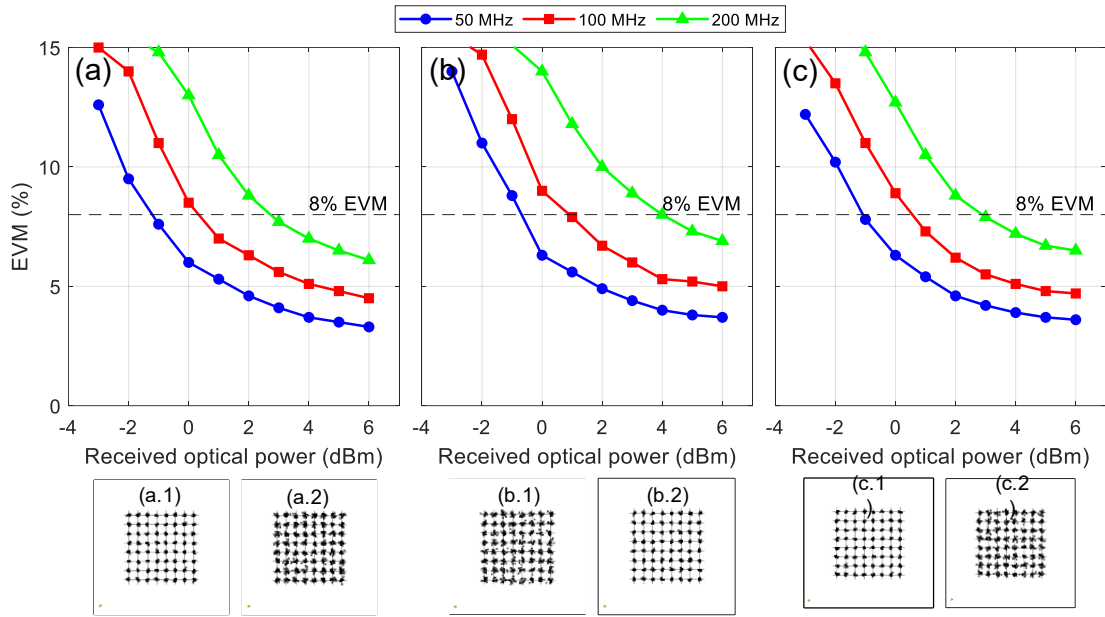


Figure 4.32. Measured EVM of 64-QAM for different signal bandwidths: (a) OB2B, (b) SSMF and (c) hybrid links. Insets show the constellations when 6 dBm RoP.

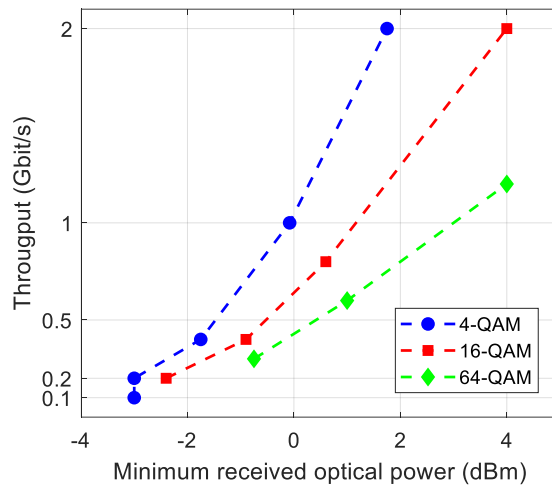


Figure 4.33. Data throughput obtained from bandwidth results in Figure 4.30, Figure 4.31 and Figure 4.32 vs minimum RoP for 10 km SSMF link at EVM limit.

4.4.3. Multiband measurements

This Section proposes to fully exploit the available bandwidth of the components, in spite of dispersion and chirp penalties, by demonstrating the system ability for multiband transmission. Three bands with same bandwidth at 0.7, 1.0 and 1.3 GHz are transmitted using 16-QAM format and EVM measurements are done with 100 and 200 MHz bandwidth of each band.

The setup depicted in Figure 4.26 is slightly modified and optimized for multiband data transmission. The multiband signal is amplified by 9 dB before launched into the DML. The baseband electrical spectrum generated for 100 and 200 MHz 16-QAM data signal is shown as insets (i) in Figure 4.34(a) and (b), respectively. After the optical transmission and opto-electronic conversion at PD, the generated electrical signal is also amplified by 40 dB before the signal analyzer.

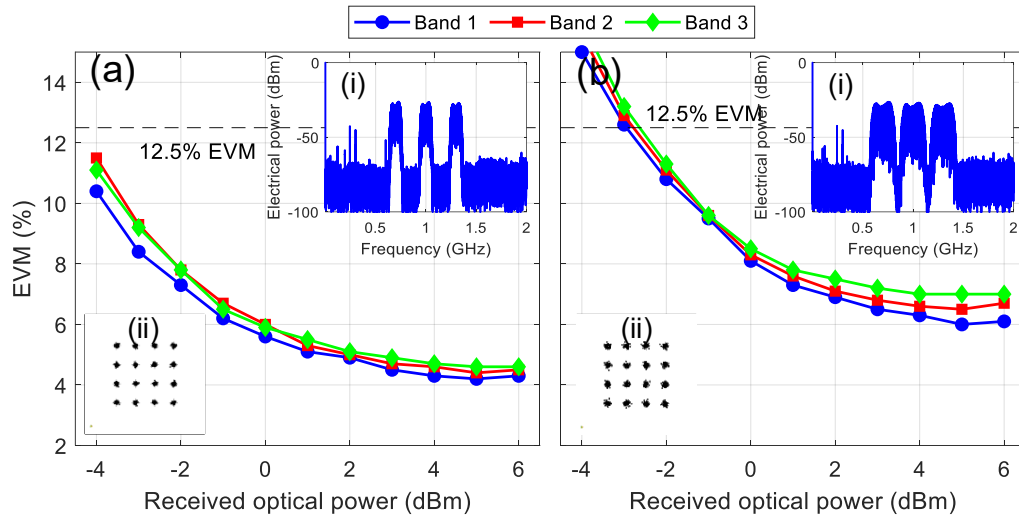


Figure 4.34. EVM of 16-QAM multiband data signal over 10 km fiber link with: (a) 100 MHz and (b) 200 MHz bandwidth. Insets: (i) electrical spectra of multiband signal (RBW = 100 kHz), (ii) constellations of band 2 with 3 dBm RoP.

The EVM measurements corresponding to the three bands are shown in Figure 4.34 (see constellations of band 2 with RoP of 3 dBm in the inset (ii)). Figure 4.34 (a) shows the EVM measurements corresponding to three bands with 100 MHz data bandwidth. EVM values are kept below the standard EVM limit for all bands within the RoP range under measurement and there is only a slight difference between frequency bands due to the DML 3 dB bandwidth frequency response. EVM measurements obtained with 200 MHz 16-QAM multibands signal are slightly higher, as shown in Figure 4.34 (b), and in any case, the EVM is below the EVM threshold with RoP higher than -3 dBm.

4.5. Conclusions

IM-DD based on DML represents an effective solution for a low complexity system compared to the conventional usage of external modulation. In general, compared to the use of MZM, direct modulation offers satisfactory RF to optical conversion efficiency and linearity but has relatively low output power and the modulation chirp is higher.

Remote and local photonic mmW signal generation schemes have been theoretically and experimentally studied for the deployment of a 5G C-RAN fronthaul link in order to estimate the capabilities and limitations of both approaches. Very good agreement has been shown between theory and measurements for both setups. The dispersive effect at IF frequencies are less significant than at RF frequencies. Indeed, the remote setup leads to higher frequency response (i.e. 15 dB gain over 25 km fiber link) than the local setup in photonicallly generated mmW band due to the combined effect of dispersion and laser chirp, whereas the behavior in baseband is significantly different. Transmission experiments using a 250 MHz QPSK signal have been done for the sake of characterization of the system performance under remote and local generation setups measured at baseband and mmW band. As theoretically predicted, experimental EVM results in the remote generation scheme show better performance than OB2B, which is led by the higher frequency response than local setup, whereas the local setup shows similar performance than OB2B. However, the measured electrical spectra show higher IMD products in remote generation schemes, which could cause significant penalties for specific scenarios. Therefore, the amplitude response of the system presented in this Chapter provides the main guidelines for photonicallly assisted mmW C-RAN network design.

The impact of harmonic and intermodulation distortion on data transmission has been experimentally studied over local and remote photonicallly generated mmW signals over an optical fiber fronthaul based on a DML and CS-external modulation for frequency up-conversion. Frequency response of the different second-order non-linear terms, i.e. $(2w_1)$,

$(w_2 - w_1)$ and $(w_1 + w_2)$, has been measured leading to -40, -30 and -30 dBm, respectively, for a 40 GHz signal under remote configuration while local and OB2B setups lead to negligible IMD levels far from the relaxation frequency (< 6.5 GHz for the used DML). Measured electrical spectra show the effect of in-band IMD, as a function of the signal bandwidth, and out-of-band IMD in multiband signals. The EVM measurements show that transmission is not feasible under remote scheme for optical power levels above certain threshold while local scheme resembles OB2B transmission. Signal transmission is limited by $(2w_1)$ -type HD and higher RoP values lead to poor signal transmission under remote compared to local setup. This effect is worse for larger bandwidth signals. The impact of $(w_2 - w_1)$ type term, which is higher than $(2w_1)$ -type term. However, the impact of $(w_1 + w_2)$ -type term has been measured as lower in good agreement with the corresponding measured IMD frequency response. Finally, IMD terms prevent the transmission of specific signals under this setup. More concretely, wideband signals with in-band IMD or multiband signals (w_1, w_2, w_3) satisfying $w_2 = 2w_1$, $w_1 = w_2 - w_1$ or $w_3 = w_1 - w_2$ are examples that need to be transmitted over local generation mmW approach in C-RAN.

Although the experiments employed a signal composed of two bands, the results can be applied to OFDM signals typically employed in 5G/6G networks. Therefore, remote configuration can be employed for OFDM waveforms provided the different subcarriers fall apart from the HD and IMD frequency terms described above, although local configuration will provide better performance due to the impact of non-linear distortion.

Finally, simulations and measurements have been performed in order to evaluate separately the impact of signal bandwidth, fiber dispersion and laser chirp for the sake of estimating the system capability in the remote configuration. The simulation of different values of chirp and fiber lengths, as well as different signal bandwidths, show penalties of 1, 2.3 and 6 dB for 4-, 16- and 64-QAM formats between non- and high chirp, respectively. In the experimental part, a low chirp commercial DML is employed and M-QAM signals with bandwidths from 50 to 1000 MHz are transmitted along 10 km SSMF and 1.5 m FSO channel with bit rates achieving from 1.2 to 2 Gbit/s occupying bandwidths from 200 to 1000 MHz depending on particular QAM format. The measurements show that the chirp in DML has a crucial influence on transmission characteristics, especially when higher-order modulation formats, i.e. 64-QAM, and high bandwidth signals are employed in such a network. Moreover, multiband signal transmission has been implemented to increase the bandwidth usability. Therefore, DML-based fronthaul solution connecting centralized BBU and RRH operating in hybrid fiber/FSO network has been demonstrated to satisfy full high data throughput requirements for 5G fronthaul links in mmW frequency spectrum.

Chapter 5. External modulation-based data transmission over photonically generated mmW

“Newton’s Third Law. The only way humans have ever figured out getting somewhere, is to leave something behind.”

– TARS, Insterstellar (2014)

This Chapter presents the external modulation as a data transmission solution in photonically generated mmW signals. In particular, the approach of two cascade MZMs is employed for data transmission for optical communications in C-RAN. A CS-DSB scheme is experimentally demonstrated with wireless transmission in the FR2. It is also provided an experimental comparison between DSB and the CS-DSB configurations for mmW signal generation setups for the sake of comparison and providing main guidelines for future deployment. Finally, the impact of thermal turbulences in FSO channel on data transmission is experimentally evaluated where various thermally induced turbulence profiles have been implemented to emulate real scenarios in C-RAN.

5.1. External data modulation

The schematic of the intensity modulation approach using an external modulator is displayed in Figure 5.1(a). It is based on MZM and the optical signal is purely intensity modulated with no phase modulation [112]. The laser emits an optical carrier which is launched into MZM. As explained in Chapter 2, a MZM can be biased at minimum transmission, maximum transmission, and quadrature bias points. The particular desired operating point for data transmission is quadrature point, i.e. $V_{bias} = 3V_{\pi}/2$, as shown in Figure 5.1(b). The quadrature bias point corresponds to a linear region which allows transmitting broadband RF signals with improved spurious free dynamic range (SFDR) [136]. Then, the optical carrier is modulated by the electrical data signal.

External data modulation presents some benefits. Zero chirp using dual drive MZM configuration can reduce the impact of fiber dispersion and extend the transmission distance or use larger bandwidth. Indeed, high-frequency modulation and high-power laser sources can be employed. However, the operating bias point of MZM undergoes voltage drift. Hence, care must be taken to maintain and control the MZM bias point for a specific application. The utilization of an extra external modulator also adds additional insertion loss, which should be compensated by an EDFA or increasing the laser optical power. Moreover, external modulators are relatively expensive and some desirable characteristics such as polarization

independence, good linearity (between drive voltage and modulated output) and smaller size are desired.

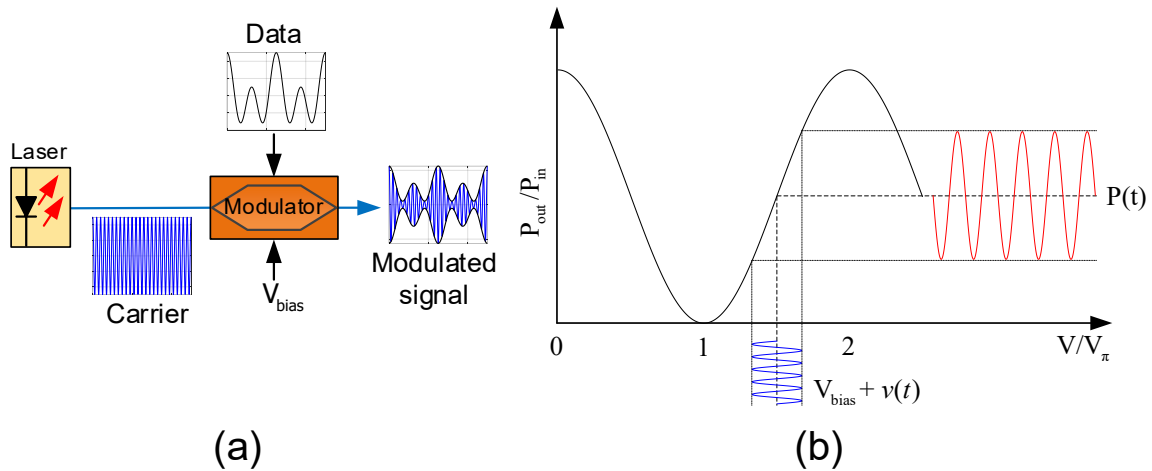


Figure 5.1. (a) Diagram layout of external modulation and (b) MZM optical power – voltage characteristic curve.

Intensive research is, nowadays, conducted to improve the maximum bit rate that can be transmitted using external modulation. Recently, several works report the capability of achieving bit rates beyond 100 Gbit/s. For example, a 100 Gbit/s/λ over 100 km optical fiber [137], 200 Gbit/s PAM-6 signals over 1 km fiber [138] or 333 Gbit/s over 20 km dispersion compensated optical fiber link [139] have been successfully demonstrated.

5.2. Optical CS-DSB signal transmission

In this Section, a photonicallly doubling RoF and radio over FSO (RoFSO) system for the mmW 5G optical fronthaul network with seamless antenna transmission at 26 GHz is experimentally demonstrated [140]. This setup is based on two cascade MZMs, as shown in Figure 5.2, and exploits the photonicallly frequency doubling technique, as explained in Chapter 3. The former corresponds to the one included in the photonic mmW signal generation scheme where the optical carrier is CS modulated (Chapter 3) by a single RF tone, $f_{RF} = f_{mmW}/2$, while the second one, biased at the quadrature point, provides the data modulation.

The laser diode (LD) (Yenista Optics Tunics T100S-HP) emits an optical carrier at 1550 nm with 11.3 dBm optical power. A PC is used to adjust the polarization state before MZM-1. The MZM-1 (Sumimoto Osaka, T.DEH1.5-40PD-ADC) is biased at the null point and fed by a 12 GHz single tone signal from a SG (Agilent 8267C) to suppress the optical carrier, whereas the MZM-2 (Avanex PowerBit F-10), biased at quadrature point for data modulation, is driven by a 5G NR signal at 2 GHz IF. Note that the single RF carrier and IF data power levels are 23 and 1 dBm, respectively.

The optical channel consists of 10 km of SSMF and a 1.1 m long FSO channel, which is realized by a pair of doublet collimators as described in previous chapters, making seamless fiber-to-FSO and vice versa connection. Note that the FSO channel loss is 8.4 dB and the FSO range is limited by the available space in the laboratory. After transmission over the optical channel, an EDFA with 16 dBm constant output power is used to compensate the system loss, and an OBPF (Alnair Labs BVF-100) is further employed to reduce the ASE noise produced by the EDFA. Before the optical-to-electrical conversion, realized by a high frequency PD (Finisar XPDV2320R), a VOA (Thorlabs EVOA 1550A) is used to adjust the RoP. Note the EDFA is placed at the remote node in the laboratory setup to provide high optical output power (i.e. 16 dBm) and therefore, provide system characterization by adding a VOA just before detection while keeping a safe power level. i.e. below 10 dBm, along the FSO link. However, real scenarios will place the EDFA at the CO for the sake of sharing resources.

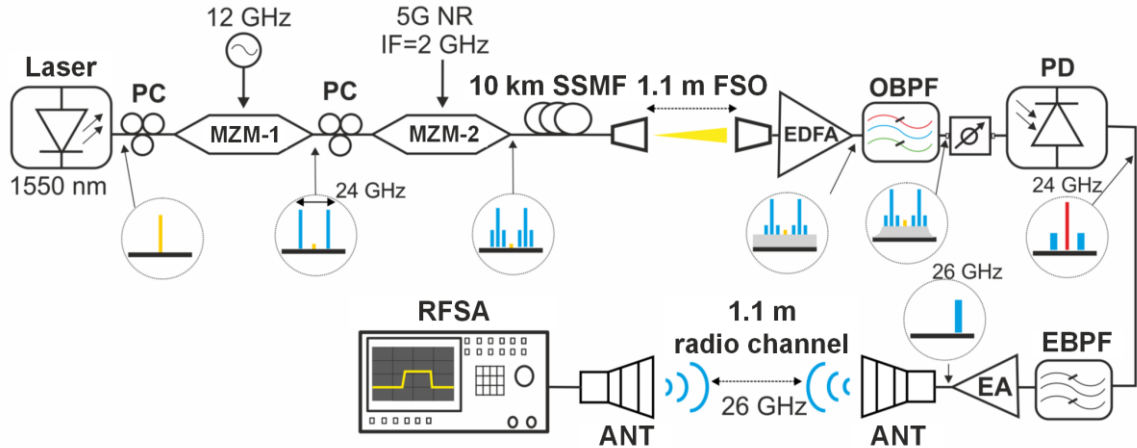


Figure 5.2. Experimental setup for optical mmW generation at 26 GHz with the seamless transmission. Insets illustrate spectra at given points [140].

After the direct detection by means of PD, the EBPF (Mini Circuits ZVBP-25875-K+) is employed to filter out the generated mmW carrier, the second sideband and all unwanted intermodulation products present in the electrical spectrum in order to obtain a single band centered at 26 GHz for further processing. Note that the passband of the filter lays between 24.25 and 27.5 GHz. The signal after the EBPF is amplified by using a broadband EA (SHF Communication Technologies AG SHF-810) and then radiated to a 1.1 m long antenna channel by means of the pair of double ridged horn antennas (ANT) (RFSpin DRH40). Afterward, the signal is received and evaluated in a RFSA.

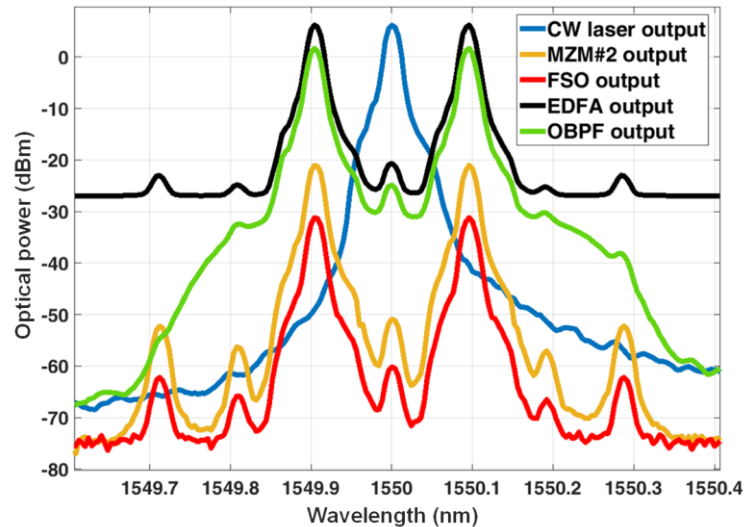


Figure 5.3. Measured optical spectra (RBW = 0.02 nm).

Figure 5.3 shows the optical spectra, captured at different parts of the setup corresponding to the scheme shown in Figure 5.2. The difference between optical spectra at the MZM-2 and FSO outputs stands only for the SSMF and FSO loss, whereas the difference between EDFA and OBPF outputs shows both loss of the OBPF and an importantly reduction of the ASE noise produced by EDFA. Note that the IF data at 2 GHz cannot be seen due to the instrument limitation and only the optical sidebands at 12 GHz spacing with the suppressed optical carrier can be observed.

Figure 5.4 displays the comparison of the electrical spectra received after PD with and without the usage of the EBPF with 64-QAM 5G NR signals having a bandwidth of 200 MHz. As it can be observed, the spectra without using the EBPF (red trace in Figure 5.4) is the generated mmW carrier at 24 GHz, as well as the two signal bands at IF of ± 2 GHz appear in

the spectrum with harmonics and many other intermodulation products, which are caused especially by the relatively high input power in the MZM. This significantly limits the system performance in terms of SNR and EVM and it needs to be treated for the antenna connection. When the EBPF is employed (blue trace in Figure 5.4), the upper sideband only remains with a small part of the newly generated mmW carrier and otherwise, the other components are filtered out. The filtered signal is then amplified by EA and radiated through a 1.1 m long mmW wireless channel.

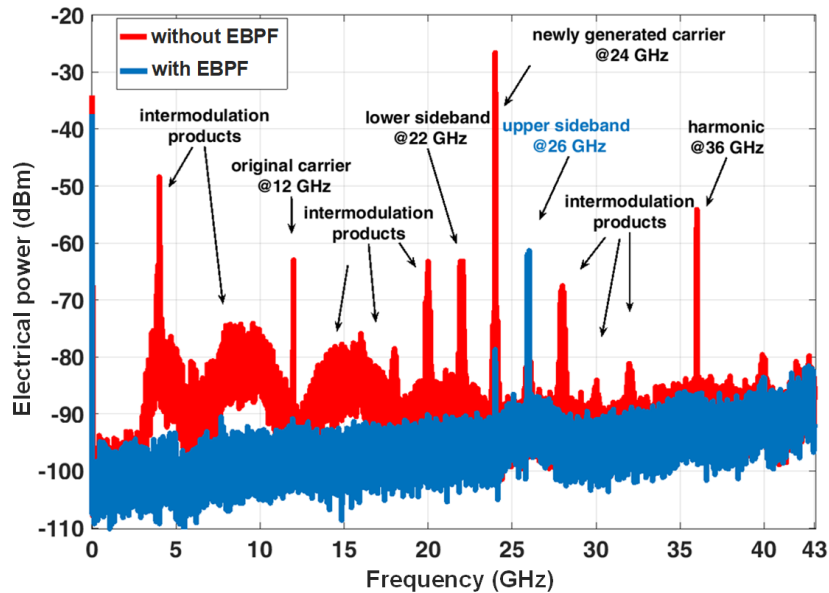


Figure 5.4. Electrical spectra w/o and w/ EBPF employed for 200 MHz bandwidth.

Finally, Figure 5.5 shows the impact of having the EBPF filter implemented after the PD when a 5G NR signal, predefined test model TM 3.1 using 200 MHz 64-QAM corresponding a maximal bit rate of 1.2 Gbit/s, is transmitted. The system performance is compared in terms of EVM for OB2B consisting of the transmission system without fiber, FSO and antenna; hybrid stands for the full system without radio channel i.e. antennas; and using the complete system with the seamless antenna link, i.e. full system. Note that in the full system scenario, there is not possible to even receive a sufficient signal quality without the EBPF, and thus only the system performance with the usage of the EBPF is shown in Figure 5.5.

There is no considerable difference between the EVM performance with and without the EBPF for OB2B whereas when hybrid is employed, i.e. 10 km of SSMF and 1.1 m long FSO without antenna channel, there is a 2.4% better EVM for the maximal ReP with the applied EBPF. It is also observed that the difference between the system with and without the EBPF tends to be less significant when the received power is decreasing. The lowest observed EVM by using the EBPF for OB2B and hybrid are 2.1 and 3.9%, respectively and the minimal received EVM for the full system with 200 MHz bandwidth and 64-QAM modulation scheme is 4.7%. In other words, to comply 9% EVM limit (see Appendix A), the required electrical power level for the full system is -52.6 dBm and, for the hybrid without EBPF, hybrid with EBPF, it is -41.5 dBm and -44.6 dBm, respectively. The minimal received power for OB2B is identical in both cases, i.e. -45 dBm.

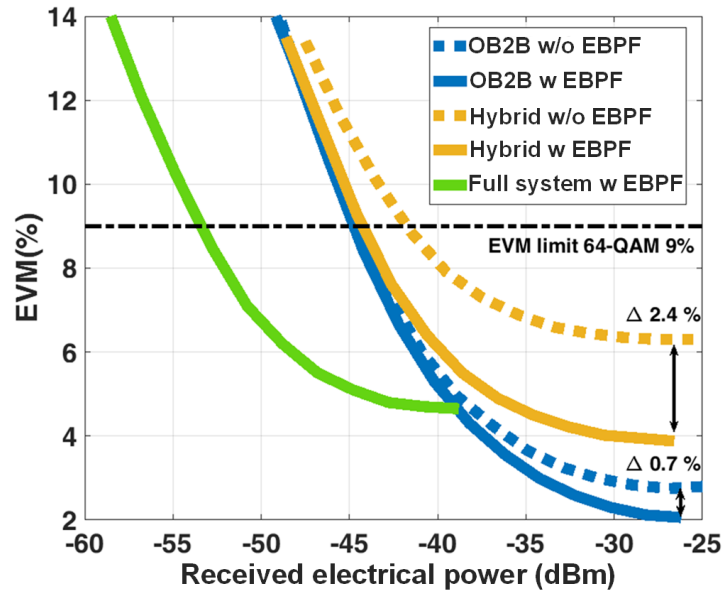


Figure 5.5. Measured EVM of 64-QAM and 200 MHz bandwidth at 26 GHz.

5.3. Comparison of DSB and CS-DSB schemes

In this Section we investigate the comparison of the system transmission performance in 39 GHz mmW signal generated by conventional DSB and photonically assisted CS-DSB approaches [140].

The two setups for performance comparison of 5G NR signal transmission is illustrated Figure 5.6(a). Both setups employ a CW laser (CoBrite DX4) at 1550.6 nm with 16 dBm of output optical power. The Setup A represents the classic approach with DSB modulation and direct detection. A 5G NR data signal at a particular mmW carrier is generated by a SG (Rohde & Schwarz SMW200A). The MZM (Optilab IML-1550-50-PM) is biased at linear point, i.e. quadrature point, and is modulated by the electrical data signal. The output optical power of the MZM is 7 dBm.

In Setup B, the optical signal is launched into the MZM-1 (Fujitsu FTM7938EZ/201), which is biased at its null point as described in Chapter 3. The MZM-1 is driven by a radio signal at the half of the target carrier frequency, $f_{RF} = f_{mmW}/2$, i.e. 12.5 GHz for 27 GHz and 18.5 GHz for 39 GHz transmission, generated by a SG (Rohde & Schwarz SMF100A) since $IF = 2$ GHz. The optical signal is then modulated with CS-DSB and launched into low-speed MZM-2 (Covega 10TM 081), which is biased at linear point and modulated by the 2 GHz IF data signal from SG (Rohde & Schwarz SMW200A). The output optical power of the MZM-2 is -2 dBm. Note that the order of the modulators is irrelevant and same results have been obtained in experimental measurements when data and RF modulation is performed in the first and second MZM, respectively.

In both setups, the resulting optical signal is transmitted over optical channel, i.e. OB2B, fiber and hybrid fiber/FSO links. Then, the optical signal is launched into the PD (Optilab PD 40) for direct detection. The recovered electrical signal is captured by a RFSA for performance assessment. Due to the lower output optical power level in Setup B, EDFA is required whereas the EDFA is only used in Setup A when the FSO link is included. Note that, in Setup B, the beating of the optical sidebands at the PD generates the signal at the double frequency of the original signal, i.e. 37 GHz plus an additional IF of 2 GHz.

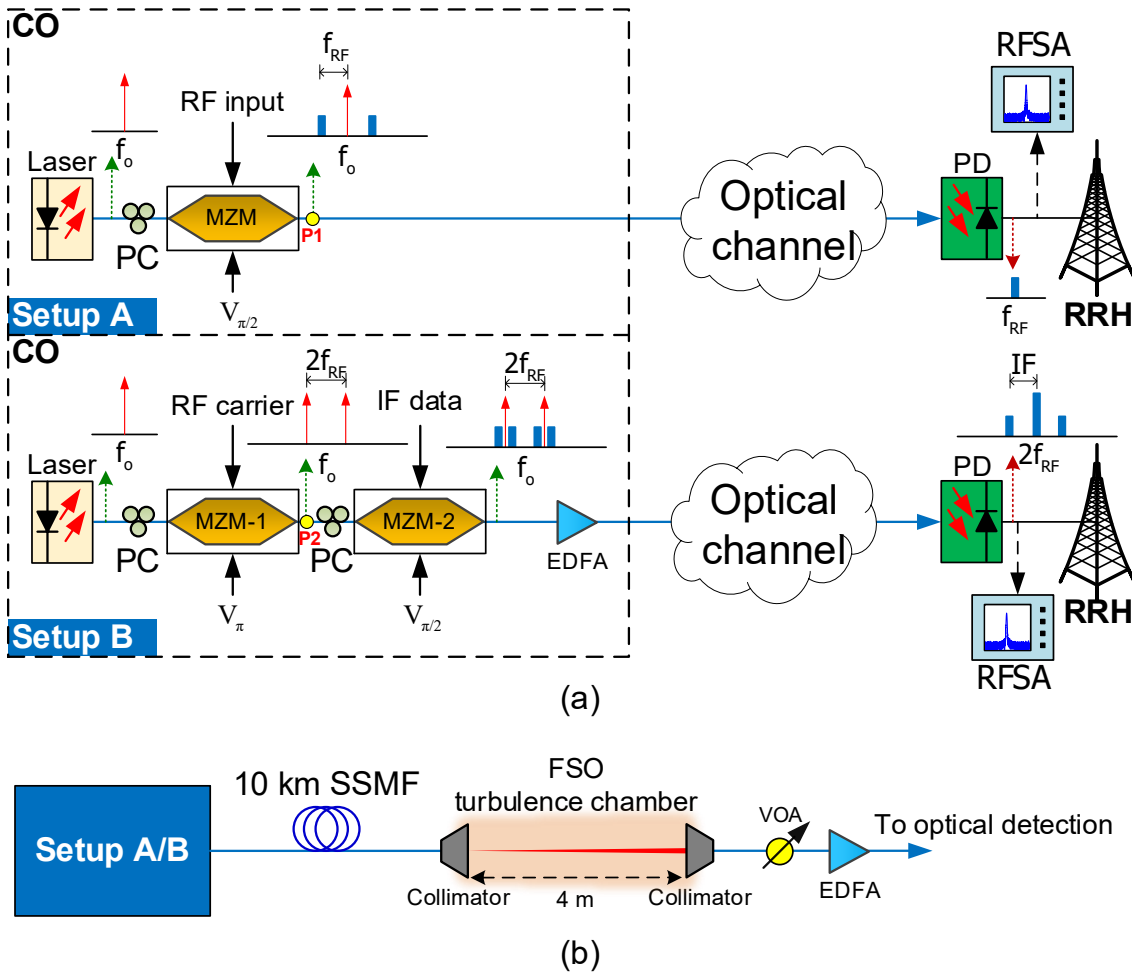


Figure 5.6. (a) Schematic of Setups A and B, and (b) optical channel.

The optical channel employed in Setup A and B consists of a 5 - 30 km SSMF and 4 m FSO link (see Figure 5.6(b)). The FSO link is composed of the transmitter and the receiver with optical doublet collimators (Thorlabs F810APC-1550), as in previous setups, for launching and capturing the optical signal from and to the optical fiber, respectively. Note that, in the FSO link the optical loss is 6 dB and a VOA (Oz optics DA-100-SC-1300/1550-9/125-S-40) is used to control the input to the EDFA whose output power is set to 3 dBm.

The measured optical spectra in both setups are shown in Figure 5.7. For Setup A, the spectrum captured in point P1, displayed in Figure 5.7(a), shows DSB optical modulation with sidebands separated from the optical carrier by the input RF, i.e. at 27 GHz, whereas Setup B shows the spectrum, obtained in point P2, of the suppressed carrier with two sidebands having the frequency difference between them equal to the double of the incoming electrical signal frequency to the modulator, i.e. 25 GHz (see Figure 5.7(b)). Note that the original carrier frequency in Setup B is half, i.e. 12.5 GHz. Due to the absence of the optical carrier and beating of these sidebands at PD, a new RF carrier emerges in the frequency corresponding to the frequency difference between the sidebands, i.e. 25 GHz, as explained in previous Sections.

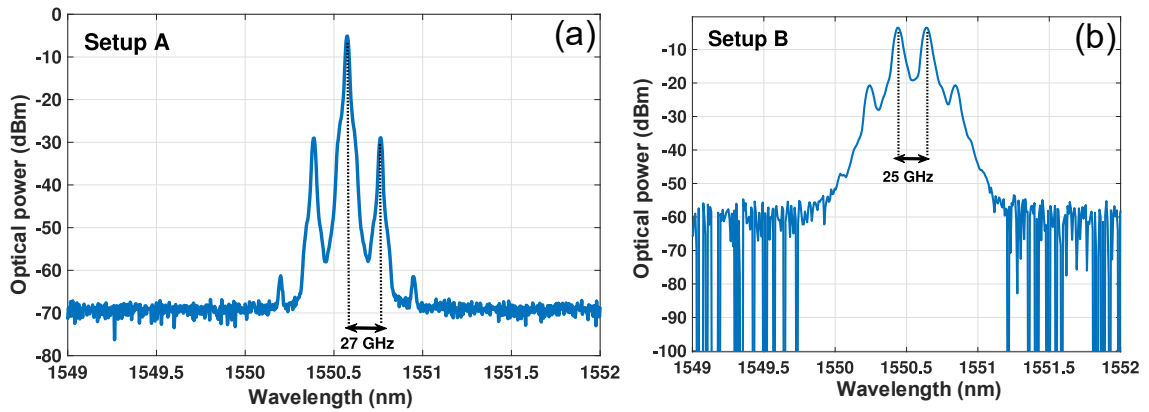


Figure 5.7. Optical spectra of (a) Setup A at P1, and (b) Setup B at P2.

At first, the impact of fiber link, i.e. 5 to 30 km SSMF, in Setup A and B is investigated and shown in Figure 5.8. Note that optical output power level is 7 dBm and no EDFA is required for Setup A meanwhile an EDFA with 7 dBm constant output optical power behind MZM-2 is employed in Setup B to compensate optical losses due to two cascade MZMs for sake of comparison with Setup A.

Figure 5.8 depicts the EVM as a function of the SSMF length for 400 MHz QPSK and 200 and 400 MHz 64-QAM signals for both setups at 27 GHz. For Setup A with optical DSB modulation format and with no filtering, the measured EVM is 9% and 18.8% for 64-QAM and QPSK, respectively, which is larger than EVM threshold level (see Appendix A) when optical fiber of 5, 15 and 25 km are employed, see marked measured points (circled) in Figure 5.8, due to the chromatic dispersion. However, Setup B with the suppressed carrier displays maximal transmission link spans of 17 and 25 km for 400 and 200 MHz 64-QAM, respectively for the EVM limits of 9%; and 30 km for 400 MHz QPSK for the EVM limit of 18.5%.

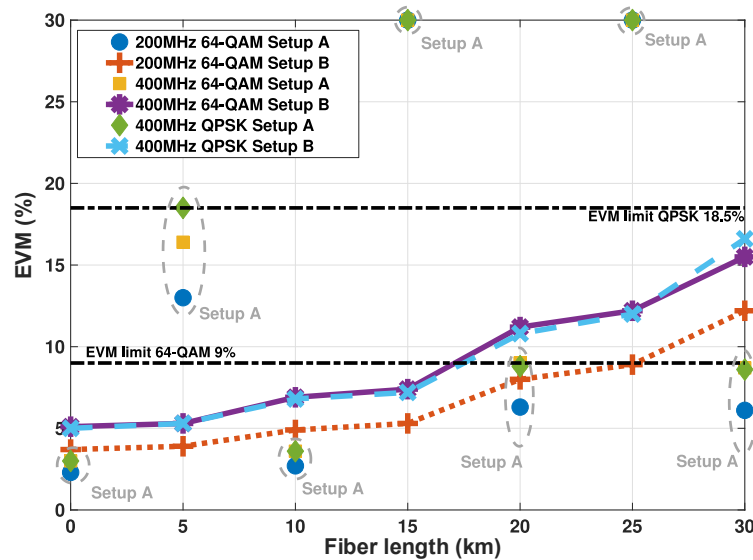


Figure 5.8. Measurements of EVM vs SSMF length for Setup A and B, using QPSK and 64-QAM signals with various bandwidth at 27 GHz.

Since the RoP is the same for both Setups A and B, considering an ideal IM-DD, the RF signal transmission, as a function of frequency will be constant. The comparison of the RF frequency responses with optical DSB and CS-DSB schemes, for OB2B and different SSMF lengths are shown in Figure 5.9.

The transmission of the DSB signal reveals a substantial power drop in the frequency response due to the chromatic dispersion-induced fading (equation (2.12)), see Figure 5.9(a). This power fading at 27 GHz occurs when fiber lengths is 5, 15 and 25 km, i.e. the EVM measurements over the threshold level (see circled points in Figure 5.8). At the frequencies where RF response vanishes, intensity modulation of light is fully converted to the optical phase modulation, i.e. the optical intensity becomes constant, thus giving rise to no measurable RF response at the PD [6].

On the other hand, for Setup B, the power transmission plots display a gradual decrease in the magnitude with the increasing SSMF length, which follows the OB2B plot, in contrast with Setup A, where a number of dips can be seen in the spectrum, which depends on the SSMF lengths.

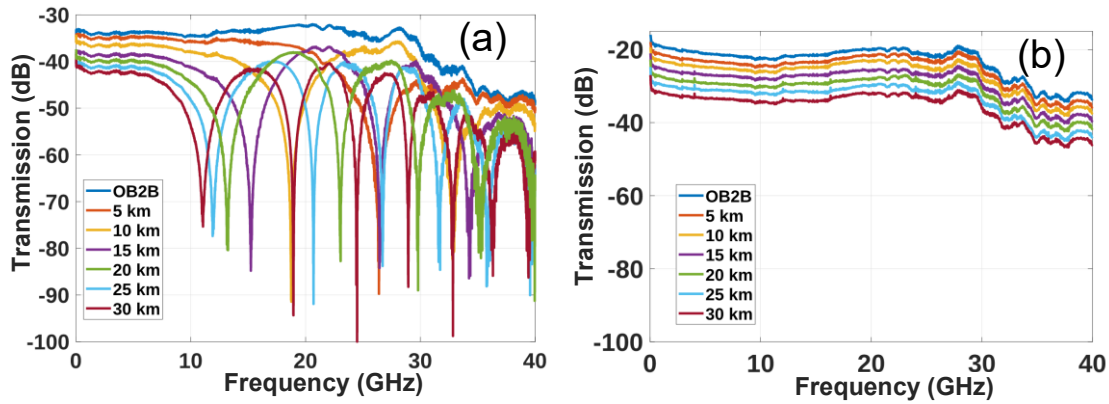


Figure 5.9. Frequency response for various SSMF lengths in (a) Setup A and (b) Setup B.

However, DSB schemes (Setup A) can avoid the chromatic dispersion induced power fading by using a filter to introduce optical single sideband transmission or by simultaneous intensity and phase modulation, but at the cost of increased complexity of the system.

5.4. Impact of FSO turbulences on data transmission

In this Section, the impact of uniform and non-uniform turbulent distribution along the FSO link on externally modulated data transmission over mmW signals which are photonicallly generated, is theoretically and experimentally evaluated.

5.4.1. Impact of turbulence strength

In the following, we experimentally evaluated the strength of induced turbulence along the FSO channel on data signal transmission [141]. For this purpose, the experimental schemes employed in this Section are the same as shown in Figure 5.6. In this case, the chamber (see Figure 5.6(c)) has 20 temperature sensors, spaced 20 cm apart, are placed within the chamber along the optical propagation path meanwhile two fan heaters blowing hot air perpendicular to the optical beam to generate a thermal gradient.

To investigate the impact of different AT levels (i.e. scintillation index, which is proportional to Rytov variance σ_R^2), on the hybrid link in a 5G fronthaul optical network, weak (T0) and strong (T1) AT regimes are generated and defined (see Chapter 2) by the refractive index structure parameter C_n^2 of $5.54 \cdot 10^{-14} \text{m}^{-2/3}$ ($\sigma_R^2 = 8.78 \cdot 10^{-6}$) and of $1.15 \cdot 10^{-11} \text{m}^{-2/3}$ ($\sigma_R^2 = 1.83 \cdot 10^{-3}$), respectively. Note that these values can be recalculated through σ_R^2 for longer transmission spans maintaining the overall scintillation effect [142]. For example, if we consider common

FSO distances of 100 and 500 m in urban areas, then we have the turbulence levels of T0 with C_n^2 of $1.52 \cdot 10^{-16}$ and $7.93 \cdot 10^{-18} \text{m}^{-2/3}$, and T1 with $3.14 \cdot 10^{-14}$ and $1.65 \cdot 10^{-15} \text{m}^{-2/3}$, respectively.

The QPSK and 64-QAM signals with the 400 MHz bandwidth at 27 GHz are transmitted to compare the EVM performance under turbulence conditions as a function of SNR in both setups, shown in Figure 5.10.

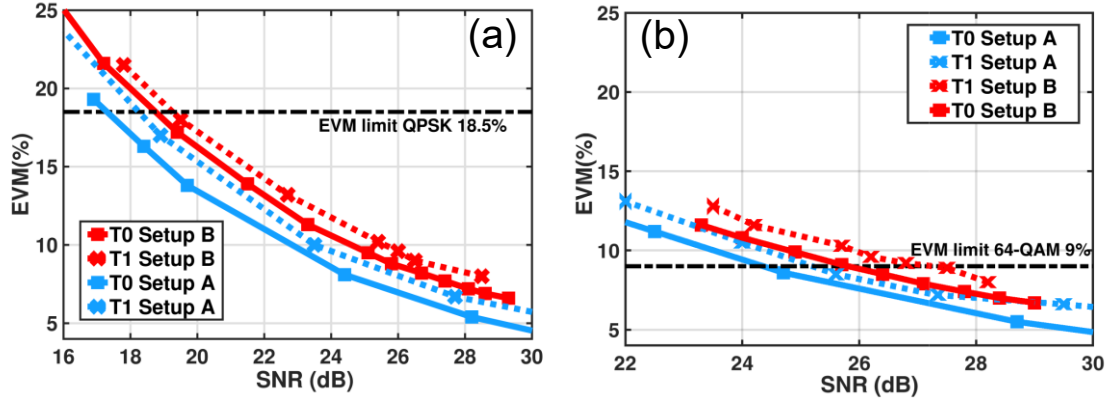


Figure 5.10. EVM vs SNR under weak and strong AT for Setup A (blue) and B (red) at 27 GHz after 10 km SSMF and 4 m FSO link with 400 MHz bandwidth for (a) QPSK and (b) 64-QAM.

Setup A shows the highest SNR, i.e. higher than 30 dB, for both modulation schemes, and lower average EVM by 3% and 1% for QPSK and 64-QAM, respectively, compared with Setup B. Under AT and for a given SNR, the average EVM increased by 2% and 1% for QPSK and 64-QAM, respectively. In any case, EVM values are below the EVM thresholds for both setups and modulation formats even under the strong AT regime.

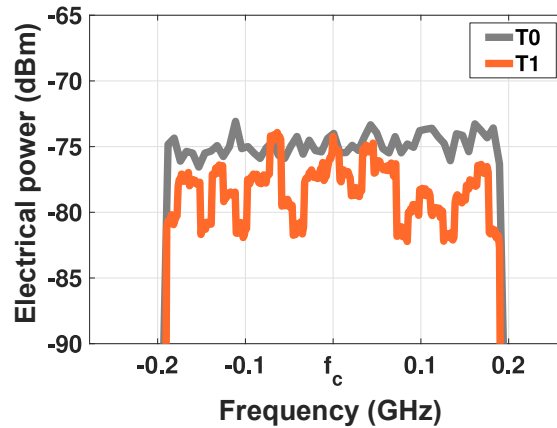


Figure 5.11. Electrical spectra for Setup A with 400 MHz 64-QAM for T0 and T1 ($f_c = 25$ GHz).

Figure 5.11 depicts the electrical power spectra for Setup A with 400 MHz 64-QAM for T0 and T1. The in-band power variation of ± 2 -3 dB around the average electrical received power value of -77 dBm for the case with T1 (orange curve) compared to T0 (grey curve), which is highly stable, i.e. flatter. The similar power variation in electrical spectrum under turbulence conditions in FSO channel has been observed e.g. in [100].

5.4.2. Impact of non-uniform turbulent distributions

In the following, we present a theoretical and experimental study of the impact of non-uniform turbulent distribution along the FSO link on the transmission of M-QAM signals with $M = 4, 16,$ and 64 in K-band (25 GHz), which are photonically generated by using an optical external intensity modulator biased at the null transmission point [110].

5.4.2.1. Simulations

In this Section, the performance of the system depicted in Figure 5.12 are evaluated under different turbulence scenarios. Simulation results employing an external modulation for data transmission approach and CS-MZM mmW signal generation are presented by using co-simulation of Optisystem and Matlab software.

The proposed system layout of signal transmission at 25 GHz over hybrid fiber/FSO link is displayed in Figure 5.12 [110]. The laser emits an optical carrier whose state of polarization is adjusted by a PC. As explained in Section 5.3, the photonically up conversion ($f_{mmW} = 2f_{RF}$) by CS-DSB is held at MZM-1 whereas the MZM-2 modulates the optical signal by the data signal which consist of an amplified pseudo-random binary sequence (PRBS) M-QAM signal, at the linear bias point. The optical signal is amplified by an EDFA to compensate the insertion losses, and filtered out by an OBPF to reduce the ASE noise over a narrow optical bandwidth. The signal is afterward transmitted over SSMF and the FSO channel. As explained in Chapter 2, the optical signal suffers attenuation due to the atmospheric propagation effects and geometrical loss and signal degradation caused by turbulence leading to significant fluctuations in the transmitted optical power. Finally, it is launched into the VOA which allows to vary the optical power just before opto-electronic conversion at PD. As explained in previous Chapters, the recovered M-QAM signal data is carried by the microwave signal at $2f_{RF}$ angular frequency, as a result of the beating between the two first-order sidebands.

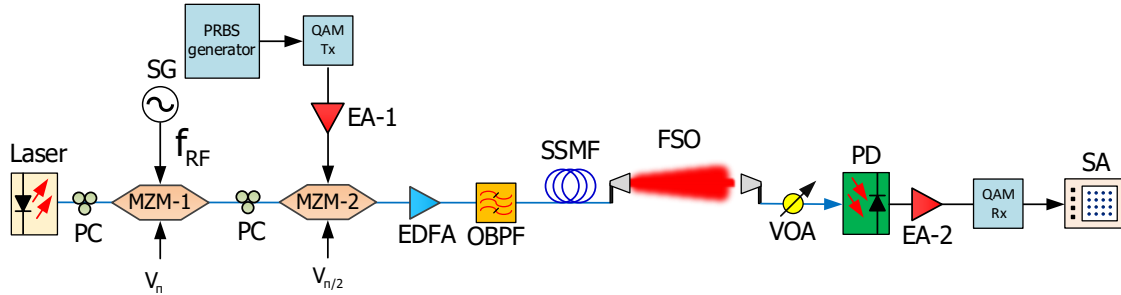


Figure 5.12. System layout of simulated M-QAM signal transmission at 25 GHz under thermal turbulence [110].

The performance of the system described in Figure 5.12 with the parameters detailed in Table 5.1 are evaluated under different turbulence scenarios. Uniform turbulence are defined according to weak ($\sigma_R^2 \ll 1$), moderate ($\sigma_R^2 \approx 1$) and strong ($\sigma_R^2 \gg 1$) regimes (denoted as U-scenarios: U1, U2, U3), whereas non-uniform scenarios include up to three different segments (denoted as N-scenarios: N1, N2, N3) with varying turbulence level along the link, as it is detailed in Table 5.2. Note that all the N-scenarios are set to have a similar average turbulence value as U2 uniform scenario for the sake of comparison.

Figure 5.13 displays the spatial distribution of turbulence along the FSO link, corresponding the parameters defined in Table 5.2 for different scenarios.

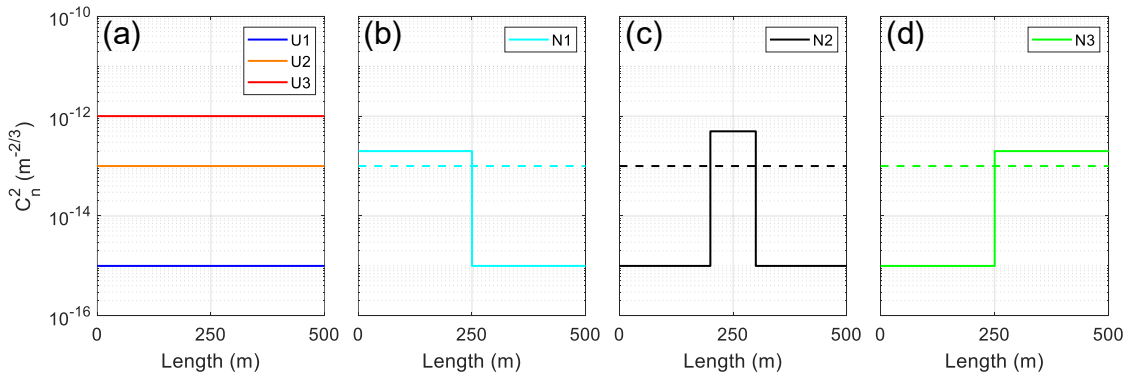


Figure 5.13. C_n^2 spatial distribution of proposed scenarios: (a) U1, U2 and U3, (b) N1, (c) N2 and (d) N3. Dashed line represents the mean value in each non-uniform scenario.

The transmission of 10 Gbit/s 4-, 16- and 64-QAM signals over combined RoF and RoFSO is simulated under six turbulence scenarios (see U and N profiles along link as depicted in Figure 5.13).

Table 5.1. Simulation parameters.

	Parameter	Value
Laser	Wavelength	1550 nm
	Output power	14 dBm
MZM-1	Switching RF voltage	4 V
SG	Carrier frequency	12.5 GHz
PRBS	Bit rate	10 Gbit/s
	Order	16
MZM-2	Switching RF voltage	4 V
Modulation formats		4-, 16-, 64-QAM
EDFA	Output power	13 dBm
	Noise figure	3 dBm
OBPF	Bandwidth	1.5 m
	Insertion loss	1 dB
SSMF	Length	5 km
	Dispersion	17 ps/km-nm
	Attenuation	0.2 dB/km
FSO	Tx aperture	2.6 cm
	Tx loss	1 dB
	Rx aperture	5 cm
	Rx loss	1 dB
	Beam divergence	0.25 mrad
	Length	500 m
VOA	Insertion loss	0 – 10 dB
PD	Responsivity	0.45 A/W
	Dark current	5 nA
EA-1	Gain	9.1 dB
EA-2	Gain	30 dB

Table 5.2. Definition of scenarios.

Scenario	Distance	$C_n^2(m^{-2/3})$	Averaged $C_n^2(m^{-2/3})$	Rytov variance
Uniform	U1 500 m	10^{-15}	10^{-15}	0.0056
	U2 500 m	10^{-13}	10^{-13}	0.5587
	U3 500 m	10^{-12}	10^{-12}	5.5869
Non-uniform	N1 250 m	$2 \cdot 10^{-13}$	10^{-13}	0.5587
		10^{-15}		
	N2 100 m	$5 \cdot 10^{-13}$	10^{-13}	0.5587
N3 250 m	10^{-15}	10^{-13}	0.5587	
	$2 \cdot 10^{-13}$			

Figure 5.14 shows the calculated EVM performance. 4-QAM modulation format leads to higher EVM values than higher-order QAM formats, as shown in Figure 5.14(a). Since degradation is directly related to the magnitude of averaged C_n^2 parameter with minor differences due to spatial distributions, there is only 1% EVM deterioration between scenarios with similar averaged C_n^2 (U2, N1, N2 and N3 – see Figure 5.13) at 0 dBm RoP. The maximum EVM difference between scenario U1 and U3 (low and high turbulence scenarios) at 0 dBm of RoP is about 6%. Note that 17.5% EVM threshold (see Appendix A) for 4-QAM is satisfied under U3 scenario with optical received power larger than 0.5 dBm.

Figure 5.14(b) shows a clear distinction of the 16-QAM results obtained for uniform turbulence scenario U2 and non-uniform scenarios N1, N2 and N3 with 4.6% maximum EVM deterioration between them at 0 dBm RoP. In this case, the uniform distribution U2 (moderate turbulence strength) leads to higher degradation in comparison with similar averaged but non-uniform turbulence N1, N2 and N3 scenarios. Likewise, to the results shown in Figure 5.14(a), U1 and U3 are identified as the best and worst scenarios due to the weak and strong turbulence characteristics, respectively, although with larger EVM deterioration, i.e. 6.9%.

Figure 5.14(c) shows EVM results when 64-QAM signal is transmitted in the proposed system. The differences due to non-uniform spatial distribution of turbulence become relevant and higher 64-QAM signal sensitivity to non-uniform turbulence profile when high turbulence magnitude in the middle of the link is applied. In this case, N3 and N1, having increased turbulence levels in the first and second half of the channel, respectively, lead to better results than uniform U2 with similar average. The scenario with a turbulence magnitude peak in the middle of the channel, N2, reaches higher values than strongest uniform distribution U3. Nevertheless, the maximum EVM penalty between the best and worst scenarios, i.e. N3 and N2, respectively, is only 2% at 0 dBm of RoP. Insets below the Figure 5.14 show the constellations for low (U1) and high (U3) turbulence obtained for every modulation format when the optical received power is 4 dBm.

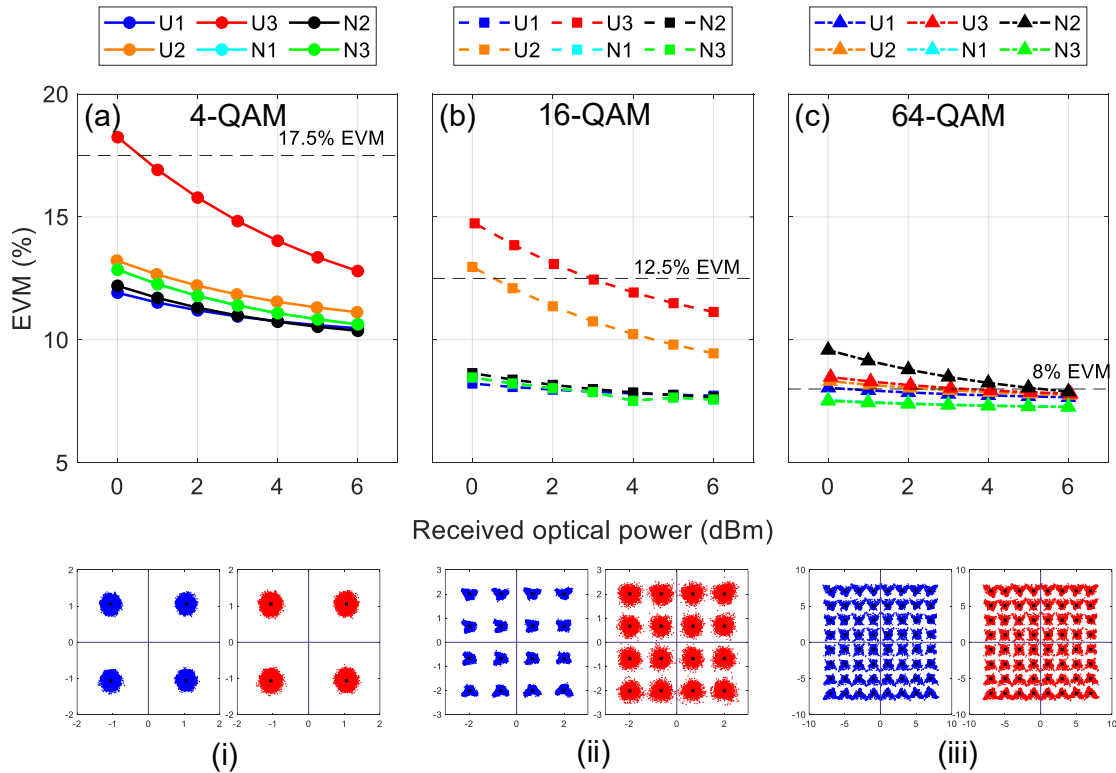


Figure 5.14. EVM vs RoP for (a) 4-QAM, (b) 16-QAM, (c) 64-QAM. Insets (i)-(iii) show constellation diagrams for U1 and U3 scenarios under RoP of 4 dBm for 4-, 16- and 64-QAM, respectively.

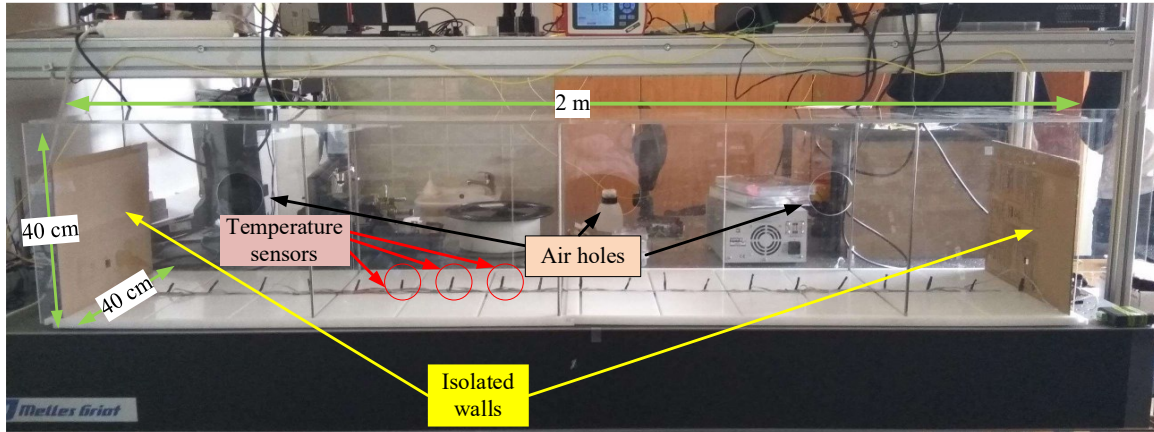
5.4.2.2. Experimental results

In the experimental setup, based on the scheme shown in Figure 5.12, a 12.5 GHz SG (Rohde & Schwarz SMF100A) is employed to drive the MZM-1 (Fujitsu FTM7938EZ/201) and a SG (Rohde & Schwarz SMW200A) is used to generate LTE 20 MHz M-QAM signals to drive the MZM-2 (Covega 10TM 081). An EDFA (CEFA-C-HG-SM-50-B130-FA-FA) with 13.2 dBm constant output power is employed to compensate the optical losses. The hybrid link consists of 5 km of SSMF and 2 m FSO long links with 4 dB of overall optical loss in the wireless segment. Finally, a VOA allows to adjust the received power just before detection by a photoreceiver (OptiLab PD-40). Post-amplification and further signal processing allows to evaluate the signal quality and recover the signal constellation at 25 GHz in the RFSA.

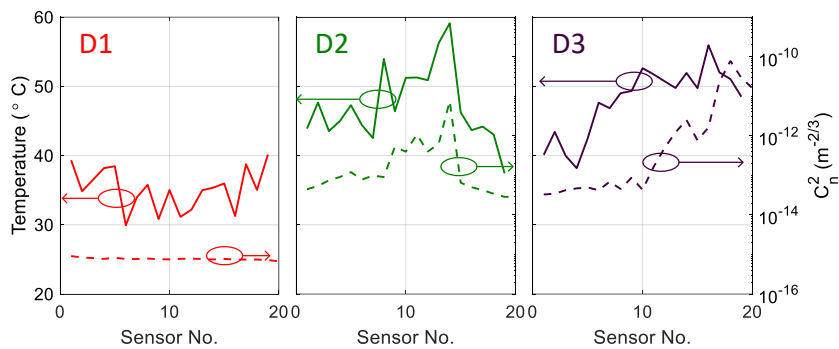
Experimental turbulence over FSO links has been created in Czech Technical University labs in Prague, as depicted in Figure 5.15(a), which shows the experimental turbulence chamber. In this case, the chamber length is 2 m and is made by methacrylate walls. Two isolated walls are used at transmitter and receiver side to avoid the metal expansion on alignment stages which produces misalignments. Sensors are 10 cm equidistantly located for recording the temperature gradient. By changing the position of airholes, the distribution turbulence profile varies as shown Figure 5.15(b). Three experimental turbulence scenarios of the FSO link D1, D2 and D3 are created in a laboratory chamber where thermal distribution is captured by thermal sensors. The corresponding refractive index structure parameter, C_n^2 is calculated along the link (see distributions in Figure 5.15). While almost flat distribution is set in case of D1 with $C_n^2 = 5.9 \cdot 10^{-14} \text{ m}^{-2/3}$ ($\sigma_R^2 = 1.3254 \cdot 10^{-5}$, low turbulence), D2 and D3 correspond to turbulence distributions with a turbulence peak in the middle of the link and increased turbulence in the last part of the link. The averaged C_n^2 values are $4.2 \cdot 10^{-11} \text{ m}^{-2/3}$ and $1.8 \cdot 10^{-11} \text{ m}^{-2/3}$ and therefore corresponding $\sigma_R^2 = 0.0094754$ and $\sigma_R^2 = 0.0041495$ for experimental D2 and D3 scenarios, respectively. Note that lower σ_R^2 values and higher C_n^2 values comparing to the simulation results are obtained due to considerably shorter FSO path, i.e. 2 m long, in the experiment.

In the following, 4- and 64-QAM modulated signals are transmitted along the experimental system to evaluate the impact of variable turbulence distributions on the different modulation formats. Figure 5.16(a) shows the measured EVM versus the RoP. It can be observed that EVM values are higher for 4-QAM, as obtained in the simulation results in the previous Section. However, 4-QAM has significantly higher EVM limit to obtain reliable transmission. As it is expected, both modulation formats lead to less degradation under low turbulence (D1 scenario) and similar degradations for D2 and D3 due to the similar turbulence level magnitude. Standard EVM limits [28], displayed as the dashed horizontal lines, for 4- and 64-QAM are satisfied under D1 scenario with a RoP of -5 dBm and -4.33 dBm, respectively. However, the power penalties with respect to D2 and D3 scenarios at the 17.5% EVM level for 4-QAM are 1.3 and 1.8 dBm, respectively, whereas the power penalties at the 8% EVM level for 64-QAM are 1.9 dB and 1.7 dB. Accordingly with the simulation results shown in Figure 5.14, the scenario with increased turbulence level in the last part of the link, i.e. N3, shows larger EVM than the one with the peak turbulence in the middle, i.e. N2, for 4-QAM whereas N2 exhibited larger EVM than N3 for 64-QAM. On the other contrary, D2 and D3 scenarios with 0 dBm RoP lead to 3.7 and 4% EVM difference between 4- and 64-QAM formats, respectively, which is in good agreement with 4% penalty calculated under U1 using similar Rytov coefficient in the previous Section.

Figure 5.16(b) shows the EVM results in terms of ReP measured at 25 GHz. 4- and 64-QAM require a minimum electrical power of -65.7 and -66.1 dBm, respectively, showing penalties lower than 0.94 and 1.7 dB for D2 and D3 in both cases.



(a)



(b)

Figure 5.15. Experimental turbulence chamber at Czech Technical University labs in Prague and (b) temperature (dashed line) and C_n^2 (solid line) for different turbulence profiles.

Figure 5.17 shows the equivalent BER levels in log scale calculated as described in [143] (see Appendix A), also showing the corresponding BER threshold levels at $5.5 \cdot 10^{-9}$ and $1.9 \cdot 10^{-3}$ for 4- and 64-QAM, respectively. Note that BER level decrease with increasing received power changes such behavior at high power values, e.g. 3 – 7 dBm due to non-linear detector response.

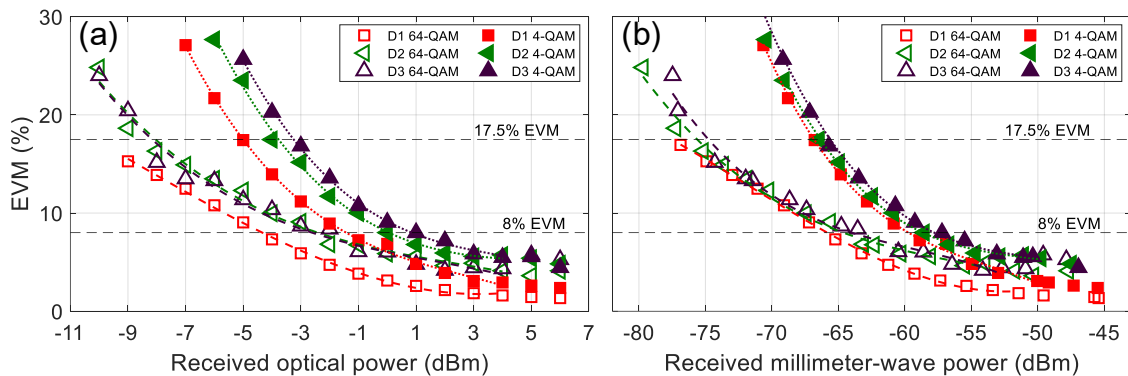


Figure 5.16. Experimental EVM vs received optical (a) and electrical (b) power for 4-QAM and 64-QAM modulation formats.

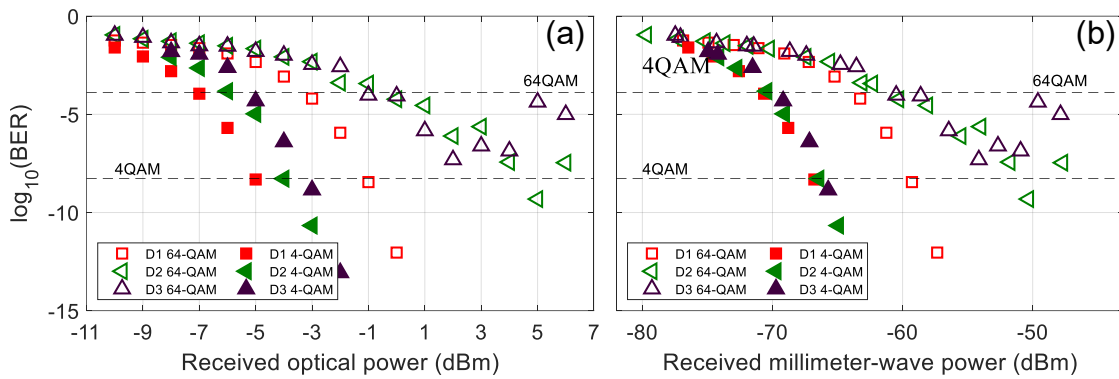


Figure 5.17. Experimental BER vs received (a) optical and (b) electrical power for 4-QAM and 64-QAM modulation formats.

Figure 5.18 shows the constellations of both recovered signals with corresponding EVM values after detection with 0 dBm of RoP. As it was explained, D1 and D2 shows similar degradation, i.e. 3.13% and 5.87% for 64-QAM and 6.86% and 8.08% for 4-QAM, respectively, whereas D3 shows slightly worse degradation. However, the measured EVM under D3 scenario is kept below the threshold level, i.e. 6.03% and 9.17%, and the data signal can be correctly recovered in all cases.

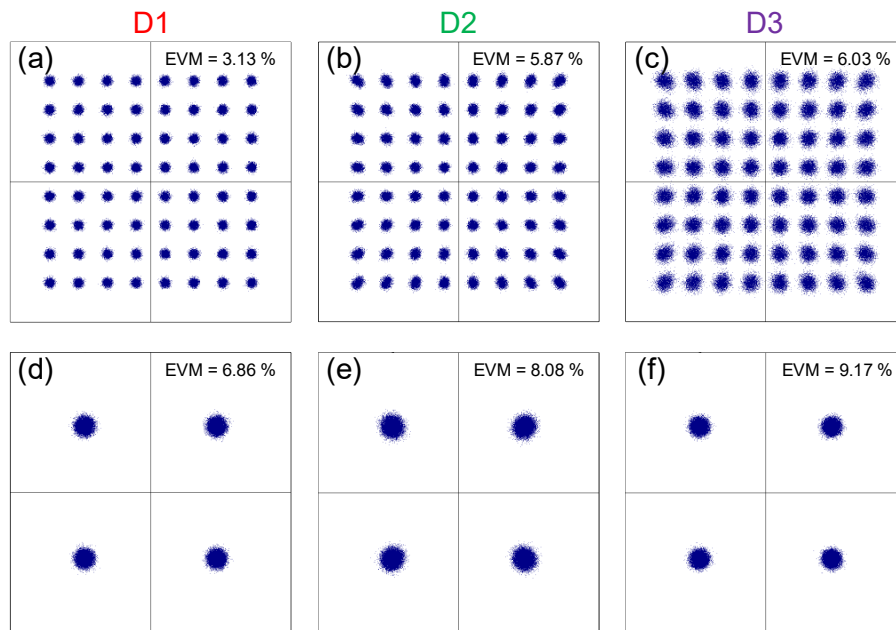


Figure 5.18. Constellations at 0 dBm RoP: (a)-(c) 64-QAM and (d)-(f) 4-QAM for D1, D2 and D3 turbulence distributions. Corresponding EVM values are displayed in the constellations.

5.5. Conclusions

Data external modulation enables higher bandwidth signal transmission than DML. Indeed, it allows zero chirp signal and can extend the transmission distance. However, the cost is relatively higher and additionally insertion loss and bias drift must be addressed.

Optical CS-DSB based mmW generation with the seamless antenna transmission at 26 GHz has been demonstrated using both the fiber and FSO to mimic an analog optical fronthaul. In particular, the usage of additional filtering enables to demonstrate the seamless transmission of 5G NR signals with reasonable SNR and the bandwidth exceeding 100 MHz. Therefore, EVM measurements demonstrate the successful transmission for the full system, i.e. fiber, FSO and wireless radio link, with 200 MHz bandwidth and 64-QAM modulation scheme.

We evaluated the performance of two setups using a conventional DSB scheme and a photonicallly mmW signal generation based on CS-DSB scheme to double the input carrier frequency. CS-DSB approach offered immunity to chromatic dispersion-induced fading for the frequency range up to 40 GHz and a SSMF length of 30 km. We demonstrated no significant difference in the performance at 27 and 39 GHz thus making it as an attractive solution for higher frequency bands for 5G. Moreover, the CS-DSB scheme can be implemented with frequency n -multiplication to further relax the bandwidth requirements. On the other hand, although the conventional DSB approach is highly sensitive to dispersion-induced fading and requires higher bandwidth, it offers improved EVM performance since MZM is biased at the quadrature point instead of the null point as in CS-DSB, higher SNR, and reduced complexity. In addition, it has been shown seamless deployment of antennas is another important issue, which needs to be considered especially in large bandwidth links (≥ 200 MHz). Finally, the highest achieved data throughput is 1.4 Gbit/s, which is sufficient for the chosen unlicensed single band.

The impact of strength of AT in FSO has been experimentally evaluated on data transmission over mmW signal. EVM shows that the signal degradation is higher with high thermally induced turbulence strength. Indeed, there is a marginal difference between T0 and T1 for both DSB and CS-DSB setups. Additionally, the analytical calculations, based on the measured results, confirm that the EVM performance fulfils the EVM threshold of the 500 m long outdoor FSO link under a moderate turbulence level (i.e. $C_n^2 = 1.65 \cdot 10^{-15} \text{m}^{-2/3}$). Finally, a data rate of 1.4 Gbit/s is transmitted under weak and strong atmospheric turbulence along 4 m FSO link.

Furthermore, the impact of different thermal-induced free space turbulence distributions on the M-QAM signal transmission in photonicallly generated K-band carrier over hybrid optical links has been theoretically evaluated. Simulation results of 10 Gbit/s signal with 4-, 16- and 64-QAM over 5 km of SSMF and 500 m long FSO link have been demonstrated under different weak to strong turbulence regimes. Non-uniform turbulence distributions are shown to have different impacts on the transmission of M-QAM modulation formats in given frequency band with practical consequences. Moreover, transmission experiments of 20 MHz 4- and 64-QAM signals over 5 km of SSMF and 2 m long FSO link confirm that turbulence distributions with higher strength in the middle of the considered link have bigger impact in terms of power penalty on 64-QAM (1.9 dB penalty) compared to 4-QAM (1.3 dB penalty). For 4-QAM, higher EVM results have been measured for distributions with larger turbulence magnitude in the second half of the link meanwhile higher signal degradation has been measured for high peak in the center of the link, what is in good agreement with simulation results. In spite of different theoretical and experimental bit rates and FSO link length, results agree on 4% EVM difference between 4- and 64-QAM at a given RoP, i.e. 0 dBm, when compared equivalent links with uniform weak turbulence. Therefore, the presented system needs careful attention when the FSO link is exposed to optical turbulences with high gradients along the optical path, e.g. in dense urban areas.

Chapter 6. Bidirectional fronthaul links

La victoire appartient au plus opiniâtre.

Victory belongs to the most tenacious.

– Eugène Adrien Roland Georges Garros

Since the literature mostly shows results on signal data transmission at mmW frequencies in downlink (DL) direction, this Thesis aims to contribute to demonstrate the feasibility of bidirectional MWP fronthaul links. This Chapter presents an experimental full-duplex data transmission over photonically generated 39 GHz for 5G networks in hybrid fiber and free-space optics DL and uplink (UL) directions. Subsequently, the data transmission between the CO and the user is experimentally demonstrated at mmW frequencies, i.e. 60 and 25 GHz for DL and UL, respectively, where a radio wireless link is included as the final segment of the fronthaul link in the C-RAN. This newly-established bidirectional fiber-FSO-5G mmW/5G NR sub-THz convergence provides a promising solution to meet the requirements for full-duplex operation.

6.1. Full-duplex transmission of 5G NR signals in 39 GHz band

In a practical 5G scenario, transmitting and receiving at the same time with full-duplex operation is imperative. This Section presents a full-duplex hybrid fiber/FSO link at 39 GHz for 5G mmW RAN [144] that can meet the requirement of full-duplex operation.

The experimental setup for the data signals in the DL, illustrated in Figure 6.1(a), may include single or multiple users, generated at different IFs by using a DG-1 (Tektronix AWG7122C). The data signal is then electrically amplified by an RF EA-1 (Wenteq ABL0300-01-2516) up to 9 dBm. The DML (OpticalZonu OZ516) has a 3 dB bandwidth of 6 GHz and a fixed power of 5.6 dBm at 1553.9 nm, see Figure 6.1(b). The optical spectrum at the DML output is shown in Figure 6.1(c). The optical signal is launched into the MZM-1 (Sumitomo T.DEH1.5-40PD-ADC) that is biased at the null transmission point (i.e. 9 V), which is employed to generate CS-DSB signal. The MZM-1 is driven by a 19.5 GHz input clock signal with 23 dBm electrical power, generated by a SG (Agilent 8267C). A PC is used to minimize the MZM polarization-dependent loss. The optical signal is amplified by an EDFA-1 (Accelink MW series) with a constant gain of 20 dB to compensate the modulation loss and boost the optical power prior to signal transmission over the ODN via the optical isolator-1 (ISO) and the directional optical circulator (CIRC) to prevent any signal reflection. The ODN consists of a 10 km SSMF and 1.2 m FSO link by using the pair of air-spaced doublet collimators (Thorlabs F810APC-1550), previously employed in other setups (see inset in Figure 6.1(a)). The FSO channel loss

is 5.5 dB and the measured refractive index, C_n^2 , is about $2.4 \cdot 10^{-14} \text{m}^{-2/3}$. After the hybrid link, the optical signal is transmitted to the BS via CIRC-2, and amplified by the EDFA-2 (Amonic, AEDFA-23-B-FA) for ODN loss compensation followed by an OBPF-1 (Finisar WaveShaper 4000S) to reduce ASE noise. Figure 6.1(c) also displays the optical spectrum measured after OBPF-1, where two sidebands with 39 GHz spacing are shown and optical carrier suppression to sideband ratio is 40 dB. A VOA is then used to reduce the RoP from the maximum value of 6 dBm into the PIN PD (u2t BPDV2020R), where the beating of the two sidebands is held to generate the desired 39 GHz signal. The recovered electrical signal is then amplified by an mmW EA-2 (25 dB gain), and can be radiated wirelessly over the radio link via an array of ANTs in real applications. Finally, the received signal is evaluated by a scope (Tektronix DPO72004C).

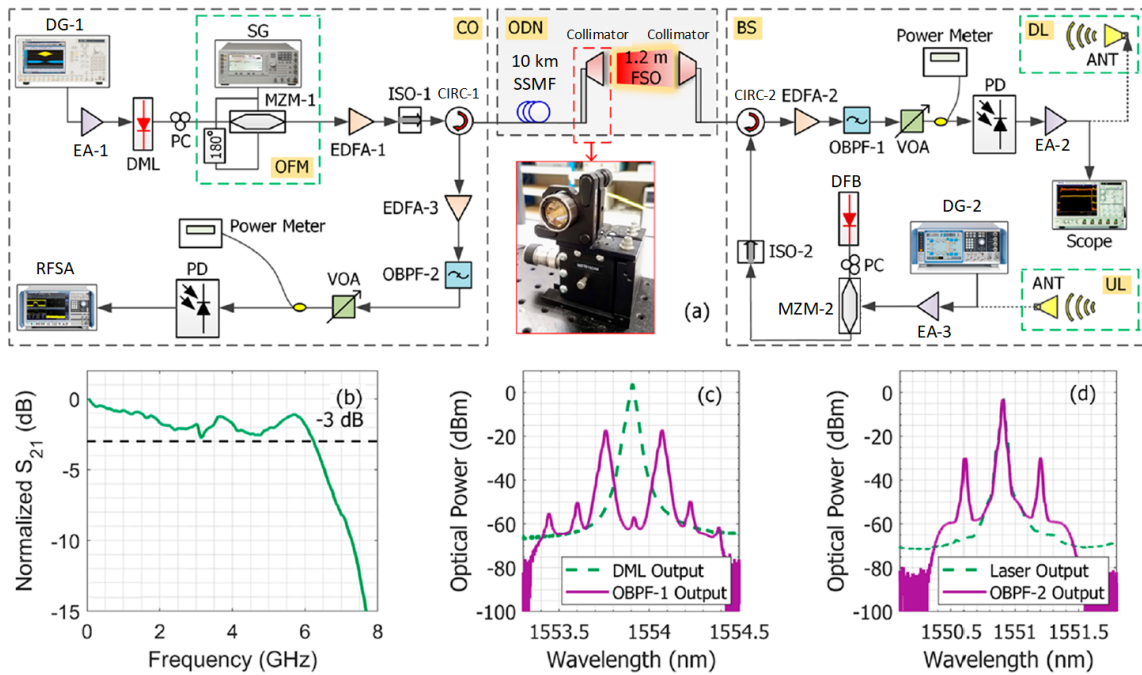


Figure 6.1. (a) Experimental setup of the proposed full-duplex based 5G mmW frequencies, (b) DML frequency response, (c) optical spectra measured in DL and (d) optical spectra measured in UL [144].

For the UL direction, a DFB laser (EXFO IQS-610) emits the optical power of 12 dBm at 1550.9 nm (see Figure 6.1(d)). After adjusting the state of polarization via a PC, the optical signal is launched into a single-drive MZM-2 (Photline MX-LN-40) for optical modulation. The MZM-2 is biased at linear point (i.e. 5.1 V) to generate a DSB signal. The optical signal is then modulated by a 37 GHz 5G NR signal with 64-QAM at bit rate of 2.4 Gbit/s, which is the NR FR3 TM 3.1, generated by a DG-2 (Rohde & Schwarz SMW200A) and amplified EA-3 (SHF Communication Technologies AG SHF-810) with 29 dB gain. The optical signal is then launched to the mutual DL/UL ODN via ISO-2 and CIRC-2. After ODN, the optical signal is demultiplexed via CIRC-1 and, amplified by EDFA-3 (Amonic, AEDFA-23-B-FA) and filtered out by OBPF-2 (AlnairLabs BVF-100), whose spectrum output featuring the DSB signal is also shown in Figure 6.1(d). The optical signal power is adjusted by the VOA and is detected by the PD and finally captured and assessed by a signal and RFSA (Rohde & Schwarz FSW43). Then, DL and UL transmission performances are evaluated in terms of EVM, BER, constellation diagrams, RoP and ReP for each QAM signal.

6.1.1. Downlink characterization

A critical point is the determination of optimal IF for OB2B system performance. Figure 6.2(a) shows the EVM performance of a single-band signal i.e. single user (4 Gbit/s 16-QAM) at different IF from 1 GHz to 5 GHz. As expected, the EVM performance, in general, is degraded

when the IF increases. The measured EVM value of about 5% is achieved for IF ranging from 1 to 3 GHz. However, for IF ranging from 3.5 to 5 GHz, there is a significant increase of EVM performance from 8.3 to 36% since the operational bandwidth of the involved electronics components, i.e. DG-1 and EA-1 which 3 dB bandwidth are 4.8 and 3 GHz, respectively. Note that the EB2B measurement, where signal generator and analyser are directly connected does not include the amplifier and satisfies the EVM limit for all IFs, i.e. 12.5% for 16-QAM [26].

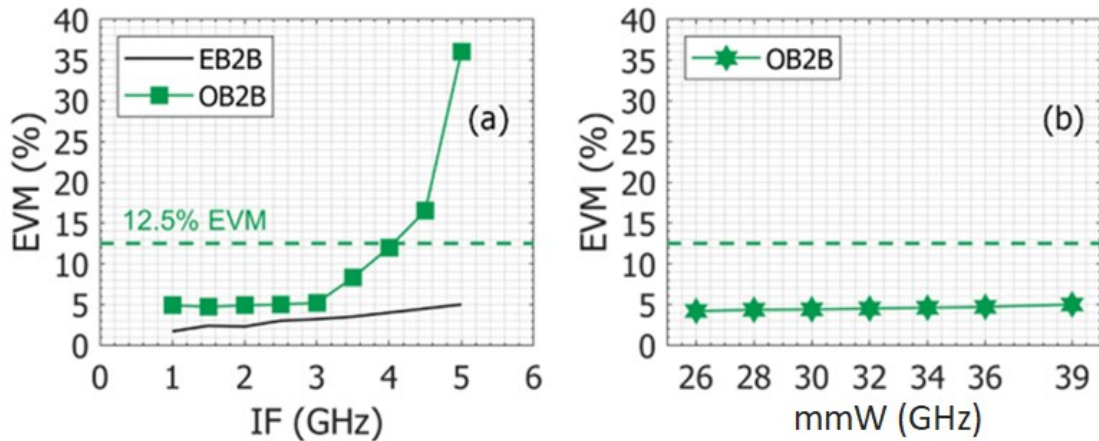


Figure 6.2. Measured EVM at different (a) IF and (b) generated mmW frequencies in OB2B DL configuration.

To examine the signal quality at different 5G mmW frequency bands, the EVM performances after OB2B transmission for generated mmW signals ranging from 26 to 39 GHz is shown in Figure 6.2(b). Note that the IF is set at 2.5 GHz for all cases. As expected, when increasing the frequency, the corresponding EVM value is slightly degraded with only 0.5% EVM penalty, which verifies the benefit of the photonic mmW signal generation approach.

6.1.1.1. Single-band transmission

As the first step, the EVM performance for the single-band signal, i.e. single user – 4 Gbit/s 16-QAM at the IF of 2.5 GHz, is measured over OB2B, fiber and hybrid links, and plotted in Figure 6.3.

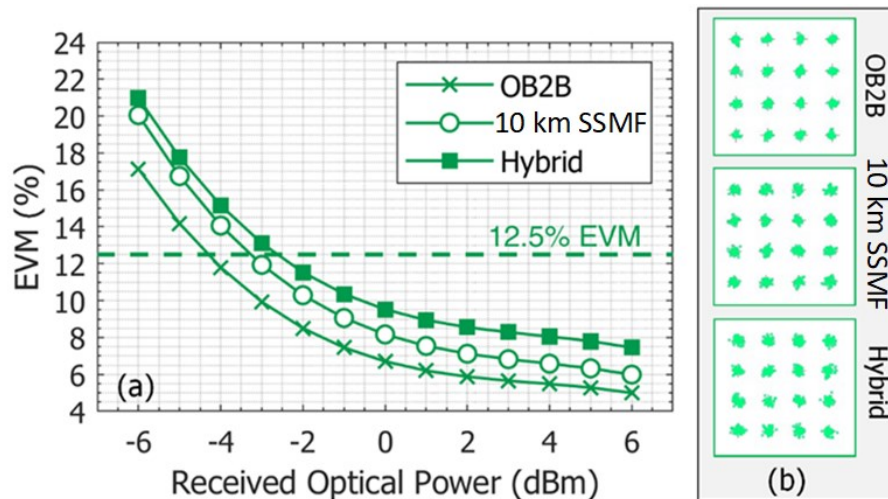


Figure 6.3. (a) Measured EVM versus RoP for a single user – 4 Gbit/s 16-QAM and (b) constellation diagrams for OB2B, 10 km SSMF and hybrid configurations.

The measured EVM shown in Figure 6.3(a) displays the exponential drop with RoP for all transmission scenarios. The EVM value for OB2B measured are 5% at 6 dBm RoP meanwhile transmission over 10 km SSMF and hybrid links leads to 6% and 7.5%, respectively, resulting

in the EVM penalties of 1 and 2.5%, compared to OB2B. OB2B and 10 km SSMF link show minima RoP of -4.3 dBm and -3.3 dBm for their threshold EVM value (see Appendix A), i.e. only 1 dB optical power penalty. When FSO channel is employed, an optical power degradation of 0.8 dB is measured, which verifies the feasibility of FSO channel in the bidirectional ODN for DL and UL. The constellation diagrams at RoP of 6 dBm, as shown in Figure 6.3(b), are very clear for all three scenarios, confirm the high-quality transmission of the single-band signal.

6.1.1.2. Multi-band transmission

In the following, the transmission of three-band signals, i.e. each band represents one user – 1 Gbit/s per user, based on the variable QAM allocations scheme over OB2B and hybrid links is experimentally evaluated, as a proof-of-concept demonstration.

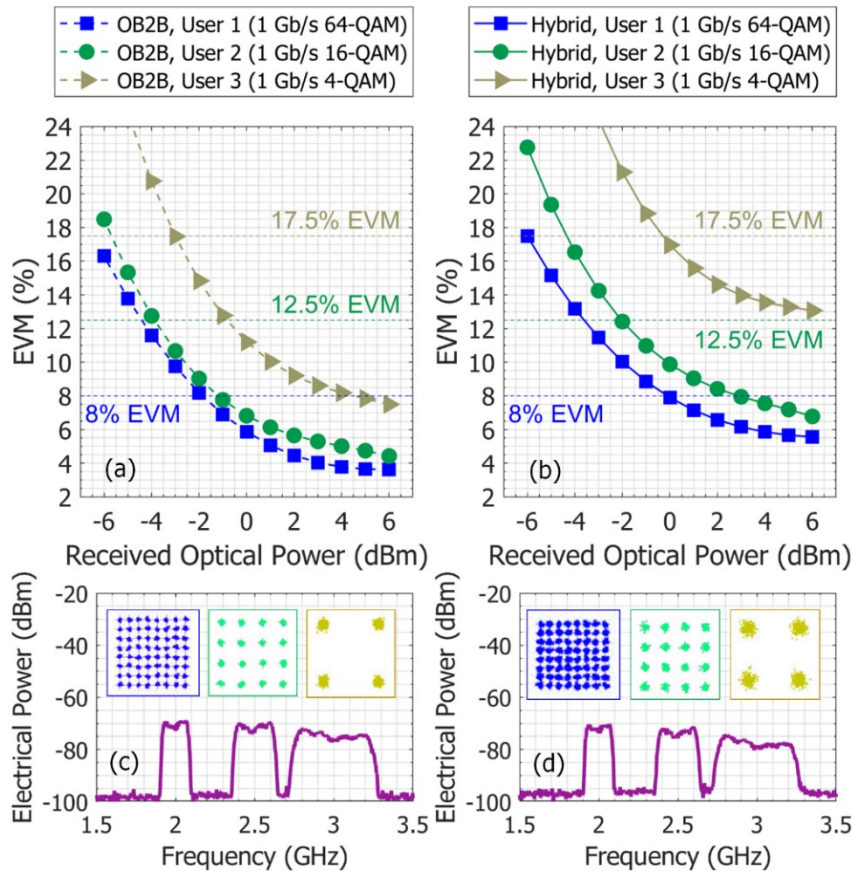


Figure 6.4. Measured EVM versus RoP for each band after (a) OB2B and (b) hybrid transmissions. (c) – (d) are the corresponding received RF spectra and constellation diagrams (as insets) of OB2B and hybrid transmissions, respectively.

The multiband signal consists of 64-, 16- and 4-QAM centered to the IF of 2, 2.5 and 3 GHz, respectively, with 0.5 GHz guard band. The measured EVMs versus RoP of the multiband signals after OB2B and hybrid transmissions are shown in Figure 6.4(a) and (b), respectively. As can be observed, all signals satisfy the EVM requirements for both configurations. For OB2B, the lowest EVMs for 4-, 16- and 64-QAM are 7.5%, 4.5% and 3.6%, respectively. The measured EVMs is 13.1%, 6.7% and 5.5% for 4-, 16- and 64-QAM at RoP of 6 dBm, respectively, when the optical signal is transmitted over hybrid link. The resultant EVM penalties between OB2B and hybrid transmissions are 5.6%, 2.2% and 1.9% for 4-, 16- and 64-QAM, respectively. This can be attributed to the chromatic dispersion and FSO loss, which degrade the SNR of the signal.

Figure 6.4(c) and (d) show the corresponding received RF spectrum and constellation diagrams, which are clear and discernible. Note that the spectrum profile is tilted, the noise floor is increased and the received power is reduced gradually for bands at higher IFs.

Finally, the BER performance as a function of ReP is plotted in Figure 6.5. The BER curves are calculated based on the measured EVM values for three-multiband signals in the hybrid condition as described in [143]. As can be seen, all bands show the best BER below the forward error correction (FEC) threshold of $3.8 \cdot 10^{-3}$ (see Appendix A). The minimum ReP to transmit 4-QAM (user 1) is about -32 dBm, while that of 16- (user 2) and 64-QAM (user 3) are about -28 dBm and -24 dBm suffering the RF power penalties of 4 dB and 8 dB, respectively, in comparison to 4-QAM user.

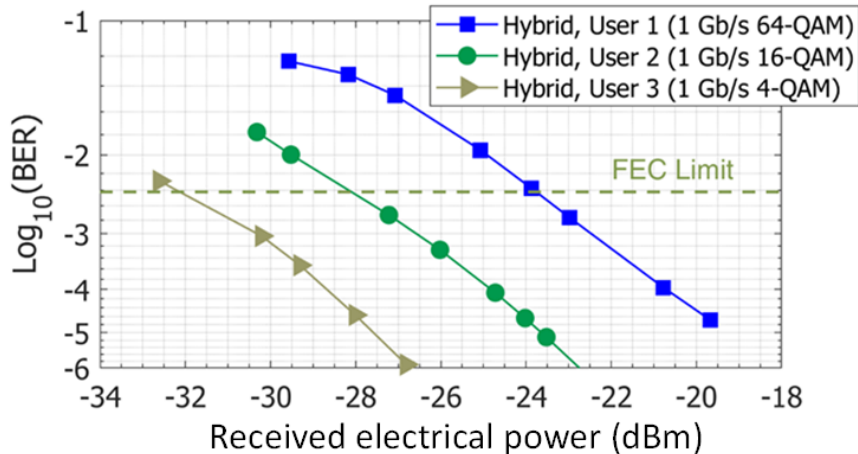


Figure 6.5. Calculated BER versus received RF power for each band after hybrid transmission.

6.1.2. Uplink characterization

For UL signal characterization, a 37 GHz 5G NR signal with 64-QAM at bit rate of 2.4 Gbit/s is transmitted over the ODN simultaneously to DL signal transmission. Since the radio wireless link cannot not be employed in this setup due to the unavailability of ANTs, the input RF power is therefore emulated by the power produced by SG, shown in Figure 6.1(a).

The measured results in the OB2B scenario are depicted in Figure 6.6, where the dynamic range (DR) is measured as 14 dB and the lowest EVM value of 3.5% is achieved at an input RF power of -18 dBm, which is also adopted for all transmission scenarios.

The EVM vs RoP of UL for OB2B, 10 km SSMF, and hybrid links is displayed in Figure 6.7(a). The measured EVMs for OB2B, 10 km SSMF and hybrid link are 3.5%, 3.8% and 4.1%, respectively, at RoP of 6 dBm, which satisfies the 8% EVM threshold (see Appendix A). The EVM penalties can be neglected since they are less than 0.6%. Compared with the required EVM limit of 8%, the required RoP for OB2B is 1.5 dBm while for 10 km SSMF and hybrid links, RoP values are about 1.5 dBm and 2 dBm, demonstrating almost no optical power penalties.

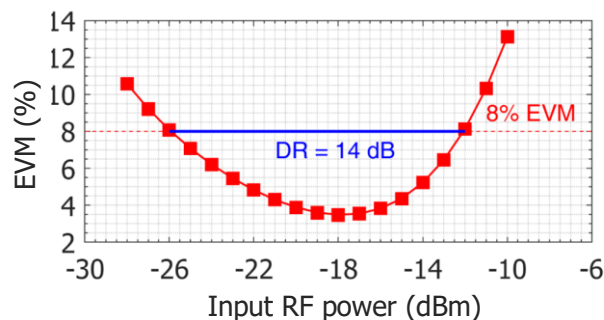


Figure 6.6. Performance of the 37 GHz 5G NR 64-QAM at 2.4 Gbit/s as a function of input RF power.

Figure 6.7(b) shows the performance of the UL transmission in terms of BER vs ReP. Note that ReP is directly measured at 37 GHz by RFSA. All cases show the best BERs below the FEC threshold (see Appendix A) with almost no RF power penalties compared to the FEC limit, $3.8 \cdot 10^{-3}$. Therefore, the minimum ReP for 64-QAM is about -47 dBm.

Finally, the received RF spectra and constellation diagrams at RoP of 6 dBm are shown in Figure 6.7(c) and (d) for OB2B and hybrid link, respectively. As expected from previous results, both spectra show good SNR and constellations are stable and clear.

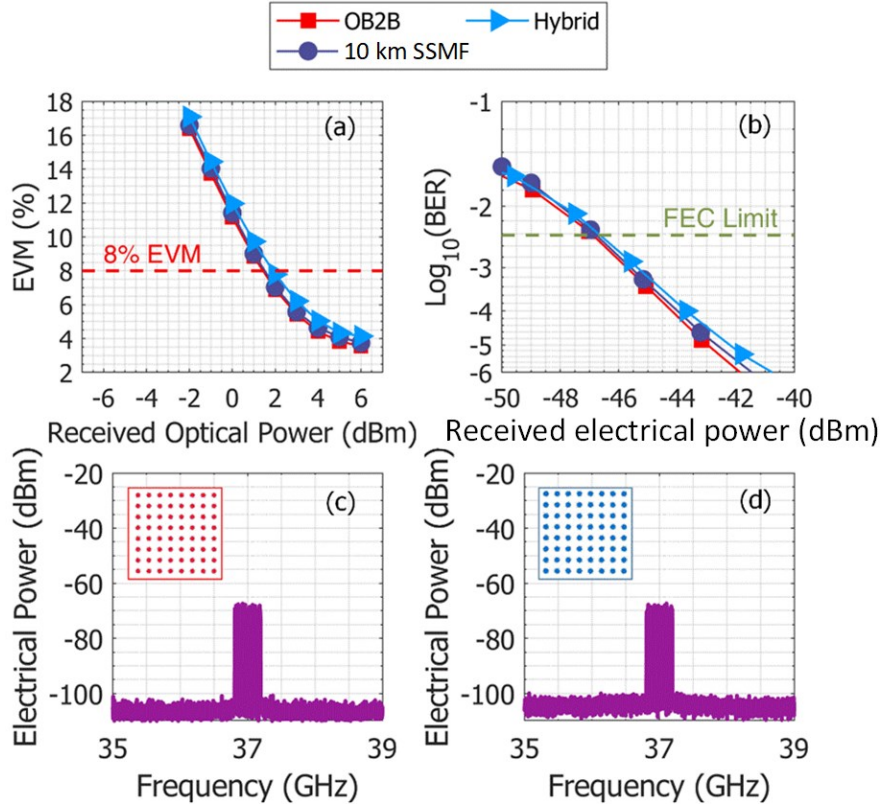


Figure 6.7. 2.4 Gbit/s 64-QAM over 37 GHz UL transmission experiments: (a) Measured EVM versus the RoP and (b) calculated BER versus received RF power after OB2B, 10 km SSMF and hybrid transmissions. (c) – (d) are the received RF spectra and constellation diagrams for OB2B and hybrid links, respectively.

6.2. Heterogenous 60/25 GHz signal transmission

In this Section, a heterogeneous system for mmW signal transmission based on a 10 km SSMF, 100 m FSO and 2 m radio seamless wireless links based on DML, as shown in Figure 6.8, is set up to demonstrate bidirectional signal performance using 60 GHz for DL and 25 GHz for UL [145].

6.2.1. Experimental setup and system optimization

As depicted in Figure 6.8(a), the DL employs a DML, which is a monolithically-integrated passive feedback laser described in [146], centered at 1551.7 nm (the optical spectrum is shown in inset (i) of Figure 6.8(a) and driven through a bias tee (SigTek SB12D2) by an electrical M-QAM OFDM LTE data signal carried at 1 GHz IF which is generated by a DG (Rohde & Schwarz SMW200A). The CS-MZM is employed for the frequency up-conversion of the DML output signal where the frequency of the electrical driving signal at the MZM (Optilab IML-1550-50-PM) is $f_{RF} = f_{mmW}/2 = 30$ GHz. The MZM output signal, whose spectrum is shown in inset (ii) of Figure 6.8(a), is transmitted over the 10 km long SSMF Section and the 100 m FSO link (see Figure 6.8(b)), which is realized by two doublet collimators (Thorlabs

F810APC-1550) with the total FSO insertion loss of 14 dB. Note that the FSO link is placed indoors so that any environmental effect can be neglected. After the FSO link, the signal is amplified in a post-amplification stage by an EDFA (Keopsys CEFA-C-HG-SM-50-B130-FA-FA) to compensate the optical losses. A VOA allows to adjust the RoP after the EDFA. The PD (Finisar XPDV3120) performs the opto-electrical conversion where both $\pm f_{RF}$ sidebands of the modulated signal beat each other to generate the desired $f_{mmW} = 60$ GHz signal. Then, the generated signal is amplified by a LNA EA (SAGE SBL-5037033550-VFVF-S1) and radiated by a pyramidal horn ANT-1 (RF spin H-A90-W25) over a 2 m long wireless radio link. Finally, the same type of the receiving antenna allows the signal reception and the further analysis is accomplished in the RFSA (Rohde & Schwarz FSW). An electrical down-converter (Rohde & Schwarz FS-Z90) is employed before the signal analysis due to the frequency limitation of the available instrumentation.

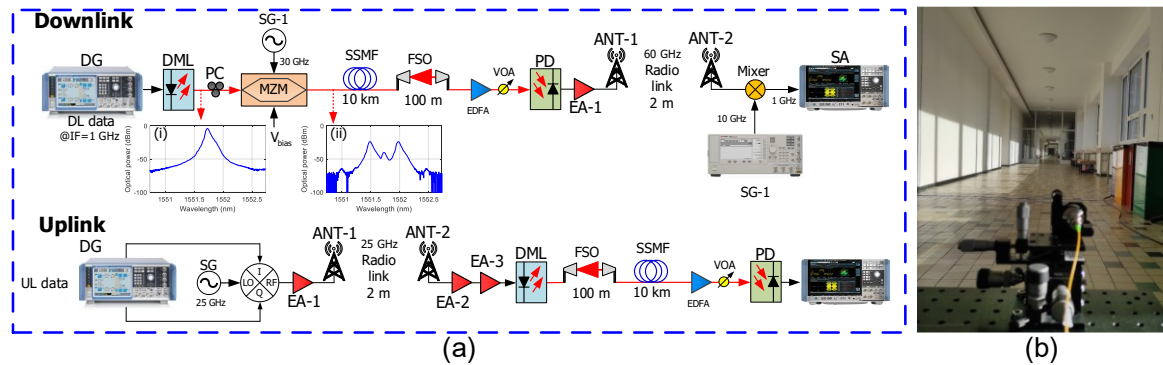


Figure 6.8. Experimental setup: (a) downlink at 60 GHz and uplink at 25 GHz and (b) photograph of the coupling from fiber to FSO. Insets show the signal spectra: (i) DML output, (ii) MZM output.

The setup for the UL link at 25 GHz, also shown in Figure 6.8, employs the same DG as in the DL to generate a fixed I/Q signal output which is combined with the local oscillator signal at 25 GHz by using an RF mixer. Note that the DL and UL are not measured simultaneously. The resulting signal is amplified by EA-1 (Wisewave AGP- 33142325-01) and transmitted by a double ridged horn antenna (RF Spin DRH40) through the 2 m long wireless radio link. The received signal is amplified in two identical cascaded amplifiers (EA-2 and EA-3) (MITEQ AMF-4F-260400-40-10P) and launched into the DML, which is already described above, for electro-to-optical conversion prior to transmission over the wired and wireless optical links. Finally, an EDFA and a VOA are also used to compensate the losses and adjust the optical power at the PD, which performs the opto-to-electronic conversion. The recovered data are then analysed in the SA.

The experimental parameters of DL and UL links are fully detailed in Table 6.1 for every component employed in the setup.

The experimental study of the optimization for each link is crucial to assure the correct performance. The radio signal employed in DL characterization is composed of LTE TM 3.1 with the bandwidth of 20 MHz and variable electrical power, P_{data} , at 1 GHz IF. Note that the predefined test model TM 3.1, designated for the base stations' testing, employs OFDM signals with 64-QAM modulation [147]. The obtained results from the characterization are shown in Figure 6.9(a). OB2B exhibits a minimum EVM value for a given $P_{data} = 5$ dBm under constant RoP = -3 dBm. As expected, the EVM decreases with increasing electrical power at low power values due to corresponding higher SNR, but for P_{data} above 5 dBm, the EVM starts to increase due to the non-linear distortion introduced by the DG and the DML at higher power levels. The same behaviour is also observed when the fiber is employed (SSMF in Figure 6.9(a)). However, it can be seen a shift of the curves due to the dispersion effects over the DML distorted output signal. This characterisation is repeated for the scenario based on SSMF followed by the radio sub-link and for the full-link, which corresponds to the complete scheme in Figure 6.8, i.e. including SSMF, FSO and the radio sub-link. Nevertheless, for both scenarios which include the antenna link, i.e. the SSMF + radio and full-link, the RoP is increased up to

8 dBm to obtain acceptable EVM levels. Similar performance is obtained in both curves provided the amount of losses is compensated by the addition of EDFAs and EAs in each scenario. The minimal EVM values are higher than in OB2B scenario due to the balance between the distortion effects and the current noise, namely shot noise. Therefore, the use of optimal P_{data} for a particular scenario is required, i.e. $P_{\text{data}} = -12$ dBm is employed for SSMF, SSMF + radio link, and full-link operation while 5 dBm is used for the OB2B scenario, as described in Table 6.1.

Table 6.1. Experimental parameters.

Downlink			Uplink			
DG	20 MHz 64-QAM LTE		DG	20 MHz, 64-QAM LTE		
	IF	1 GHz		V_{data} (IQ)	0.5 V	
	P_{data}	5 dBm (OB2B) -12 dBm (others)				
SG	f_{RF}	30 GHz	SG	f_{RF}	12.5 GHz	
	P_{LO}	24 dBm		P_{LO}	18 dBm	
DML	λ	1551.7 nm	Radio link	L_{RF}	2 m	
	BW	33 GHz		EA1	G_{EA1}	28.5 dB @25 GHz
	P_{DML}	0 dBm		EA2	G_{EA2}	29 dB @ 25 GHz
SSMF	L_{SSMF}	10 km	EA3	G_{EA3}	29 dB @ 25 GHz	
	α	0.2 dB/km	DML	BW	33 GHz	
FSO	L_{FSO}	100 m		P_{DML}	0 dBm	
	α_{FSO}	14 dB		λ	1551.7 nm	
EDFA	P_{out}	10 dBm	FSO	L_{FSO}	100 m	
				α_{FSO}	14 dB	
PD	BW	70 GHz	EDFA	P_{out}	10 dBm	
	\mathfrak{R}	0.6 A/W		SSMF	L_{SSMF}	10 km
EA1	G_{EA1}	35 dB @ 60 GHz	α		0.2 dB/km	
	NF_{EA1}	5 dB	PD	BW	33 GHz	
RF link	L_{RF}	2 m		\mathfrak{R}	0.72	
ANT	BW	60-90 GHz	ANT	BW	4-40 GHz	
	Gain	25 dBi @60 GHz		Gain @25 GHz	14.2 dBi	

Similar optimisation is also done for the UL direction. As described above, in this case the LO at 25 GHz frequency is mixed with I and Q data from the DG to create the mmW signal at the desired frequency while the radio signal for the UL is the same as for the DL optimization. The electrical power of the LO, P_{LO} , is varied to obtain the EVM performance characterisation of the UL under different configurations and constant RoP of 8 dBm. Note that during the characterization, the I/Q signal voltage is kept the same for all configurations, i.e. 0.5 V. The obtained curves in Figure 6.9(b) show a similar EVM behaviour for all the scenarios, which are EB2B, radio + OB2B, radio + SSMF, and full-link. The different EVM levels at the $P_{\text{LO}} = 18$ dBm indicate the penalty introduced by the OB2B, SSMF and SSMF + FSO links with regards to the

EB2B configuration, which is 2.9%, 5.1% and 6.4% for the radio link + OB2B, radio link + SSMF and full-link, respectively. An EVM peak at $P_{LO} = 15$ dBm is found due to the electrical RF mixer response which is used for the UL mmW signal generation, since it is shown also in the EB2B measurement where no optical components are involved. Regarding P_{LO} , the lowest EVM value is 7.3% and is obtained under the full-link configuration with $P_{LO} = 18$ dBm and thus in this work we adopted this P_{LO} value, as detailed in Table 6.1, for further UL experiments. It is worth to mention that similar low EVM is recorded also for $P_{LO} = 7$ dBm, however we adopted $P_{LO} = 18$ dBm in order to get higher electrical power in the receiver after optical transmission.

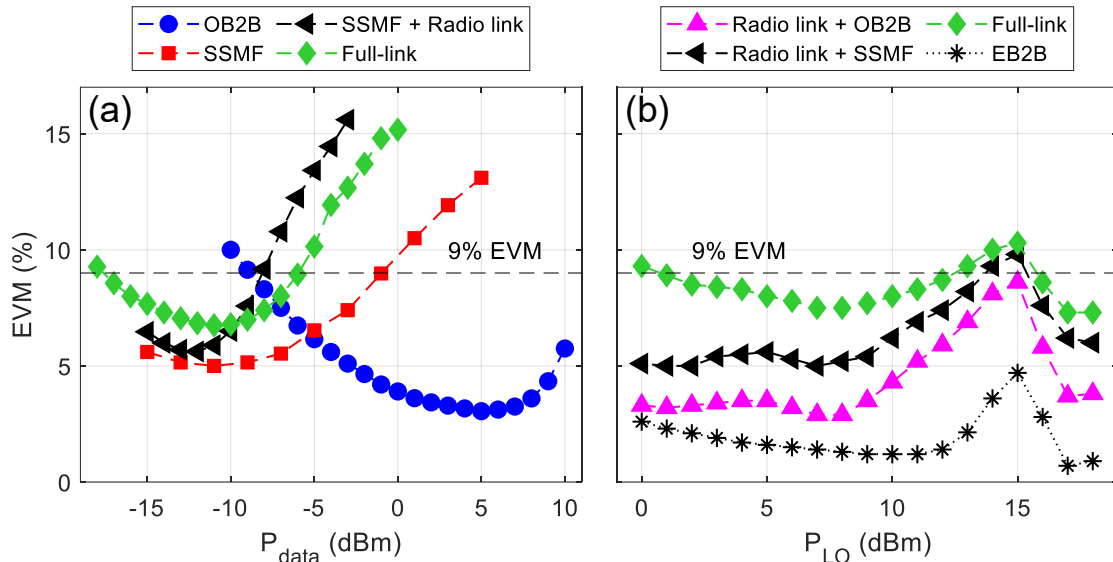


Figure 6.9. (a) DL Signal parameters optimization: measurement of EVM vs. P_{data} for OB2B and SSMF: RoP = -3 dBm; SSMF + radio and full-link: RoP = 8 dBm and (b) UL signal parameters optimization: measurement of EVM vs P_{LO} for different configurations (RoP = 8 dBm) including the EB2B measurement.

6.2.2. Bidirectional signal transmission measurements

In the following part, the DL and UL performances are characterised by measuring the dependence of the EVM on the RoP for a 64-QAM signal transmission in the 60 GHz band (DL) and in the 25 GHz band (UL). Note that according to the previous results, the DL OB2B scenario employed different P_{data} compared to other DL scenarios, i.e. 5 dBm (OB2B) vs -12 dBm (others), so the comparison between them is not straightforward.

The EVM dependence on the RoP obtained for the DL and UL with a 64-QAM are depicted in Figure 6.10. As expected, Figure 6.10(a) shows that the DL EVM decreases with the increasing optical power while the SSMF + radio and full-links imply a power penalty at the 9% threshold (see Appendix A) of 5 and 7 dB, respectively, with regards to the SSMF scenario power level. This is because the SSMF + radio and full-link both contain the 2 m long radio link at 61 GHz, which deteriorates the overall EVM performance. The results imply that for the full-link scenario, the acceptable transmission quality requires a minimum RoP of -2.7 dBm. Note that the additional optical loss, introduced by the VOA, is 11 dB in this case. Insets (i) and (ii) in Figure 6.10(a) then show the 64-QAM constellations for the DL under the OB2B and full-link scenarios, respectively.

Figure 6.10(b) then shows the EVM dependence on the RoP for UL where a penalty of 1.5 and 3 dB is observed when the SSMF and full-links are introduced, respectively, with regard to the OB2B scenario. The required RoP, in this case, is -1 dBm for the full-link operation to keep the EVM below 9%. Note that the maximal additional optical insertion loss is 10 dB in this case and thus 1 dB lower compared to the DL. The difference among particular UL scenarios is less significant, compared to the DL, because the radio link is involved in all of them due to the UL definition. Insets (iii) and (iv) in Figure 6.10(a) depict the constellations for radio link + OB2B and full-link scenarios in UL.

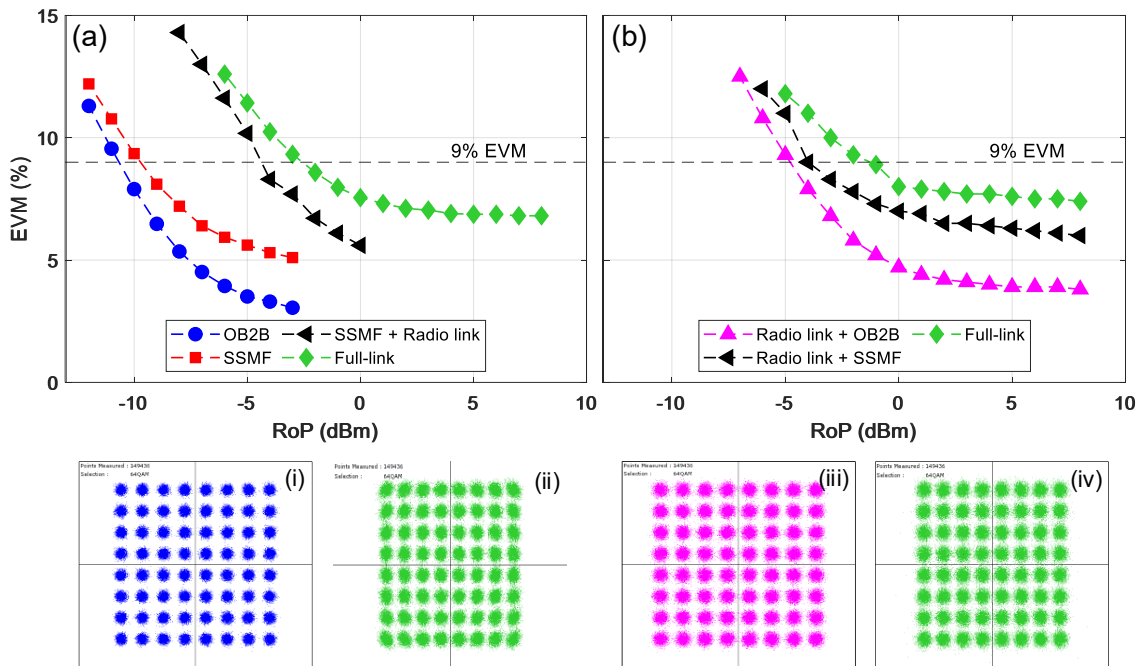


Figure 6.10. EVM vs RoP for 64-QAM with different configuration in both links: (a) 61 GHz DL (b) 25 GHz UL. Corresponding insets show constellations for DL: (i) OB2B (RoP = -3 dBm), (ii) full-link (RoP = 8 dBm); and for UL: (iii) radio and OB2B (RoP = 3 dBm), (iv) full-link (RoP = 9 dBm).

In the following, the EVM characterization is depicted also in terms of the ReP in the mmW band for both DL and UL as shown in Figure 6.11. Note that the different ReP values are set by adjusting the VOA. In the DL, a slight degradation can be seen in Figure 6.11(a) when only the SSMF, i.e. without radio link, is included with respect to OB2B due to the propagation effects of the distorted signal at the DML output. Note that the EVM results experience a significant improvement in terms of ReP in those scenarios where the radio link is present due to the electrical improvement. In the case of the UL, the radio link is present in all scenarios. The Figure 6.11(b) shows similar UL performance results for all the scenarios compared to the DL. According to Figure 6.11, the required ReP = -70 dBm and -57 dBm for the full DL and UL scenarios, respectively.

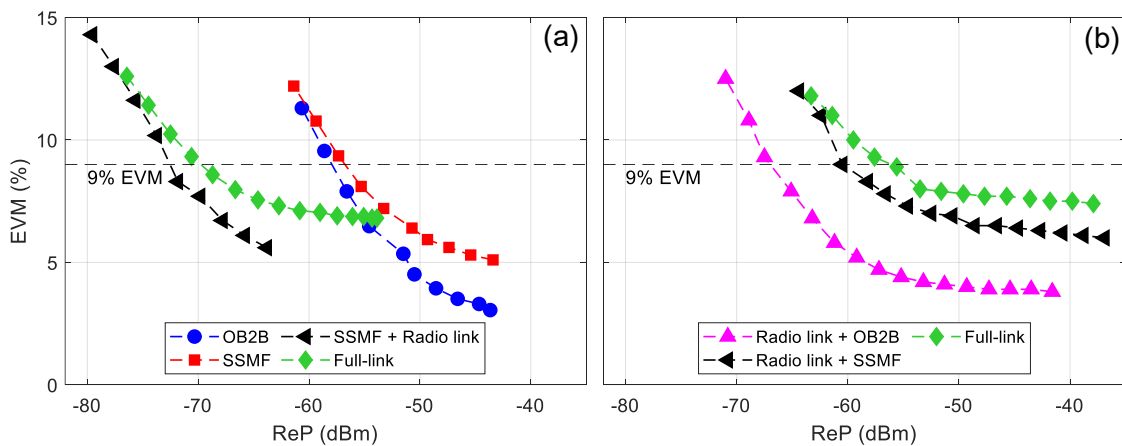


Figure 6.11. EVM vs ReP for 64-QAM signal for: (a) 61 GHz DL, (b) 25 GHz UL.

In the DL, the minimal ReP to keep the EVM below 9% is higher for the scenarios with radio links, i.e. SSMF + radio link and full-link, which is caused by the different power budget in scenarios with and without seamless antenna link. On the other hand, the UL results for the RoP and ReP demonstrate similar behaviour with different EVM for a particular configuration

and fixed ReP. In other words, radio link + OB2B requires lower RoP and ReP value than the radio link + SSMF and full-link scenarios in order to keep the EVM under 9%. It is because the radio link is employed in all the UL scenarios, as already described above.

The DL characterization is done with the 64-QAM and 16-QAM modulation formats (LTE test model TM 3.2) and the EVM dependence on the SNR is measured to provide information about the distortions in the DL transmission system. The 16-QAM performance in Figure 6.12(a) shows very similar behaviour for all scenarios, with an estimation of the minimal required SNR above 22 dB to achieve EVM levels below the 13.5% limit at 16-QAM. Further, Figure 6.12(b) shows the corresponding results for the 64-QAM signal transmission, where a maximum 2.5 dB penalty is observed in the full-link characterization with respect to the OB2B link at the 9% EVM limit. A minimal SNR of 23.7 dB is required for the correct transmission of the 64-QAM signal at 61 GHz for all the scenarios in the DL. Insets in Figure 6.12(a) and (b) show the corresponding constellation diagrams of transmitted signals over the full-link with an SNR of 28 dB. As explained above, good EVM performance in the UL requires the maximization of the electrical power in the receiver and that leads to increased amplifiers noise and IMD, which both affect the measured SNR magnitude. In this case, varying the optical losses does not provide valuable information with regards to the SNR, and therefore, EVM vs. SNR is not shown for UL.

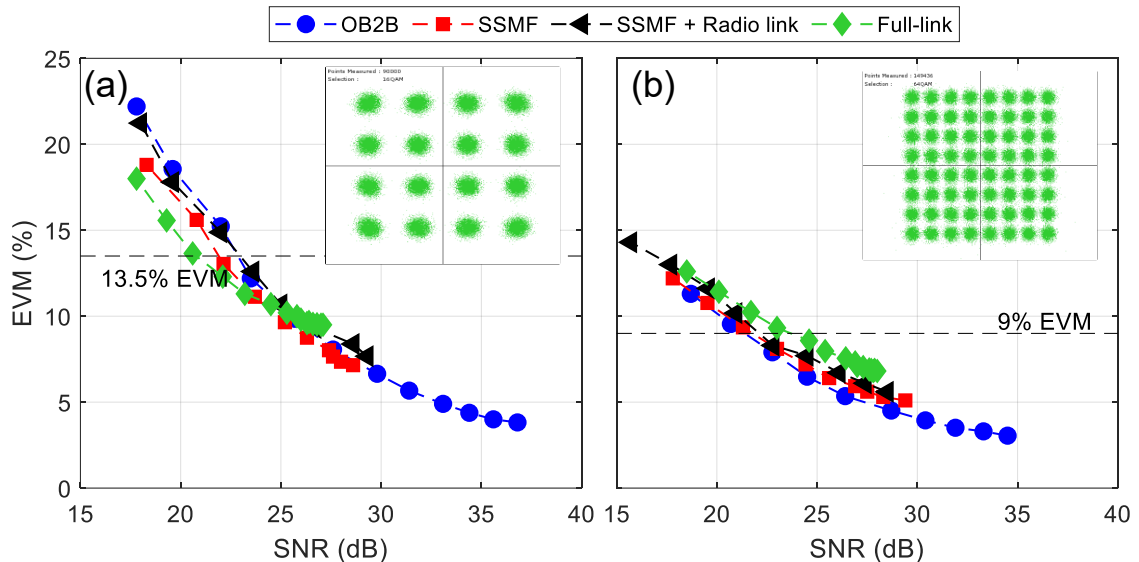


Figure 6.12. EVM vs SNR measured for DL with different modulation formats: (a) 16-QAM, (b) 64-QAM. Insets: Constellations of transmitted signals over the full-link with an SNR of 28 dB.

6.3. Conclusions

In this Chapter, a hybrid full-duplex MWP scheme has been experimentally demonstrated in mmW 5G RAN with a cost-effective and flexible deployment. Experimental results demonstrate data transmission meanwhile DL and UL signals are simultaneously transmitted over the ODN. More concretely, single user – 4 Gbit/s and three multi-user – 1 Gbit/s per user (3 Gbit/s in total) at 39 GHz, and a single user – 2.4 Gbit/s at 37 GHz have been transmitted over hybrid links for DL and UL direction, respectively. Indeed, multiband signals transmission, i.e. multi-user, shows the effectiveness of using the variable QAM allocations scheme for delivering different multi-Gbits/s signals over the full-duplex hybrid link in DL direction, i.e. 1 Gbit/s in DL. The achieved EVMs and BERs for all DL and UL signals are well below the required threshold level which confirm the potential use of the proposed system to provide high-speed broadband services in full-duplex fronthaul links.

Secondly, a LTE M-QAM signal transmission over the 60 and 25 GHz bands for the DL and UL over an optical heterogeneous fronthaul network has been demonstrated

experimentally. The experimental setup implements the bidirectional fronthaul link consisting of 10 km optical fiber and 100 m FSO as real distance to circumvent obstacles, e.g. river or lake. Moreover, it is also included a 2 m seamless radio link as a distance between the user and BS in a femtocell, i.e. low-power, low-range cellular base stations (from 10 m to 1 km). The measurement results of full-duplex system show the feasibility of DML usage in both DL and UL links exhibits some benefits. For the DL, the DML is a very cost-effective solution, which reduces cost and complexity especially because it combines the laser and modulator into one device and even for the 60 GHz transmission. Further, it benefits from the frequency doubling in the photonic generation approach, resulting in a significant reduction of the equipment requirements. Additionally, the use of the high frequency bandwidth DML for the UL also reduces complexity and potential costs because of the DML, which having smaller footprint compared to the laser and MZM, can be produced in a large series and then become more affordable. Therefore, the BS in the cell site can be significantly simpler in future B5G networks deployment.

Chapter 7. Conclusions and future work

“At my signal, unleash hell.”

– Maximus, Gladiator (2000)

7.1. Conclusions

This Thesis aims to make a step forward in enabling architectures and technologies for the new standard, 5G, which can satisfy the ever-growing user demand. The main goals include experimental mmW signal generation and data transmission in 5G networks. More concretely, this Thesis has been oriented towards the implementation of the fronthaul link in the new RAN architectures, the use of MWP technology for mmW signal generation and RoF transmission, and also, the signal transmission employing FSO, which can be directly used in 5G optical communications. Extensive experiments are conducted to confirm new potential schemes employing the aforementioned enabling technologies for 5G networks.

The basic analytical formulation of CS-DSB configuration based on MZM, which has enabled to employ a simplified and practical approach for mmW signal generation and transmission over hybrid links, has been studied in detail. CS-DSB scheme enables to reduce the bandwidth components while experimental results show high frequency mmW signals, i.e. up to 90 GHz, and low phase noise, i.e. -87 dBc/Hz. CS-DSB configuration can be also employed in potential reconfigurable signal distribution schemes which provides huge flexibility of frequency allocation in 5G networks. Moreover, non-linear effects, e.g. FWM, can assist CS-DSB schemes and enable huge reduction of electronic bandwidth requirements, e.g. the electro-optic modulator. However, the optical signal transmitted over FSO channel undergoes atmospheric turbulences which degrades the generated mmW signal, as has been evaluated in this work. More concretely, the thermally induced turbulence profiles generate optical power fluctuations which lead to an electrical power reduction, and therefore, an increase of the signal phase noise.

The intensity modulation of a DML provides sufficient bit rate with reduced complexity and cost in 5G network. In particular, theoretical analysis of remote and local photonic mmW signal generation schemes have been presented showing very good agreement with measurement results. More concretely, since the photonic mmW signal generation is held at CO in remote setup, the interplay between the DML chirp and chromatic fiber dispersion leads to higher frequency response than the local setup, although higher HD and IMD products are obtained under remote configuration. Indeed, the impact of harmonic and intermodulation distortion on data transmission has been experimentally studied when multiband signals are transmitted. The experimental results of in-band and out-of-band in multiband signals shows poor signal

transmission under remote scheme for certain frequency values and/or bandwidth, and local generation mmW approach in C-RAN must be employed. Finally, the system capability has been evaluated by simulations and measurements in terms of signal bandwidth, fiber length and laser chirp. Very good agreement has been shown between simulations and measurement results, where the DML chirp has a crucial influence on signal transmission, specially in long fiber length and high bandwidth links.

The external modulation, which provides higher bandwidth compared with a laser directly modulated, can be also employed for data transmission. An experimental setup based on CS-DSB and data external modulation with seamless antenna transmission at 26 GHz has been demonstrated, where the usage of electrical filter at mmW signal enables the seamless wireless transmission of 5G signals, e.g. 200 MHz 64-QAM. Moreover, the CS-DSB scheme has been compared with the DSB classical approach at mmW frequencies. The results show that CS-DSB offers immunity to chromatic dispersion-induced fading, but DSB exhibits better EVM performance, i.e. higher bandwidth/bit rate, since the MZM is biased at the linear point instead of the null point in CS-DSB. Finally, data transmission over mmW signal over thermally induced atmospheric turbulent FSO has been simulated and experimentally evaluated. Experimental results of uniform turbulence confirms that high turbulence regime produce higher optical signal degradation which cause poor EVM. On the other hand, simulations and experimental results of non-uniform turbulences show good agreement showing signal degradation produced by high peak thermal turbulence in the FSO channel.

Finally, this Thesis presents two experimental demonstrators of bidirectional DL and UL for 5G networks at mmW frequencies, which employ the techniques explained in the previous Chapters. First, a hybrid full-duplex scheme enables single- or multi-user DL and UL signal transmission simultaneously over hybrid link at 39 and 37 GHz, respectively, with a maximum bit rate of 4 Gbit/s and 1 Gbit/s for DL and UL, respectively. Secondly, signal transmission at 60 and 25 GHz over a hybrid link and seamless radio link for DL and UL, respectively, has been presented and demonstrated. In particular, the experiment employs 100 m FSO as a practical fronthaul distance and a high frequency bandwidth DML for the UL which reduces complexity and potential costs, and emulates the full-link by a wireless mmW signal transmission. This scheme has been successfully demonstrated experimentally, and therefore, confirm the simplification of the BS in the cell site for 5G and beyond network deployment while provides high speed broadband services in full-duplex fronthaul links.

7.2. Future work

This Thesis has contributed to the development of new mmW signal transmission and distribution schemes for hybrid fronthaul links in 5G networks. However, there are several aspects related to this Thesis which might be further developed and therefore, they are suggested as future work.

Some experiments have been limited by the bandwidth of the available components, e.g. the DML bandwidth is lower than 10 GHz. Further experiments employing a DML with larger bandwidth can be done so electrical signals can be directly modulated without external modulation at UL. No external modulator is required and, then, the complexity and cost of the BS can be reduced. Moreover, if such lasers are available, other MWP-based technique employing DSB and optical filters will avoid the use of MZM in DL, as proposed in this Thesis. It is worth to mention that such technique was employed in some of the previous work and the obtained mmW signals presented worse quality due to carrier suppression reduction. Further work might be done to optimise such scheme where highly linear lasers are required.

In this Thesis, second and third order distortion of local and remote schemes based on DML have been evaluated. Since non-linear response of the DML has been mainly considered, the analytical evaluation of the distortion can be extended to include non-linear modulator response and also, the radio wireless link to identify is the impact in real systems.

In full-duplex scheme, mmW signals are generated and transmitted in the DL direction employing MWP techniques. Then, the generated mmW signal at PD is radiated by the

antenna. However, since the 5G standard enables mmW frequencies at DL and UL, high frequency LOs may be need at BS for down conversion, which increase costs. Therefore, remote optical LO delivery can be proposed. In this scheme, the CO can employ WDM techniques to transmit optical signals and an optical LO. After optical transmission, the signals are demultiplexed and a mmW signal tone is generated. Consequently, wireless UL signals can be down converted at mmW frequencies by the generated tone and, then, directly modulated using low speed DMLs for optical transmission to the CO which reduce the cost and complexity of BS.

Moreover, alternative photonic mmW signal generation techniques can be introduced. Following the fundamental approach, as explained in Chapter 2, based on the optical heterodyning of two free-running lasers. The use of two independent lasers, e.g. DML and DFB laser, would be a challenge since a mmW signal with high phase noise is generated. To demonstrate an optical mmW signal generation system without RF source, i.e. two free-running lasers, and signal data transmission, where the phase noise will not play a critical role would be very attractive. Moreover, the local configuration can be employed to provide higher frequency flexibility. Of course, novel schemes and further optimization will be necessary to reduce the cost and complexity.

Finally, in this Thesis, mmW enabling technology has been proposed and studied for 5G networks. However, spectrum key enabling technologies, e.g. THz and optical wireless communication (OWC), including visible light communication (VLC), are also proposed for 5G and B5G. Since a standalone enabling technology is usually developed, further studies of coexistence between the key technologies, i.e. mmW, THz and OWC, may be promoted in terms of schemes/architectures and performances to allow full exploitation of mobile standards in energy efficient future generation communication networks.

Appendix A

A.1. Complex data signal on IM-DD systems

In IM-DD technique, the input signal must be real and positive to be modulated by optical intensity without information loss [148, 149, 150]. After optical transmission, direct detection is held by a photodiode at the receiver. Since the optical signal is modulated by a positive and real data signal, the data signal is recovered by detecting the intensity of received light (explained in Section 4.1), i.e. the envelope of the optical signal (equation (4.2), without loss of information.

Figure A.1(a) shows the schematic diagram of a signal data generator [151] when a M-QAM or QPSK signal is used. At the transmitter, after appropriate digital signal processing (DSP), the I/Q data streams are generated and are modulated by an IF. The two orthogonal modulated signals are then combined to generate a real-value modulated signal at the IF frequency which can be intensity modulated. On the other hand, at the receiver (Figure A.1(b)), the transmitted signal is demodulated with the IF, and I/Q components of complex amplitude are obtained at the baseband which are decoded by the DSP.

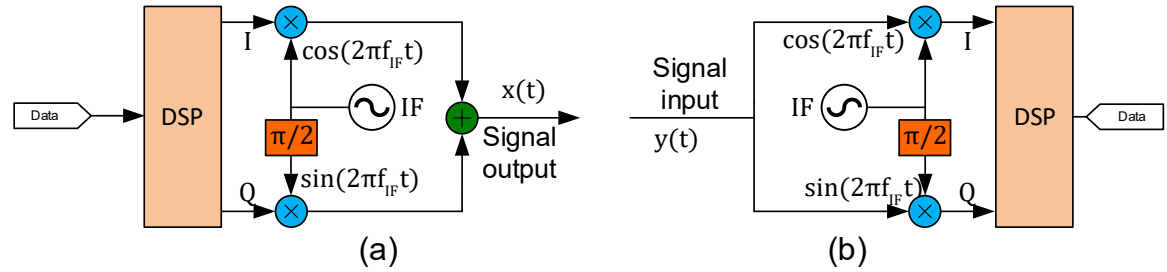


Figure A.1. (a) I/Q electrical modulator and (b) demodulator scheme.

In OFDM IM-DD, the Hermitian symmetry technique is used to obtain a real signal in the system where the incoming symbols are restricted to inverse Fast Fourier transform (IFFT) at which the imaginary signal is excluded [152, 153]. Figure A.2(a) shows a simplify transmitter diagram of OFDM Hermitian symmetry technique. The complex data signal, $X = [X_0, X_1, X_2, \dots, X_{N-1}]$ is launched into the IFFT. The X signal is constrained to have Hermitian symmetry, as defined:

$$X_m = X_{N-m}^* \text{ for } 0 < m < \frac{N}{2}, \quad (\text{A.1})$$

with X_0 and $X_{N/2}$ are set to zero, i.e. $X_0 = X_{N/2} = 0$. Due to the Hermitian symmetry of the input, the output signal of the IFFT, x , is real and can be directly employed in IM-DD systems [154]. At the receiver, the data signal is recovered by detecting the intensity of received light, and a reverse process back to the transmitter, shown in Figure A.2(b), is implemented.

Figure A.3(a) displays a OFDM transmitter using IF up conversion [155]. At the transmitter, after parallel to serial mapping, the data streams are converted into analog signal by DAC. This allows the complex baseband OFDM signal to be mixed with an IF carrier which can be intensity modulated. The analog up conversion allows flexible placement of the signal spectrum relative to the optical carrier and the IF frequency is independent of the DAC sample rate. At the receiver, after detecting the intensity of received light, the data signal is recovered by an inverse process to the transmitter, illustrated in Figure A.3(b).

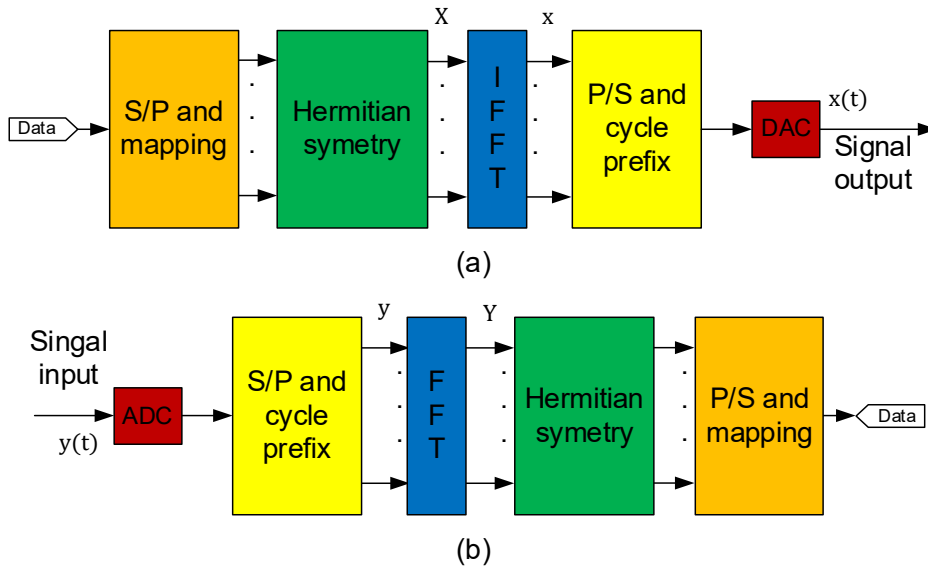


Figure A.2. Block diagram of an IM-DD system using OFDM signals. (a) Transmitter and (b) receiver.

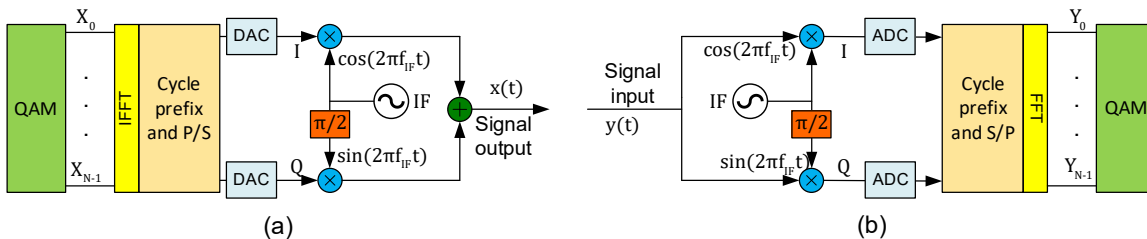


Figure A.3. Transmitter (a) and receiver (b) block diagram of OFDM signals in IM-DD system using up conversion.

A.2. Error vector magnitude

EVM is a common parameter to measure the quality of modulated telecommunication signals. It expresses the difference between the expected symbol and the value of the actual received symbol. An ideal communication system will have equal value of measured and reference vector, which indicates its EVM parameter would be zero.

The EVM concept is illustrated in Figure A.4. A transmitted signal by an ideal transmitter or received signal by a receiver would have all constellation points at their ideal positions. However, the communication system will cause the actual received constellation points to deviate from the ideal positions.

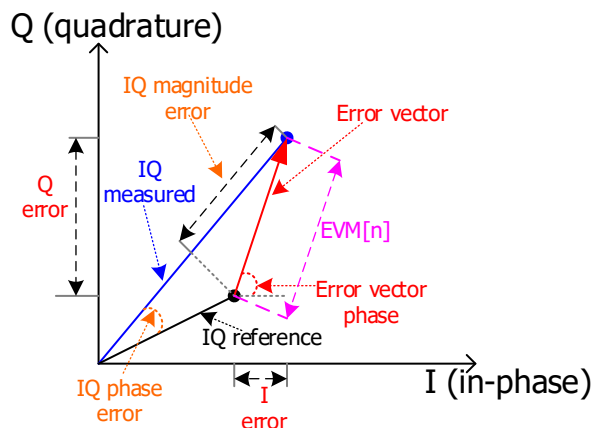


Figure A.4. EVM diagram.

In general, EVM is averaged over an ensemble of symbol trajectories and can be defined numerically as [156]:

$$EVM_{rms} = \sqrt{\frac{\frac{1}{k} \sum_{k=1}^N |s_t - s_r|^2}{\frac{1}{k} \sum_{k=1}^N |s_t|^2}}, \quad (\text{A.2})$$

where k is the number of received symbols, s_t and s_r are the n^{th} ideal transmitted and received symbol, respectively.

The EVM thresholds for 4G and 5G standard according to the 3GPP are shown in Table A.1 [147] and Table A.2 [28].

Table A.1. LTE EVM thresholds [147].

Modulation format	EVM (%)
QPSK	18.5
16-QAM	13.5
64-QAM	9
256-QAM	4.5

Table A.2. 5G EVM threshold for FR2 [28].

Modulation format	EVM (%)
QPSK	17.5
16-QAM	12.5
64-QAM	8
256-QAM	3.5

A.3. Bit error rate

BER provides an estimation of digital transmission quality based on the quantity or percentage of transmitted bits that are received incorrectly. In a digital transmission, it is the number of bits with errors divided by the total number of bits that have been transmitted, received or processed over a given time period, i.e.:

$$BER = \frac{\text{number of bits with errors}}{\text{total number of bits sent}}. \quad (\text{A.3})$$

When the signal is only corrupted by additive white Gaussian noise (AWGN) and if the EVM is measured over large values of number of bits [143, 156], it can be rewrite as:

$$EVM_{rms} \approx \frac{1}{\sqrt{SNR}}, \quad (\text{A.4})$$

where SNR is the signal-to-noise ratio.

Finally, the BERs of M-ary QAM from the EVMs based on the relationship can be calculated as [143, 156]:

$$BER = \frac{2}{\log_2 M} \left(1 - \frac{1}{\sqrt{M}}\right) \cdot \text{erfc} \left(\sqrt{\frac{3}{2(M-1)} SNR} \right), \quad (\text{A.5})$$

where M is the modulation format order and $\text{erfc}(\cdot)$ is the complementary error function. Note that the above equation holds for QAM signals but not for binary phase shift keying (BPSK) signals. The relationship between BER and EVM (equation (A.5)) is shown in Figure A.5. BER vs EVM performance curves for M-QAM modulation format .Figure A.5 for different M-QAM modulation format, i.e. 4, 16, 64 and 256.

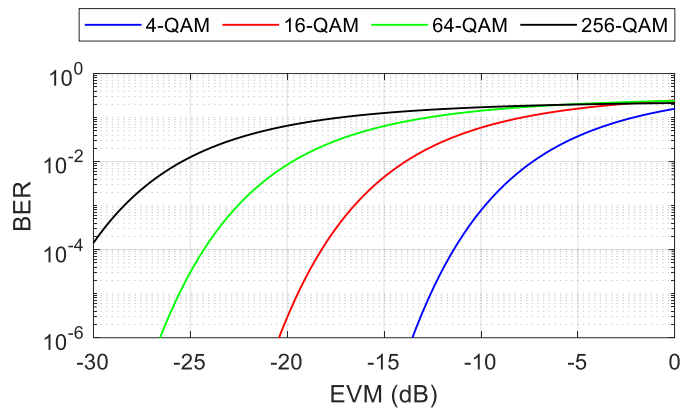


Figure A.5. BER vs EVM performance curves for M-QAM modulation format [143].

The FEC is usually characterized by the minimum SNR that allows a decoder to recover all transmitted information without any error. However, in optical communications it typically characterizes FEC performance by the maximum tolerable pre-FEC bit BER, called the 'FEC threshold', that still allows the FEC to correct errors down to a very low value. For example, for 7% overhead hard decision-FEC with a net coding gain (NGC) of 9.19 dB at a corrected BER of 10^{-15} , the pre-FEC BER should be lower than $3.8 \cdot 10^{-3}$ [157, 158], which is regarded as 'error-free' in the context of optical transport networks.

A.4. Signal generators and analyzers

Along the Thesis, the experimental setups required to generate and analyse a variety of signals, as described in the document. This Section presents some details of the equipment mostly employed in the different experiments.

The AWG7122C is an arbitrary waveform generator, shown in Figure A.6(a), with up to 24 GS/s, 9.6 GHz analog bandwidth and 10 bit vertical resolution. This allows for easy generation of very complex signals. In this Thesis, RFXpress software, included in the generator, allows the complex signal generation, i.e. single and multiband M-QAM signals. In this case, the data signal can be delivered through channel #1 or #2, as a real signal, explained above.

The SMW200A is a vector signal generation which covers the frequency range up to 40 GHz. It can generate signals with a maximum 2 GHz modulation bandwidth and supports the 5G NR standard. This generator enables the real data signal generation through the RF output port and the complex data signal generation, i.e. I/Q components, through the I and Q output ports located at the front and rear panel, respectively.

The DPO72004C oscilloscope, shown in Figure A.7(a), delivers exceptional signal acquisition performance and analysis capability. It is equipped with four channels with 20 GHz analog bandwidth. The RF signal is launched into the RF port, located in the front panel, and is analyzed by the SignalVu software. This software enables to apply an adaptive equalizer to a digitally modulated signal to compensate for linear distortions in the signal. During the measurement process, the mode, i.e. specifies whether the equalizer is in learning mode or analysis mode; the convergence, i.e. specifies the update rate; and the number of taps, i.e. the number of filter coefficients are adjusted in the equalizer.

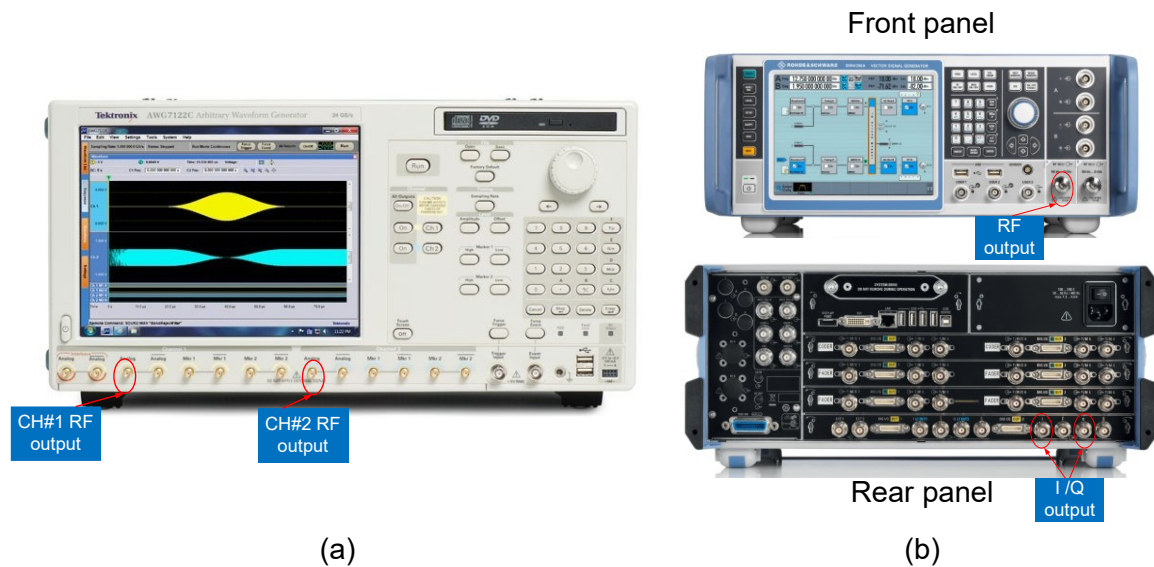


Figure A.6. Signal generators employed in this Thesis: (a) Tektronix AWG7122C and (b) Rohde & Schwarz SMW200A -front and rear view.

Finally, the high-performance FSW43 signal and spectrum analyzer allows to accomplish the Thesis measurements with 5G NR standard. It covers the frequency range 2 Hz to 43.5 GHz and provides a 5 GHz analysis bandwidth. The RF signal is launched into the RF port, located in the front panel. The 5G NR signals are analyzed by its 5G NR application and no equalization is required. However, the data signals, i.e. M-QAM, are analyzed by the RFSA. In this case, the RFSA equalizer has to be adjusted, i.e. mode, convergence and number of taps in order to compensate for the transmitter, channel and receiver impairments.



Figure A.7. Signal analyzers employed in this Thesis: (a) Tektronix DPO72004CC and (b) Rohde & Schwarz FSW43.

List of publications

Journals

- J.1. **L. Vallejo**, B. Ortega, J. Mora, D. -N. Nguyen, C. Guerra, J. Bohata, J. Spacil, S. Zvanovec, "Demonstration of M-QAM OFDM Bidirectional 60/25 GHz Transmission over 10 km Fiber, 100 m FSO and 2 m Radio Seamless Heterogeneous Fronthaul Link," submitted to *Optical Fiber Technology*, 2022.
- J.2. **L. Vallejo**, J. Mora, B. Ortega, "Harmonic and Intermodulation Distortion Analysis in Directly Modulated Lasers over Local and Remote Photonicallly Generated Millimeter-Wave Signals," in *Journal of Lightwave Technology*, vol. 40, no. 15, pp. 5128-5140, 2022, doi: 10.1109/JLT.2022.3172771.
- J.3. J. Bohata, **L. Vallejo**, B. Ortega and S. Zvanovec, "Optical CS-DSB Schemes for 5G mmW Fronthaul Seamless Transmission," in *IEEE Photonics Journal*, vol. 14, no. 2, 2022, doi: 10.1109/JPHOT.2022.3161087.
- J.4. D. -N. Nguyen, **L. Vallejo**, V. Almenar, B. Ortega, P. T. Dat, S. T. Le, J. Bohata, and S. Zvanovec, "39 GHz Full-Duplex Transmission of Multi-Gb/s Subcarrier Multiplexing and 5G NR Signals over Fiber and Space for Industry 4.0," in *Applied Optics*, vol. 61, no. 5, pp. 1183-1193, 2022, doi: 10.1364/AO.447529.
- J.5. J. Bohata, D. -N. Nguyen, J. Spáčil, M. Komanec, B. Ortega, **L. Vallejo**, Z. Ghassemlooy, and S. Zvánovec, "Experimental comparison of DSB and CS-DSB mmW formats over a hybrid fiber and FSO fronthaul network for 5G," in *Optics Express*, vol. 29, no. 17, pp. 27768-27782, 2021.
- J.6. **L. Vallejo**, J. Mora, D. -N. Nguyen, J. Bohata, V. Almenar, S. Zvanovec, and B. Ortega, "On the 40 GHz Remote versus Local Photonic Generation for DML-based C-RAN Optical Fronthaul," in *Journal of Lightwave Technology*, vol. 39, no. 21, pp. 6712-6723, 2021, doi: 10.1109/JLT.2021.3102818.
- J.7. **L. Vallejo**, B. Ortega, D. -N. Nguyen, J. Bohata, V. Almenar and S. Zvanovec, "Usability of a 5G Fronthaul Based on a DML and External Modulation for M-QAM Transmission Over Photonicallly Generated 40 GHz," in *IEEE Access*, vol. 8, pp. 223730-223742, 2020, doi: 10.1109/ACCESS.2020.3042756.
- J.8. D.-N. Nguyen, **L. Vallejo**, J. Bohata, B. Ortega, Z. Ghassemlooy and S. Zvanovec, "Wideband QAM-over-SMF/turbulent FSO downlinks in a PON architecture for ubiquitous connectivity," in *Optics Communications*, vol. 475, no. 126281, 2020, doi: 10.1016/j.optcom.2020.126281.
- J.9. **L. Vallejo**, D. Nguyen, J. Bohata, B. Ortega, and S. Zvanovec, "M-QAM signal transmission at the photonicallly generated K-band over thermal-induced turbulent FSO links with different turbulence distributions," in *Applied Optics*, vol. 59, no. 16, pp. 4997-5005, 2020, doi: 10.1364/AO.390103.
- J.10. **L. Vallejo**, M. Komanec, B. Ortega, J. Bohata, D.-N. Nguyen, S. Zvanovec and V. Almenar, "Impact of Thermal-Induced Turbulent Distribution Along FSO Link on Transmission of Photonicallly Generated mmW Signals in the Frequency Range 26–40 GHz," in *IEEE Photonics Journal*, vol. 12, no. 1, 2020, doi: 10.1109/JPHOT.2019.2959227.
- J.11. **L. Vallejo**, B. Ortega, J. Bohata, S. Zvanovec and V. Almenar, "Photonic multiple millimeter wave signal generation and distribution over reconfigurable hybrid SSMF/FSO links," in *Optical Fiber Technology*, vol. 54, 2020, doi: 10.1016/j.yofte.2019.102085.

Conference proceedings

- C.1. **L. Vallejo**, J. Bohata, D.-N. Nguyen, B. Ortega, J. Mora, and S. Zvanovec, "Heterogeneous RoF, RoFSO and RF bidirectional links in n79 5G band," *2022 13th International Symposium on Communication Systems, Networks and Digital Signal Processing (CSNDSP)*, 2022.
- C.2. **L. Vallejo**, B. Ortega, D. -N. Nguyen, J. Bohata, J. Mora, and S. Zvanovec, "Multiband IFoF signal transmission based on DML with local photonic 40 GHz up conversion," *2021 17th International Symposium on Wireless Communication Systems (ISWCS)*, 2021, doi: 10.1109/ISWCS49558.2021.9562239.
- C.3. **L. Vallejo**, D. -N. Nguyen, B. Ortega, J. Bohata, V. Almenar and S. Zvanovec, "Flexible Multiband Signal Transmission using a Directly Modulated Laser over Photonicallly Generated 40 GHz," *2021 Joint European Conference on Networks and Communications & 6G Summit (EuCNC/6G Summit)*, 2021, doi: 10.1109/EuCNC/6GSummit51104.2021.9482455.
- C.4. **L. Vallejo**, D. -N. Nguyen, S. Zvanovec, B. Ortega and J. Bohata, "64-QAM LTE signal transmission at 25 GHz over hybrid SSMF and non-uniform turbulent FSO channel," *2020 3rd West Asian Symposium on Optical and Millimeter-wave Wireless Communication (WASOWC)*, 2020, pp. 1-5, doi: 10.1109/WASOWC49739.2020.9409970.
- C.5. D. -N. Nguyen, J. Bohata, **L. Vallejo**, S. Zvanovec, B. Ortega and Z. Ghassemlooy, "On N-PAM and M-QAM implementation within the hybrid RoF-FSO-PON system," *2020 3rd West Asian Symposium on Optical and Millimeter-wave Wireless Communication (WASOWC)*, 2020, pp. 1-5, doi: 10.1109/WASOWC49739.2020.9410197.
- C.6. **L. Vallejo**, D. -N. Nguyen, S. Zvanovec, B. Ortega, J. Bohata and V. Almenar, "Comparison of carrier suppressed and quadrature bias point external modulation for 40 GHz millimeter-wave photonic generation using a 16-QAM signal with directly modulated laser," *2020 12th International Symposium on Communication Systems, Networks and Digital Signal Processing (CSNDSP)*, 2020, pp. 1-5, doi: 10.1109/CSNDSP49049.2020.9249619.
- C.7. D. -N. Nguyen, **L. Vallejo**, J. Bohata, S. Zvanovec, B. Ortega and Z. Ghassemlooy, "Transmission of 2 bits/symbol over RoF and RoFSO links with different architectures for ubiquitous coverage," *2020 12th International Symposium on Communication Systems, Networks and Digital Signal Processing (CSNDSP)*, 2020, pp. 1-5, doi: 10.1109/CSNDSP49049.2020.9249594.
- C.8. J. Bohata, T. Lonsky, J. Spacil, P. Hazdra, M. Komanec, S. Zvanovec, **L. Vallejo** and B. Ortega "Antenna Phased Array Beamforming at 26 GHz Using Optical True Time-Delay," *2020 12th International Symposium on Communication Systems, Networks and Digital Signal Processing (CSNDSP)*, 2020, pp. 1-4, doi: 10.1109/CSNDSP49049.2020.9249587.
- C.9. J. Bohata, J. Spacil, D. Nguyen, S. Zvanovec, **L. Vallejo** and B. Ortega, "Radio over 50 km Fiber and Joint 80 m FSO/Wireless Links Using Photonic Frequency Doubling for 5G," *2019 IEEE Global Communications Conference (GLOBECOM)*, pp. 1-6, 2019, doi: 10.1109/LFSO 38437.2019.9013212.
- C.10. **L. Vallejo**, B. Ortega, V. Almenar, J. Bohata, S. Zvanovec and D.-N.-Nhat Nguyen, "SOA-aided photonic signal generation for hybrid fibre and FSO 5G transmission links," *Proceedings Volume 11358, Nonlinear Optics and its Applications 2020; 113581R*, 2020, doi: 10.1117/12.2552726.
- C.11. **L. Vallejo**, B. Ortega, J. Bohata, S. Zvanovec, and V. Almenar, "Experimental photonic 40-90 GHz millimetre-wave signal generation and 10 Gb/s 32-QAM signal transmission

over hybrid fiber/FSO 5G networks”, *2019 21st International Conference on Transparent Optical Networks (ICTON)*, pp. 1-4, 2019, doi: 10.1109/ICTON.2019.8840435.

References

- [1] T. Huang, W. Yang, J. Wu, J. Ma, X. Zhang and D. Zhang, "A Survey on Green 6G Network: Architecture and Technologies," *IEEE Access*, vol. 7, pp. 175758-175768, 2019.
- [2] Cisco, "Cisco annual internet report (2018-2023)," *White paper*, 2020.
- [3] Ericsson, "Ericsson mobility report," 2020.
- [4] ITU-R, "IMT Vision – Framework and overall objectives of the future development of IMT for 2020 and beyond," 2015.
- [5] R. Waterhouse and D. Novack, "Realizing 5G: Microwave Photonics for 5G Mobile Wireless Systems," *IEEE Microwave Magazine*, vol. 16, no. 8, pp. 84-92, 2015.
- [6] G. Barb and M. Otesteanu, "4G/5G: A Comparative Study and Overview on What to Expect from 5G," *2020 43rd International Conference on Telecommunications and Signal Processing (TSP)*, 2020.
- [7] B. M. Shah, M. Murtaza and M. Raza, "Comparison of 4G and 5G Cellular Network Architecture and Proposing of 6G, a new era of AI," *2020 5th International Conference on Innovative Technologies in Intelligent Systems and Industrial Applications (CITISIA)*, 2020.
- [8] C. Lim, Y. Tian, C. Ranaweera, T. A. Nirmalathas, E. Wong and K.-L. Lee, "Evolution of radio-over-fiber technology," *Journal of Lightwave Technology*, vol. 37, no. 6, pp. 1647-1656, 2019.
- [9] J. Yao, "Microwave photonics," *Journal of Lightwave Technology*, vol. 27, no. 3, pp. 314-335, February 2009.
- [10] A. J. Seeds and K. Williams, "Microwave Photonics," *Journal of Lightwave Technology*, vol. 24, no. 12, pp. 4628-4641, 2006.
- [11] S. Bloom, E. Korevaar, J. Schuster and H. Willebrand, "Understanding the performance of free-space optics [Invited]," *Journal of Optical Networking*, vol. 2, no. 6, pp. 178-200, 2003.
- [12] W. Jiang, B. Han, M. A. Habibi and H. D. Schotten, "The Road Towards 6G: A Comprehensive Survey," *IEEE Open Journal of the Communications Society*, vol. 2, pp. 334-366, 2021.
- [13] C. Lim and A. Nirmalathas, "Radio-Over-Fiber Technology: Present and Future," *Journal of Lightwave Tehcnology*, vol. 39, no. 4, pp. 881-889, 2021.
- [14] C. Ranaweera, E. Wong, A. Nirmalathas, C. Jayasundara and C. Lim, "5G C-RAN with optical fronthaul: an analysis from a deployment perspective," *Journal of Lightwave Technology*, vol. 36, no. 11, pp. 2059-2068, 2018.
- [15] M. A. Habibi, M. Nasimi, B. Han and H. D. Schotten, "A Comprehensive Survey of RAN Architectures Toward 5G Mobile Communication System," *IEEE Access*, pp. 70371-70421, 2019.
- [16] H. Asplund, D. Astely, P. Butovitsch, T. Chapman, M. Frenne, F. Ghasemzadeh, M. Hagström, B. Hogan, G. Jongren, J. Karlsson, F. Kronestedt and E. Larsson,

- Advanced Antenna Systems for 5G Network Deployments, 1st ed., Academic Press, 2020.
- [17] M. Peng, Y. Sun, X. Li, Z. Mao and C. Wang, "Recent Advances in Cloud Radio Access Networks: System Architectures, Key Techniques, and Open Issues," *IEEE Communications Surveys & Tutorials*, vol. 18, no. 3, pp. 2282-2308, 2016.
- [18] A. Udalcovs, M. Levantesi, P. Urban, D. A. A. Mello, R. Gaudino, O. Ozolins and P. Monti, "Total Cost of Ownership of Digital vs. Analog Radio-Over-Fiber Architectures for 5G Fronthauling," *IEEE Access*, pp. 223562-223574, 2020.
- [19] C.-L. I, J. Huang, R. Duan, C. Cui, J. Jiang and L. Li, "Recent Progress on C-RAN Centralization and Cloudification," *IEEE Access*, vol. 2, pp. 1030-1039, 2014.
- [20] A. Checko, H. L. Christiansen, Y. Yan, L. Scolari, G. Kardaras, M. S. Berger and L. Dittmann, "Cloud RAN for mobile networks - A technology overview," *IEEE Communications Surveys & Tutorials*, vol. 17, no. 1, pp. 405-426, 2015.
- [21] R. T. Rodoshi and W. Choi, "A Survey on Applications of Deep Learning in Cloud Radio Access Network," *IEEE Access*, pp. 61972-61997, 2021.
- [22] I. A. Alimi, A. L. Teixeira and P. Pereira Monteiro, "Toward an efficient C-RAN optical fronthaul for the future networks: a tutorial on technologies, requirements, challenges, and solutions," *IEEE Communications Surveys & Tutorials*, vol. 20, no. 1, pp. 708-769, 2018.
- [23] L. Gonzalez Guerrero, M. Morant, T. Li, M. J. Fice, A. J. Seeds, R. Llorente, I. H. White, R. V. Penty and C. C. Renaud, "Integrated Wireless-Optical Backhaul and Fronthaul Provision Through Multicore Fiber," *IEEE Access*, vol. 8, pp. 146915-146922, 2020.
- [24] M. Peng, C. Wang, V. Lau and V. Poor, "Fronthaul-Constrained Cloud Radio Access Networks: Insights and Challenges," *IEEE Wireless Communications*, pp. 152-161, 2015.
- [25] R. Waterhouse and D. Novack, "Realizing 5G: Microwave Photonics for 5G Mobile Wireless Systems," *IEEE Microwave Magazine*, vol. 16, no. 8, pp. 84-92, 2015.
- [26] W. Hong, Z. H. Jiang, C. Yu, D. Hou, H. Wang, C. Guo, Y. Hu, L. Kuai, Y. Yu, Z. Jiang, Z. Chen, J. Chen, Z. Yu, J. Zhai, N. Zhang, L. Tian, F. Wu, G. Yang, Z.-C. Hao and J. Y. Zhou, "The Role of Millimeter-Wave Technologies in 5G/6G Wireless Communications," *IEEE Journal of Microwaves*, vol. 1, no. 1, pp. 101-122, 2021.
- [27] ETSI, "5G; NR; User Equipment (UE) radio transmission and reception; Part 1: Range 1 Standalone (3GPP TS 38.101-1 V17.5.0 Release 17)," 2022.
- [28] ETSI, "5G; NR; User Equipment (UE) radio transmission and reception; Part 2: Range 2 Standalone (3GPP TS 38.101-2 version 17.5.0 Release 17)," 2021.
- [29] X. Wang, L. Kong, F. Kong, Q. Fudong, M. Xia, S. Arnon and G. Chen, "Millimeter Wave Communication: A Comprehensive Survey," *EEE Communications Surveys & Tutorials*, vol. 20, no. 3, pp. 1616-1653, 2018.
- [30] Qualcomm, "Global update on spectrum for 4G & 5G," 2020.
- [31] R. Bajracharya, R. Shrestha and H. Jung, "Future Is Unlicensed: Private 5G Unlicensed Network for Connecting Industries of Future," *Sensors*, vol. 20, no. 10, 2020.
- [32] ITU-R, "Recommendation ITU-R P.676-12; Attenuation by atmospheric gases and related effects," 2019.

- [33] J. G. Proakis and M. Salehi, *Digital Communications*, McGraw-Hill, 2008.
- [34] C. Han and S. Duan, "Impact of Atmospheric Parameters on the Propagated Signal Power of Millimeter-Wave Bands Based on Real Measurement Data," *IEEE Access*, pp. 113626-113641, 2019.
- [35] R. A. Linke, "Optical heterodyne communications systems," *IEEE Communications Magazine*, vol. 27, no. 10, pp. 36-41, 1989.
- [36] V. Urick Jr., J. D. McKinney and K. J. Williams, *Fundamentals of Microwave Photonics*, Wiley, 2015.
- [37] C. Browning, E. P. Martin, A. Farhang and L. P. Barry, "60 GHz 5G Radio-Over-Fiber Using UF-OFDM With Optical Heterodyning," *IEEE Photonics Technology Letters*, vol. 29, no. 23, 2017.
- [38] J. Beas, G. Castañón, I. Aldaya, A. Aragon-Zavala and G. Campuzano, "Millimeter-Wave Frequency Radio over Fiber Systems: A Survey," *IEEE Communications Surveys & Tutorials*, vol. 15, no. 4, pp. 1593-1619, 2013.
- [39] A. Hurtado, I. D. Henning, M. J. Adams and L. F. Lester, "Generation of Tunable Millimeter-Wave and THz Signals With an Optically Injected Quantum Dot Distributed Feedback Laser," *IEEE Photonics Journal*, vol. 5, no. 4, 2013.
- [40] X.-H. Huang, C.-Y. Li, H.-H. Lu, C.-R. Chou, H.-M. Hsia and Y.-H. Chen, "A Bidirectional FSO Communication Employing Phase Modulation Scheme and Remotely Injection-Locked DFB LD," *Journal of Lightwave Technology*, vol. 38, no. 21, pp. 5883-5893, 2020.
- [41] C.-Y. Li, H.-H. Lu, C.-R. Chou, H.-M. Hsia, C.-Y. Feng, Y.-H. Chen, Y.-T. Huang and A. Nainggolan, "A Flexible Bidirectional Fiber-FSO-5G Wireless Convergent System," *Journal of Lightwave Technology*, vol. 39, no. 5, pp. 1296-1306, 2021.
- [42] A. T. Ramos and A. J. Seeds, "Fast heterodyne optical phase-lock loop using double quantum well laser diodes," *Electronics Letters*, vol. 28, no. 1, pp. 82-83, 1992.
- [43] K. Balakier, M. J. Fice, L. Ponnampalam, A. J. Seeds and C. C. Renaud, "Monolithically Integrated Optical Phase Lock Loop for Microwave Photonics," *Journal of Lightwave Technology*, vol. 32, no. 20, pp. 3893-3900, 2014.
- [44] H. R. Rideout, J. S. Seregelyi, S. Paquet and J. Yao, "Discriminator-Aided Optical Phase-Lock Loop Incorporating a Frequency Down-Conversion Module," *IEEE Photonics Technology Letters*, vol. 18, no. 22, pp. 2344-2346, 2006.
- [45] F. Z. Fan and M. Dagenais, "Optical generation of a megahertz-linewidth microwave signal using semiconductor lasers and a discriminator-aided phase-locked loop," *IEEE Transactions on Microwave Theory and Techniques*, vol. 45, no. 8, pp. 1296-1300, 1997.
- [46] S. Rommel, D. Dodane, E. Grivas, B. Cimoli, J. Bourderionnet, G. Feugnet, A. Morales, E. ÇPikasis, C. Roeloffzen, P. van Dijk, M. Katsikis, K. Ntonti, D. Kritharidis, I. Spaleniak, P. Mitchell, M. Dubov, J. Barros Carvalho and I. Tafur Monroy, "Towards a Scaleable 5G Fronthaul: Analog Radio-over-Fiber and Space Division Multiplexing," *Journal of Lightwave Technology*, vol. 38, no. 19, pp. 5412-5422, 2020.

- [47] L. A. Johansson and A. J. Seeds, "Generation and transmission of millimeter-wave data-modulated optical signals using an optical injection phase-lock loop," *Journal of Lightwave Technology*, vol. 21, no. 2, pp. 511-520, 2003.
- [48] X. Chen, Z. Deng and J. Yao, "Photonic generation of microwave signal using a dual-wavelength single-longitudinal-mode fiber ring laser," *IEEE Transactions on Microwave Theory and Techniques*, vol. 54, no. 2, pp. 804-809, 2006.
- [49] F. van Dijk, G. Kervella, M. Lamponi, M. Chtioui, F. Lelarge, E. Vinet, Y. Robert, M. J. Fice, C. C. Renaud, A. Jimenez and G. Carpintero, "Integrated InP Heterodyne Millimeter Wave Transmitter," *IEEE Photonics Technology Letters*, vol. 26, no. 10, pp. 965-968, 2014.
- [50] M. J. Fice, E. Rouvalis, F. van Dijk, A. Accard, F. Lelarge, C. C. Renaud, G. Carpintero and A. J. Seeds, "146-GHz millimeter-wave radio-over-fiber photonic wireless transmission system," *Optics Express*, vol. 20, no. 2, pp. 1769-1774, 2012.
- [51] F. Lelarge, B. Dagens, J. Renaudier, R. Brenot, A. Accard, F. van Dijk, D. M. A. Le Gouezigou, J.-G. Provost, F. Poingt, J. Landreau, O. Drisse, E. Derouin, B. Rousseau, F. Pommereau and G.-H. Duan, "Recent Advances on InAs/InP Quantum Dash Based Semiconductor Lasers and Optical Amplifiers Operating at 1.55 μm ," *IEEE Journal of Selected Topics in Quantum Electronics*, vol. 13, no. 1, pp. 111-124, 2007.
- [52] J. Qin, R. Dai, Y. Li, Y. Meng, Y. Xu, S. Zhu and F. Wang, "20 GHz actively mode-locked thulium fiber laser," *Optics Express*, vol. 26, no. 20, pp. 25769-25777, 2018.
- [53] M.-C. Lo, R. Guzman, C. Gordon and G. Carpintero, "Mode-locked laser with pulse interleavers in a monolithic photonic integrated circuit for millimeter wave and terahertz carrier generation," *Optics Letters*, vol. 42, no. 8, pp. 1532-1535, 2017.
- [54] F. Van Dijk, M. Faugeron, F. Lelarge, M. Tran, M. Chtioui, Y. Robert, E. Vinet, A. Enard and J. Jacquet, "Asymmetrical cladding quantum dash mode-locked laser for Terahertz wide frequency comb," *2012 IEEE International Topical Meeting on Microwave Photonics*, pp. 282-28, 2012.
- [55] E. V. Viktorov, P. Mandel, A. G. Vladimirov, M. Wolfrum, G. Fiol, M. Kuntz and D. Bimberg, *CLEO/Europe - EQEC 2009 - European Conference on Lasers and Electro-Optics and the European Quantum Electronics Conference*, 2009.
- [56] F. van Dijk, B. Charbonnier, S. Constant, A. Enard, S. Fedderwitz, S. Formont, I. F. Lealman, F. Lecoche, F. Lelarge, D. Moodie, L. Ponnampalam, C. Renaud, M. J. Robertson, A. J. Seeds, A. Stohr and M. Weiss, "Quantum dash mode-locked lasers for millimeter wave signal generation and transmission," *2010 23rd Annual Meeting of the IEEE Photonics Society*, 2010.
- [57] R. Khayat-zadeh, J. Poette and B. Cabon, "Impact of phase noise in 60-GHz radio-over-fiber communication system based on passively mode-locked laser," *Journal of Lightwave Technology*, vol. 32, no. 20, pp. 3529-3535, 2014.
- [58] L. A. Coldren, S. W. Corzine and M. L. Masanovic, *Diode Lasers and Photonic Integrated Circuits*, John Wiley & Sons Inc, 2012.
- [59] L. Zhang, X. Xin, B. Liu, Y. Wang, J. Yu and C. Yu, "OFDM Modulated WDM-ROF System based on PCF-Supercontinuum," *Optics Express*, vol. 18, no. 14, pp. 15003-15008, 2010.

- [60] T. Nakasyotani, H. Toda, T. Kuri and K. Kitayama, "Wavelength-division-multiplexed Millimeter-waveband radio-on-fiber system using a supercontinuum light source," *Journal of Lightwave Technology*, vol. 24, no. 1, pp. 404-410, 2006.
- [61] G. Qi, J. Yao, J. Seregelyi, S. Paquet and C. Belisle, "Optical generation and distribution of continuously tunable millimeter-wave signals using an optical phase modulator," *Journal of Lightwave Technology*, vol. 23, no. 9, pp. 2687-2695, 2005.
- [62] P. Shen, J. James, N. J. Gomes, P. G. Huggard and B. N. Ellison, "Low-Cost, Continuously Tunable, Millimeter-Wave Photonic LO Generation Using Optical Phase Modulation and DWDM Filters," *IEEE Photonics Technology Letters*, vol. 20, no. 23, pp. 1986-1988, 2008.
- [63] X. Li, J. Xiao and J. Yu, "W-Band Vector Millimeter-Wave Signal Generation Based on Phase Modulator With Photonic Frequency Quadrupling and Precoding," *Journal of Lightwave Technology*, vol. 35, no. 13, pp. 2548-2558, 2017.
- [64] M. Zhao, W. Zhou, L. Zhao, J. Xiao, X. Li, F. Zhao and J. Yu, "A New Scheme to Generate Multi-Frequency Mm-Wave Signals Based on Cascaded Phase Modulator and I/Q Modulator," *IEEE Photonics Journal*, vol. 11, no. 5, 2019.
- [65] G. M. Hasan, M. Hasan and T. J. Hall, "Performance Analysis of a Multi-Function Mach-Zehnder Interferometer Based Photonic Architecture on SOI Acting as a Frequency Shifter," *Photonics*, vol. 8, no. 12, 2021.
- [66] Y. Zhu, X. Miao, Q. Wu, L. Yin and W. Hu, "Imbalanced Mach-Zehnder Modulator for Fading Suppression in Dispersion-Uncompensated Direct Detection System," *Electronics*, vol. 10, no. 22, 2021.
- [67] P.-T. Shih, J. J. Chen, C.-T. Lin, W.-J. Jiang, H.-S. Huang and P.-C. Peng, "Optical millimeter-wave signal generation via frequency 12-tupling," *Journal of Lightwave Technology*, vol. 28, no. 1, pp. 71-78, 2010.
- [68] T. Wang, M. Chen, H. Chen, J. Zhang and S. Xie, "Millimeter-Wave Signal Generation Using Two Cascaded Optical Modulators and FWM Effect in Semiconductor Optical Amplifier," *IEEE Photonics Technology Letters*, vol. 19, no. 16, pp. 1191-1193, 2007.
- [69] M. Alom, S. Haxha and A. Aggoun, "Photonic Mixer Incorporating All-Optical Microwave Frequency Generator Based on Stimulated Brillouin Scattering Using Single Laser Source," *IEEE Access*, vol. 8, pp. 37045-37051, 2020.
- [70] X. S. Yao, "Brillouin selective sideband amplification of microwave photonic signals," *IEEE Photonics Technology Letters*, vol. 10, no. 1, pp. 138-140, 1998.
- [71] T. Schneider, D. Hannover and M. Junker, "Investigation of Brillouin scattering in optical fibers for the generation of Millimeter waves," *Journal of Lightwave Technology*, vol. 24, no. 1, pp. 295-304, 2006.
- [72] M. Junker, T. Schneider, K.-U. Lauterbach, R. Henker, M. J. Amman and A. Schwarzbacher, "High Quality Millimeter Wave Generation via Stimulated Brillouin Scattering," *2007 Conference on Lasers and Electro-Optics (CLEO)*, 2007.
- [73] Huber+Suhner, "SUCOFLEX_570_S," 2022.
- [74] D. Che, "Analog vs Digital Radio-Over-Fiber: A Spectral Efficiency Debate From the SNR Perspective," *Journal of Lightwave Technology*, vol. 39, no. 16, pp. 5325-5335, 2021.

- [75] J. Guillory, E. Tanguy, A. Pizzinat, B. Charbonnier, S. Meyer, C. Algani and H. Li, "A 60 GHz Wireless Home Area Network With Radio Over Fiber Repeaters," *Journal of Lightwave Technology*, vol. 29, no. 16, pp. 2482-2488, 2011.
- [76] R. Beresford, W. Cheng and P. Roberts, "Low cost RF over fiber distribution for radio astronomy phased arrays," *2017 XXXIInd General Assembly and Scientific Symposium of the International Union of Radio Science (URSI GASS)*, 2017.
- [77] T.-S. Cho and K. Kim, "Optimization of radio-on-fiber systems employing ODSB signals by utilizing a dual-electrode Mach-Zehnder modulator against IM3," *IEEE Photonics Technology Letters*, vol. 18, no. 9, pp. 1076-1078, 2006.
- [78] T. Chikama, S. Watanabe, T. Naito, H. Onaka, T. Kiyonaga, Y. Onoda, H. Miyata, M. Suyama, M. Seino and H. Kuwahara, "Modulation and demodulation techniques in optical heterodyne PSK transmission systems," *Journal of Lightwave Technology*, vol. 8, no. 3, pp. 309-322, 1990.
- [79] C.-T. Lin, J. Chen, S.-P. Dai, P.-C. Peng and S. Chi, "Impact of Nonlinear Transfer Function and Imperfect Splitting Ratio of MZM on Optical Up-Conversion Employing Double Sideband With Carrier Suppression Modulation," *Journal of Lightwave Technology*, vol. 26, no. 15, pp. 2449-2459, 2008.
- [80] L. Vallejo, J. Mora, D.-N. Nguyen, J. Bohata, V. Almenar, S. Zvanovec and B. Ortega, "On the 40 GHz Remote Versus Local Photonic Generation for DML-Based C-RAN Optical Fronthaul," *Journal of Lightwave Technology*, vol. 39, no. 21, pp. 6712-6723, 2021.
- [81] H.-M. Nguyen, C.-C. Wei, C.-Y. Chuang, J. Chen, H. Taga and T. Tsuritani, "Reducing the Impact of Nonlinear Distortion in DML-Based OFDM Transmission by Frequency Gap," *Journal of Lightwave Technology*, vol. 36, no. 23, pp. 5617-5625, 2018.
- [82] G. H. Smith, D. Novak and Z. Ahmed, "Overcoming Chromatic-Dispersion Effects in Fiber-Wireless Systems Incorporating External Modulators," *IEEE Transactions on Microwave Theory and Techniques*, vol. 45, no. 8, pp. 1410-1415, 1997.
- [83] Y. Cui, K. Xu, J. Dai, X. Sun, Y. Dai, Y. Ji and J. Lin, "Overcoming Chromatic-Dispersion-Induced Power," *IEEE Photonics Technology Letters*, vol. 24, no. 15, pp. 1173-1176, 2012.
- [84] V. J. Urick and F. Bucholtz, "Compensation of arbitrary chromatic dispersion in analog links using a modulation-diversity receiver," *IEEE Photonics Technology Letters*, vol. 17, no. 4, pp. 893-895, 2005.
- [85] J. Ma, J. Yu, C. Yu, X. Xin, J. Zeng and L. Chen, "Fiber Dispersion Influence on Transmission of the Optical Millimeter-Waves Generated Using LN-MZM Intensity Modulation," *Journal of Lightwave Technology*, vol. 25, no. 11, pp. 3244-3256, 2007.
- [86] E. Sanchez, D. Perez-Lopez, P. dasMahapatra and J. Capmany, "Modeling amplified arbitrary filtered microwave photonic links and systems," *Optics Express*, vol. 29, no. 10, pp. 14757-14772, 2021.
- [87] D. Killinger, "Free Space Optics for Laser Communication Through the Air," *Optics and Photonics News*, vol. 13, no. 10, pp. 36-42, 2002.
- [88] W.-S. Tsai, H.-H. Lu, C.-Y. Li, T.-C. Lu, C.-H. Liao, C.-A. Chu and P.-C. Peng, "A 20-m/40-Gb/s 1550-nm DFB LD-Based FSO link," *IEEE Photonics Journal*, vol. 7, no. 6, 2015.

- [89] Z. Zhao, Z. Zhang, J. Tan, Y. Liu and J. Liu, "200 Gb/s FSO WDM Communication System Empowered by Multiwavelength Directly Modulated TOSA for 5G Wireless Networks," *IEEE Photonics Journal*, vol. 10, no. 4, 2018.
- [90] H.-H. Lu, C.-Y. Li, W.-S. Tsai, P.-S. Chang, Y.-T. Chen, C.-X. Liu, T. Ko and Y.-Y. Lin, "Simultaneous Transmission of 5G MMW and Sub-THz Signals Through a Fiber-FSO-5G NR Converged System," *Journal of Lightwave Technology*, vol. 40, no. 8, pp. 2348-2356, 2022.
- [91] J. Libich and S. Zvanovec, "Influences of turbulences in near vicinity of buildings on free-space optical links," *IET Microwaves, Antennas & Propagation*, vol. 5, no. 9, pp. 1039-1044, June 2011.
- [92] K. Niachou, I. Livada and M. Santamouris, "Experimental study of temperature and airflow distribution inside an urban street canyon during hot summer weather conditions. Part II: Airflow analysis," *Building and Environment*, vol. 43, no. 8, pp. 1393-1403, August 2008.
- [93] D.-N. Nguyen, J. Bohata, J. Spacil, D. Dousek, M. Komanec, S. Zvanovec, Z. Ghassemlooy and B. Ortega, "M-QAM transmission over hybrid microwave photonic links at the K-band," *Optics Express*, vol. 27, no. 23, pp. 33745-33756, 2019.
- [94] H. Kaushal and G. Kaddoum, "Free Space Optical Communication: Challenges and Mitigation Techniques," *arxiv*, vol. arXiv:1705.10630, 2015.
- [95] D. K. Borah and D. G. Voelz, "Pointing Error Effects on free-space optical communication links in the presence of atmospheric turbulence," *Journal of Lightwave Technology*, vol. 27, no. 18, pp. 3965-3973, September 2009.
- [96] M. A. Esmail, A. Ragheb, H. Fathallah and M.-S. Alouini, "Investigation and demonstration of high speed full-optical hybrid FSO/fiber communication system under light sand storm condition," *IEEE Photonics Journal*, vol. 9, no. 1, pp. 1-12, 2017.
- [97] H. Kaushal, V. K. Jain and S. Kar, *Free-Space Optical Channel Models*, Springer, 2017.
- [98] S. A. Al-Gailani, M. F. M. Salleh, A. A. Salem, R. Q. Shaddad, U. U. Shik, N. A. Algeelani and T. A. Almohamad, "A Survey of Free Space Optics (FSO) Communication Systems, Links, and Networks," *IEEE Access*, vol. 9, pp. 7353-7374, 2020.
- [99] L. C. Andrews, R. L. Phillips and C. Y. Hopen, *Laser Beam Scintillation with Applications*, SPIE Press, 2001.
- [100] L. Vallejo, M. Komanec, B. Ortega, J. Bohata, D.-N. Nguyen, S. Zvanovec and V. Almenar, "Impact of thermal-induced turbulent distribution along FSO link on transmission of photonically generated mmW signals in the frequency range 26–40 GHz," *IEEE Photonics Journal*, vol. 12, no. 1, 2020.
- [101] C. Henrique de Souza Lopes, E. Saia Lima, L. A. Melo Pereira, R. Maia Borges, A. Carvalho Ferreira, M. Abreu, W. Damascena Dias, D. Henrique Spadoti, L. Leonel Mendes and A. Cerqueira Sodre Junior, "Non-Standalone 5G NR Fiber-Wireless System Using FSO and Fiber-Optics Fronthauls," *Journal of Lightwave Technology*, vol. 39, no. 2, pp. 406-417, 2021.
- [102] A. Malik and P. Singh, "Free Space Optics: Current Applications and Future Challenges," *International Journal of Optics*, vol. 2015, 2015.

- [103] A. K. Majumdar and J. C. Ricklin, *Free-Space Laser Communications: Principles and Advances*, Springer, 2010.
- [104] G. Qi, J. Yao, J. Seregelyi, S. Paquet, C. Belisle, X. Zhang, K. Wu and R. Kashyap, "Phase-Noise Analysis of Optically Generated Millimeter-Wave Signals With External Optical Modulation Techniques," *Journal of Lightwave Technology*, vol. 24, no. 12, pp. 4861-4875, 2006.
- [105] G. Ning, P. Shum and J. Zhou, "Dispersion effect and compensation in optical-carrier-suppressed modulation transport systems," *Journal of the Optical Society of America A*, vol. 24, no. 11, pp. 3432-3436, 2007.
- [106] C. Lim, A. Nirmalathas, M. Bakaul, P. Gamage, K.-L. Lee, Y. Yang, D. Novak and R. Waterhouse, "Fiber-Wireless Networks and Subsystem Technologies," *Journal of Lightwave Technology*, vol. 28, no. 4, pp. 390-405, 2010.
- [107] L. Vallejo, B. Ortega, J. Bohata, S. Zvanovec and V. Almenar, "Experimental Photonic 40 – 90 GHz Millimetre-Wave Signal Generation and 10 Gb/s 32-QAM Signal Transmission over Hybrid Fiber/FSO 5G Networks," *2019 21st International Conference on Transparent Optical Networks (ICTON)*, pp. 1-4, 2019.
- [108] L. Vallejo, B. Ortega, J. Bohata, S. Zvanovec and V. Almenar, "Photonic multiple millimeter wave signal generation and distribution over reconfigurable hybrid SSMF/FSO links," *Optical Fiber Technology*, vol. 54, 2020.
- [109] L. Vallejo, B. Ortega, V. Almenar, J. Bohata, S. Zvanovec and D.-N. Nguyen, "SOA-aided photonic signal generation for hybrid fibre and FSO 5G transmission links," *Proceedings Volume 11358, Nonlinear Optics and its Applications 2020; 113581R*, 2020.
- [110] L. Vallejo, D.-N. Nguyen, J. Bohata, B. Ortega and S. Zvanovec, "M-QAM signal transmission at the photonic generated K-band over thermal-induced turbulent FSO links with different turbulence distributions," *Applied Optics*, vol. 59, no. 16, pp. 4997-5005, 2020.
- [111] S. Kumar and M. J. Deen, *Fiber Optic Communications: Fundamentals and Applications*, Wiley, 2014.
- [112] K. Zhang, Q. Zhuge, H. Xin, W. Hu and D. V. Plant, "Performance comparison of DML, EML and MZM in dispersion-unmanaged short reach transmissions with digital signal processing," *Optics Express*, vol. 26, no. 26, pp. 34288-34304, 2018.
- [113] A. Chaaban and M. S. Alouini, "Optical intensity modulation direct detection versus heterodyne detection: A high-SNR capacity comparison," *2015 5th International Conference on Communications and Networking (COMNET)*, 2015.
- [114] R. S. Tucker, "Green Optical Communications—Part I: Energy Limitations in Transport," *IEEE Journal of Selected Topics in Quantum Electronics*, vol. 17, no. 2, pp. 245-260, 2010.
- [115] M. Shahin, K. Ma, A. Abbasi, G. Roelkens and G. Morthier, "45 Gb/s Direct Modulation of Two-Section InP-on-Si DFB Laser Diodes," *IEEE Photonics Technology Letters*, vol. 30, no. 8, pp. 685-687, 2018.
- [116] B. G. Kim, S. H. Bae, H. Kim and Y. C. Chung, "RoF-based mobile fronthaul networks implemented by using DML and EML for 5G wireless communication systems," *Journal of Lightwave Technology*, vol. 36, no. 14, pp. 2874-2881, 2018.

- [117] L. A. Neto, E. Didier, G. Naveena, C. Philippe, D. Qian, T. Fatoumata, A. Thomas, H. Rajaâ and A.-B. Christelle, "Simple estimation of fiber dispersion and laser chirp parameters using the downhill simplex fitting algorithm," *Journal of Lightwave Technology*, vol. 31, no. 2, pp. 334 - 342, 2013.
- [118] D. Large and J. Farmer, *Broadband Cable Access Networks*, Morgan Kaufmann, 2009.
- [119] I. Tomkos, I. Roudas, R. Hesse, N. Antoniadis, A. Boskovic and R. Vodhanel, "Extraction of laser rate equations parameters for representative simulations of metropolitan-area transmission systems and networks," *Optics Communications*, vol. 194, pp. 109-129, 2001.
- [120] K. S. C. Yong, M. K. Haldar and J. F. Webb, "Harmonic and Intermodulation Distortion in Direct Intensity Modulated Quantum Cascade Lasers," *Journal of Lightwave Technology*, vol. 32, no. 20, pp. 3735-3741, 2014.
- [121] J. C. Cartledge and A. S. Karar, "100 Gb/s Intensity Modulation and Direct Detection," *Journal of Lightwave Technology*, vol. 32, no. 16, pp. 2809-2814, 2014.
- [122] Y. Matsui, T. Pham, T. Sudo, G. Carey, B. Young, J. Xu, C. Cole and C. Roxlo, "28-Gbaud PAM4 and 56-Gb/s NRZ Performance Comparison Using 1310-nm Al-BH DFB Laser," *Journal of Lightwave Technology*, vol. 34, no. 11, pp. 2677-2683, 2016.
- [123] K. Van Gasse, J. Van Kerrebrouck, A. Abbasi, G. Torfs, H. Chen, X. Yin, J. Bauwelinck and G. Roelkens, "480Mbps/1 Gbps radio-over-fiber link based on a directly modulated III-V-on-Silicon DFB laser," *2016 IEEE International Topical Meeting on Microwave Photonics (MWP)*, pp. 328-331, 2016.
- [124] J. Bohata, M. Komanec, J. Spáčil, Z. Ghassemlooy, S. Zvánovec and R. Slavík, "24-26 GHz radio over fiber and free space optics for 5G systems," *Optics Letters*, vol. 43, no. 5, pp. 1035-1038, Mar. 2018.
- [125] T. Shao, E. P. Martin, P. M. Anandarajah and L. P. Barry, "60-GHz direct modulation-direct detection OFDM-RoF system using gain-switched laser," *IEEE Photonics Technology Letters*, vol. 27, no. 2, pp. 193-196, 2015.
- [126] L. Vallejo, J. Mora, D.-N. Nguyen, J. Bohata, V. Almenar, S. Zvanovec and B. Ortega, "On the 40 GHz Remote Versus Local Photonic Generation for DML-Based C-RAN Optical Fronthaul," *Journal of Lightwave Technology*, vol. 39, no. 21, pp. 6712-6723, 2021.
- [127] I. P. Kaminow, T. Li and A. E. Willner, *Optical Fiber Telecommunications Volume VIB: Systems and Networks*, Academic Press, 2013.
- [128] J. Van Kerrebrouck, H. Li, S. Spiga, M. C. Amann, X. Yin, J. Bauwelinck, P. Demeester and G. Torfs, "10 Gb/s Radio-Over-Fiber at 28 GHz Carrier Frequency Link Based on 1550 nm VCSEL Chirp Enhanced Intensity Modulation after 2 km Fiber," *2018 Optical Fiber Communications Conference and Exposition (OFC)*, pp. 1-3, 2018.
- [129] L. Vallejo, J. Mora, D.-N. Nguyen, J. Bohata, V. Almenar, S. Zvanovec and B. Ortega, "On the 40 GHz Remote versus Local Photonic Generation for DML-based C-RAN Optical Fronthaul," *Journal of Lightwave Technology*, vol. 39, no. 21, pp. 6712-6723, 2021.
- [130] L. Vallejo, J. Mora and B. Ortega, "Harmonic and Intermodulation Distortion Analysis in Directly Modulated Lasers over Local and Remote Photonically Generated

- Millimeter-Wave Signals,” *Journal of Lightwave Technology*, vol. 40, no. 15, pp. 5128-5140, 2022.
- [131] J. Le Bihan and G. Yabre, “FM and IM intermodulation distortions in directly modulated single-mode semiconductor lasers,” *IEEE Journal of Quantum Electronics*, vol. 30, no. 4, pp. 89-904, 1994.
- [132] L. Zhang and D. A. Ackerman, “Second- and third-order harmonic distortion in DFB lasers,” *IEEE Journal of Quantum Electronics*, vol. 31, no. 11, pp. 1974-1980, 1995.
- [133] L. Vallejo, B. Ortega, D.-N. Nguyen, J. Bohata, V. Almenar and S. Zvanovec, “Usability of a 5G Fronthaul Based on a DML and External Modulation for M-QAM Transmission Over Photonically Generated 40 GHz,” *IEEE Access*, vol. 8, pp. 223730-223742, 2020.
- [134] C. Sanchez, B. Ortega, J. L. Wei, Tang, J. and J. Capmany, “Analytical formulation of directly modulated OOFDM signals transmitted over an IM/DD dispersive link,” *Optics Express*, vol. 21, no. 6, pp. 7651-7666, 2013.
- [135] R. Zhang, F. Lu, M. Xu, S. Liu, P.-C. Peng, S. Shen, J. He, H. J. Cho, Q. Zhou, S. Yao and G.-K. Chang, “An ultra-reliable MMW/FSO A-Rof system based on coordinated mapping and combining technique for 5G and beyond mobile fronthaul,” *Journal of Lightwave Technology*, vol. 36, no. 20, pp. 4952-4959, 15 October 2018.
- [136] Y. Fu, X. Zhang, B. Hraimel, T. Liu and D. Shen, “Mach-Zehnder: A Review of Bias Control Techniques for Mach-Zehnder Modulators in Photonic Analog Links,” *IEEE Microwave Magazine*, vol. 14, no. 7, pp. 102-107, 2013.
- [137] P. Torres-Ferrera, G. Rizzelli, H. Wang, V. Ferrero and R. Gaudino, “Experimental Demonstration of 100 Gbps/λ C-Band Direct-Detection Downstream PON Using Non-Linear and CD Compensation with 29 dB+ OPL Over 0 Km–100 Km,” *Journal of Lightwave Technology*, vol. 40, no. 2, pp. 547-556, 2022.
- [138] Y. Zhu, F. Zhang, F. Yang, L. Zhang, X. Ruan, Y. Li and Z. Chen, “Toward Single Lane 200G Optical Interconnects With Silicon Photonic Modulator,” *Journal of Lightwave Technology*, vol. 38, no. 1, pp. 67-74, 2020.
- [139] H. Yamazaki, M. Nagatani, H. Wakita, Y. Ogiso, M. Nakamura, M. Ida, H. Nosaka, T. Hashimoto and Y. Miyamoto, “IMDD Transmission at Net Data Rate of 333 Gb/s Using Over-100-GHz-Bandwidth Analog Multiplexer and Mach–Zehnder Modulator,” *Journal of Lightwave Technology*, vol. 37, no. 8, pp. 1772-1778, 2019.
- [140] J. Bohata, L. Vallejo, B. Ortega and S. Zvanovec, “Optical CS-DSB Schemes for 5G mmW Fronthaul Seamless Transmission,” *IEEE Photonics Journal*, vol. 14, no. 2, 2022.
- [141] J. Bohata, D. N. Nguyen, J. Spacil, M. Komanec, B. Ortega, L. Vallejo, Z. Ghassemlooy and S. Zvanovec, “Experimental comparison of DSB and CS-DSB mmW formats over a hybrid fiber and FSO fronthaul network for 5G,” *Optics Express*, vol. 29, no. 17, pp. 27768-27782, 2021.
- [142] L. Andrews and R. Phillips, *Laser Beam Propagation Through Random Media*, SPIE Press, 2005.
- [143] X. Chen and J. Yao, “A high spectral efficiency coherent microwave photonic link employing both amplitude and phase modulation with digital phase noise cancellation,” *Journal of Lightwave Technology*, vol. 33, no. 14, pp. 3091-3097, 2015.

- [144] D.-N. Nguyen, L. Vallejo, V. Almenar, B. Ortega, P. T. Dat, S. T. Le, J. Bohata and S. Zvanovec, "Full-duplex transmission of multi-Gb/s subcarrier multiplexing and 5G NR signals in 39 GHz band over fiber and space," *Applied Optics*, vol. 61, no. 5, pp. 1183-1193, 2022.
- [145] L. Vallejo, B. Ortega, J. Mora, D.-N. Nguyen, C. Guerra, J. Bohata, J. Spacil and S. Zvanovec, "Demonstration of M-QAM OFDM Bidirectional 60/25 GHz Transmission over 10 km Fiber, 100 m FSO and 2 m Radio Seamless Heterogeneous Fronthaul Link," *Optical Fiber Technology*, 2022.
- [146] J. Kreissl, V. Vercesi, U. Troppenz, T. Gaertner, W. Wenisch and M. Schell, "Up to 40 Gb/s Directly Modulated Laser Operating at Low Driving Current: Buried-Heterostructure Passive Feedback Laser (BH-PFL)," *IEEE Photonics Technology Letters*, vol. 24, no. 5, pp. 362-364, 2012.
- [147] ETSI, "LTE; Evolved Universal Terrestrial Radio Access (E-UTRA); Base Station (BS) and repeater ElectroMagnetic Compatibility (EMC) (3GPP TS 36.113 version 15.3.0 Release 15)," 2019.
- [148] F. Effenberger and X. Liu, "Power-efficient method for IM-DD optical transmission of multiple OFDM signals," *Optics Express*, vol. 23, no. 10, pp. 13571-13579, 2015.
- [149] K. Kikuchi, "Fundamentals of Coherent Optical Fiber Communications," *Journal of Lightwave Technology*, vol. 34, no. 1, pp. 157-179, 2016.
- [150] Keysight Technologies, "Digital Modulation in Communications Systems - An Introduction," *Application Note*, 2014.
- [151] Rohde & Schwarz, "Modulation and Signal Generation with R&S Signal Generators," *Educational Note*, 2016.
- [152] M. S. Moreolo, R. Munoz and G. Junyent, "Novel Power Efficient Optical OFDM Based on Hartley Transform for Intensity-Modulated Direct-Detection Systems," *Journal of Lightwave Technology*, vol. 28, no. 5, pp. 798-805, 2010.
- [153] J. Yu and N. Chi, *Digital Signal Processing In High-Speed Optical Fiber Communication Principle and Application*, Springer, 2020.
- [154] S. D. Dissanayake and J. Armstrong, "Comparison of ACO-OFDM, DCO-OFDM and ADO-OFDM in IM/DD Systems," *Journal of Lightwave Technology*, vol. 31, no. 7, pp. 1063-1072, 2013.
- [155] B. J. C. Schmidt, A. J. Lowery and J. Armstrong, "Experimental Demonstrations of Electronic Dispersion Compensation for Long-Haul Transmission Using Direct-Detection Optical OFDM," *Journal of Lightwave Technology*, vol. 26, no. 1, pp. 196-203, 2008.
- [156] H. A. Mahmoud and H. Arslan, "Error vector magnitude to SNR conversion for nondata-aided receivers," *IEEE Transactions on Wireless Communications*, vol. 8, no. 5, pp. 2694-2704, 2009.
- [157] Y. Tan, F. Zhao, M. He, Y. Wang, W. Zhou, J. Zhang, M. Zhu, Y. Shi and J. Yu, "Transmission of High-Frequency Terahertz Band Signal Beyond 300 GHz Over Metallic Hollow Core Fiber," *Journal of Lightwave Technology*, vol. 40, no. 3, pp. 700-707, 2022.

- [158] J. Cho, C. Xie and P. J. Winzer, "Analysis of soft-decision FEC on non-AWGN channels," *Optics Express*, vol. 20, no. 7, pp. 7915-7928, 2012.

